COAL FLY ASH AND THE CIRCULAR ECONOMY

by

ROBERT BLISSETT

A thesis submitted to
The University of Birmingham
for the degree of
DOCTOR OF ENGINEERING

School of Chemical Enigineering
College of Engineering and Physical Sciences
The University of Birmingham
June 2015

Abstract

Coal fly ash (CFA) can be regarded as a unique material with the potential to be a showcase waste to illustrate the concept of the circular economy. Like many waste materials it is inherently heterogeneous. The application of a processing scheme to power station CFA allows the exploitation of multiple components of the product. The CFA can be separated into low density, carbon, and magnetic concentrates as well as the residual fly ashes. This work contributes to an ever growing body of research that suggests multicomponent utilisation of CFA is technologically, environmentally, and economically imperative. The thesis explores five separate but related themes that attempt to increase the exploitation of CFA.

In the first it is shown that CFA products that are derived from a commercial scale processing scheme exhibit differences in bulk chemistry, mineralogy, and particle size. Some of these results are surprising, for instance, the magnetic concentrate actually contains a small amount of magnetite relative to the amount of total iron. It was also shown that in a particular CFA from the UK that elevated levels of rare earth elements are concentrated in the residual ash fractions. CFA was separated into density fractions and analysed for chemical and mineral content. As a result of this, it is suggested that potassium content could play a crucial role in cenosphere formation because of its role as a network extender with resulting increases in melt viscosity.

In the second theme, a study of the rheology of CFA suspensions allowed the development of an empirical modeling procedure that is capable of describing the shear thinning behaviour of high concentrations of CFA with both suspension concentration and shear rate.

The third aspect of the thesis explores the current method of recovering lightweight cenospheres from bulk CFA. It is shown that the current stirred tank design is inefficient. Two competing mechanisms limit the efficiency of separation: the requirement to maintain

an off-bottom suspension and operating the impeller at a speed below that at which cenospheres are pulled down from the surface. A new design is proposed based on the settling data of the CFA and theoretical thickener design principles.

The fourth part of the thesis covers the separation of carbon from CFA using an environmentally benign waste material such as vegetable oil. The recovery of carbon from the CFA was achieved using an oil agglomeration technique. A design of experiment matrix was conducted in which it was shown that, contrary to previous literature on the subject, the content of carbon in the agglomerate increases with increases in all experimental factors: impeller speed, time, and oil. A mechanism for this disparity is suggested based on the presence of two different carbon forms in the CFA. The procedure was improved by the use of an emulsified binding agent which had the effect of extending the binder allowing a two-fold reduction in the quantity of oil required.

Finally, a silver activated titanium dioxide floating photocatalyst has been manufactured using a facile slurry hydrolysis technique and cenospheres as a readily abundant industrially derived substrate. The importance of using a substrate diameter as low as practically possible has been shown. Silver activation was found to enhance activity of the catalyst up to a certain loading. Mixing of the system was shown to improve the decoloration efficiency of a model pollutant system which has important implications for industrial use.

To my wonderful wife Deirdre...

for your stoic endurance, your unwavering support, and most of all, for your love, I dedicate this work to you.

ACKNOWLEDGEMENTS

I have a number of people and institutions who have been instrumental in allowing me to complete this thesis. Firstly I'd like to thank my supervisor Professor Neil Rowson for his support, advice, and good humour throughout my time at the University of Birmingham. My industrial supervisor Nigel Smalley has also provided useful discussions along the way despite a difficult commercial environment for my sponsoring company RockTron Mineral Services Ltd. Dr Richard Greenwood does a superb job of managing the EngD students in the centre for Formulation Engineering and I'd like to thank him for his willingness to give his time reading my thesis and offering advice throughout my time spent completing my EngD. I'd also like to thank Dr Helen Brannon of Kratos and Dr Andreia Molea of the Technical University of Cluj-Napoca for their help performing the XPS and UV-vis analysis in Chapter 7 respectively. I'd like to thank Thomas Mothersdale for help in performing some of the experiments in Chapter 6.

I'd like to thank the University of Birmingham, the Engineering and Physical Sciences Research Council (EPSRC), RockTron Mineral Services Ltd for funding and hosting my EngD. A special thanks goes to the Royal Commission for the Exhibition of 1851 who awarded me an Industrial Fellowship.

I'd like to thank my parents: my Mum always encouraged a love of reading that has fared me well over the past few years even if the subject matter has often been a little dry; my Dad was my direct inspiration, it has always been a great source of comfort to know that if he could do a PhD, then so could I; although I maintain that an EngD in formulation engineering is eminently more useful than a PhD in astrophysics.

Finally, to all my friends along the way. You've been nothing but an immensely fun

distraction, this was completed in spite of your presence in my life.

CONTENTS

LIST OF FIGURES

LIST OF TABLES

ABBREVIATIONS

Materials

CFA	Coal fly ash
FAC	Fly ash cenosphere
HREY	Heavy rare earth plus yttrium element
HVFA	High volume fly ash
IFA-C	Coarse improved fly ash residue
IFA-F	Fine improved fly ash residue
IFA-UF	Ultra fine improved fly ash residue
LOI	Loss-on-ignition
LREY	Light rare earth plus yttrium element
Mag	Magnetic concentrate
MO	Methyl orange
MREY	Medium rare earth plus yttrium element
OPC	Ordinary portland cement
PGPR	PolyGlycerol PolyRicinoleate
PSD	Particle size distribution
SCFAC	Size classified fly ash cenosphere
REO	Rare earth element plus yttrium oxide
REY	Rare earth element plus yttrium
TiTP	Titanium isopropoxide

Methods

EDS	Energy dispersive spectroscopy
FIB	Focused ion beam
ICP-AES	Inductively coupled plasma atomic emission spectroscopy
ICP-MS	Inductively coupled plasma mass spectroscopy
SEM	Scanning electron microscopy
XRD	X-ray diffraction
XPS	X-ray photoelectron spectroscopy

CHAPTER 1

INTRODUCTION

1.1 Background

The concept of sustainable development emerged in the early and mid 1980s as an attempt to *"bridge the gap between environmental concerns about the increasingly evident ecological consequences of human activities and socio-political concerns about human development issues"* [1]. Since *Our Common Future* popularised the concept of sustainable development [2], researchers and industrialists have searched for ways of making industrial processes more sustainable.

Industrial ecology (IE) is a discipline that has gained traction over the past decades. It maintains that the most efficient way to achieve sustainable development is via the imitation of the natural world. To conserve and optimise natural resource consumption, a practitioner of IE would advocate that the by-product generated in a particular industrial process should be assimilated by other industrial activities. This minimises the overall material and energy consumption as well as reducing environmental impacts and economic costs [3].

The traditional linear model of industrial production is becoming increasingly outdated. This model relies on the assumption that resources are abundant, that the supply chain to obtain them is easy, and that waste that is produced during their use is cheap to dispose of. This has not gone unnoticed by policy makers. The European Commission

recently underlined their understanding that a reliance on linear industrial production threatens the competitiveness of Europe by publishing a report entitled *"Towards a circular economy: a zero waste programme for Europe"* [4]. It is interesting to note the way the language in the report is couched; it talks of business, innovation, and growth rather than a sole focus on the environmental benefits that eliminating waste will undoubtedly provide. Importantly for the science and engineering academic community, the report calls for new ways of turning waste into a resource.

Coal fly ash (CFA) is generated during the combustion of pulverised coal in coal-fired power stations; as such it is an industrial by-product that if not put to beneficial use, is a recognised environmental pollutant. CFAs are generated at 1200-1700°C from the various inorganic and organic constituents of the feed coal. Because of the scale of the variety of the components, CFAs are one of the most complex anthropogenic materials that can be characterised. For example, approximately 316 individual minerals and 188 mineral groups have been identified in different CFAs [5].

CFA is an excellent illustration of the concept of IE in progress. It's reuse has a history dating back to the industrial revolution. In Victorian Britain it was mixed with lime to manufacture bricks [6]. However, it was not until large amounts of the material became available because of the introduction of air quality standards that obligated power utilities to capture fine fly ash, that it's use became more widespread. It is said that coal fly ash was used in the construction of the Hoover dam to help control the heat of hydration of concrete although a reliable source to back this claim up could not be found.

Despite having a long history of utilisation, CFA is still sent to landfill or stored in lagoons. Some 750 million tonnes of CFA are generated globally and of this only 20-50 % is utilised in applications other than land reclamation and restoration projects [7, 8]. There is clearly scope for further improvement. Novel applications for coal fly ash are numerous in the academic literature and emergent over the last 15 years has been the concept of multi-component utilisation [5,7,9–12]. The objective of this is to make use of the intrinsic heterogeneity of CFA to separate it into distinct fractions: namely a low density, enriched

carbon, magnetic, and a residual aluminosilicate material. To successfully turn this from concept to reality requires further research into both the separation technology and the applications for the products of CFA processing.

The problem of CFA disposal is only expected to get worse as the demand for energy grows. In 2010 it was predicted that the next two decades would see the installation of the same amount of power generation capacity as that installed over the whole of the 20th century. Part of this increase in demand is likely to be fulfilled by renewable energy sources; however, due to its abundance in energy intensive countries such as China and India, coal is likely to become an increasingly dominant fuel for power generation [13].

1.2 Objectives

The ultimate global aim for the field of CFA research is to provide enough understanding of the properties of CFA to be able to recommend an application, or a processing route to provide products for a series of applications such that it's utilisation rate approaches 100%. The objectives of this research were determined in order to contribute to this understanding:

1. Complete a thorough review of the literature in the area of multi component utilisation of CFA so that the subsequent experimental research could be more targeted. There were already a multitude of papers on the applications of CFA in its unrefined state [12] and on the potential application of extracted products [14], however little work had been carried out to summarise the processing aspects from a purely engineering aspect.

2. A characterisation of CFA and the products derived from CFA on a commercial basis. This has previously been carried out on laboratory isolation of components [5, 9–11], but not for commercial scale separations.

3. An understanding of the processes required to separate hollow low density spheres

from a CFA slurry including an investigation into the slurry rheology, a laboratory scale investigation of a mixer settler separation device, and a theoretical investigation of a new process design.

4. An assessment of whether an emulsified vegetable oil allows a reduction in the quantity required to achieve good separation performance in the extraction of unburned carbon from bulk CFA.

5. Improvement of the formulation of TiO_2 coated hollow spheres and gain an understanding of the unique implications of how the floating properties of the manufactured photocatalyst relate to the degradation kinetics of a model pollutant.

1.3 Relevance to RockTron Mineral Services Ltd.

This work was sponsored by RockTron Mineral Services Ltd. a small company that owns the core technology to enable total beneficiation of raw fly ash from coal fired power plants. Their products are marketed as eco-minerals, a reflection of the fact that using recycled material begins to address the requirements of a resource efficient economy. It is directly relevant to the company because finding novel applications for CFA derived products will help to establish a immature technology into the market place. In addition by helping to improve the efficiency of existing processes, or to offer process alternatives, an economical solution to CFA beneficiation in a wide range of circumstances can be found.

1.4 Thesis Outline

The thesis begins in Chapter 2 which provides a comprehensive literature review of the topics that concern the multicomponent utilisation of CFA: namely the characterisation, current applications, future applications, and processing of CFA. This is an abridged

version of the paper published in *Fuel* in 2012 [7].

Chapter 3 is split into three standalone, but related investigations surrounding material characterisation. Section 3.1 is a comprehensive characterisation of the products of RockTron's beneficiation technology, Section 3.2 is an investigation into the rare earth element content of six CFAs and the products of RockTron's beneficiation technology, and Section 3.3 details the characterisation of CFA that has been separated on the basis of apparent density. Section 3.2 was published with minor changes in a short communication in *Fuel* in 2014 [8].

Chapters 4 - 5 are related in the sense that Chapter 4 informs aspects of the work in Chapter 5. Chapter 4 is an investigation into how the suspension viscosity of CFA slurry changes with shear rate and concentration. An empirical model was developed for both a CFA and a CFA derived product. Chapter 4 was published with minor changes in *Fuel* in 2013 [15]. Chapter 5 comprises of a laboratory scale study of RockTron's cenosphere separation technology. It included semi-continuous extraction experiments, minimum impeller suspension speed determinations, cloud height assessment, and a brief qualitative and subsequently theoretical examination of the speed required to drawdown cenospheres from a water surface. Following on from this a theoretical design was suggested based on the principles of a thickening tank.

The process of carbon separation from CFA was examined in Chapter 6. The process chosen was oil agglomeration which is a very effective technique for the upgrading of high ash coal of small particle size. However, its use has been limited by excessively high oil application rates required. Chapter 6 examines the agglomeration operating parameters that affected the separation efficiency of the process in a response surface factorial experimental design. Then the use of a novel emulsified vegetable oil binder was assessed for separation efficacy.

The final set of results are contained in Chapter 7 and they focus on a particular application that was deemed promising by initial literature review. Floating photocatalysts are synthesised, characterised and evaluated for the removal of organic compounds

from contaminated water. The photocatalysts consist of a cenosphere substrate, a TiO_2 coating applied using a hybrid slurry technique, and an activation step of depositing silver nano-particles onto the TiO_2 surface. The investigation then characterises these materials using bulk and surface techniques before evaluating them in a photocatalytic reactor. Special consideration was paid to the effect of the substrate particle size with regard to the reactant degradation kinetics.

CHAPTER 2

A LITERATURE REVIEW OF THE MULTI-COMPONENT APPLICATIONS AND PROCESSING OF COAL FLY ASH

2.1 Characterisation of Fly Ash

2.1.1 Mineralogy and Chemistry

The principle components of fly ash are silica, alumina, ferrous oxide, and calcium oxide with varying amounts of carbon as measured by a Loss on Ignition (LOI) test [12]. In general it can be seen from the summary data in Table 2.1 that CFAs have a bulk chemical composition containing a variety of metal oxides in the order $SiO_2 > Al_2O_3 > Fe_2O_3 > CaO > MgO > K_2O > Na_2O > TiO_2$. However, it is evident from Table 2.1 that there are significant differences in composition, not only between regions, but also within the regions themselves.

CFA chemistry is determined by the type of coal burned to produce it. Generally it has been observed that CFA from sub-bituminous and lignite coals are characterised by higher CaO, MgO, and SO_3 and lower SiO_2 and Al_2O_3 relative to the higher grade fuels such as bituminous and anthracite coals. Bituminous and lignite CFAs that contain less than 10% CaO in total often consist mainly of aluminosilicate glass and usually do not contain any crystalline compounds of calcium. CFAs that contain more than 15% total

Table 2.1: Bulk Chemical Composition of CFA by Region

Component	Range (mass %)				
	Europe[a]	US[b]	China[c]	India[d]	Australia[e]
SiO_2	28.5-59.7	37.8-58.5	35.6-57.2	50.2-59.7	48.8-66.0
Al_2O_3	12.5-35.6	19.1-28.6	18.8-55.0	14.0-32.4	17.0-27.8
Fe_2O_3	2.6-21.2	6.8-25.5	2.3-19.3	2.7-14.4	1.1-13.9
CaO	0.5-28.9	1.4-22.4	1.1-7.0	0.6-2.6	2.9-5.3
MgO	0.6-3.8	0.7-4.8	0.7-4.8	0.1-2.1	0.3-2.0
Na_2O	0.1-1.9	0.3-1.8	0.6-1.3	0.5-1.2	0.2-1.3
K_2O	0.4-4	0.9-2.6	0.8-0.9	0.8-4.7	1.1-2.9
P_2O_5	0.1-1.7	0.1-0.3	1.1-1.5	0.1-0.6	0.2-3.9
TiO_2	0.5-2.6	1.1-1.6	0.2-0.7	1.0-2.7	1.3-3.7
MnO	0.03-0.2	nd	nd	0.5-1.4	nd
SO_3	0.1-12.7	0.1-2.1	1.0-2.9	nd	0.1-0.6
LOI	0.8-32.8	0.2-11.0	nd	0.5-5.0	nd

[a] Data from 41 CFAs reported in [17, 18] [b] Data from 38 CFAs reported in [19–21] [c] Data from 8 CFAs reported in [22–24] [d] Data from 7 CFAs reported in [25, 26] [e] Data from 4 CFAs reported in [27]

Table 2.2: Classification systems of the US and European standards bodies for fly ash use in concrete

ASTM C618				
Class	SiO_2 + Al_2O_3 + Fe_2O_3	SO_3	Moisture	LOI
C	$> 50\%$	< 5 %	< 3 %	< 6 %
F	$> 70\%$			$< 12\%$
EN 450-1				
Class	SiO_2 + Al_2O_3 + Fe_2O_3	SO_3	Reactive Silica	LOI
A				$<5\%$
B	$> 70\%$	$< 3\%$	$> 25\%$	2-7%
C				4-9%

CaO are composed of calcium aluminosilicate glass in addition to substantial proportions of crystalline calcium compounds including C_3A, C_4A_3S, CS, and CaO [16].

The chemical composition of CFA has traditionally been the basis for assessing its suitability for use as a cement replacement material. The American Society for Testing and Materials (ASTM) group CFA into two classes: C and F. Table 2.2 shows that in the ASTM classification Class F CFA has a combined SiO_2, Al_2O_3, and Fe_2O_3 content of greater than 70% compared to greater than 50% for Class C CFA. It is for this reason that it is sometimes held that class C CFA is derived from lignite and sub-bituminous coals and class F CFA is derived from bituminous and anthracite coals [28]. Table 2.3 provides

Table 2.3: Bulk Chemical Composition of CFA by coal type [12]

Component (wt %)	Bituminous	Sub-bituminous	Lignite
SiO_2	20-60	40-60	15-45
Al_2O_3	5-35	20-30	10-25
Fe_2O_3	10-40	4-10	4-15
CaO	1-12	5-30	15-40
MgO	0-5	1-6	3-10
Na_2O	0-4	0-2	0-6
K_2O	0-3	0-4	0-4
SO_3	0-4	0-2	0-10
LOI	0-15	0-3	0-5

an overview of the general concentration ranges that can be expected as a function of coal type.

The distinction is also important in relating the mineralogy to certain applications for the CFA. Class F ash is regarded as a pozzolanic material. A pozzolan is a siliceous, or a siliceous and aluminous, material that has no intrinsic cementitious property. In a very finely divided form however, it will chemically react with $Ca(OH)_2$ at ordinary temperatures and in the presence of moisture to form compounds exhibiting cementitious properties. The high CaO content of many of the lignite and sub-bituminous fly ashes will result in the formation of cementitious products in the absence of $Ca(OH)_2$; as such, they are not true pozzolans [16].

The classification systems devised by ASTM and the European standards body use a system designed to distinguish CFA types that will be suitable for use as a cement replacement. They are prescriptive, rather than based on performance, so they can be controversial because in practice many class C ashes can meet the performance requirements of class F ashes [16]. What is explicitly ignored in the classifications listed in Table 2.2 is a consideration of the different mineralogy of CFA types. Vassilev and Vassileva [18] argue that although systems of classification have been created based on the industrial use of CFA they do not have systematic scientific basis. They present a new classification system based on an analysis of 41 European CFAs. It groups the main bulk oxides together to create the four tier classification system presented in Table 2.4. The use of

Table 2.4: Approach for classification of CFA based on chemical composition [18]

Class	$SiO_2 + Al_2O_3 + K_2O + TiO_2 + P_2O_5$	$CaO + MgO + SO_3 + Na_2O + MnO$	Fe_2O_3
Sialic	$> 77\%$	$< 11.5\%$	$< 11.5\%$
Calsialic	$< 89\%$	$> 11.5\%$	$< 11.5\%$
Ferrisialic	$< 89\%$	$< 11.5\%$	$> 11.5\%$
Ferricalcsialic	$< 77\%$	$> 11.5\%$	$> 11.5\%$

this system could help in assessing a particular CFA for use in applications other than cement.

In the classification system of Vassilev and Vassileva a further distinction is made between the phase and mineralogical composition of the CFA. In most CFAs the phase and mineral composition includes the following: an inorganic constituent comprised of amorphous and crystalline mineral matter; an organic constituent composed of char materials; and a fluid constituent comprised of liquid, gas, and gas-liquid inclusions. In the order of decreasing amounts CFA comprises of glass, mullite, quartz, char, hematite-magnetite, anhydrite-gypsum, feldspars, lime-portlandite, clay and mica minerals, cristobalite-tridymite, calcite-ankerite, corundum, jarosite, and some Ca and CaMg silicates [18]. For most CFAs the major phases consist of mullite, quartz, and hematite [28]. The mineralogy classification system divided four phase-mineral fly ash types namely Pozzolanic (P), Inert (I), Active (A), and Mixed (M): this is based on the distinct behaviour of (1) glass; (2) quartz + mullite; and (3) the sum of any other mineral bearing phases such as Fe-Ca-Mg-K-Na-Ti-Mn oxyhydroxides, sulphates, carbonates, and silicates. Classifying CFA in this way should help to simplify the choice of application for each unique CFA composition.

The chemical properties of CFA have been well studied and it is known that CFAs contain many elements at concentrations of greater than 50 mg/kg. Some of these are of environmental concern [29]. Table 2.5 shows the concentrations of trace elements in 23 European CFAs. They are in broad agreement with the elemental composition of Australian CFAs analysed by Jankowski *et al.* [27]. It is noticeable that elements such as As, Cr, Pb, and Se are present in significant quantity. Because of this, mobility

Table 2.5: Average trace element content in 23 European CFAs [17]

Element	Trace Element Composition (ppm)		
	25^{th} Perc.	Median	75^{th} Perc.
As	40	55	97
B	135	259	323
Ba	639	1302	1999
Be	6	8	12
Cd	1	2	2
Co	30	35	48
Cr	137	148	172
Cu	73	86	118
Ge	3	7	15
Hg	0.2	0.2	0.3
Li	150	185	252
Mo	7	11	13
Ni	87	96	144
Pb	59	80	109
Rb	50	108	147
Sb	4	4	8
Se	6	7	13
Sn	7	8	10
Sr	384	757	1647
Th	25	30	37
U	9	12	18
V	202	228	278
Zn	123	154	175

studies have been conducted to assess the likelihood of these elements escaping to the environment. The leachability of the elements is closely related to the phase with which they are associated and the leaching conditions such as pH that they are exposed to [27].

2.1.2 Morphology

The morphology of CFA particles is controlled primarily by the combustion temperature and subsequent cooling rate. Scanning electron microscopy (SEM) analysis has revealed that CFA samples consist of solid spheres, hollow spheres (cenospheres), and irregular unburned carbon. Mineral aggregates containing corundum, quartz, and magnetite particles have also been observed [30, 31].

The inorganic materials in coal have two modes of occurrence; they are said to be included within the organic particle or excluded completely as discrete mineral grains. The formation of fly ash particles is represented schematically in Figure 2.1. The first step of

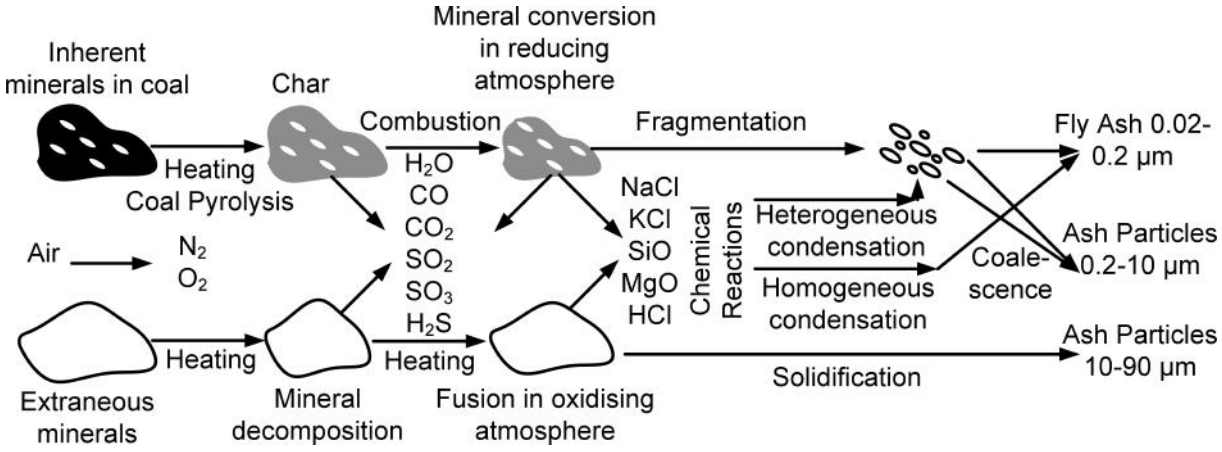

Figure 2.1: Simplified mechanism of CFA formation from pulverised fuel combustion adapted from [32]. All particles in the diagram are considered as *coal fly ash* for the purposes of this thesis.

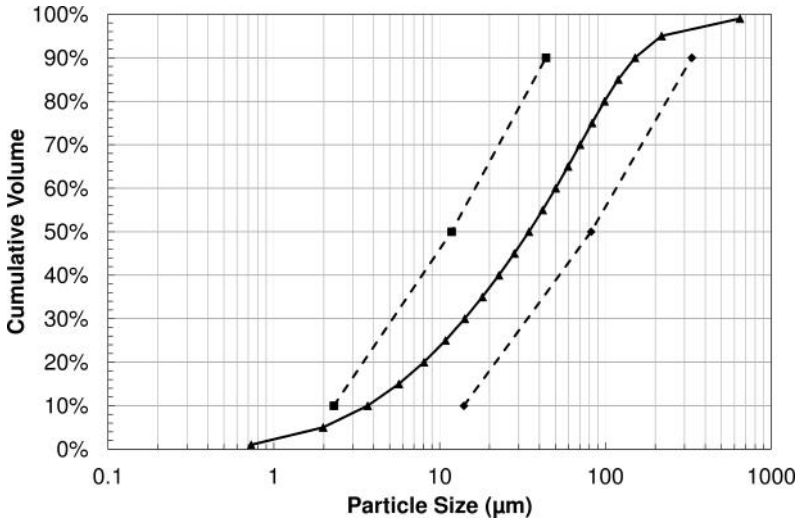

Figure 2.2: Typical particle size distribution of an UK CFA in comparison to upper and lower ranges from 23 European CFAs [17]

the generally accepted coal combustion mineral matter transformation mechanism is the conversion of the coal to char. The char materials burn out at much higher temperatures. The fine included minerals gradually reduce at the higher temperature and are released from within the char as it fragments. At this point the minerals decompose and convert to gases and eventually condense to form solid ash particles. Homogeneous condensation results in ash particles between 0.02-0.2 μm and fragmentation of included mineral matter results in the formation of particles between 0.2-10 μm. The excluded mineral matter undergoes a series of complex transformations to form predominantly spherical particles in the size range 10-90 μm [33].

Figure 2.2 illustrates the particle size distribution of a UK CFA obtained from the Ferrybridge power station analysed using a laser diffraction method by the current authors. Superimposed on this plot are the upper and lower ranges of 23 European CFAs [17]. The particle size distribution of UK CFA neatly fits in the middle of the upper and lower bounds. What the plot illustrates, with reference to Figure 2.1, is that although the formation mechanism accounts for the majority of the ash, at the upper bound a CFA might contain up to 50 % by volume which exceeds the 90 μm specified in the formation mechanism. The reason for the ashes containing particles exceeding this value could be due to particle grouping in liquid and plastic states. Mutual germination of spheres, spheroids, debris, and other particles has also been suggested. However, they could be of primary origin [34].

The other possibility for particle sizes exceeding 90 μm is that are made up of the organic constituent or the unburnt coal (char) components. It has been shown that the larger fractions of a CFA contain a greater content of carbon particles [35]. The char particles are represented by particles which are slightly changed, semi-coked, or coked. The coked and semi-coked are produced from the complete and partial melting of the various organic components, while the slightly changed particles are those which are exposed to temperatures no higher than 550°C. These slightly changed particles are typical for coarse-grained fractions over 100 μm in size. While the coked and semi-coked particles undergo melting and thus condense as spheres and spheroids, the coarser particles undergo incomplete oxidation, so they retain the irregularity of shape from the coal precursor [34].

2.1.3 Separable Components

The complex composition of CFA has proved a barrier to its bulk utilisation in many fields. Each component may be useful or inert in a particular application, but actively detrimental in another. For example, excess or variable char content in CFA hinders its use in concrete applications due to its propensity to adsorb the speciality surfactants that are used in concrete mixtures to stabilise air bubbles [36]. On the other hand, the adsorption

capacity of the char in CFA could be advantageous in pollution control applications. It has been shown that, although complex, the composition of CFA predominantly contains some mixture of glass, quartz-mullite, char, Ca silicate-oxyhydroxide, iron rich, and salt fractions in a separable form [10]. In a series of publications the research group of Vassilev utilised a variety of techniques in a sequential separation process to fully characterise the following CFA fractions: (1) a ceramic cenosphere concentrate (CCC), (2) a water soluble salt concentrate (WSC), (3) a magnetic concentrate (MC), (4) a char concentrate (CC), (5) a heavy concentrate (HC), and (6) an improved CFA residue (IFA) [5, 9–11].

2.2 Current Applications for CFA

CFA has predominantly been used as a substitute for material in the construction industry. Figure 2.3 presents a breakdown of the uses of CFA in Europe. By far the biggest current use for CFA is either as a raw material or as an additive in the cement industry [37].

Because most CFAs have pozzolanic properties they are widely used as partial replacement for clinker the major component in Ordinary Portland Cement (OPC). CFA use in blended cements in a well established technology, but there are strict standards governing its use such as the American Society for Testing Materials ASTM C 618 in the US and the European Standard EN 450-1 in Europe, as shown in Table 2.2.

Concerns have been raised about using CFA as a cement substitute in concrete. Kikuchi [39] highlights the problem that both the construction industry which uses CFA in its cement and the coal fired power plants that produce the CFA are seasonal. The different activities peak at different times; the construction industry needs most of the cement in the summer months when building conditions are optimum, whereas most of the ash is generated during the winter. In the summer months coal generators tend to be restricted to double shifting *e.g.* operating during breakfast and evening meal times to satisfy peak demand and in doing so the LOI content of the ash is increased [40]. The increase in LOI is a measure of the increase of unburnt carbon. It changes the adsorption

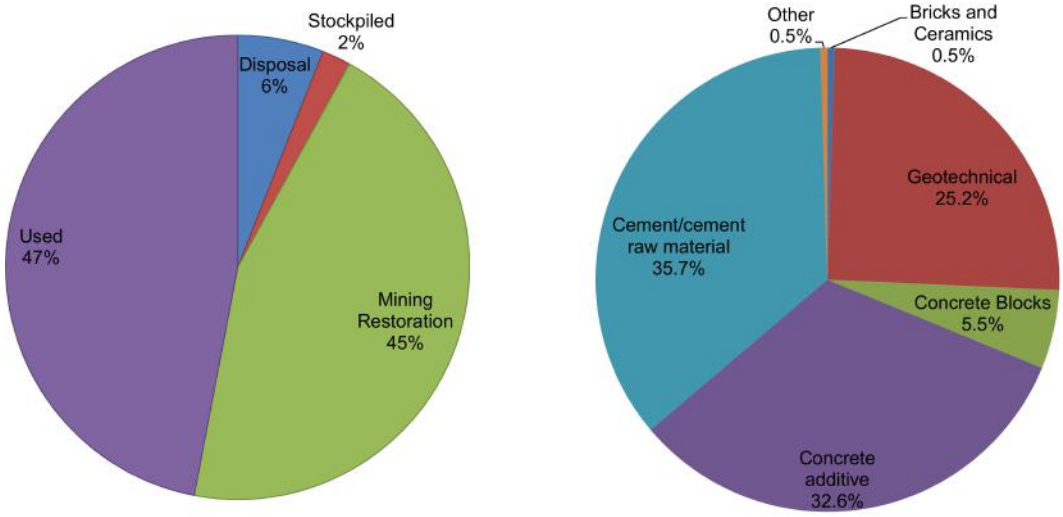

Figure 2.3: CFA Utilisation Trends in Europe in 2008 [38] adapted and updated from [37]. The right-hand pie chart shows a breakdown of the used component of the left-hand chart.

properties of the ash in terms of the air entrainment admixture that are added in cement mixes. According to both ASTM C 618 and EN 450-1 an increase in LOI reduces the quality of the CFA.

Other changes in the coal fired power generation have also contributed to an increase in the LOI content of CFAs such as the advent of low-NO_x burners and selective catalytic reduction SCR supported by the injection of ammonia [41]. High carbon content can also lead to discolouration of the concrete and mixture segregation [42].

After its use in cement, CFA is commonly used in geotechnical applications as is shown in Figure 2.3. Geotechnical is a broad term that encompasses its use in different applications: grouting, asphalt filler, sub-grade stabilisation, pavement base course, general engineering fill, structural fill, soil amendment, and infill [37].

CFA has been used as stabiliser for soil because of the beneficial properties it imparts. It is found that the addition of CFA to soils tends to decrease the propensity for the soil to absorb water and thus less swelling of the soil results. For soils with high montmorillonite content, the swelling problems can be severe; they tend to expand when wet and shrink when dry. This movement exerts pressure which can crack pavements, basement floors, driveways, pipelines and, foundations. It is thought that the addition of CFA to the soil changes the mineralogy due to pozzolanic reaction. The soil becomes more granular and

holds less water which results in a decrease of swelling associated with water absorption [43, 44].

2.3 Future Applications for Single Component Utilisation

2.3.1 Adsorbents

CFA has been investigated for its direct use as an adsorbent in both gaseous and aqueous applications. Adsorbents are often used in pollution control applications and the use of CFA for this purpose provides an excellent example of how mutually beneficial industrial synergies can be built. As early as 1984, CFA was considered as a potential adsorbent to remove Copper(II) ions from industrial waste waters [45]. An experimental analysis of a particular CFA led to the fitting of the results to the Langmuir isotherm which produced design data suitable to produce pilot scale reactors. More recently the use of mixed CFAs with different chemical compositions has been evaluated for the removal of a variety of different metal ions from waste waters: Cu [46–50]; Pb [47–50]; Zn [46,47,49,50]; Mn [49]; Cd [47, 49, 50]; Cr [50]; and Ni [50]. A recent review on the use of low cost adsorbents for the removal of heavy metals from industrial waste water concluded that CFA has great potential for use in the treatment of wastewater; this potential is limited by the variability in chemical composition of CFA and the large volumes that might be required for it to be effective [51].

Aksu and Yener [52] investigated the potential for CFA to be used in place of activated carbon for the adsorption of phenol. They reported an adsorption capacity of 27.9 mg/g for the CFA compared to 108.0 mg/g for activated carbon. CFA has also been used for the removal of 2-chlorophenol and 2,4-dichlorophenol with adsorption capacities of 1 mg/g and 1.7 mg/g respectively [53]. This does not compare well with the results reported in a further study by Aksu and Yener [54], in which they found the adsorption

capacity of CFA to be 98.7 mg/g and 118.6 mg/g for 2-chlorophenol and 4-chlorophenol respectively, although this appears to be due to difference in experimental conditions. 2,4-dichlorophenol and pentachlorophenol have been removed from waste water in a fixed bed column operating continuously; removal efficiencies of over 99% were achieved for an initial concentration of 10 mg/L of chlorophenols [55].

CFA has been found to be effective for the removal of two types of polychlorinated biphenyls (PCB): 2,3,4-trichlorobiphenyl (PCB no. 21; TCB) and 2,2',3,3',4,5,6- heptachlorobiphenyl (PCB no. 173; HeCB) [56]. The general conclusion from studies such as these is that, although CFA is an inferior adsorbent relative to activated carbon, its low cost could make it an economically viable alternative for the removal of organics from waste water.

Sorbents for the flue gas desulphurisation (FGD) process have been made by mixing $Ca(OH)_2$ with CFA. The results show that the desulphurisation properties of the sorbents increase with the CFA/$Ca(OH)_2$ ratio. This higher reactivity appears to be due to a larger BET surface area and the formation of certain compounds such as calcium aluminate and calcium silicate [57, 58]. More recently the sorbent synthesis process was optimised for specific surface area using an integrated modelling and optimisation approach [59]; the optimum specific surface area is obtained by mixing 13.1 g CFA with 5.5 g calcium sulphate in a hydration process with 100 ml of water and 5 g calcium oxide for a hydration time of 10 h. This is an application area that fits well with the IE ethos because the FGD process would lie in close proximity to the CFA generation.

2.3.2 Agriculture

An example of a direct application of CFA is its employment as a soil amelioration agent for a variety of different purposes. Recent reviews provide a comprehensive discussion of the issues surrounding the use of CFA to improve soil for agricultural purposes [60, 61] and for the reclamation of mine spoil [62].

The majority of crops prefer a pH level of 6.5-7 for optimum growth. Therefore the

application of CFA, which can be alkaline or acidic, to the soil results in a buffering action by the CFA. The addition of alkaline CFA to acidic soil can raise the pH. This is explained by the release of Ca, Na, Al, and OH ions under these conditions [61]. The majority of studies that demonstrate the ability of CFA to raise the pH of acidic soil use class C CFA, *i.e.*, ash with high CaO contents ($> 15\%$), and were applied at excessively high rates. It has been shown that for the most part class F ashes with low CaO content have limited potential to ameliorate soil acidity with the exception of ashes that contain relatively high calcium contents. For example, an ash derived from burning brown coal with a $CaCO_3$ equivalent value of 2.43% raised the pH of acidic soil by up to 2.3 points [63].

Researchers have noted other beneficial effects of the application of CFA soil systems: it improves the texture of the soil; it reduces the bulk density of the soil; it improves soil aeration, percolation, and water retention in the treated zone; it reduces crust formation; it reduces the consumption of other soil amelioration agents such as fertilisers or lime; it serves some purpose as an insecticide; and it can decrease the mobility and availability of metal in the soil [61]. On the other hand, harmful effects such as the reduction in bioavailability of some nutrients resulting from application of alkaline CFA have been reported. Other undesirable effects of CFA application to soil include excess salinity and a high content of phytotoxic elements; high levels of boron are an example of potential toxic side effects.

2.3.3 Aluminium and Titanium Recovery

Several methods for the acid recovery of aluminium from CFAs have been proposed. Direct sulphuric acid leaching at low concentration and ambient temperatures does not yield high aluminium recoveries, and the non-target metals readily leach into the acid causing purity issues [64]. A 2005 study of direct sulphuric acid leaching yielded an aluminium extraction of just 18% [65].

In contrast CFA pelletised with fine coal and lime and calcined then leached with sulphuric acid yielded an 85 % recovery. Three extraction methods were compared: se-

lective pH precipitation, crystallisation, and solvent extraction. The only viable method was found to be solvent extraction using Primene JMT in illuminating paraffin as the solvent extractant. The aqueous leachate was contacted with the organic solvent, and this selectively loaded Ti^{4+} and Fe^{3+} ions into the organic phase. The product obtained was a high purity alumina (99.4%). A 92-97% TiO_2 by-product could also be produced.

Shabtai and Mukmenev [66] described a novel biomagnetic titanium-aluminium extraction process. The authors used concentrated sulphuric acid to leach both valuable and toxic elements from the CFA. The pH was lowered until titanium precipitated from solution. This was carried out concurrently with a biomagnetic adsorption process. The bacteria *Rhodococcus GIN-l (NCIMB 40340)* was cultivated and added to a suspension containing magnetic particles which resulted in the adsorption of the bacteria onto the magnetic particles. The suspension was added to the leachate prior to precipitation. As the titanium precipitates out of the solution it adsorbs along with the magnetite onto the bacteria. When subjected to a magnetic field the titanium is lifted selectively out of the precipitate. This biomagnetic separation procedure is carried out twice to yield a titanium dioxide rich product with ferrous, silicate, and sulphate impurities. An aluminium rich precipitate was obtained by raising the pH to 6.5.

In a more recent study, a CFA reported to have an extremely high aluminium content of 40-45% was assessed for its potential to produce aluminium commercially [67]. In order to increase the Al_2O_3/SiO_2 ratio of the ash, a silica extraction step was carried out first using a NaOH solution. The desilicated ash was then mixed with lime and sodium carbonate and sintered before alumina extraction with a sodium carbonate and sodium hydroxide solution. Using this method, essentially a lime-soda sinter alkali leach process, an extraction efficiency of 90% was reported.

High purity alum (>99.9%) has also been prepared from CFA and ammonium sulphate [68]. The ammonium sulphate and the CFA were reacted at 400°C. The product from this reaction was hydrothermally leached with sulphuric acid. The leaching liquor was mixed with ammonium hydroxide and aged for 24 h. The purity of the precipitate was

increased via a method of dissolution precipitation. The final precipitate was calcined using conventional and microwave heating. Using conventional heating the noncrystalline transition γ-Al_2O_3 was formed, while under microwave conditions the crystalline α-Al_2O_3 was observed.

2.3.4 Catalysts

Using CFA in catalytic applications has been investigated for its potential to reduce the consumption of materials that have limited reserves and/or that are costly to manufacture. For an extensive and detailed review of the use of CFA in catalytic applications the reader is referred to the study of Wang [28]. The application of CFA as material to be used in heterogeneous catalysis has received a great deal of attention. Heterogeneous catalysis is appealing because it is often easier to recover the catalysts after reaction completion relative to homogeneous catalysts. For heterogeneous catalysis, catalytic materials can be supported on other materials; their activity depends on both the active component and its interaction with the support matter. Commonly catalyst supports include a range of metal oxides such as Al_2O_3, SiO_2, TiO_2, and MgO [69]. Given that CFA is primarily made up of Al_2O_3 and SiO_2, CFAs offer desirable properties such as thermal stability for use as a support. However, CFA has also been employed as the catalytically active component.

CFA has been used as a support material for nickel in the application of CO_2 methane reforming. It was shown that treatment of the CFA with CaO prior to Ni loading could produce catalysts capable of high conversion and stability with activities close to the well reported Ni/Al_2O_3 and Ni/SiO_2 systems [69].

Another study has shown the potential for the selective catalytic reduction of NO by ammonia with CFA supported Fe, Cu, Ni, and V catalysts; the Cu loaded CFA displayed the highest activity [70]. TiO_2, well known to be effective for photocatalytic reactions, has been used to coat CFA and then evaluated for its potential to remove NO from a gas stream. After heat treatment the removal rate of NO was reported to be as high as 95% [71].

Organic dyes in waste water represent a problem because they cannot be degraded by biological action [28, 72]. There are many techniques to remove the water contaminants originating from dyes. One such technique is called the advanced oxidation process (AOP). These AOPs are based on powerful oxidants such as OH radical species. They are formed when H_2O_2 is reacted in the presence of transition metal ions, UV light, and alkali or acid [72]. It has been demonstrated that H_2O_2 can be activated by a Fe^{3+} loaded CFA and subsequently used to oxidise the dye reactive black 5. A photocatalyst was prepared from a high iron content CFA by leaching iron ions from the CFA under acidic conditions and then precipitating amorphous FeOOH onto the surface of the residual CFA. The catalyst was tested to determine its activity in the photocatalytic degradation of methyl orange. It was found to be effective up to a pH condition of 9.0 thereby extending the traditional range of such systems [73].

Recently the synthesis of a highly active nano-crystalline thermally stabilised solid acid catalyst was achieved by loading sulphated zirconia on to CFA via a sol-gel technique. The catalyst was tested for its performance in the liquid phase benzylation of benzene and toluene with benzyl chloride; high conversions of benzene (87%) and toluene (93%) were reported [74]. Activation of CFA by acid pre-treatment followed by thermal treatment was also found to increase the catalytic activity of CFA supported Ru decomposition of ammonia. However the activity reported was between 10-15% for these catalysts and was not close to values reported elsewhere in the literature for fumed silica supported Ru catalysts [75].

Catalytic oxidation of volatile organic compounds (VOCs) in thermal processes is one of the methods that have been used to degrade VOCs in air. CFA has been used as the active component to mediate oxychlorination and the deep oxidation reaction of phenol and monochlorophenols [76].

Metallic sulphides are emitted from various industrial processes such as paper mills and tanneries amongst others. Mallik and Chaudhuri [77] investigated the oxidation of sodium sulphide in air. They reported a 3.5 factor increase in reaction rate with a CFA

loading of 4 wt%. This is compared to a factor of 4.52 relative to no CFA addition at the same loading and temperature, but using H_2O_2 as the oxidant.

CFA has been assessed for its potential for use as a photocatalyst for the removal of dyes from water under visible light. It was reported that the removal of 60% of thionine is possible after 4 h from a starting concentration of 1 x 10^{-4}M [78].

An interesting study documents the acid activation of CFA to produce a nano crystalline solid acid catalyst. The catalysts was employed for the esterification of salicylic acid with acetic anhydride and methanol to produce acetylsalicylic acid (aspirin) and methyl salicylate (oil of wintergreen) in a single step, without the need for solvents; greater than 90% yield and purity was reported [79]. In a similar manner the synthesis of solid base catalysts from CFA using NaOH pre-treatment followed by thermal activation has been described. These catalysts were found to have high conversion (>70%) and selectivity (>80%) in the condensation reaction of benzylaldehyde and cyclohexanone to dibenzylidenecyclohexanone [80].

2.3.5 Ceramics and Glass

As CFA is made up of oxides such as SiO_2, Al_2O_3, CaO, and Fe_2O_3 it has received attention as a low cost material for the manufacture of ceramics, glass-ceramics, and glass materials [81]. The basis of manufacture is the temperature activation of the raw CFA with variations in temperatures and co-reagents directing the final form of the glass or ceramic.

Erol *et al.* [81] manufactured glass, glass-ceramic, and ceramic material from CFA using the general stages outlined in Figure 2.4 without the addition of any additives. Physical and mechanical property tests revealed that the three materials manufactured from waste CFA compared well with literature values for glasses and ceramics derived from waste and non waste sources.

CFA has been considered as a replacement for kaolinite in the manufacture of the ceramic cordierite [82]. Classified ash (<44μm) was mixed with industrial alumina and

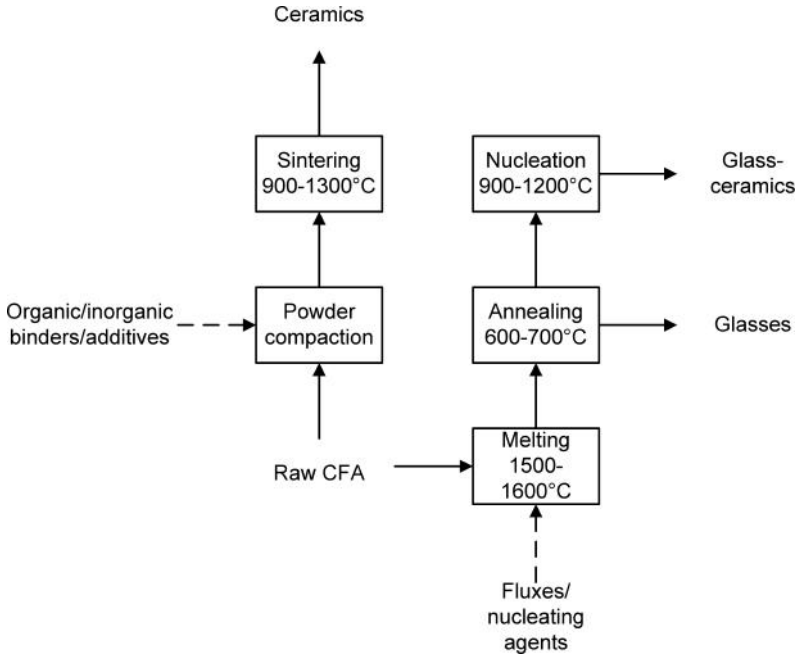

Figure 2.4: An overview of the thermal processes to produce ceramics, glass, and glass-ceramics from CFA [81–83]

magnesium carbonate powders. This mixture was milled with methyl cellulose and the blended components were then pressed into discs before sintering at temperatures between 900-1300°C. Results show that a raw material composition of 64-68 wt% CFA, 10% alumina, and 22-26% magnesium carbonate produced cordierite as the dominant phase at sintering temperatures of over 1200°C.

CFA has been used in a 60:40 weight ratio with kaolinic clay to manufacture category BIII ceramic tiles according to EN 14411 [84]. The authors hoped that using a CFA with high CaO content and lower particle size would decrease the firing shrinkage that is evident in classical CFA high temperature ceramics. The study reported that firing shrinkage was reduced, but at the expense of an increase in porosity, a decrease in bending strength, and an increase in SO_2 in the flue gases.

The chemical composition of CFA makes it particularly suitable for the manufacture of structural glass-ceramics [83]. Glass-ceramics were made using two different fluxes: Na_2CO_3 and $CaCO_3$ with and without the addition of HBO_2. Glasses made using the different fluxes both formed wollastonite ($CaSiO_3$) and anorthite ($CaAl_2Si_2O_8$) as the main crystalline phase. It was found that, although both ceramics exhibited good mechanical

properties, the ceramics made with fluxes including the HBO_2 were superior. Other fluxes have also been considered. Kim and Kim [85] prepared glasses by melting ash along with CaO and TiO_2 as nucleating agents to decrease the temperature of melt process. The melts were annealed at the glass transition temperature (+10°C). Glass-ceramics produced using the optimal conditions showed good wear resistance and fracture toughness indicating their potential for use as building materials. A separate study suggested the use of Cr_2O_3 as a nucleating agent in order to prepare glass ceramics [86].

Ceramic microfiltration tubular membranes were produced from CFA with the objective of filtering the effluent from textile dyeing processes [87,88]. The membrane included both a macroporous support and a microfiltration active layer. The support was manufactured in two stages; the CFA is first calcined and then mixed with binding agents to form a paste. The paste is extruded into tubes and sintered. The microfiltration layer was applied using ground CFA (0.5 and 2μm). The layer was deposited on the support using a slip-casting method in dip solution containing the CFA powder and polyvinyl alcohol as a binder. When the prepared ceramic membrane was used for the cross flow membrane treatment of textile dye effluent, it achieved a 75% removal of chemical oxygen demand (COD) and 90% removal of colour. The overall stabilised permeate flux (circa 100 L/mh) was the same as that of a conventional alumina ceramic membrane highlighting the potential of CFA for this application. A similar study [89] reported that a double coated membrane had a smaller pore size and narrower size distribution than a single coated membrane.

2.3.6 Geopolymers

Alkali-activation of aluminosilicates is a technology, often called geopolymerisation, first developed in the 1970s by Joseph Davidovits. It involves a chemical reaction between alumino-silicate oxides and alkali metal silicate solutions under strongly alkaline conditions; this yields amorphous or semi-crystalline polymeric structures of Si-O-Al bonds. Geopolymers exhibit good physical, chemical, and mechanical properties: these include

low density, micro and nano porosity, low shrinkage, high mechanical strength, good thermal stability, durability, surface hardness, fire, and chemical resistance. Given these desirable properties they are seen as potential alternative materials for industrial applications such as construction, transport, aerospace, mining, and metallurgy [90–92]. The major focus however, is that they can replace the use of OPC as a binder in concrete applications [93].

Conceptually similar to zeolite synthesis, the alkaline activation of a alumino-silicate material can be described as the reaction of a liquid with a high alkaline concentration and a solid with a high proportion of reactive silicate and aluminate. Once mixed in a liquid solid ratio of 0.2-1 the formed paste can then set and harden like OPC. The alkaline activated binder forms a gel with the composition $Na_2O.Al_2O_3.rSiO_2.nH_2O$, with r ranging from approximately 2 - 5. This is often shortened to N-A-S-H in the literature [94]. These gels show 3-dimensional order on a nano-scale only; on a micro scale and as determined by XRD they appear to be amorphous. Often crystalline and semi crystalline phases are observed. These are generally zeolitic and appear to be more prevalent when the synthesis conditions are hydrothermal with high alkaline dilution rates. This is thought to be as a result of improved solution phase transport [95].

CFA geopolymers harden rapidly at room temperature and the development of mortar compressive strengths of 80-120 MPa [96–98] and concrete strengths of circa 70 MPa have been reported in the literature [99]. The large-scale application of such geopolymers is much more complex, but high performance geopolymer concretes are starting to become commercialised [100].

There are many factors that affect the desired properties of any geopolymer product. The metal cation in the alkaline activator plays an important role in the formation of the geopolymeric network. While the OH^- ion acts as the reaction catalyst, the alkaline metal cation acts as the structure forming element. It balances the negative framework charge carried by the tetrahedral aluminium. Given that the first stage of the reaction is controlled by the capacity of the alkaline solution to liberate silica and alumina from CFA

into solution, it might be expected that KOH, being a stronger alkali than NaOH, would exhibit the greater dissolution ability. In reality this is not the case, and it is thought that the reason for this is the smaller ion size of Na^+ relative to K^+. This could be because of its ability to migrate more easily through the gel network or because of a higher charge density [95]. Komljenovic *et al.* [101] in a comparative study found that KOH had a much lower geopolymerisation potential relative to NaOH, but that both NaOH and KOH were inferior to sodium silicate activators.

Lee and van Deventer [102] conducted a study of the leaching of CFA in alkaline solutions of KOH and NaOH to assess the effect of the addition of soluble silicate solutions on dissolution rates. It was found that when the soluble silicate dosage was low ($<$ 200 mM), the dissolution was retarded by secondary precipitation on the CFA particle surface. Conversely when the soluble silicate dosage was high ($>$ 200 mM), significant structural alteration was observed. The enhanced aluminosilicate dissolution was followed by precipitation of a new aluminosilicate gel phase: the mechanism displayed believed to be that of the formation of geopolymers.

The conclusions drawn from the study conducted by Lee and van Deventer can be evidenced in other studies examining the compressive strength of alkali activated CFA geopolymers. Panias *et al.* [92] showed that the addition of sodium silicate increases the compressive strength of the produced geopolymer concrete linearly up to a certain SiO_2 content. Over this value (2.31 mol/dm^3) the compressive strength dropped off, and this was attributed to increased viscosity of the geopolymer pastes hindering the workability and thus the moulding properties. The molar ratio of SiO_2/Na_2O has also been found to have a noticeable effect on the strength of geopolymers in other studies. Research has shown that the optimum molar ratio for compressive strength is somewhere between 1 and 2 [99, 101, 103].

The strength of the alkali solution has been observed to play an important role in the overall strength of the manufactured geopolymer. Panias *et al.* [92] reported that a sodium hydroxide solution of 6.6 M was optimal for geopolymer production. In contrast

Hardjito *et al.* [99] found that the compressive strength of geopolymers was highest under alkali concentrations of 14 M, and no deterioration of strength over a certain concentration was observed.

The extent of the dissolution of the aluminium and silicon ions in strong alkaline solutions is dependent on particle size, morphology, and the chemical composition of the raw material with more importance attached to the vitreous phase of the material [104]. Previous research has shown that the reactivity of the source material can significantly affect the strength of the prepared geopolymer. Two different CFAs were used as source materials: one was predominantly amorphous, and the other had a significant crystalline component. The CFA that had a high crystalline fraction produced a material with a much lower early mechanical strength than that compared to the amorphous CFA [105]. Other studies have also shown that the chemical composition of the CFA can affect the application of the geopolymer. For example it has been shown that high iron contents appear to have a negative effect on the high temperature performance of geopolymers [106]. It seems likely that this is as a result of the fact that amorphous iron oxide particles within the CFA do not dissolve into NaOH and silicate solutions [93], resulting in their retention in the produced geopolymer as a filler particle.

2.3.7 Germanium and Gallium Recovery

The rise of new developing economies, in particular China, has resulted in an increased appetite for raw materials, and this has been of great concern to developed countries. The fear of a supply shortfall and of losing access to raw materials led the European Commission to analyse the raw materials that are critical to economic growth and employment. As a result germanium (Ge) and gallium (Ga) are defined as a critical strategic metal; this means that their production is concentrated in few countries, and the EU is highly dependent on external sources [107].

Germanium is a valuable element used in the manufacture of light emitting diodes (LEDs), photovoltaic (PV) cells, infrared devices, fibre optics, and as a catalyst for

polyethylene terephthalate (PET) production. Various coal basins contain matter with relatively high concentrations; in a survey of trace elements in twenty-four coals of UK origin the Ge levels ranged from 0.3-15 ppm, and it is suspected that it is associated with the organic matter in the coal [108]. In CFAs the Ge can be concentrated to values up to 10 times higher than in the original coal [109]. The Ge content in coal and coal combustion ashes is regarded as a potential source once more accessible resources have been depleted. It has been suggested that the Ge and Ga content of coal ash exceeds production by a factor of 200 [110].

Recovery methods have been pioneered which make use of the occurrence of Ge as water soluble species (GeS_2, GeS, and hexagonal-GeO_2) in gasification CFA from the 335 MW Puertollano IGCC power plant in Spain [109]. Hernandez-Exposito *et al.* [111] used catechol as a complexing agent to selectively bind the Ge and dodecylamine as a collector in a froth flotation cell. Under optimal conditions the froth contained 100% of the Ge in the leachate and a GeO_2 purity of 53% was obtained. Activated carbon was used to adsorb a Ge-catechol complex made with a synthetic aqueous Ge solution designed to replicate an integrated gasification combined cycle (IGCC) ash leachate [112]. Preliminary studies have suggested that this method is selective for Ge when other elements are present in solution. Similarly, strongly basic anionic ion exchange resins have been used in place of the activated carbon [113]. A maximum recovery of 96.1% was retained on the resin. Reutilisation of the resin was tested with extraction yields in the range 97.6-98.3%

Another promising method appears to be that of solvent extraction whereby a solvent is used to selectively extract a Ge-complex. Catechol has been used as a complexant with trioctylamine (TOA) diluted in kerosene as the extractant [114]. The aqueous phase containing the Ge-catechol complex is mixed with the organic TOA/kerosene phase and then left to settle. The Ge-catechol passes into the organic phase and is then stripped using a suitable acid or base. Ge recovery into the organic phase is as much as 97% in less than 3 minutes of mixing time.

Recently Arroyo *et al.* [115] published a study detailing the industrial design of a

solvent extraction unit using data from a pilot scale investigation [114, 116]. The authors took data from a 5 kg/h pilot plant, capable of producing 1.3 g/h of Ge, to economically evaluate the potential of scaling this design up to process 200 kg/h of CFA. They estimated a capital cost of €1.5 m without any solvent recovery unit included. Operating costs and sales analysis were not considered.

Gallium is used widely in applications such as optoelectronics, telecommunication, aerospace, alloys, computers, and DVDs [117]. Traditionally Ga is not refined directly but recovered from the refining processes of aluminium and zinc. Bauxite is the largest source of Ga with typical contents of 0.003-0.008% and is the result of treating an effluent stream of the Bayer process [117]. Although Ga crustal abundance is just 16 ppm, certain coals are enriched in Ga, and when combusted the Ga content of the CFA is enriched further. Reported Ga concentrations in CFAs range from 37.5-320 ppm [118, 119].

There have been several approaches to the extraction of Ga metals from CFA sources. Fang and Gesser [118] reported that a two-stage leaching with 2M hydrochloric acid was sufficient to recover 95% of the Ga in the CFA. The processes used required the removal or modification of impurities in the leachate. Impurities included SiO_3 ions, Fe^{3+}, and Ca^{2+}. They were removed prior to Ga extraction which was carried out by contacting the leachate with a polyurethane foam sponge. Gutierrez *et al.* [120] also used HCl to leach Ga from CFA. The leachate was then subjected to a dual stage solvent extraction process. During the first stage Ga, and unavoidably Fe, ions were extracted into an organic phase consisting of Amberlite LA-2. The Fe and Ga were stripped with water. The pH was increased until $Fe(OH)_3$ was precipitated. Finally the Ga was removed from the aqueous solution with a LIX 54 solution. A final concentrate of Ga 114 ppm was achieved at a recovery of 83% of the Ga in the initial solution.

CFA from the Puertollano power plant described previously was also investigated as a potential source of gallium [119]. NaOH was used under different conditions to yield Ga extraction of 60-86% equivalent to 197-275 mg of Ga/kg of CFA. Ga in solution was recovered by carbonation; the impurities precipitating out at higher pH than the Ga.

Re-dissolution of the precipitate at pH 0 increased the Ga content of the precipitate to 30% which is of suitable quality for purification via electrolysis.

2.3.8 High Volume Fly Ash Concrete

As a species, humans do not use any other material in a greater quantity than concrete apart from water; even small reductions in the embodied CO_2 emissions of concrete can make significant global impacts. Flower and Sanjayan [121] estimate that 80% of the CO_2 emissions generated by commercial concrete mixes are due to the inclusion of Portland cement. The Portland cement industry generates an estimated 7% of global anthropogenic CO_2 emissions [122].

There is a perception among engineers and architects that concrete codes are prescriptive with regards to CFA substitution in cement. In general this is well justified, ASTM C 595 limits substitution to 40% while EN 197-1 specifies a maximum of 35%. However, a new performance based standard ASTM C 1157 places no limit on the components of blended cements, and the International Building Code (IBC) defers to ASTM C 618 which states that the optimum amount of CFA or natural pozzolan is determined by the required properties of the concrete and is to be established by testing [123].

Commonly in commercial practice, CFA substitution is limited to 15-20%. This is sufficient to have a beneficial effect on the workability and cost economy of concrete. However, levels of 25-30% can improve the durability to sulphate attack, alkali-silica expansion, and thermal cracking. Higher substitutions of more than 50% are possible and increasingly common. The use of cement at this level of substitution is referred to as High Volume Fly Ash (HVFA) concrete and is constituted by a minimum of 50% fly ash, a low water content (130 kg/m^3), low cement content (<200 kg/m^3), and a low water/cement ratio (< 0.4) [122, 123].

The interest in HVFA concrete has increased recently because of the environmental and economic benefits associated with its use. Levels of 50-75% substitution in laboratory studies and field trials are routinely reported [122–127]. There are also technical benefits

associated with the use of HVFA concrete relative to conventional concrete some of which are summarised below [122]:

1. Improved workability.

2. Early strength up to 7 days which can be accelerated with changes in the mix design as the situation requires.

3. Later strength gain between 28 and 90 days or more. This has the result that it is unnecessary to over-design for a specific strength.

4. Superior dimensional stability as result of increased resistance to thermal, autogeneous, and drying shrinkage.

5. After 3-6 months, it exhibits a higher electrical resistivity and resistance to chloride penetration.

6. Greater durability to concrete reinforcement corrosion, alkali-silica expansion, and sulphate attack.

Although the later strength development can be beneficial with respect to making concrete over-design unnecessary, it also results in a significant disadvantage to using HVFA concrete in practice. Despite the use of these mixtures in the field increasing, it is commonly remarked on by contractors that HVFA mixes can be susceptible to long delays in finishing and occasionally lack the required early age strength [126]. It is noticeable in Figure 2.5, that the increase in CFA incorporation into HVFA concrete reduces the final strength and the rate of strength development. Setting times can be increased by as much as 2 hours with HVFA mixes [122]. This problem can be alleviated to some extent by incorporating rapid hardening cement or $Ca(OH)_2$ powders. The reduction in setting time is ash specific and requires further field study [126, 128].

Despite concerns over its early strength development, CFA has been substituted at a level of 100% replacement. Cross *et al.* [129, 130] demonstrated the performance of 100%

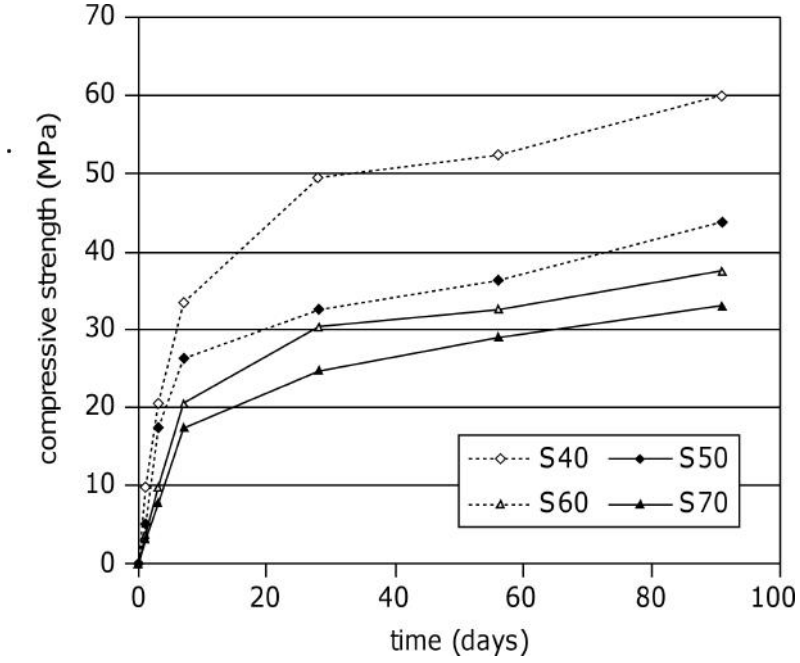

Figure 2.5: The compressive strength development of HVFA concrete with 40, (S40), 50 (S50), 60 (S60), and 70 (S70) % CFA substitution [127]

CFA concrete manufactured using a high calcium class C ash with respect to its performance in workability, short-term strength gain, long-term ultimate strength, durability, and structural behaviour. The results were achieved using conventional concrete mixing equipment. Readily workable mixtures (152.4 mm slump) were obtained without using water reducing admixtures. Early strengths of 27.5 MPa and long terms strengths of up to 55.2 MPa (1 year) were produced.

2.3.9 Mesoporous Materials

Porous solids are a valuable class of materials largely because of their use in a variety of separation and catalytic processes. In the early 1990s Mobil scientists reported the discovery of the M41S family of materials. These new materials possessed uniform mesopores [131, 132]. There is a great demand for new materials for the manufacture of mesoporous materials due to high cost and toxicity of conventional reagents [132].

CFA has been investigated for its potential as a silica source for the manufacture of mesoporous silica because of its low cost, abundance and the fact that it is a recycled

material. The methods of manufacture of these materials are very closely related to those of zeolite manufacture. The main difference is that, during or prior to crystallisation, structure directing templates are added. Kumar *et al.* [132] adopted the first stage of the alkaline fusion method for zeolite manufacture. After mixing the fused CFA powder with water and ageing for 24 hours, the solution was filtered and the supernatant was mixed with cetyltrimethylammonium bromide (CTAB), water, and ammonia solution. Hydrothermal treatment of the mixture was undertaken for 4 days. The foregoing method was used to obtain MCM-41, but was subsequently aluminated using trimethylaluminium to produce Al-MCM-41, which incorporates aluminium into the framework. SBA-15 was also synthesised using a triblock polymer $(EO)_{20}(PO)_{70}(EO)_{20}$, hydrochloric acid, and sodium metasilicate. It is suggested that Al-MCM-41 material is suitable for use in the cracking of cumene, but that it is not as effective a materials synthesised from pure reagents.

More recently a similar method was employed to synthesise MCM-41 to good effect; the synthesised material had a surface area of 732 m^2/g and median pore diameter of 2.5 nm in comparison to a surface area of 1100 m^2/g and pore diameter of 2.7 nm for MCM-41 manufactured from pure reagents [133]. A similar study by the same authors reported surface area values of 740 m^2/g and pore diameter of 2.3 nm [134].

Mesoporous silica SBA-16 has been manufactured using CFA as a silica source and subsequently employed as a template to manufacture mesoporous carbon [135]. The CFA was alkaline fused and a triblock polymer$(EO)_{106}(PO)_{70}(EO)_{106}$, hydrochloric acid, and n-butanol mixture was used as the structure directing agent. When an additional sodium metasilicate solution was added to the supernatant prior to reaction, the surface area was reported to be 649 m^2/g; this compares well to the conventional methods of synthesis which produced materials with a surface area of 683 m^2/g. The pore volume however was larger (5.4 nm) when using CFA as a silica source than when using pure raw materials (4.1 nm).

Methods based on the two-step hydrothermal synthesis of zeolites have also been

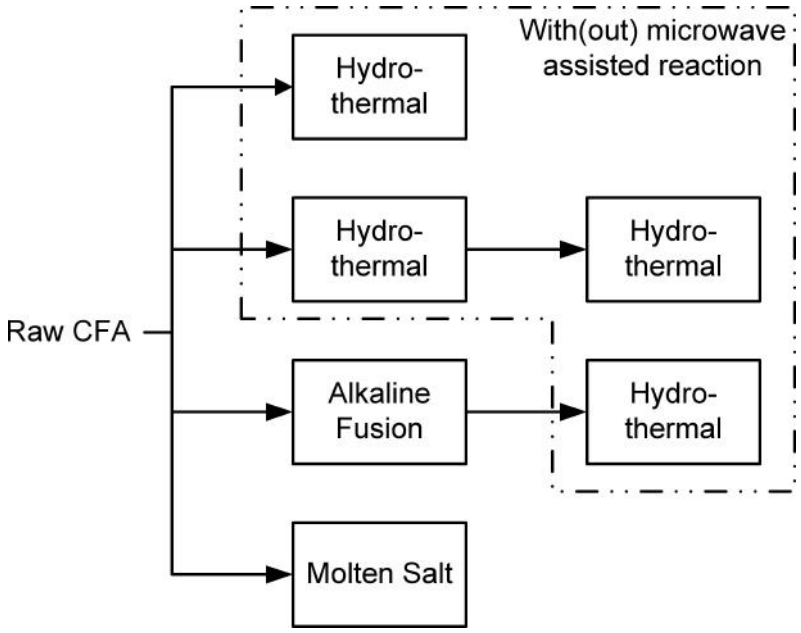

Figure 2.6: Schematic of the experimental approaches to the manufacture of zeolites from CFA

reported. Extraction of silica was conducted hydrothermally using a NaOH solution [136]. The solution was mixed with CTAB and ethyl acetate was added. The silica extraction method was hoped to provide more economical extraction conditions in addition to ethyl acetate being both cost effective and environmentally benign. Although a wide range of pH reaction conditions were studied, there was no reference to how pure reagent materials performed in the study so it is difficult to judge its efficacy. Generally it was found that material synthesised at a higher pH had a larger pore size and were more hydrothermally stable.

Although much attention has been paid to the manufacture of CFA derived mesoporous silica solids, there has been little scrutiny of the potential applications for such materials. Recently however, MCM-41 was synthesised using the alkaline fusion method and CTAB as the template [137]. It was tested for its utility in the catalysis of the classical Mannich reaction. The CFA derived MCM-41 prepared in this study compared favourably to other catalysts studied in the literature.

2.3.10 Zeolites

Zeolites comprise of an important group of crystalline aluminosilicate minerals; they possess an infinitely extending three-dimensional anion network made up of $(SiO_4)^{4-}$ and $(AlO_4)^{5-}$ tetrahedra that link at the corners via their shared oxygen atoms. The three-dimensional nature of the framework is what gives rise to the special properties of zeolitic materials. The voids and internal channel of the network allow easy access of molecules leading to fast diffusion rates that make zeolites particularly suitable materials for adsorption processes. The substitution of Si(IV) by Al(III) in the structure is what accounts for the overall negative charge; this means that the zeolites have the potential to show high cation exchange capacities (CEC) (up to 5 meq g^{-1}) [138] leading to possible applications in ion exchange or as a molecular sieve.

Zeolites require a source of Si and Al ions, an alkaline environment, and usually an elevated temperature for synthesis to proceed. Zeolitisation times may be of the order of hours, days, weeks, or even months depending on the nature of the reactants and the temperature employed [139]. Holler and Wirsching [140] are widely credited with the first application of alkaline hydrothermal synthesis of zeolites using CFA as a source of Al and Si ions. Figure 2.6 summarises the subsequent approaches that have been taken to the synthesis of zeolites from CFA.

Following Holler and Wirsching [140], many attempts have been made to derive zeolites from CFA using a one stage hydrothermal method [39, 141–148]. The main obstacle to synthesising zeolites from CFA is that, to speed up the reaction, temperatures in the range of 125-200°C must be applied in order to dissolve the silica and alumina. Under these conditions the formation of many of the larger pore, and more valuable, zeolites (A and X) is hindered. However, KM (equivalent to phillipsite), NaP1, Na-chabazite (herschelite), K-chabazite, Linde F, and other high-CEC zeolites have been obtained with high synthesis yields in the range of 125-200°C [138].

The variations in zeolite type and yield tend to result from the combination of experimental conditions that are employed; activation solution/fly ash ratio, temperature,

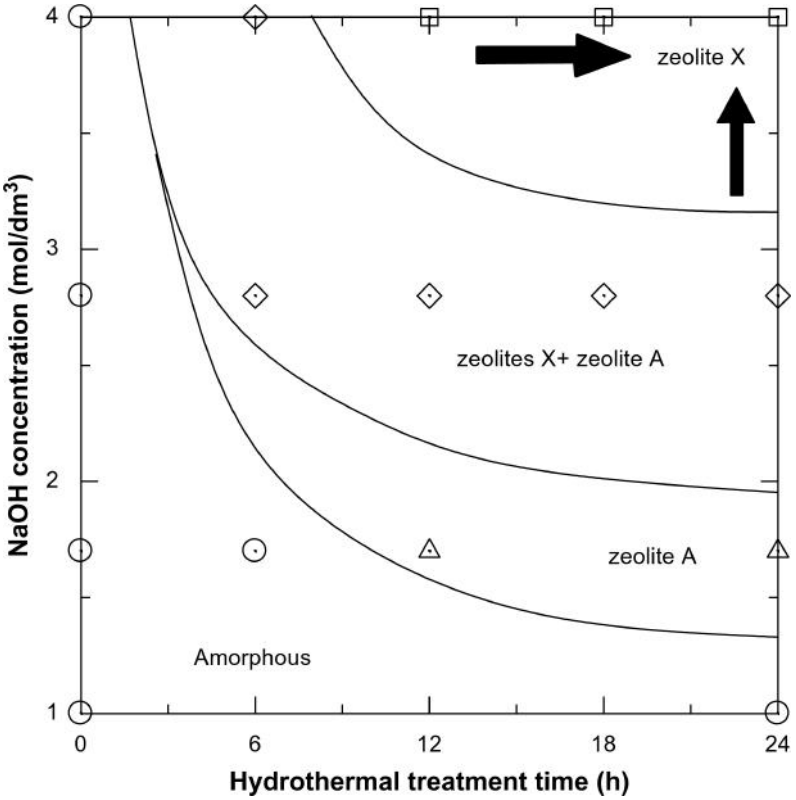

Figure 2.7: Schematic of the hydrothermal formation of zeolites following alkaline fusion [149]

pressure, and reaction time have all been varied to synthesise up to 13 different zeolite types from the same fly ash [144]. In general it was found that a high activation temperature and alkaline concentration (200°C and 5M) led to the formation of low CEC zeolites such as sodalite, and conversely low activation temperature and alkaline concentration (<150°C and 0.5-3M) led to the formation of higher CEC zeolites such as NaP1, NaA, or chabazite [138].

A method of pre-fusion of the CFA with a solid alkali at high temperatures (>500°C) prior to the conventional hydrothermal growth of the zeolites was introduced by Shigemoto *et al.* [150] and Berkgaut and Singer [141], but more recently interest has been renewed in this method [149, 151–155].

Berkgaut and Singer [141] mixed NaOH and CFA into a paste with water prior to heating. This enabled the decomposition of all of the mullite phase of the fly ash precursor. Zeolites X and NaP1 were formed depending on whether the fused material was

aged prior to the hydrothermal step. The purity of the zeolite was found to be high containing only small amounts of residual materials from the fly ash such as carbon and iron oxides. In Figure 2.7 the schematic summarises research into the conditions needed in the hydrothermal crystallisation stage to form particular zeolites [149]. It was found that a higher concentration and longer reaction times favoured the formation of zeolite X, but at the highest NaOH concentration some sodalite formed as a by-product.

Hollman *et al.* [143] pioneered the two stage hydrothermal method which has been the subject of considerable subsequent interest [136, 156–160]. Much like alkaline fusion, the method relies on two steps: the first has the effect of extracting the silica and to a more limited extent the alumina from the CFA into a sodium hydroxide solution. The Si/Al ratio of this solution is adjusted and then a zeolite crystallisation stage at temperatures of circa (<100°C) is carried out. Hollman *et al.* present a mass balance which suggests that 8% of the raw fly ash can be converted into pure zeolite (A, X, and NaP1) depending on the conditions employed. The solid residue can be mixed with the solution from the second step of the process to form further zeolite material but at lower purity. The disadvantages of the manufacture of the zeolite in this way is that its water usage is intensive, the extra reagent costs, and fairly long incubations times (<72 h). However, good CEC values were obtained ranging from 3.6-4.3 meq/g for the pure zeolites compared to 2.0-2.5 meq/g for the residual fly ash contaminated zeolites. A tentative cost comparison estimated that, in 1999, the two step process would cost $40 per keq of exchange capacity as opposed to $25 per keq for the one step. The authors concluded that the greater application potential of the highly pure zeolites in waste water treatment for heavy metal ion removal justified the use of the more expensive process

Other authors have studied the two step method to produce pure zeolites using a waste stream from the aluminium industry to provide the source of Al ions [156]. Fly ash extraction as high as 190 g SiO_2/kg in a single step process (6h) was achieved. The silica extraction fluid was mixed with a waste solution from the etching baths of an aluminium anodising company containing 57.6 and 14.9 g/L of Al and NaOH respectively. The

decisive factors that increased the silica extraction yield was to have a raw material with specific properties: (1) a high bulk silica content, (2) high silica/low alumina contents of the glass matrix, and (3) the presence of opaline phases in the raw fly ash. This results in a high silica yield and low alumina yield. In consequence the fixation of silica into zeolite or amorphous aluminosilicate is prevented. It was estimated that the cost, in 2005, of producing the zeolite mixture in this manner was 1.7 €/kg which was said to be competitive with the cost of commercial adsorbents [161].

The use of microwave irradiation has been demonstrated to reduce the conversion time of zeolite synthesis from CFA [142]. Kim and Lee [159] combined this approach with two step silica extraction. They applied the microwave heating source to both the first and second stage of the process. Microwave dissolution of Si and Al was increased relative to conventional heating. In the crystallisation stage, a combination of microwave heating followed by conventional heating gave the highest purity zeolite product. They reported zeolite A purities of 91 % with CEC values of 5.5 meq/g. Tanaka *et al.* [157] used a similar method; however, they applied the microwave irradiation only to the extraction step. Microwave extraction was capable of the dissolution of 57% of the amorphous silica in the CFA in just 1 hour which is a much faster rate relative to conventional heating.

One of the most unusual methods of zeotilisation consists of a zeolite synthesis without the use of any water. Park *et al.* [162, 163] developed the technique of thermally treating the CFA (<350°C) with a mixture of a variety of salts and bases for a range of times not exceeding three days. Although the need for the use of water was eliminated, high temperatures and potentially long activation periods, in addition to a low selectivity for high CEC zeolites, somewhat limit the potential for this method.

2.3.11 Overview of Potential Applications

There are some examples of the direct application of CFA in which it does not require any pre-treatment to develop the required functionality such as its use in agriculture, as an adsorbent, or in some circumstances as a catalyst. There is an obvious benefit to

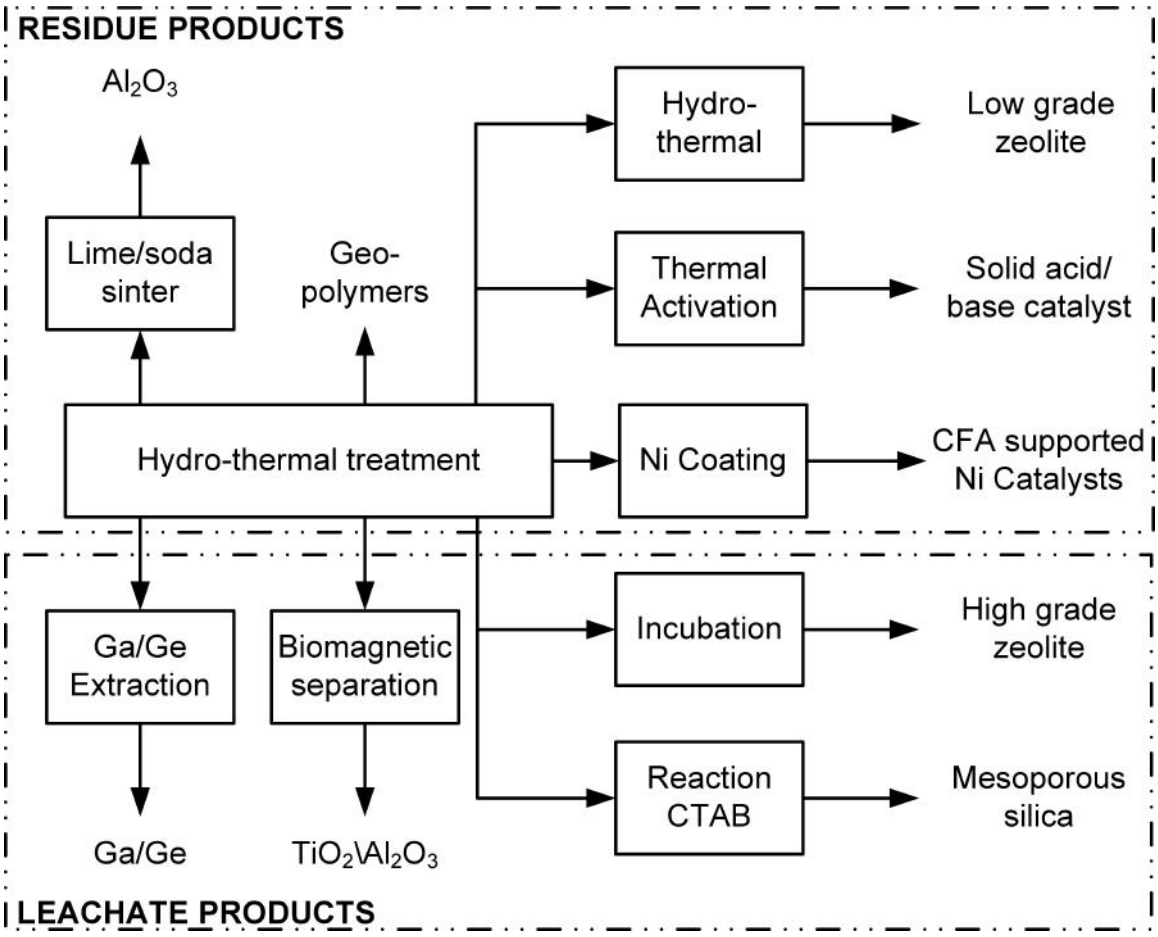

Figure 2.8: Overview of the ash products that have been obtained from 1-step or multi-step hydrothermal activation.

being able to use the CFA directly, but this may come at the expense of effectiveness. For example, although CFA is used directly as a soil amelioration agent there are issues regarding potentially mobile toxic elements being applied to soil which is being used to grow crops. In this case pre-treatment steps have been considered [61]. The variability in chemistry, mineralogy, and morphology of different CFA samples also hinders its use directly.

The indirect applications of CFA usually combine a series of chemical, thermal, and/or mechanical activation methods in order to produce the requires formulation. Figure 2.8 illustrates how a similar initial processing step can lead to the formulation of a variety of different products. This is potentially of significance with respect to the design of new CFA derived products. In order to maximise productivity and minimise waste, it is important to recognise where multiple products might be obtained from the same processing step.

Essentially high purity zeolites and mesoporous silica are manufactured using the same method; the difference being that the structure directing agent CTAB is employed in the crystallisation stage in MCM-41 synthesis. The same principle applies to an alkaline fusion first stage.

2.4 CFA Separation Technology

2.4.1 Carbon Recovery

There are various different options for the beneficiation of CFA with respect to reducing the LOI value. Electrostatic separation has been attempted by several investigators [164–166]. It operates on the principle of bipolar charging of dry particles either by particle-particle contact or by particle-wall collision under turbulent conditions. It is then possible to separate the positively charged carbon particles from the negatively charged ash particles in an electric field. Although this technology has been commercialised it has to be ensured that the ash is sufficiently dry prior to the beneficiation process or the separation efficiency can be significantly diminished [167].

Other beneficiation technology that has been commercially applied is that of fluidised bed reactors. These combustors are capable of processing a continuous stream of CFA using a thermal process designed to burn out the residual carbon. The heat from the flue gas and product ash is recovered and used to preheat the steam condensate from the power station and in doing so reducing the thermal load on the power station. This has proved to be a robust system and has been implemented at the Wateree Station of South Carolina Electric and Gas in 1999; it is capable of processing 180,000 tonnes of ash per year. A second unit with a capacity of 200,000 tonnes per year was installed at the Winyah Station of Santee Cooper in 2002 [168]. Cammarota *et al.* [41] reports an extension of the principle of operation and used a conical fluidised bed reactor to both burn the residual carbon and separate the remaining product ash into two narrow size

distributions.

One of the most promising methods to liberate unburned carbon from CFA is that of froth flotation. This is a highly versatile method for separating particles based on the ability of air bubbles to selectively adhere to the surface of a particular mineral surface. The particles attached to the air bubbles become positively buoyant and rise through the slurry while those that remain wetted sink to the bottom of the vessel. As carbon is naturally hydrophobic it means that the flotation of carbon from other mineral particulates is a well known process in the flotation of coal fines. Coal flotation tests were conducted in US laboratories as early as 1915 [169]. This extensive experience of floating fine coal particles from ash minerals has led to an interest in applying similar technology to carbon recovery from CFA using a flotation cell [170] and with particular respect to ash beneficiation using a flotation column [171]. CFA beneficiation has also been commercialised in the US with reported carbon grade recoveries of up to 70% [172]. Other methods have been compared to froth flotation, including an air sparged hydrocyclone which was found to compare unfavourably to a conventional mechanical froth flotation cell [173]. A combination of sieving and froth flotation has been employed to achieve high carbon yields and grades, but this was primarily for the purpose of characterisation studies [9].

A similar technology to froth flotation is that of oil agglomeration. This relies on the preferential wetting of oleophilic/hydrophobic particles by oil added to an aqueous slurry. In the present case this would involve the carbon particles wetted by the oil and the ash mineral particles remaining in suspension. The vessel is agitated and this allows the oil coated particles to collide with each other and form agglomerates. The oil/carbon agglomerates being less dense than the ash suspension rise to the top of the vessel [174]. Using this method and employing cyclohexane as the solvent, high carbon purity (66-71%), and high carbon recoveries (55-57%) were achieved [175]. Other researchers reported similar carbon purities in their agglomerates using vegetable oil as their solvent but, as this was a characterisation study, no recovery data was included [35].

In a study that compared a flotation column, an oil agglomeration column, and a triboelectrostatic separator, it was observed that the flotation column performed the best with grades of 61% and recoveries of 62%. However the ash product was only beneficiated to the extent of LOI $< 8\%$ and the researchers suggested that a multi-stage process or further optimisation of the flotation column was required to obtain an acceptably low LOI ash product [165].

2.4.2 Cenosphere Recovery

One of the earliest, but certainly not the first, descriptions of the presence of hollow spherical particles in CFA was given in by Fisher *et al.* [176]. The hollow spheres were called cenospheres and are considered to be one of the most important value-added components of CFA; they are similar in composition to the CFA though they tend to have a larger particle size [177].The unique properties of cenospheres, namely their sphericity and their low density relative to water, make them amenable to a variety of different applications.

The methods of extraction of cenospheres have traditionally relied on the storage of CFA in large lagoons from where the cenospheres can be removed from the surface of the water. Concern has been raised over this type of process because of the potential for CFA to leach toxic elements [177]. However studies into the leaching behaviour of a typical CFA sample in the US found that it was safe under natural leaching conditions [178]. Nonetheless, extraction of cenospheres from ash lagoons is both space and time intensive and does not allow for integration into a continuous CFA processing plant.

An alternative method of cenosphere extraction was described in a study by Gurupira *et al.* [179] whereby a triboelectric separation system was used. However, this method is reliant on the definition of the cenospheres as having a specific gravity of less than 2. This definition was first used by Ghosal and Self [180] and is based on the fact that a solid particle of pure silica should have a higher density than that exhibited by the ash particles. Taking this into account the gas bubbles could be trapped in particles with specific gravity of greater than 1. However, this is generally not the accepted definition in

the bulk of the literature; regardless, many of the high value applications for cenospheres rely on their very low density.

There are very few other studies that have examined the extraction of cenospheres. When trying to integrate the extraction of cenospheres into a wider CFA beneficiation process, a continuous operation is desirable. A theoretical treatment of the cenosphere recovery process was carried out on a wet and dry basis [177]. The authors felt that wet processing caused too many environmental problems and imposed space restrictions. A comparison is made between the wet and dry separation by using a size density distribution of industrial cenospheres and CFA. By calculating the terminal velocity of these particles using either water or air as the medium, then setting an upward fluid flow rate equal to the terminal velocity, the percentage of particles reporting to the underflow and overflow can be determined. What is instructive in this analysis is that, using water as the separation medium, the cenosphere particles are lifted upwards by their positive buoyancy, so a density separation governs. However, using air both the cenospheres and the CFA particles have a density much larger than the air, and it is the size that governs the separation. For water, the upward velocity that can be used is limited by the size of the smallest ash particles. Conversely for air separation, any overlap in the size distributions of the ash and cenospheres will reduce the efficiency of the separation. The theoretical analysis found that dry separation performance was marginally less efficient than wet separation.

The same research group went on to publish an experimental study comparing two types of air separators: the micron and the closed-type pneumatic separator [181]. The micron separator was found to be superior to the closed-type pneumatic, but both were much less efficient than the theoretical maximum. After the dry separation the underflow product (cenosphere concentrated) was subjected to a wet float and sink. It was observed that the 80% of the cenospheres could be recovered with close to a 90% reduction in the ash that required further processing via wet separation.

2.4.3 Magnetic Sphere Recovery

The removal of magnetic concentrate (MC) from CFA is also a significant opportunity to create added value. The amount of magnetic material varies in each particular CFA depending on the coal source and operating conditions of the coal boiler, but it can vary from between 0.5-18% [182]. There is little in the literature about the specifics of magnetic material recovery from CFA. However, magnetic separation of materials is a mature and well established technology emerging from the mid 19th century. Magnetic filtration has been used to capture 15% of CFA emanating from a power station, but this was for the purposes of pollution control rather than ash beneficiation. The basic principle behind magnetic separation is straightforward; it relies on the fact that materials with different magnetic moments experience varying forces in the presence of magnetic field gradients. In this way, an externally applied magnetic field can lift out those materials with similar magnetic properties [183].

Although the literature is not extensive there are some studies that relate to the specific example of magnetic recovery from CFA [184–186]. However, the primary objective of these studies was to be able to characterise the magnetic material and little attention is paid to the separation. Groppo and Honaker [187] conducted a pilot scale investigation into the potential for recovering the magnetic fraction from bottom ash for the purposes as a dense medium in coal cleaning circuits. The process involved feeding the ash slurry through concentrating spirals which separated the ash into heavy and light fractions. From here the heavy ash fraction was fed to a continuous high gradient magnetic separator (HGMS). In a HGMS a large static magnetic field is applied to a column containing a matrix such as steel wool. The irregular surface of the matrix generates high magnetic gradients which generate enough force to capture weakly magnetic particles [183]. The processing scheme of Groppo and Honaker was capable of producing magnetic material with an iron content of almost 75%.

2.4.4 Separation Process Economics

A full economic evaluation of the wet separation procedure is beyond the scope of this review. However, the various wet separation processes are only viable in an economic sense if sufficient value has been added to the starting CFA, so a brief consideration of the topic will follow. It is hard to estimate the value for the products in part due to their commercially sensitive nature and in part due to the fluctuating nature of the commodities they replace. It must also be noted that for all the products the specification will usually be for low moisture content, so this necessitates a drying stage in the processing scheme.

Although literature regarding the prices of CFA derived products is scarce, there have been some estimates. For cenospheres, in 2001, an average selling price of $700 per tonne was reported [179]. This compares to an implied value of €2667 per tonne in the German market given in a review of hollow microspheres in 2004 [188]. The carbon enriched product can reasonably be compared to the price of coal as it is of sufficient carbon content to be combusted for power generation. In this case the latest bulk price for coal for steam is somewhere in the region of $100 per tonne [189]. In section 2.4.3 the use of the magnetic spheres for coal cleaning as a magnetite replacement was reported [187]. In this study the price of magnetite to the coal industry in the US was given as $150-200 per tonne; its use as a functional filler would probably be a higher value market. Finally, an IFA residue that consistently meets the specifications required by its incorporation into cement could conceivably be sold for prices approaching that of cement which, in 2010, in the US were $100 per tonne [190]. Given that the separation process is capable of improving the low quality ash with little, or no resale value, it seems economically favourable.

2.5 Applications for Fractionated Ash Products

2.5.1 Cenospheres

The unique properties of cenospheres, namely their sphericity and their low density relative to water, make them amenable to a variety of different applications.

The fact that they float on water is of special interest to researchers investigating new photocatalysts. They can be used as a buoyant carrier to enhance catalytic activity as they increase the exposure of the particle to light sources [191–195]. The fact that they float also means that they are easily recovered from water after the reaction. This feature of the cenospheres has also attracted interest for their use in water purification applications such as the removal of excess fluoride from drinking water; this was achieved by producing magnesia loaded cenospheres using a relatively simple wet impregnation method of magnesium chloride [196]. This principle can be extended by applying functional layers onto the CFA cenosphere. A process of electroless plating of nickel followed by hydrothermal synthesis of the zeolite ZSM-5 has been used to create a cenosphere/Ni/ZSM-5: a composite structure that is a molecular sieve, floatable, and magnetic [197].

Cenosphere properties have also been altered by coating with various metals. Their use as lightweight materials in the fields of electromagnetic interference shielding, electromagnetic wave absorbance, and high light reflectivity has been suggested by some researchers. A variety of different methods of plating have been used, but some of the most widely investigated include electroless plating [198–201], magnetron sputtering [202–204], and heterogeneous precipitation [205, 206]. The advantages of using a cenosphere as the carrier are its sphericity, non-toxicity, low weight, and high strength. This makes it ideal for its incorporation into materials such as silicone rubber in order to increase the conductivity of the rubber. Furthermore, this enhances its suitability for use as an electromagnetic wave absorbing material which can be used in electronic and radar applications [201].

The lightweight nature of the cenospheres renders them suitable for the design of light weight composite materials. A variety of different composites have been evaluated,

such as CFA incorporation into concrete [207, 208], polymers and resins [209–211], and metal alloys [212–214]. Their use in these applications reduces the extent to which energy intensive and resource dependent materials are used. In the case of the metal alloys their use also confers some advantages to the composite structure. Traditionally porosity in cast metal is an undesirable property; however, by using the cenospheres to enclose porosity inside strong hollow structures embedded inside metals several properties of the composite are enhanced, and the structural weight is decreased. Materials of this sort are highly suited for use in weight sensitive applications such as the automotive and aerospace industries [214].

The use of hollow spheres in ceramic composite foams has also been of significant interest. In this case they are being investigated for their likelihood to exhibit high temperature performance and low thermal conductivity particularly for refractory materials [215]. Other studies have taken a different approach and evaluated the possibility of using them as coating materials for similar reasons. They were coated onto a silicon carbide substrate using an electrophoresis method; they exhibited a lower thermal conductivity relative to pure CFA coatings, but they were extracted based on size rather than density so caution should be exercised in the interpretation of the results [216].

Economically the use of cenospheres makes sense in applications that have traditionally used manufactured hollow spheres made of glass. For this reason they were assessed for their potential to act as a sensitiser for emulsion explosives. Their performance was comparable to glass spheres made by 3M [217].

2.5.2 Fly Ash Carbon

In section 2.4.1 the technology to recover carbon from raw CFA was discussed. The uses for this enriched carbon product are numerous and much attention has been paid to them in recent research. Because the carbon grade of the recovered material is usually between 70-80%, there is the potential to use it as a coke in the metallurgical industry. However, for this to be the case the phosphorous content must be reduced to less than 20 ppm.

In order to reach this target a process of carbon chlorination was able to reduce the phosphorus content of a carbon enriched CFA from 2000 ppm to 24 ppm [218].

Enriched carbon from CFA has also been used as a precursor for activated carbon preparation. Various methods have been evaluated including the use of steam in a fluidised bed at 900°C [219–221], in a horizontal furnace with steam at 850°C [222, 223], and soaked in KOH solution prior to activation at 780°C [224]. Another study investigated more thoroughly the steam activation procedure using temperatures ranging from 750-850°C. The effect of the addition of ammonium salt solution pre-treatment using different solution/solid ratios was reported. The addition of KOH was also studied [225]. It was found that pre-treatment with ammonium-salt solution produced activated carbon samples with better adsorption properties relative to conventional steam activation, and that the addition of KOH is effective at increasing the specific surface area, but it also reduces the yield.

Activated carbon manufactured from CFA has been proposed for a variety of applications such as for the removal of sulphur dioxide (SO_2) from flue gases [220, 221, 226]. SO_2 is an air pollutant that can cause acid rain and photochemical smog. For this reason it has been increasingly regulated in the exhaust emissions from fossil fuel combustion sources. The SO_2, H_2O, and O_2 from the flue gases are adsorbed onto the internal surface of the carbon, and the adsorbed SO_2 is then oxidised to sulphuric acid and stored within the pores [221]. In a very similar application the adsorption capacity for the retention of NOx has been investigated [219, 226]. Another coal combustion pollutant that is attracting scrutiny is mercury emission. In the US in 2003 the Environmental Protection Agency (EPA) proposed a permanent cap to be implemented by 2018 stipulating a 68% reduction. A promising mitigation strategy is to inject fine carbon adsorbent upstream of the electrostatic precipitator that collects the CFA. The use of recovered carbon as a source for activated carbon offers a cheap and effective way of acting on the mercury regulations [222]. Other uses for activated carbons from CFA, such as the treatment of liquid waste, have also been of interest. Activated carbon from the unburned coal in bottom

ash was used to examine the capacity for removal of various organic compounds from an aqueous stream; adsorption capacities were increased relative to the raw CFA [223].

The unburned carbon from CFAs has been assessed for its suitability as a precursor in the manufacture of graphite; it was found that graphite materials made from CFA carbon were similar in both physical properties and in performance in lithium-ion batteries [227–229]. With its relatively high specific charge capacity, high cycling efficiency, and low irreversible charge, graphite is the conventional choice for the majority of commercially available lithium-ion batteries which are the energy source of choice for most portable electronic device manufacturers. As the demand for these lithium-ion batteries increases this will affect the graphite market both in terms of production and price [229].

2.5.3 Improved CFA Residue

It has been discussed in section 2.2 that high carbon content adversely affects CFA concrete. Improved coal fly ash residue (IFA) can be used for the highest quality EN 450-1 category A ash which has the highest market value. Most CFAs have a particle size distribution that would mean that a fraction of the material would not conform to these specifications, so a classification process is required that yields a fine and a coarse IFA product.

The coarser ($> 45\mu$m) material could still be utilised; because it has been processed, the chemical composition of the ash is uniform enough to be suitable for the delicate balancing of feedstock to manufacture quality cement. One study has found that fly ash is a suitable raw material for cement manufacture, and its residual carbon content can decrease the energy required in the cement kiln [230].

Both fine and coarse IFA could be used in any of the applications discussed in section 2.3. Indeed, the use of IFA in zeolite production could be very beneficial. As the iron oxide content is significantly reduced, the extent of its dissolution in the alkaline leaching step of zeolite production would be reduced; researchers have shown that a reduction in iron oxide improves the CEC of the zeolite [231]. It is also conceivable that the fine IFA

would show increased zeolite yield due to its small size and increased area which should enhance silica reactivity with NaOH and hence its extraction.

The use of an IFA is particularly relevant to its application as a filler in polymer blends. In this case, it has been found that a particle size of $< 5\mu$m is suitable. It not only extends the bulk polymer volume, but also facilitates compounding and processing. In addition it has been shown to improve the physical properties of the plastic products made from it [232]. Yang *et al.* [233] described the surface modification of a purified fly ash in order to improve the interfacial bonding between fly ash and polymer. They showed that treating a purified ash with $Ca(OH)_2$ and CO_2 created a rougher surface which improved the polymer-CFA bonding.

2.5.4 Magnetic Spheres

Groppo and Honaker [187] evaluated the possibility of incorporating a magnetic recovery process into an existing CFA remediation plant in Kentucky to assess the CFA derived magnetite for its suitability to use as a dense medium in coal cleaning circuits. They found that the CFA magnetite had similar or better performance to conventional magnetite after the CFA magnetite had been milled for a period of time to increase its suspension stability. Magnetite use for dense medium separation in coal cleaning circuits could provide an excellent opportunity to utilise the magnetic fraction of the CFA and at the same time provide another example of industrial synergy.

Other uses for magnetite include as a filler material for polymers used in recording media and medical applications. It can also be used as a filler in thermoplastics and rubbers intended for the automotive interior and building industries due to its sound damping behaviour, high density, and electrical and magnetic properties [234]. Magnetic spheres derived from CFA have also been assessed for their suitability as catalysts for deep oxidation of methane with limited success [235].

CHAPTER 3

CHARACTERISATION OF COAL FLY ASH AND THE DERIVED PRODUCTS OF COAL FLY ASH

In order to fully utilise the separable components of CFA, it is necessary to characterise them. It has already been discussed that CFA is a heterogeneous product and a full profile of the physical and chemical properties of the CFA derived material is required in order to proceed with investigation into the processing or potential applications. This chapter is divided into 3 sections: (1) CFA and RockTron products; (2) the rare earth content of UK and Polish CFAs; and (3) the characterisation of a density fractionated CFA.

3.1 RockTron Products

3.1.1 Introduction

RockTron devised a process flow sheet capable of separating distinct components of CFA. The process overview is shown in Figure 3.1. CFAs of UK origin and the products of the processing scheme were characterised with respect to their particle size, bulk chemistry, mineralogy, morphology, and trace elements. Although similar work has previously been carried out in detail [5,9–11], this is the first time to the author's knowledge that products of a commercial scale have been characterised.

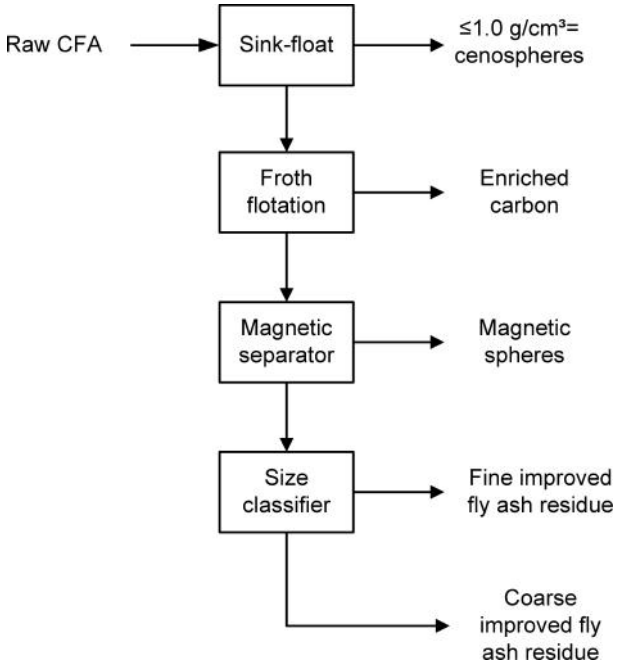

Figure 3.1: Sequential fly ash separation schematic

3.1.2 Experimental

The samples were analysed for particle size after ultrasonic de-agglomeration using a Malvern Mastersizer 2000. A refractive index of 1.65 was used in the calculation model. The density was determined using a Micrometrics helium pycnometer: for each material one sample was analysed; the values represent the average of 5 measurement cycles (n=5); 20 purge cycles were conducted prior to each measurement; each run usually took *ca.* 1 hour to complete. For bulk chemical analysis a prepared sample (0.200 g) was added to lithium metaborate/lithium tetraborate flux (0.90 g), mixed well, and fused in a furnace at 1000 °C. The resulting melt was then cooled and dissolved in 100 mL of 4% HNO_3 / 2% HCl solution. This solution was then analysed by inductively coupled plasma - atomic emission spectrometry (ICP-AES) and the results were corrected for spectral inter-element interferences. 30 trace elements were determined in a method in which a prepared sample (0.200 g) was added to lithium borate flux (0.90 g), mixed well and fused in a furnace at 1000 °C. The resulting melt was then cooled and dissolved in 100 ml of 4% HNO_3 / 2% HCl solution. This solution was then analysed by inductively coupled plasma - mass spectrometry (ICP-MS). For carbon content a sample (1.0 g) is placed in an oven at

1000 °C for one hour, cooled and then weighed. The percent loss on ignition (LOI) was calculated from the difference in weight. Mineralogy was assessed using a Bruker D5005 powder diffractometer. The samples were ground in an agate pestle and mortar with 10 wt% corundum and then scanned from $2\theta = 15°$ to 60° with a step size of 0.02° and a rate of 6 seconds per step. The scans were analysed using the Rietveld refinement software MAUD [236] to quantitatively determine the mineral content of each density fraction. Minerals were initially identified using the search match function in the Bruker software EVA. Diffraction patterns were loaded into Maud from either the software database, or they were download as cif files from an internet resource [237]. Background refinement was carried using an interpolated polynomial background function. Quantitative analysis was carried out allowing the crystal cell dimensions to be refined. Two microscopes have been used to image CFA and components thereof: a Philips Xl30 scanning electron microscope with a LaB6 filament emission source based at the centre for microscopy at the University of Birmingham and an ultra high resolution Carl Zeiss SEM equipped with a field emission source based at the National History Museum in London.

3.1.3 Results and Discussion

Bulk Chemistry

With respect to the bulk chemistry of the tested samples, it is interesting to note that all of the samples (with the exception of the carbon concentrate) as defined by the American Society for Testing and Materials (ASTM) in the standard ASTM C618 would be classified as Class F CFAs despite the fact that the magnetic concentrate has a significantly different chemistry relative to the other CFAs. In Vassilev and Vassileva's more systematic CFA classification scheme [18] presented in Fig.3.2, all of the CFA and CFA derived products are classified as *sialic* apart from the magnetic concentrate which is classified as *ferrisialic* due to a relatively larger Fe_2O_3 content. Given the nature of the separation of this component this is unsurprising, but it does give rise to the notion that relying on specifications for

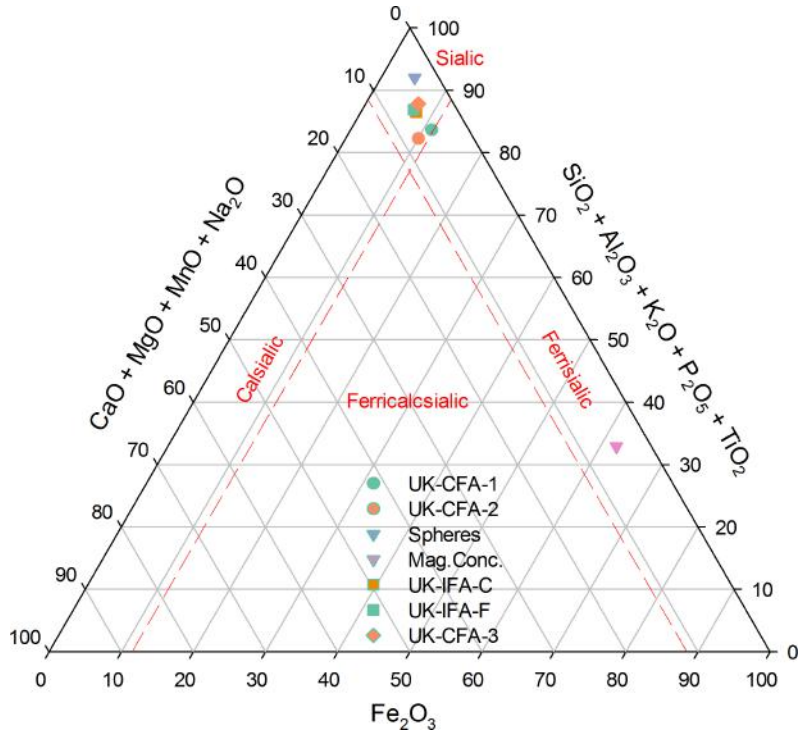

Figure 3.2: Two CFAs originating from the UK and 5 components of CFA resulting from multi-stage processing plotted on the ternary axis as devised by Vassilev and Vassileva [18]. Axis values are in mass percentages of each group.

one particular industry may be misleading. What is also noteworthy from Fig.3.2 is that both the CFA-1 and CFA-2, whilst being in the *sialic* region are very close to the borderline for *ferrisialic* ashes which means that they contain rather high iron contents. The two IFA residue products have almost identical positions on the ternary plot which highlights the effect of the multi-stage processing on producing consistent compositions across different size fractions of ash. The cenosphere samples exhibits the highest degree of alumino-siliceous content which might provide an avenue for investigation into the necessary formation mechanisms for these particle types.

Table 3.1: Bulk chemistry of three CFAs originating from the UK and 5 components of CFA resulting from multi-stage processing

Sample	SiO_2	Al_2O_3	Fe_2O_3	CaO	K_2O	MgO	TiO_2	Na_2O	P_2O_5	MnO	LOI	SiO_2/Al_2O_3
CFA-1	48.4	25.5	10.5	2.6	1.6	0.5	2.8	1.0	0.1	0.3	6.8	1.9
CFA-2	44.7	25.2	9.0	4.0	2.2	0.5	2.5	1.0	0.1	0.4	10.3	1.8
CFA-3	45.8	24.9	6.2	2.1	1.2	0.6	2.1	0.9	0.1	0.6	15.1	1.8
IFA-F	49.2	27.8	6.6	3.2	1.6	0.7	3.0	1.0	0.1	0.4	6.4	1.8
IFA-C	52.2	26.2	7.3	3.2	1.7	0.5	2.9	1.0	0.1	0.3	4.7	2.0
Mag. Conc.	20.3	11.3	62.3	2.9	1.5	0.1	0.7	0.4	0.2	0.2	-0.1	1.8
Spheres	55.8	29.7	4.6	1.0	1.6	0.6	4.1	0.9	0.0	0.1	1.3	1.9
Carb Conc.											74.6	

Table 3.2: Density of two CFAs originating from the UK and 5 components of CFA resulting from multi-stage processing

CFA-1	CFA-2	CFA-3	IFA-F	IFA-C	Spheres	Mag. Conc.	Carb. Conc.
2.26	2.31	2.30	2.33	2.19	0.79	3.47	1.97

Density

The specific gravity results that are shown in Table 3.2 show the difference in density of the components which range from 0.79-3.47. As has been alluded to previously, the cenospheres are less dense than water and for this reason their collection methods are usually based on their ability to float. It also clear that the carbon is marginally less dense than the ash fractions, and the magnetite is much more dense than the ash fractions. The information presented, in conjunction with the particle size data might prove useful when trying to design new separation systems for the cenospheres. It is also important to note that these densities represent an average of all the particle classes and yield no information as to the spread of the densities within each class.

Mineralogy

The mineralogy of coal fly ashes varies widely with different combustion conditions and coal sources resulting in different mineral profiles. This is reflected in Table 3.3 and Figure 3.3. It is obvious graphically that CFA-3 is quite different from CFA-1 and CFA-2. The most marked difference is the hump around 20-25° which seems to become very slightly more pronounced for CFA-2 relative to CFA-1 and markedly more pronounced for CFA-3. This would appear to be a result of the increasing values of carbon content that were given in Table 3.1. It is also clear from the scans that the corundum (Al_2O_3) peak from the internal reference spike in CFA-3 is larger relative to the other mineral peaks. This is more apparent in Table 3.3 where it is shown that CFA-3 has the least amount of crystalline components with just 10.4% registering from the Rietveld refinement. It is necessary to point out here that there is most likely a range of minor mineral content that is not accounted for in the Rietveld refinement because the low concentrations mean that it is extremely hard to distinguish from the background. While the mineral profiles for CFA-1 and CFA-2 are quite similar, CFA-3 is characterised by a low quartz (SiO_2) content and an undetectable level of hematite ($Fe2O_3$). The absence of hematite makes sense as CFA-3 has a lower iron content that the other two parent ashes. The other noteworthy

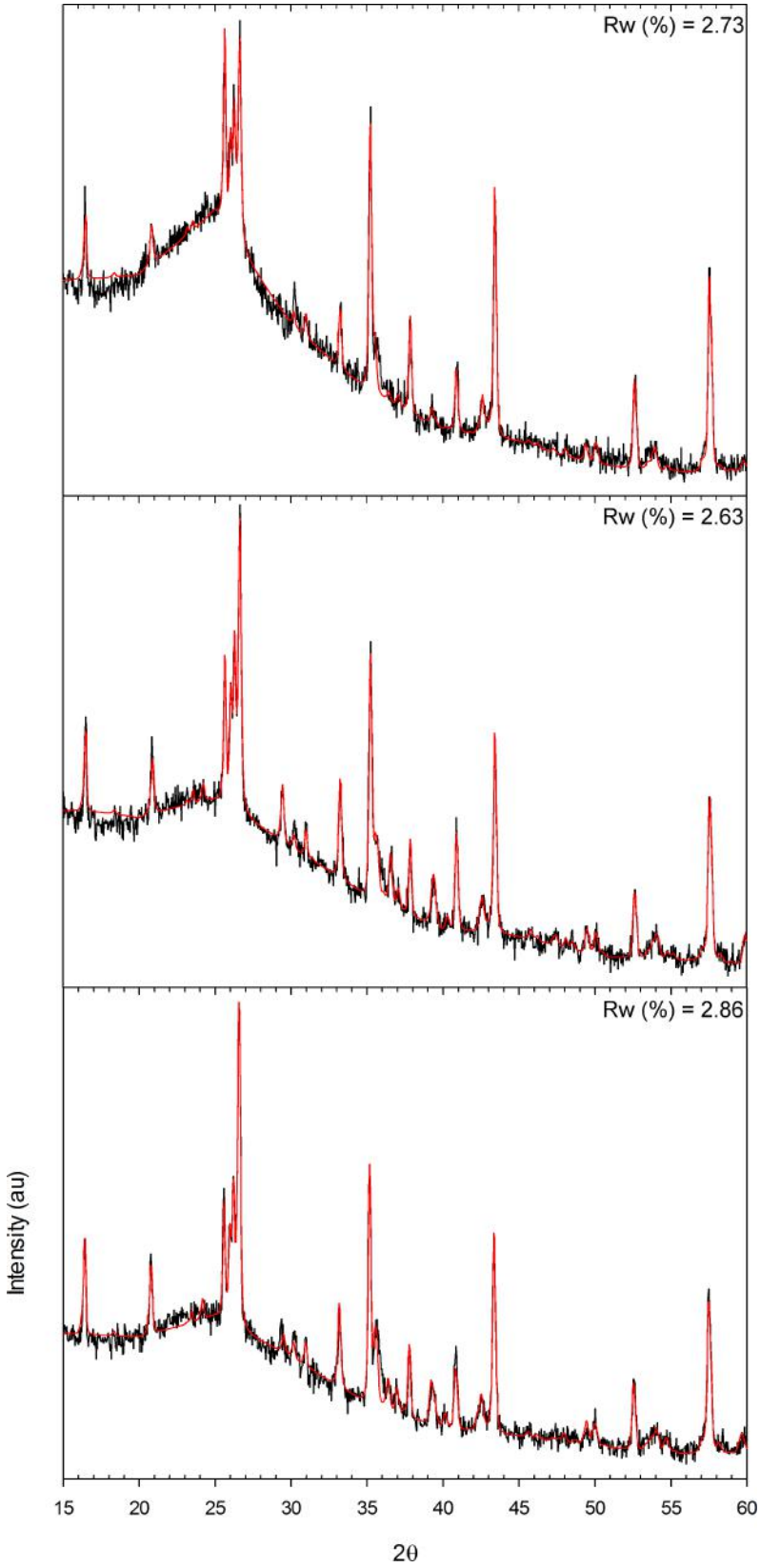

Figure 3.3: Three CFAs originating from the UK: CFA-1 (bottom), CFA-2 (middle), and CFA-3 (top). The solid lines (——) are the diffraction pattterns and the red lines (——) are the Rietveld refinement fits from the software MAUD.

difference is the calcite concentration which is relatively large for CFA-2, however for CFA-3 it is undetectable and it is extremely low for CFA-1. A plausible reason for the difference between CFA-1 and CFA-2 is that the former was stored in an ash lagoon and therefore it is likely that the calcium carbonate was solubilised to a large extent.

From the foregoing it is clear that all three of the CFAs originating from the UK are primarily amorphous aluminosilicates with lesser extents of char and mineral matter. The mineral abundance for all is in the order mullite ($Al_6Si_2O_{13}$) > quartz > hematite-magnetite (Fe_3O_4) > calcite ($CaCO_3$). Other minerals are almost certainly present, but not in sufficient quantities to be sure of their identification. Mullite is usually produced as a secondary mineral not present in the parent coal in combustion processes of pulverised coal at temperatures greater than 900°C . It has been observed that there might be an association between the mullite concentration and the ratio of Al_2O_3/SiO_2 ; excess Al_2O_3 in the glass phase was found to be associated with higher mullite contents [238]. The CFAs studied have low mullite concentrations (7.5-9.4%) relative to the ashes characterised by Font *et al.* [238], despite lower Al_2O_3/SiO_2 than many of them. The extent of mullite formation is likely to be related to the rate of CFA cooling after combustion with slower cooling resulting in lower mullite contents. Quartz presence is lower than mullite in all of the samples. The fact that there are no other SiO_2 species present (e.g., cristabollite or trydimite) is a likely indicator that the quartz is primary in nature. If this is the case it is likely that the quartz will be concentrated in the larger size fractions of CFA [10]. Iron oxides tend to be formed from decomposition reactions of pyrite and Fe-carbonate species in the parent coals. Hematite crystallises at temperature exceeding 500°C and magnetite crystallises at higher temperatures. This is the reason that for CFA-1 and CFA-2 the hematite concentration is higher than the magnetite, However CFA-3 is anomalous in that it contains no hematite and 0.6% magnetite. This suggests that the boiler conditions that generate UK-CFA-3 are highly reducing - as a result of oxygen depletion [238] - such that Fe-rich melt drops crystallise into magnetite in preference to hematite.

Table 3.3: Semi quantitative mineral contents of 3 CFAs of UK origin and the products of RockTron's processing scheme derived from XRD. An extra magnetite sample was also calcined at 850°C for 1 hour

Sample	Glass	Mullite	Quartz	Magnetite	Hematite	Calcite
CFA-1	83.6	8.4	5.3	0.8	1.5	0.4
CFA-2	81.2	9.4	6.1	0.7	1.3	1.1
CFA-3	89.6	7.5	2.4	0.6		
IFA-F	85.1	9.0	4.3		1.1	0.5
IFA-C	76.4	13.5	8.3		0.9	0.8
Mag. Conc.	77.5		2.0	17.1	3.5	
spheres	80.4	17.2	2.2			0.3
Mag. Conc. 850	77.6		0.7	8.5	13.1	
Carb Conc	79.7	12.8	3.9			3.6

The mineralogy and chemistry of the magnetic concentrate is intriguing. It was impossible to resolve the difference between maghemite and magnetite although it was fairly likely that both were contained within the magnetic concentrate; this was due to the similarity in XRD patterns [106]. The magnetic concentrates contain 62% (Fe_2O_3 basis) but the concentration of hematite and magnetite is only *ca.* 20.6%. There is the possibility that this is an exaggerated result of micro absorption effects that occur due to the difference in attenuation coefficients of aluminosilicates and iron oxides [106], however it is unlikely to account for the whole disparity. The XRD patterns point towards an Fe-rich amorphous phase into which is set crystalline growths of hematite and magnetite. Such mineralogy in magnetic concentrates has been observed previously [11]. The peaks in the XRD patterns are fairly broad (see Figure 3.4) and it was postulated that the iron oxides phases might be exhibiting poor crystallinity and that this was the reason for the lower mineral content relative to amorphous. To test this theory the magnetic concentrate was calcined and the results can be seen in Figure 3.4. In the results it is noticeable the hematite peaks in the calcined samples are now higher relative to the magnetite. Table 3.3 emphasises this; the hematite in the calcined sample increases from 3.5-13.1% while the magnetite has reduced from 17.1-8.5%. It appears that the calcination has merely converted some of the magnetite into hematite without any hematite crystallising from the amorphous component.

The cenosphere samples studied have a higher mullite content (17.2%) than the bulk CFAs. This has been observed previously [11], although in those cenospheres the higher mullite content (14%) was concomitant with a higher quartz content (6%) as well as small amounts of cristabolite (2%). In this earlier study it was revealed, through the use of a hydrofluoric etch and SEM, that the mullite crystallises in the form of fine needles and was attributed to heterogeneous nucleation in the molten aluminosilicate bubbles and then a rapid cooling period. The absence of any cristabolite, in addition to the low quartz content of the UK cenospheres, suggests that the quartz is a relict mineral from the parent coal that has been somehow captured in the glass melt. The high mullite content in the

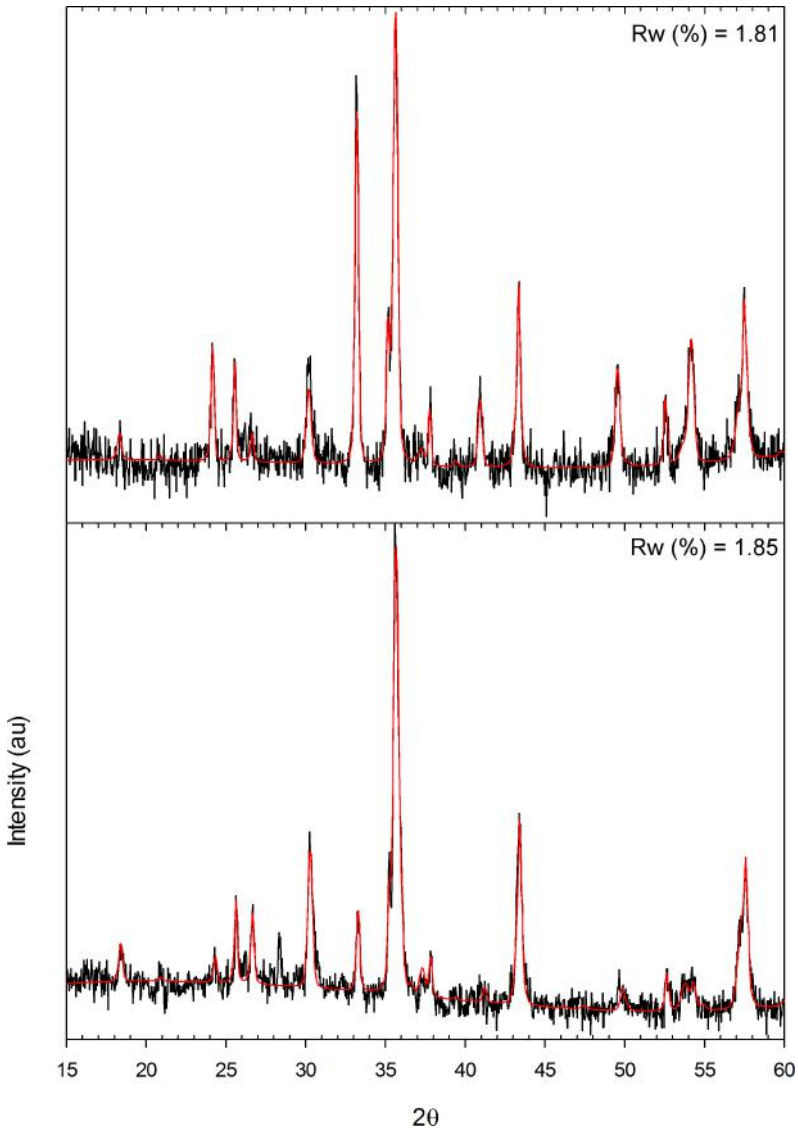

Figure 3.4: XRD patterns of magnetic concentrate (bottom) and a magnetic concentrate sample calcined at 850°C for 1 hour (top). The solid lines (—) are the original patterns and the red lines (—) are the Rietveld refinement fits from the software MAUD.

cenosphere skeletal wall is important from a practical point of view as it suggests a degree of resistance to both heat and chemical attack.

The carbon XRD pattern is shown in the top of Figure 3.5. The presence of carbon is apparent in the form of diffuse (002) and carbon bands (01) at *ca.* 26° and 44°. These diffuse peaks, together with an absence of any 3-dimensional graphite peaks at 44.7° and 50.8° indicate what is known as turbostratic order in the carbon [11, 239]. The individual layers have the same structure as graphitic basal planes and they have interlayer spacings that are similar. However the layers are translated or rotated in the planes in which they reside so that carbon atoms in a particular plane have no specific orientation to carbon atoms in adjacent planes. The diffuse band at (002) is also noticeable in the XRD pattern of CFA-3 in Figure 3.3 due to relatively high carbon content of that particular ash. The minerals identified in the carbon were mullite, quartz, and calcite, but they were only present in very small quantities. This indicates that the inorganic matter associated with the carbon is primarily in glass form. Whether this is due to slagging deposits on the carbon surface or mineral decomposition within unburned carbon particles is unclear.

The processing scheme is by design aimed at removing cenospheres and magnetic particles which are enriched in mineral matter. The classification of the coarse and fine IFA reveal that there is a size association with mineral matter. IFA-F shows a similar content of both mullite (9.0%) and quartz (4.3%) to CFA-1 and CFA-2 albeit with marginally smaller quartz content. However, IFA-C has both elevated mullite levels (13.5%) and the highest quartz (8.3%) content of all the samples. This appears to support the suggestion made previously that the quartz is primary in nature and features as discrete grains in the coarse size fraction. The high mineral content of the coarse grained IFA has implications for possible utilisation. The current author suggested its use for the synthesis of zeolites [240] as a relatively pure source of both silica and alumina. However, the current data suggest that its dissolution upon contact with sodium hydroxide will be limited by the mineral content.

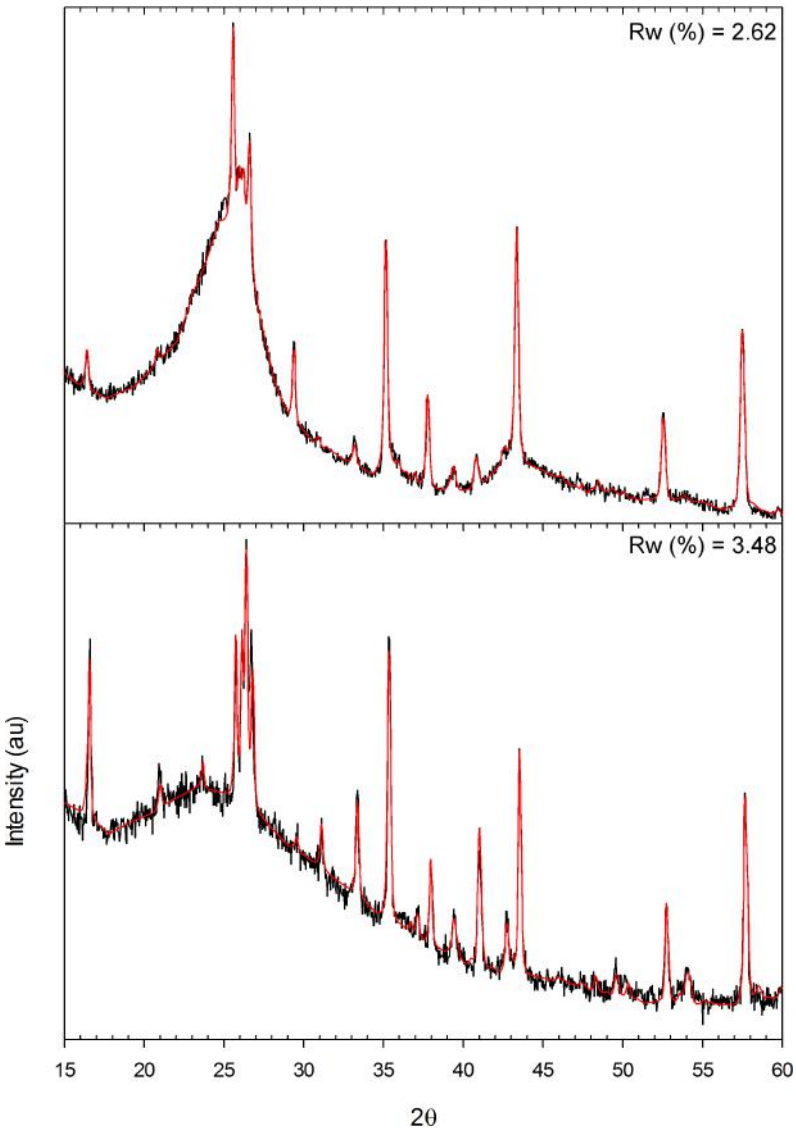

Figure 3.5: XRD pattern of cenospheres (bottom) and carbon concentrate (top). The solid lines (—) are the original XRD patterns the red lines (—) are the Rietveld refinement fits from the software MAUD.

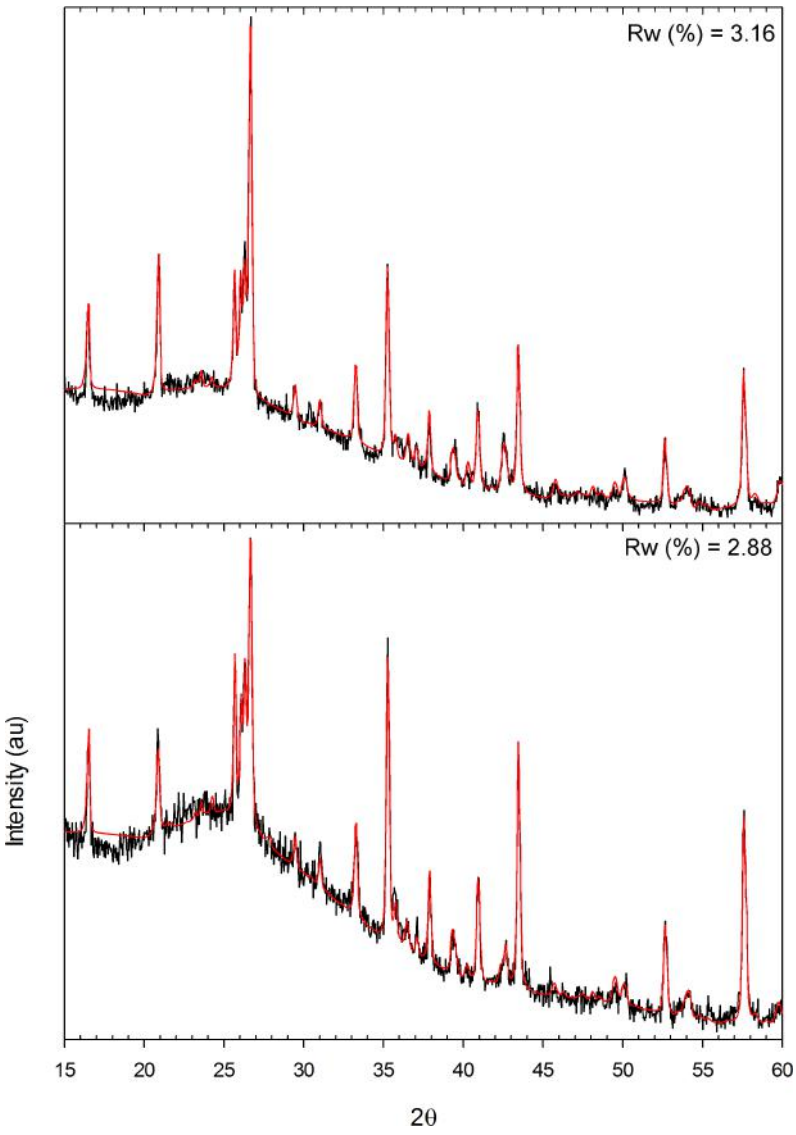

Figure 3.6: XRD patterns of fine (bottom) and coarse (top) fly ash residue. The solid lines (—) are the original XRD patterns and the red lines (—) are the Rietveld refinement fits from the software MAUD.

Morphology

Figure 3.7 illustrates quite dramatically the heterogeneity of typical CFA samples. Although there are many particles which are almost perfect spheres, the images contain completely irregular particles, hollow spheres with broken shells, spheres that have fused together, and spheres with varying degrees of porosity. It is also noticeable that there is a wide range of sizes of particles spanning at least two orders of magnitude. All of these feature are enhanced when viewing the separable components in isolation.

The finest size fraction of the residual ash after processing is shown in Figure 3.8[1]. This represents what remains of the ash after cenospheres, carbon, and magnetic fraction have been removed. What is striking in these images is that at this level of magnification it is clear that the surfaces of the particles are not smooth, they are covered in many nano sized particles. It is not clear from these images whether the extraneous particles are glassy or crystalline in nature, but given that XRD revealed that there was some calcite in the sample it is likely that calcite has crystallised on the surfaces to some extent. This calcite was likely to be the result of storage in atmospheric conditions. Although the images taken in Figure 3.9 are not at the same resolution, the contrast between the coarse fraction and the fine fraction is extremely pronounced. There are many more particle types, with the images being more closely representative of the images taken of the bulk CFA. Broken cenospheres, and broken plerospheres (spheres contained within a larger sphere) can be observed in the top image. A majority of the particles would be more accurately be described as spheroid rather than the perfect spheres that are present in the fine fraction. The bottom image highlights a particle that has a clear porosity. It appears as if several spheroid particles have agglomerated and/or been encompassed by a larger slag particle. This network structure of pores is particularly relevant to the discussion in the third section of this chapter.

The lightweight fraction is widely known as cenospheres; a compound of the greek *ceno*

[1]Images were taken using a ultra high resolution Carl Zeiss SEM equipped with a field emission source based at the National History Museum in London.

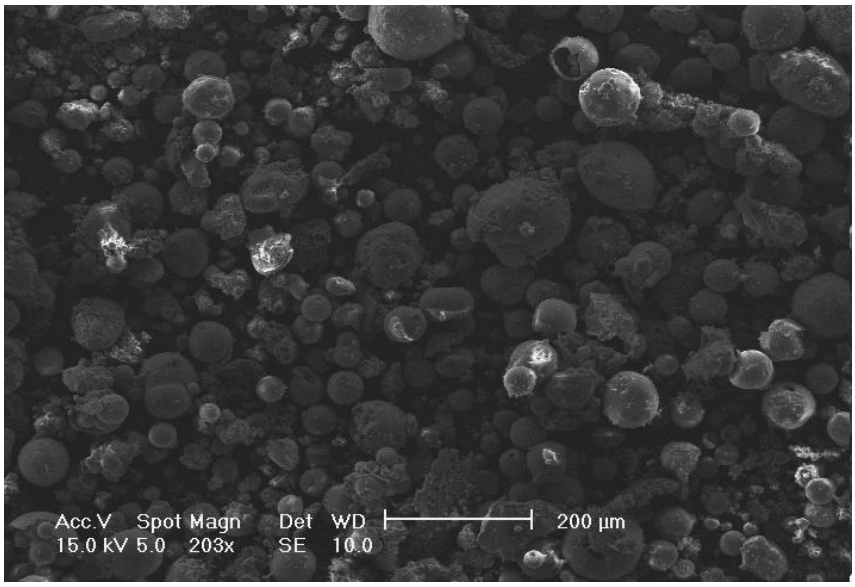

(a) UK-CFA-1

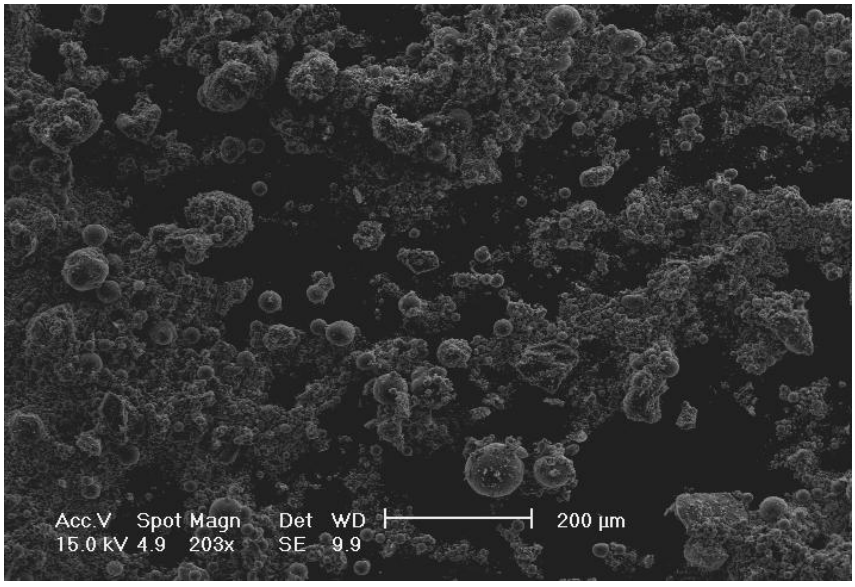

(b) UK-CFA-2

Figure 3.7: SEM images of two UK coal fly ashes

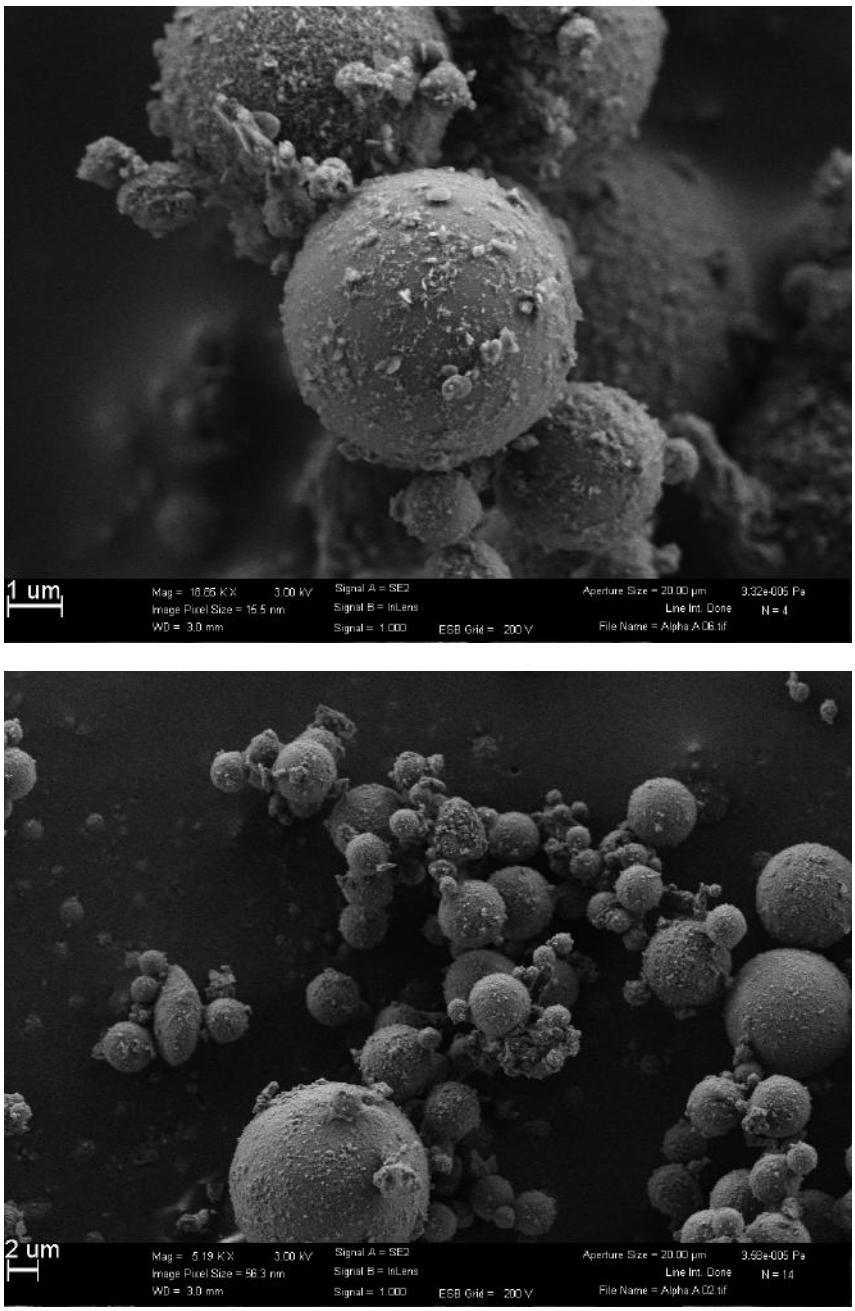

Figure 3.8: SEM images of fine IFA residue

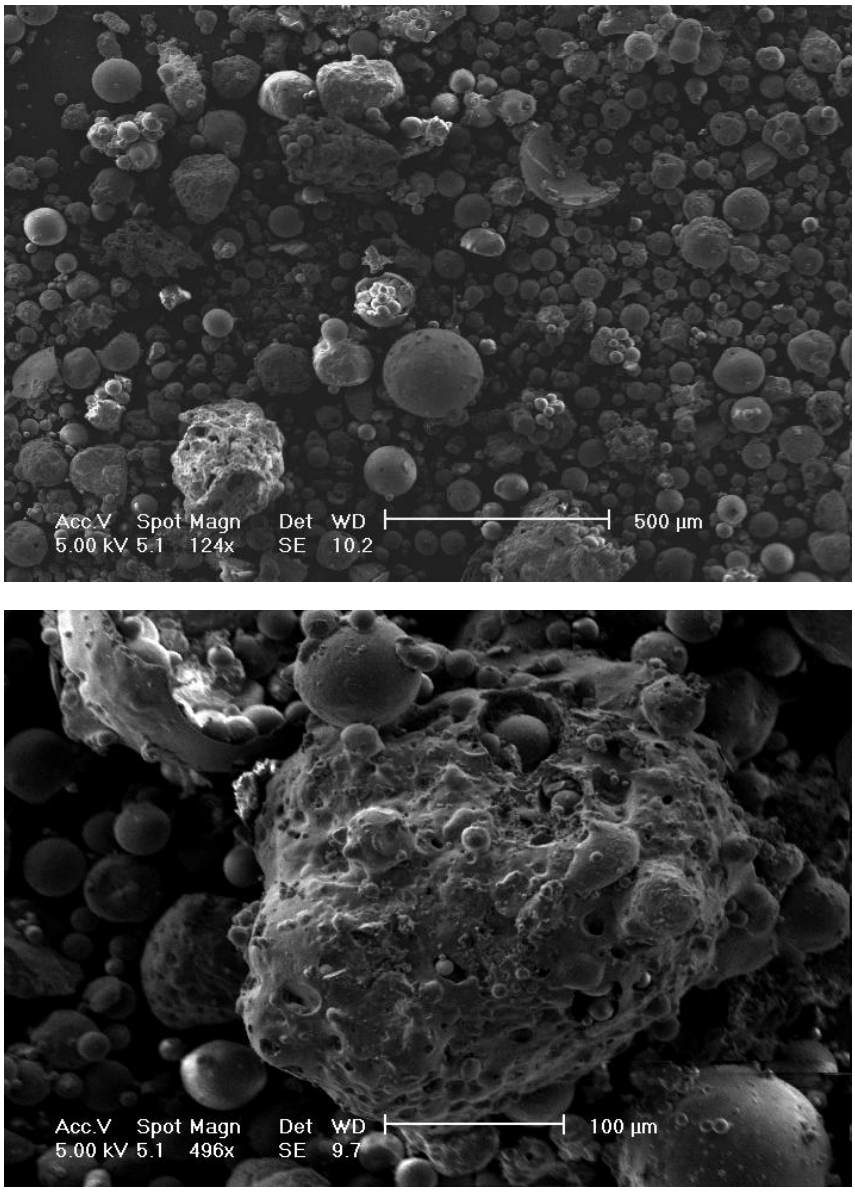

Figure 3.9: SEM images of coarse IFA residue

(meaning empty) and sphere. The cenospheres, because they are hollow, form a large portion of the lightweight fraction. However, because they are collected in a sink/float process, all particles less dense than water, whether they are spherical or non-spherical, porous or non-porous, are considered to be ash cenosphere products. The SEM images in Figure 3.10 are typical of the cenosphere product produced. The surfaces of the particle again are not totally smooth and appear to have some degree of crystallisation present. Not all of the spheres are completely spherical which suggests that they have been formed either from a partially molten slag, or that they are the result of an agglomeration of multiple particles. The image of the broken cenosphere is important because it reveals the present of voids in the particle walls. Although it impossible to ascertain, the presence of the voids might have been a contributing factor to the fact that the sphere has broken as they have reduced the structural integrity of the shell.

From the top picture of 3.11 it is not clear that there is anything noticeably different between these particles and other ash fractions. However when magnified it is clear that the surface of the particle is much rougher. Clear crystals can be observed which protrude from the surface. This agrees with previous observations of Vassilev *et al.* that have described these magnetic spheres as containing iron crystals set in a lattice of amorphous alumina and silica [9]. It also reinforces the results of the XRD investigation which showed magnetite and hematite particles in addition to a highly iron enriched aluminosilicate glass melt. Given the high appearance of crystallisation in these images, and the relatively small amount of crystal detected in the XRD it suggests that there may have been preferential crystallisation on the surface of the sphere perhaps as the result of faster heat transfer.

The carbon enriched product possesses an entirely different morphology to the other ash fractions. The cenospheres, magnetic particles, and fine ash are primarily spherical in nature; in contrast the carbon is a larger porous structure exhibiting a more irregular shape. The reason for this difference is largely explained by the CFA formation mechanisms described in section 2.1.2. The large porous carbon particles result from an incomplete oxidation of the precursor coal. Because of the increase in porosity, the carbon

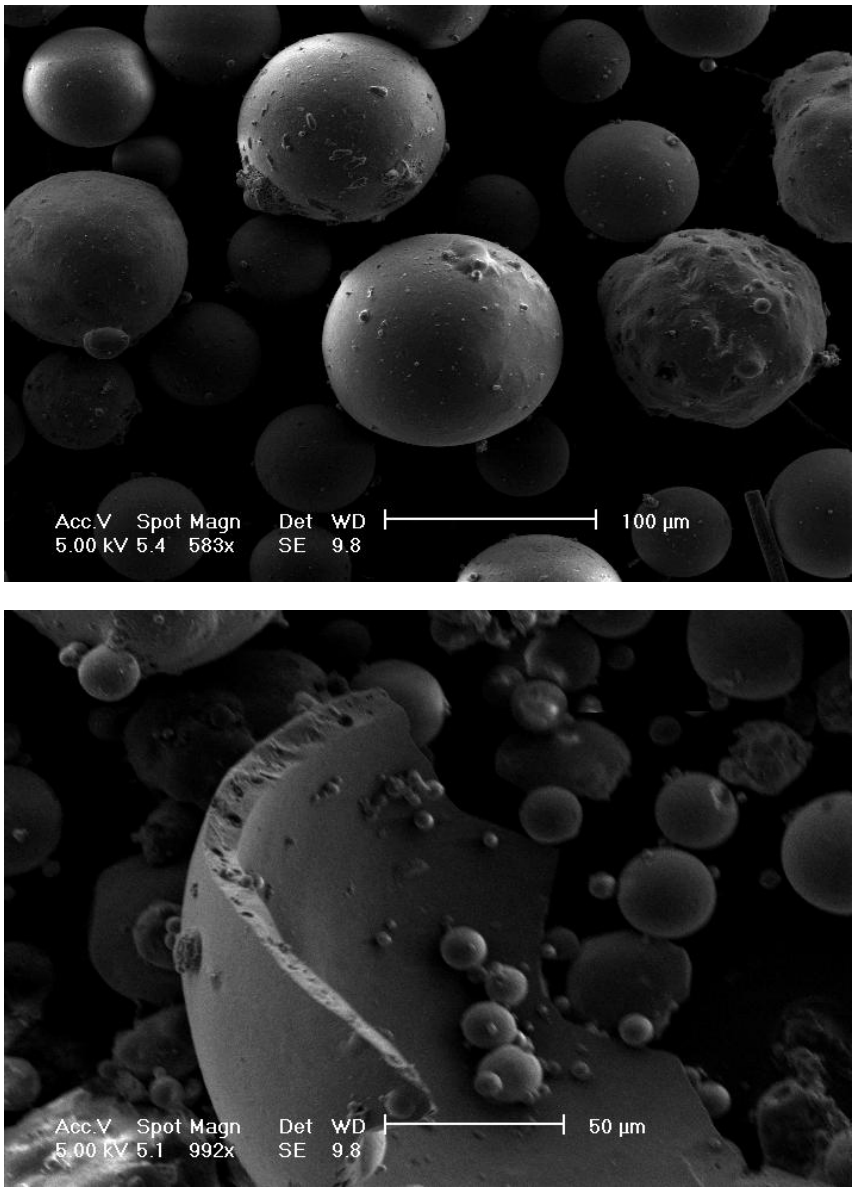

Figure 3.10: SEM images of Censopheres

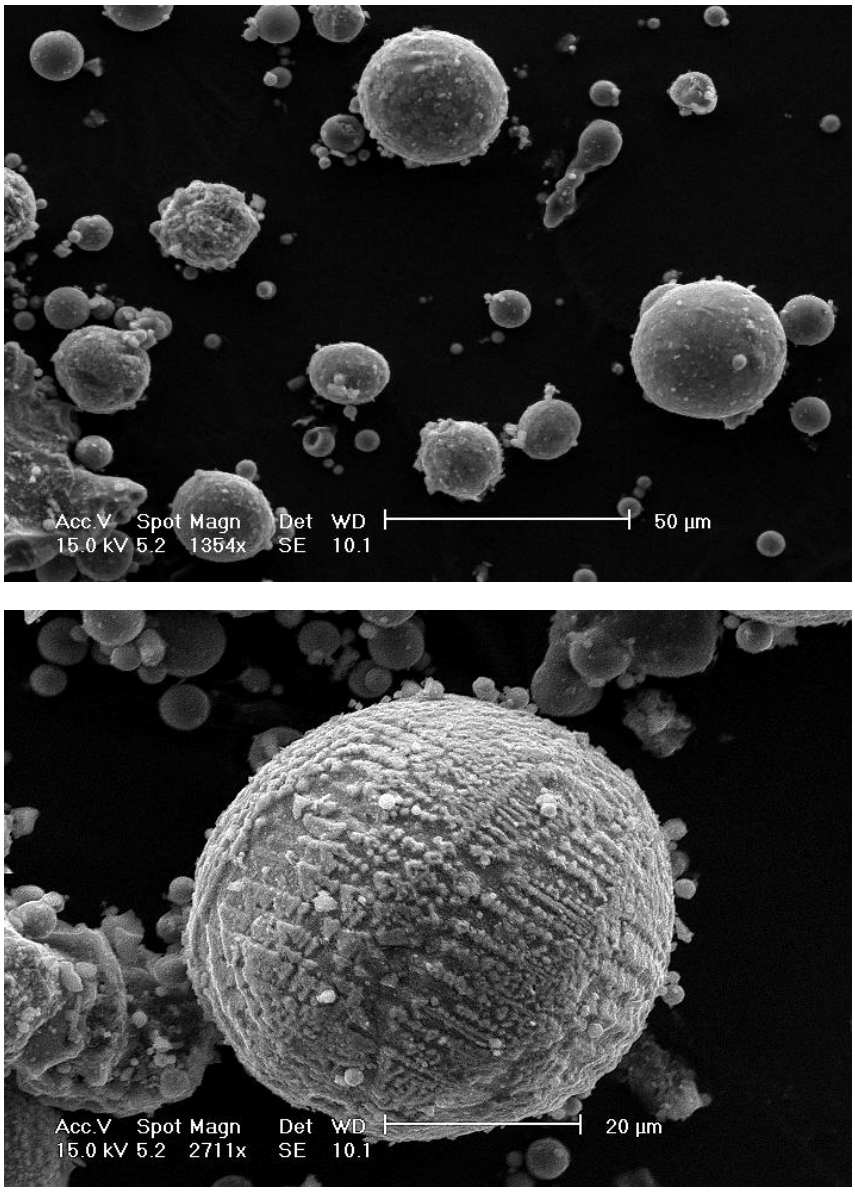

Figure 3.11: SEM images of magnetic concentrate

has a higher surface area relative to the inorganic matter contained in the CFA. In a paper investigating the detrimental effect of high carbon content in CFA concrete it was shown that the surface area of the mineral matter is 0.7-0.8 m^2/g CFA which is considerably lower than the 45-400 m^2/g found for carbon [36]. This is also a likely explanation for the enhanced adsorption capacity of unburned carbon.

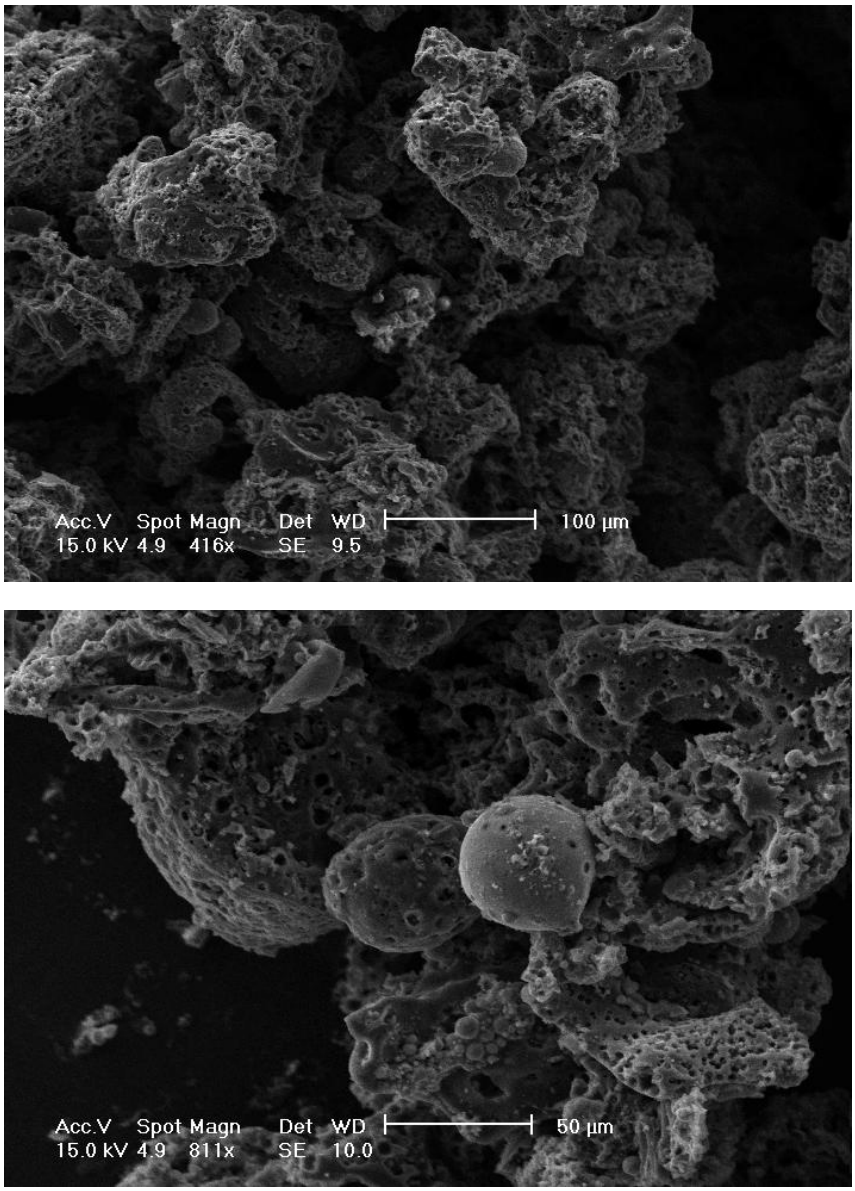

Figure 3.12: SEM images of carbon concentrate

Particle size distribution

It is clear from Figures 3.13 & 3.14 that the 5 different fractions of FA all have very different particle size distributions. The IFA-F contains the smallest ash fraction of the original CFA, while the IFA-C contains the larger.

EN 450-1 the European standard regulating CFA addition in concrete specifies the fineness of the ash that can be used: category N requires that no more than 40% of the ash be retained on a 45 μm sieve, while category S requires that no more than 12% be retained. Figure 3.13 shows that while the IFA-F product meets the requirements for category S, the IFA-C product cannot be used as a partial replacement for OPC in blended cements.

While IFA-F makes a perfect cement replacement material, the coarseness of the IFA-C product makes it unsuitable for this purpose. However, the IFA-C product can be utilised as a feed material for the manufacture of OPC. Because it has been processed the chemical composition of the ash is uniform enough to be suitable for the delicate balancing of feedstock to manufacture quality cement. Certain studies have found that fly ash is a suitable raw material for cement manufacture, and indeed its residual carbon content can decrease the energy required in the cement kiln [230].

The cenospheres have the largest particle size distribution, while the magnetite and carbon are somewhere in the middle. This leads to the possibility of using some kind of size separation method, but in order to fully design a separation on this basis an understanding of the density distribution must be obtained.

Trace Elements

The chemical properties of CFA have been well studied and it is known that CFAs contain many elements at concentrations of greater than 50 mg/kg. Some of these are of environmental concern [29]. It is evident from Table 3.4 that As, Cr, and Pb are present in relatively high levels in some, or all, of the CFAs. As appears to present itself in the smaller size ranges of the alumino-siliceous material as is evidenced by a value of 118

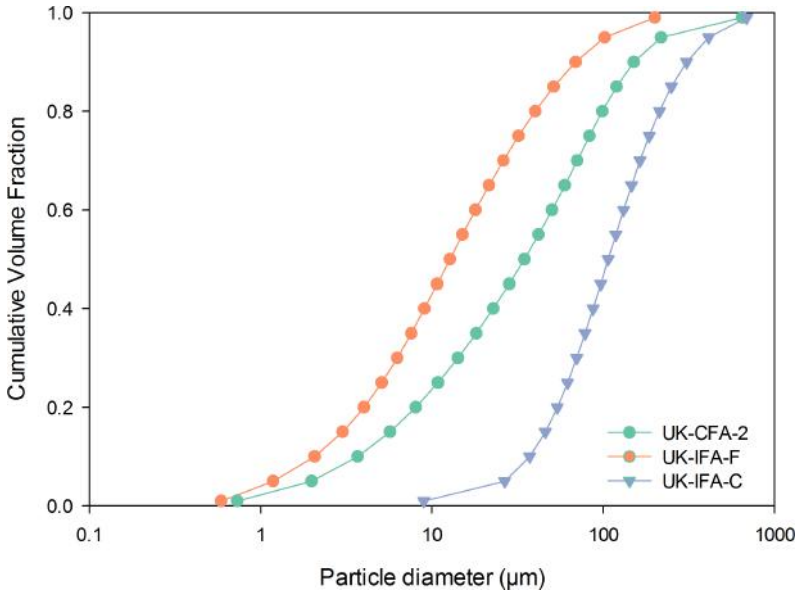

Figure 3.13: Particle size distribution of UK CFA and two IFA residues classified to fine (-F) and coarse (-C) fractions

mg/kg in the fine IFA fraction compared to values of under 40 mg/kg for the other CFA products. Cr is also a concern being distributed widely across all the CFA products with the exception of the enriched carbon. The Pb values are similar to As in their nature, seemingly it presents itself in the smaller ash particles as the IFA-F value of 250 mg/kg suggests. The presence of these elements means that caution and careful testing must be undertaken to ensure that no mobile toxic elements can leach and cause environmental or health problems in their desired applications.

The rise of new developing economies, in particular China, has resulted in an increased appetite for raw materials, and this has been of great concern to developed countries. The fear of a supply shortfall and of losing access to raw materials led the European Commission to analyse the raw materials that are critical to economic growth and employment. As a result germanium (Ge) and gallium (Ga) are defined as a critical strategic metal; this means that their production is concentrated in few countries, and the EU is highly dependent on external sources [107].

Various coal basins contain matter with relatively high concentrations; in a survey of trace elements in twenty-four coals of UK origin the Ge levels ranged from 0.3-15 ppm, and it is suspected that it is associated with the organic matter in the coal [108]. In

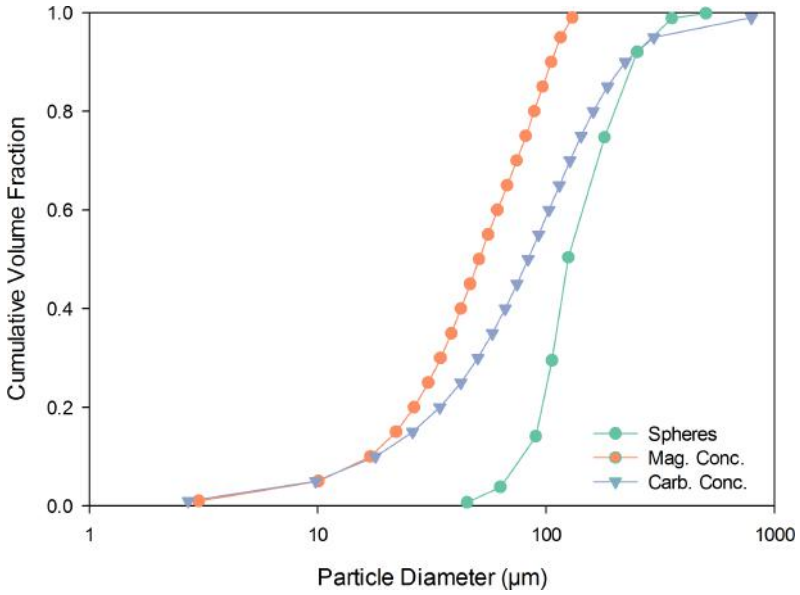

Figure 3.14: Particle size distribution of cenospheres, magnetic concentrate, and carbon concentrate

CFAs the Ge can be concentrated to values up to 10 times higher than in the original coal [109]. None of the CFAs analysed in Table 3.4 have particularly high Ge content, although UK-CFA-2 does have 34 mg/kg. What is interesting to note is that contrary to expectation, it does not associate with the organic fraction, the carbon contains just 2 mg/kg. It is possible that the Ge occurs as water soluble species (GeS_2, GeS, and hexagonal-GeO_2) [109] and that the wet processing route has leached the Ge content away.

Ga is widely present in concentrations of up to 47 mg/kg in the IFA-F fraction. This makes it comparable to the content found in bauxite which is where most of the world's Ga resource comes from [117]. However in the case of bauxite the recovery comes from a waste stream of the Bayer process to make extract aluminium, and so it is not necessarily clear how a CFA source would compare economically.

3.1.4 Conclusions

The analysis carried out in this section have revealed that the products of a commercial scale CFA processing scheme have well defined physical, chemical, and mineralogical

Table 3.4: Trace element content of two CFAs originating from the UK and 5 components of CFA resulting from multi-stage processing

Sample		UK CFA-1	UK-CFA-2	UK-IFA-F	UK-IFA-C	Spheres	Mag. Conc.	Carb. Conc.
Element	Unit							
Ag	ppm	0.5	0.8	0.9	<.5	<.5	<.5	<.5
Al	%	12.6	12.4	13.0	13.1	14.6	5.82	1.87
As	ppm	90	103	118	39	21	37	32
Ba	ppm	1500	1408	1532	1421	938	948	370
Be	ppm	10	11	11	8	7	7	3
Bi	ppm	<5	<5	<5	<5	<5	<5	<5
Ca	%	1.83	2.88	2.28	2.24	0.72	2.03	0.71
Cd	ppm	1	2	1	<1	<1	1	<1
Ce	ppm	113	131	120	119	122	52	27
Co	ppm	52	56	46	46	28	152	9
Cr	ppm	156	170	155	131	123	202	33
Cu	ppm	188	204	222	141	119	296	63
Fe	%	7.42	6.78	4.75	5.18	3.21	43.8	1.17
Ga	ppm	36	44	47	18	17	19	6
Ge	ppm	16	34	23	7	<2	9	2
Hg	ppm	<1	1	1	<1	<1	3	<1
K	%	2.33	2.06	2.57	2.37	3.36	0.63	0.23
La	ppm	67	78	68	69	67	33	15
Li	ppm	238	235	271	260	289	90	29
Mg	%	0.96	1.30	0.93	1.05	0.96	0.86	0.21
Mn	ppm	635	1088	472	756	271	1579	122
Mo	ppm	7	14	8	6	3	17	5
Na	%	0.43	0.43	0.55	0.42	0.45	0.14	0.06
Nb	ppm	20	23	22	19	19	9	<5
Ni	ppm	168	210	164	115	78	459	43
P	%	0.14	0.17	0.16	0.12	0.06	0.08	0.07
Pb	ppm	180	316	250	73	70	62	28
Rb	ppm	155	113	163	147	210	<50	<50
S	%	0.06	0.21	0.18	0.06	0.03	0.08	0.15
Sb	ppm	6	9	9	5	<5	<5	<5
Sc	ppm	33	30	35	32	31	20	7
Se	ppm	<10	<10	<10	<10	<10	<10	<10
Sn	ppm	5	7	7	<5	<5	6	<5
Sr	ppm	399	770	462	398	304	258	134
Ta	ppm	<2	<2	<2	<2	<2	<2	<2
Te	ppm	<5	<5	<5	<5	<5	<5	<5
Th	ppm	21	21	21	21	20	13	6
Ti	ppm	5482	5611	5852	5648	5661	2522	899
Tl	ppm	<5	<5	<5	<5	<5	<5	<5
U	ppm	<10	<10	<10	<10	<10	11	<10
V	ppm	296	377	311	265	232	320	74
W	ppm	<5	<5	<5	191	83	<5	<5
Y	ppm	56	56	57	54	43	36	14
Zn	ppm	445	579	498	165	120	252	67
Zr	ppm	200	196	209	198	208	102	33

differences. Cenospheres, because of their hollow internal morphology are lower density than water. The are enriched in SiO_2 and Al_2O_3 and contain the highest levels of mullite which is presumed to be in the form of fine crystalline needles within the skeletal wall of the cenosphere, which would suggest a high degree of resistance to chemical attack or thermal shock. The magnetic particles had a high level of Fe_2O_3 and were more dense than the parent CFA but had a relatively low level of crystalline magnetite and hematite. The SEM images of magnetic particles showed crystalline material protruding from the particle surface which suggests that magnetite might have preferentially formed at the particle surface due to cooling time. Carbon concentrate particles had a high level of organic material and were observed to show a porous structure under SEM magnification. The residual ash fractions IFA-F and IFA-C were both largely amorphous aluminosilicates. However, the larger IFA-C contained a relatively large amount of quartz, which in combination with a lack of cristabollite found by XRD, suggests that quarts occurs as a relict material as distinct grains. The finest fraction of residual ash was found to contain relatively high levels of elements of environmental concern such as As, Cr, and Pb. In addition to this IFA-F also contained the valuable metal gallium in a concentration of 47 ppm which was an enrichment compared to parent CFA. The work in this section will help target applications of various CFA products as well as inform further research in this chapter.

3.2 Rare Earth Elements

3.2.1 Introduction

In 2010 the Raw Materials Supply Group of the European Commission published a report highlighting a group of materials that were to be defined as critical: a raw material is defined critical "*when the risks of supply shortage and their impacts on the economy are higher compared with most of the other raw materials*" [241]. Forty-one raw materials

were analysed with respect to the politico-economic stability of the producing country, their geographical concentration, their substitution potential, and their rate of recycling. As a result of this analysis a list of 14 raw materials were defined critical at an European Union level. Rare earth elements (REY) (15 lanthanides plus yttrium and scandium) were included on this list. REY use is expected to increase over the next decade, and it is expected to do so in many clean technology areas [242]. In order to maintain Europe's competitive standing in these areas, alternative sources to conventional mining deposits of these materials may need to be considered.

Hard coal fly ashes (CFA) have been estimated to contain 445 ppm REY on an average global basis [243]. There have been many reports of CFAs with REY contents that far exceed the world average (circa 0.1-1.0 wt%): elevated REY levels have been reported in the Russian Far East coal deposits [244–246]; Western Siberia, Russia [247]; the Daqingshan and Jungar coalfields, Inner Mongolia [248–251]; the Heshan and Fusui coalfields of southern China [252, 253]; the Songzo coalfield, southwestern China [254]; eastern Yunnan, China [255]; and the Fire Clay coal bed in Eastern Kentucky, United States [256, 257]. For a review of coal deposits as a potential source of REY, readers are referred to the work of Seredin and Dai [258].

Although some work has been done on analysing utility combustion CFAs (see for example: [249, 257]), a large proportion of the reported elevated levels of REY come from exploratory coal samples that have been laboratory ashed for analysis. This is extremely useful for identifying coal resources that might be exploited for a dual energy REY extraction purpose, but it does not address the large amount of CFA currently being produced, or that already in landfill. A recent study examined a variety of CFAs that are collected from different rows of the electrostatic precipitators in various power plants [259]; total REY content ranged from 187-600 ppm. Two Bulgarian CFAs and four Turkish CFAs analysed as part of that study were found to have REY content in the range 209-230 ppm.

In 2009 Europe produced 35 Mt of CFA [38]. A larger selection of European CFA

samples must be analysed in order to asses the potential for it to be considered as a REY resource. To this end a preliminary screening study of six CFAs, three from the UK, and three from Poland was undertaken. The most promising CFA was then selected and subjected to both a size classification and a more comprehensive separation process to assess whether the REY is concentrated in particular size and/or mineralogical fractions.

Table 3.5: REY content of six industrial CFAs. The results are in ppm and are the result of a one-off analysis by a certified laboratory and cross checked against in-house laboratory standards

Element	P-1	P-2	P-3	UK-1	UK-2	UK-3
La	61.4	52.6	60.7	85.7	51.0	41.9
Ce	124.5	107.5	125.5	176.5	104.0	86.6
Pr	13.9	12.2	13.7	19.3	11.8	9.4
Nd	56.6	48.6	56.6	77.6	45.6	37.2
Sm	11.6	10.0	10.1	15.4	9.2	7.1
Eu	2.6	2.5	2.6	3.2	2.0	1.7
Gd	11.3	9.1	10.4	13.4	7.9	7.4
Tb	1.5	1.6	1.8	1.9	1.4	1.2
Dy	9.7	8.1	9.5	11.1	7.5	6.9
Y	51.4	44.0	53.8	60.7	42.5	37.3
Ho	1.9	1.7	2.0	2.2	1.7	1.4
Er	5.7	5.0	5.2	6.1	4.1	3.7
Tm	0.7	0.7	0.7	0.9	0.6	0.5
Yb	4.7	4.1	5.4	5.8	3.8	3.4
Lu	0.7	0.7	0.7	0.8	0.6	0.5
$\sum$REY	358	308	359	481	294	246
LREY (%)	74.8	74.9	74.3	77.9	75.5	74.0
MREY (%)	21.4	21.2	21.8	18.8	20.9	22.1
HREY (%)	3.8	3.9	3.9	3.3	3.6	3.9
Critical	127	110	130	161	103	88
Uncritical	98	84	95	134	80	66
Excessive	133	115	134	186	111	92
Outlook	0.96	0.96	0.96	0.86	0.93	0.95
Critical %	35.6	35.6	36.1	33.4	35.1	35.8
$\sum$REO	431	371	432	579	354	297
LOI @ 950 °C	4.0	6.6	8.9	14.8	10.7	12.0

3.2.2 Experimental

Six different CFAs were obtained via the CFA processing company RockTron International Ltd. Hereafter, they will be referred to as UK-1, UK-2, UK-3, P-1, P-2 and, P-3: the Polish ashes are derived from bituminous coal; UK-2 and UK-3 from a bituminous

coal/biomass blend; and UK-1 is from a semi-anthracitic coal source. One of the samples was further sieved into six size fractions. In addition to the CFA samples, also provided were samples from various points in RockTron's CFA processing pilot plant (for further details see [7]). The source of each CFA is shown in Table 1. Trace element analysis was carried out as per Section 3.1.2.

3.2.3 Results and Discussion

Geochemically, REY distribution can be classified into three groups: the total REY can be split into light (LREY - La, Ce, Pr, Nd, and Sm), medium (MREY - Eu, Gd, Tb, Dy, and Y), and heavy (HREY - Ho, Er, Tm, Yb, and Lu) groups. Yttrium, although not a lanthanide, possesses an ionic radius similar to Ho and so is often shown on REY distribution plots between Dy and Ho. Seredin and Dai [258], following analysis by the Industrial Minerals Company of Australia (IMCOA), devised a new classification which bears more relation to the likely supply and demand forecast over the next few years. This is also a threefold classification: it is made up of critical (Nd, Eu, Tb, Dy, Y, and Er), uncritical (La, Pr, Sm, and Gd), and excessive (Ce, Ho, Tm, Yb, and Lu) groups. This classification makes assessing the distribution more relevant to the requirements of industry.

Table 3.5 summarises the ICP-MS results. All of the CFAs analysed had favourable distributions in terms of their critical element content. With a critical content of greater than 30%, and an outlook coefficient (critical/excessive) of greater than 0.7, the CFAs would be termed as *Group II - promising* using Seredin and Dai's criteria [258]. Counter to this is the fact that none of the CFAs had total rare earth oxide (REO) content over 600 ppm. Seredin and Dai [258] also discuss the relevant cut-off grade for REO from the combustion products of coal. This is given as 800-900 ppm for coal seams more than 5 m in thickness. However, all of the samples analysed currently are already being produced on an industrial basis. There is no mining or exploration cost associated with them. Further work is required to assess the ease of extraction of the current samples, but it is

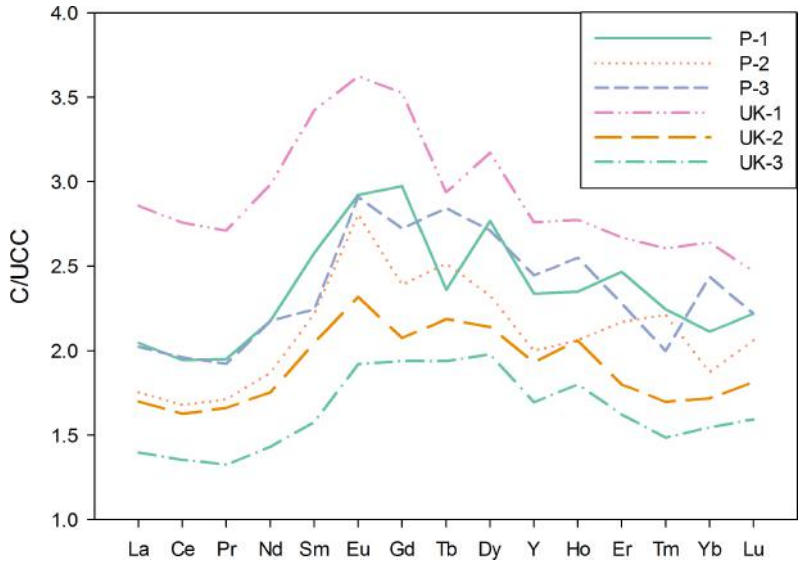

Figure 3.15: M-type rare earth elemental distribution normalised to data for the upper continental crust [260] for six European CFAs

conceivable that on this basis the cut-off grade might be reduced.

All of the CFAs show a broadly similar REY distribution as evidenced by Fig.3.15. UK-1 CFA had the highest total REO content of the samples analysed at 579 ppm. It has a pronounced Eu maximum and is classified as M-type, subtype 2; this distribution is typical of certain hydrothermal REY ores and also of certain alkali mafic volcanic ashes [255], although it has also been ascribed to the higher sorption of MREY in humic matter relative to LREY and HREY [258].

In another recent paper on the subject, Hower *et al.* [259] summarised data on REY content of size classified CFA from Dai *et al.* [249]. They report a similar trend to that observed in Table 3.6: namely, an increase in total REO content as the particle size decreases. As their study was the only one known to have reported such data, they were unable to ascertain whether this finding is consistent with other CFAs. The current study provides further data to support this suggested trend. It is also evident, that on a percentage basis, there appears to be a minimum of critical REY content, as well as a maximum of LREY content, between 63-90 μm. This is in contrast to the trend observed in Hower *et al.* [259] which shows the critical REY content with a maximum between 48-96 μm.

Table 3.6: REY content of size classified UK-1 CFA

Element	d < 38 μm	38 ≥ d < 63 μm	63 ≥ d < 90 μm	90 ≥ d < 125 μm	125 ≥ d < 150 μm	d > 150 μm
La	99.3	68.5	57.2	54.3	50.2	56.0
Ce	207.0	142.5	114.0	107.0	102.5	108.0
Pr	24.2	16.5	13.4	12.6	12.0	13.2
Nd	93.4	63.1	50.3	48.1	48.7	49.5
Sm	17.6	12.2	8.7	9.1	8.9	10.3
Eu	3.8	2.7	2.0	2.0	1.8	2.0
Gd	15.9	10.3	8.6	7.8	7.4	8.8
Tb	2.3	1.5	1.2	1.1	1.0	1.3
Dy	13.5	9.3	7.1	7.4	7.2	7.4
Y	74.6	46.6	37.1	38.1	35.5	40.7
Ho	2.6	1.6	1.4	1.5	1.3	1.4
Er	7.1	4.9	3.8	3.9	3.6	4.2
Tm	1.2	0.7	0.6	0.6	0.5	0.7
Yb	6.4	4.5	3.6	3.4	3.7	3.6
Lu	1.0	0.6	0.5	0.6	0.5	0.5
$\sum$REY	570	385	309	297	285	307
LREY (%)	77.5	78.6	78.7	77.7	78.1	77.1
MREY (%)	19.3	18.2	18.1	19.0	18.6	19.6
HREY (%)	3.2	3.2	3.2	3.3	3.4	3.4
Critical	195	128	101	101	98	105
Uncritical	157	107	88	84	79	88
Excessive	218	150	120	113	108	114
Outlook	0.89	0.85	0.84	0.89	0.90	0.92
Critical %	34.2	33.2	32.8	33.8	34.3	34.2
$\sum$REO	686	464	372	358	343	370
LOI @ 900 °C	8.2	14.2	20.1	36.4	31.7	31.6

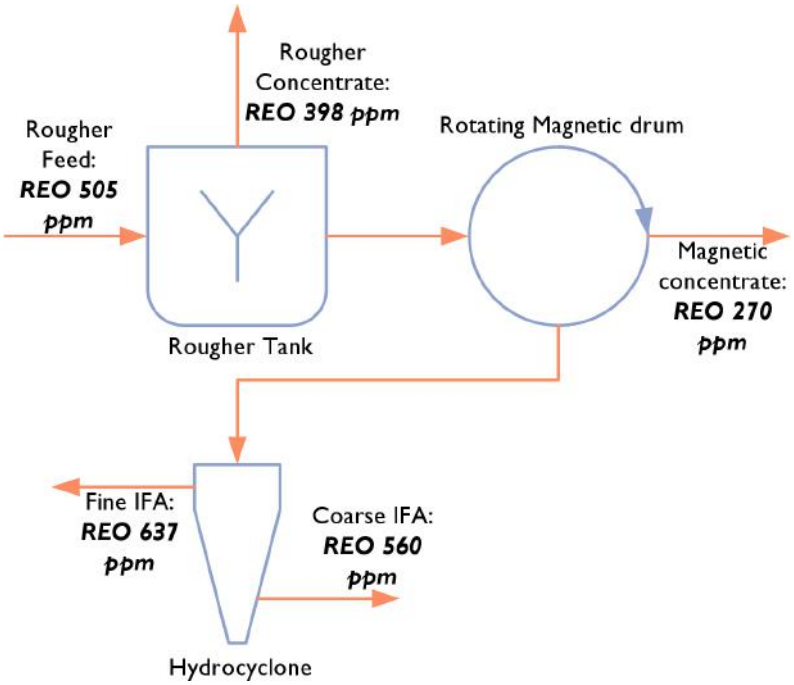

Figure 3.16: The REE appears to be concentrated in the non-magnetic inorganic matter of UK-1 ash according to the samples taken at various places in the processing scheme

Interest has grown in recent years in the concept of multi-component utilisation of CFA [7, 14]. Within this concept it is envisaged that CFA, an intrinsically heterogeneous product, can be separated into distinct components. Fig.3.16 illustrates a processing scheme capable of separating a raw CFA feed into four components: (1) an organic concentrate, (2) a magnetic concentrate, (3) a coarse improved residual fly ash (IFA), and (4) a fine IFA. It can be calculated from Fig.3.16 that, relative to the feed CFA, the REO content is reduced by 47% and 21% in the magnetic concentrate and organic concentrate, respectively. Conversely, the REO content increases by 11% and 26% in the coarse and fine IFA, respectively. This result is in accordance with the size fraction analysis, but it also suggests that a large proportion of the REY in CFA is present in the non-magnetic inorganic material. Recent research has shown [261], using Ce as a proxy for all the lanthanides, that REY elements reside homogeneously within the glass phase. This has implications for REY extraction as it requires that the leaching agents must contact the entire particle. This in itself might explain why the REY appears to be more concentrated in the smaller size fractions because, as both Table 3.6 and previous studies show [35],

Table 3.7: REY content of various products of processed UK-1 CFA

Element	Rougher Feed	Rougher Concentrate	Magnetic concentrate	Hydrocyclone Underflow	Hydrocyclone Overflow
La	72.6	54.3	35.7	81.1	90.7
Ce	146.0	108.5	74.3	159.5	177.5
Pr	17.1	13.5	8.8	18.9	21.6
Nd	65.7	52.3	33.9	76.2	83.3
Sm	13.0	11.7	7.4	15.3	17.0
Eu	2.7	2.6	1.5	3.6	4.0
Gd	13.5	10.9	7.3	14.7	17.5
Tb	1.8	1.5	1.1	2.0	2.3
Dy	11.2	9.8	6.4	11.8	15.1
Y	61.1	52.5	37.7	66.1	80.6
Ho	2.1	1.7	1.3	2.2	2.7
Er	5.6	5.0	3.8	6.5	7.9
Tm	0.9	0.8	0.6	1.0	1.1
Yb	5.2	4.5	3.4	5.8	6.9
Lu	0.7	0.6	0.4	0.8	0.9
$\sum$REY	419	330	224	465	529
LREY (%)	75.0	72.8	71.6	75.4	73.7
MREY (%)	21.5	23.4	24.1	21.1	22.6
HREY (%)	3.5	3.8	4.3	3.5	3.7
Critical	148	124	84	166	193
Uncritical	116	90	59	130	147
Excessive	155	116	80	169	189
Outlook	0.96	1.07	1.05	0.98	1.02
Critical %	35.3	37.5	37.7	35.7	36.5
$\sum$REO	505	398	270	560	637
LOI @ 950 °C	14.2	50.8	na	1.3	1.2

larger size fractions of CFA tend to have a higher carbon content. The relatively modest reduction in REY content in the organic concentrate might in fact be masked in this instance by the fact that the sample is taken from only the first stage in a multi-stage froth flotation circuit. It is evident from Table 3.7 that the organic content of the flotation concentrate is just 50.8 %. As such, a sample taken at this point will have a higher fine CFA content than the concentrate from a stage further down the froth flotation circuit. This analysis shows that it is possible to enrich CFA through a multi-stage processing route to levels approaching that required for economic extraction. If the carbon concentrate is re-burned in the power plant [7], and the magnetic concentrate is low volume and low REY content, then this enrichment does not come at the cost of a large reduction in REY recovery. However, it is worth noting that the magnetic concentrate has the highest proportion of critical REY and the lowest proportion of LREY of the processed materials.

Annual production of UK-1 ash is somewhere in the region of 300-350 kt. More importantly, there is at least 16 Mt stockpiled. Applying a REO content of 500 ppm to this represents a potential resource of 8000 t. At 2012 US prices, this represents a potential value of $136 M (mischmetal price [262]) although it should be noted that REY prices are volatile and have recently reduced. For 2030, it has been projected that emerging technologies will themselves result in global REO demand of 27,900 t [241]. Clearly, if extraction is technically and economically feasible, this resource is not insignificant. It is important to note that the foregoing relies on the assumption that the entire stockpile contains a similar level of REY. The latter is unlikely to be the case given that REY content varies in both the coal seam and its position in the seam [258].

The technical feasibility of extraction is the next critical parameter that must be investigated to assess the viability of any process. It has been claimed that many REY ores that are found in coal basins are characterised by carbonate and ion-exchangeable modes of occurrence [242]. If this is the case, then extraction processes may be devised that are similar in nature to those developed for the weathered crust elution-deposited ore deposits which typically have a low REY content (0.03-0.25 %) and small reserves (3-12

kt) [242]. The weathered crust deposits are viable because of the ease of the extraction. In many ways, a CFA stockpile is analogous to these reserves if they have a similar ease of extraction. The results of this study make it clear that an investigation into the extraction process of UK-1 CFA is necessary. It also lends further support to the idea that other CFAs should be analysed for REY content; it is possible that there are other CFA stockpiles that might contain even higher levels.

3.2.4 Conclusions

The current study has highlighted the potential for CFA stockpiles to contain significant REY reserves. It confirms the finding of Hower *et al.* [259] that REY content in size classified CFA increases as the particle size of the sieved fraction decreases. For the first time, CFA products at various points in a pilot scale processing plant have been analysed for REY content. The results suggest that both fine and coarse IFA can be considered potential REY reserves in UK-1 ash. Extraction of the REY should now be studied to examine the technical feasibility of such a process.

3.3 Characterisation of CFA by Density

3.3.1 Introduction

The term cenosphere was used as early as 1928 by Sinatt [263] to describe the hollow carbonaceaous particles formed during the devolatisation of coal to coke. This followed the usage in biology to describe a form of sea organism *cenosphaera* of the sub order *sphaeroidea* of the order *spumellaria*. By 1965 [264] it appears to be in common usage as they are referred to during the analysis of density distributions to describe CFA particles of specific gravity of less than one. Raask [265] provides the first characterisation of cenospheres in pulverised fuel ash shortly after in 1968. This is followed by Fisher *et al.* [176] who, with more drama, describe the *"mystery of the spheres"* in *Science*. That

some CFAs contained cenospheres was obvious to power station workers. The practice of storing CFA in lagoons meant that the cenospheres would float to the surface of the lagoon forming a thick layer. Hence they were also referred to as *floaters*. That they float on water has usually been the way of characterising the extent of cenospheres within any individual CFA. This makes a great deal of sense if the traditional method of cenosphere collection is used: skimming off the top of the lagoon. This classification is not necessarily relevant when considering cenosphere extraction as one stage within a multistage processing operation. The classification then needs to be made with reference to their application. Clearly if their buoyancy in water is their desired function in applications, such as substrates for photocatalysis [195,266,267], then they must have a specific gravity of less than one. On the other hand if a more general low density is required, for example in using them in metal matrix composites [212,268], then the specific gravity criteria is set arbitrarily at one because of the collection method, not because of the desired properties.

All available evidence suggests that in cenospheres extracted from CFA there is a range of wall thickness and indeed internal morphology. Examining only the case for an ideal thin walled sphere it becomes clear that there may well exist hollow spheres that have an effective density greater than water.

The wall thickness, t, is defined as a fraction of the external diameter of the hollow sphere as shown in Figure 3.17 as follows:

$$t = \frac{(d_o - d_i)}{2d_o} \tag{3.1}$$

The particle void space can be calculated.

$$\epsilon = \frac{d_i^3}{d_o^3} \tag{3.2}$$

And so by substitution and rearrangement, an expression for the particle void space in terms of T can be written.

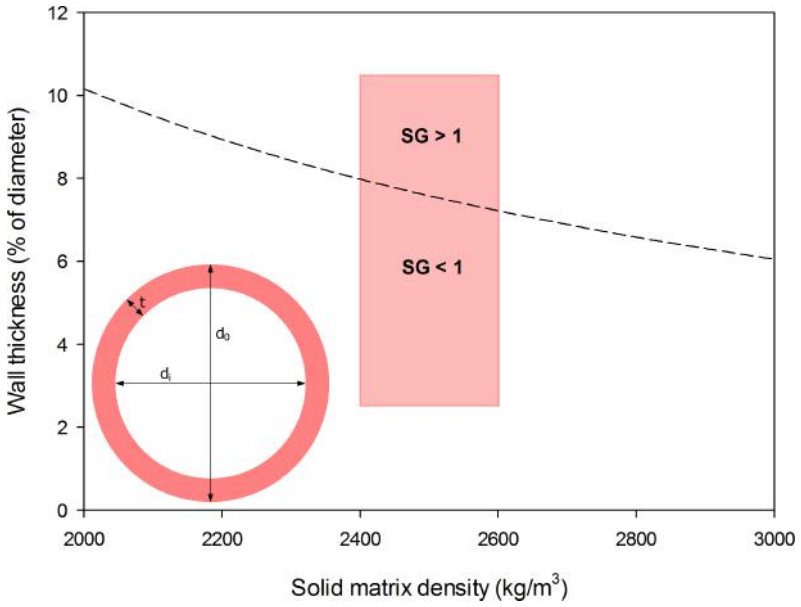

Figure 3.17: Critical wall thickness for water buoyant ideal spheres as a function of matrix density

$$\epsilon = 1 - 6t + 12t^2 - 8t^3 \tag{3.3}$$

$$\rho_{eff} = \epsilon\rho_g + (1 - \epsilon)\rho_m \tag{3.4}$$

The effective density of the sphere can be estimated additively. By setting the effective density to $1000\,\mathrm{kg\,m^{-3}}$ and solving Equation 3.3 for t at different values for the matrix density, Figure 3.17 can be drawn. Using a glass density calculation spreadsheet, a typical CFA is estimated to have a matrix density of circa $2500\,\mathrm{kg\,m^{-3}}$. Scanning electron microscopy (SEM) analysis of cenospheres extracted using water revealed a lower bound of t = 2.5% and an upper bound of t = 10.5 % [269]. This shows that there should be cenospheres that have an effective density greater than water.

The present research is concerned on the density classification of a CFA and a CFA derived product to examine the chemical and physical differences between various density fractions. Although there has been some work performed in this area, this study is the most comprehensive to date and it should ensure that cenospheres within CFA are both defined and targeted with the correct application in mind.

3.3.2 Experimental

Two CFA products were obtained from the CFA processing technology company RockTron Mineral Services Ltd. The first (UK-CFA) was an unrefined CFA from a power station in the UK. The 2nd (UK-IFA) was a processed CFA that had undergone froth flotation to remove organic constituents, magnetic separation, and then size classification. The density classifications were conducted using LST Fastfloat; it consists of low toxicity sodium heteropolytungstates dissolved in water. Initially 100 g of CFA was mixed with separating fluid and subjected to a sink float test in a separating funnel. The funnel was placed in a sonicating bath for 10 minutes before settling for 24 hours. The sinks and floats were separated, filtered, and washed thoroughly to remove any LST Fastfloat. The products were dried and then weighed. The process was conducted sequentially from a specific gravity of one upwards to obtain ashes of particular density. For UK-IFA only one separation was made at a specific gravity of two. Bulk chemistry, trace element, density and particle size analyses were carried out as per Section 3.1.2. The morphology of two density fractions of UK-IFA was investigated using a CFEI Quanta 3D FEG FIB-SEM. A number of particles were cut using the FIB and images were obtained.

3.3.3 Results and Discussion

The density fractionation revealed that there is a distribution of density within a particular CFA. It is evident from Figure 3.19 that for an arbitrary glass SiO_2 -Al_2O_3 -Fe_2O_3 glass density of 2.5 g/cm^3, that there is roughly an even split of density lower and higher than this value. Particularly pertinent to the focus of the current investigation is that in addition to 1% frequency low density fraction that has a specific gravity less than water, there is another 1% of particles that have a specific gravity of *ca.* 1.2. This is revealing because the cenosphere component of a CFA is able to command the highest value. This analysis suggests that by redefining the cenospheres to include a slightly higher density would potentially increase the extractable content by a factor of 2. The frequency

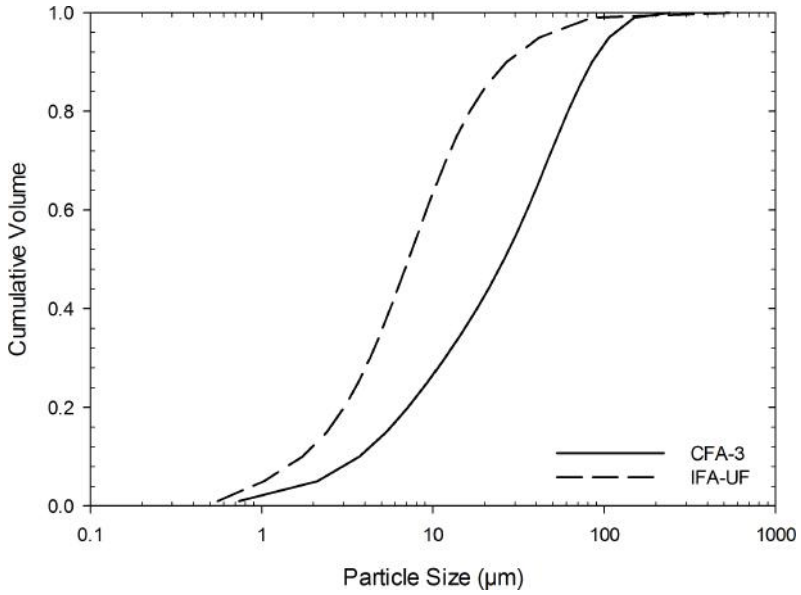

Figure 3.18: Particle size distribution of CFA-3 and IFA-UF

diagram in Figure 3.19 is cut at 2.89 on the right hand side due to the lack of heavier liquids. However it appears to show a distribution centred around 2.5 g/cm^3 as would be expected for a glass without voids. It is also noticeable that the particle size is largest in the density region 1.6-2.0 g/cm^3, but at densities larger than 2.0 g/cm^3 the particle sizes decrease dramatically. The density distribution shows a remarkable similarity to a CFA from the now closed Carmarthen Bay site in one of the earliest and still one of the only other studies of this type [264].

In the earlier study, of the three British CFAs analysed for density distribution all had frequency peaks around 2.5 g/cm^3, but they had differing peak intensity. Microscopical analysis suggested that in density fractions *ca.* 2.5 g/cm^3 the particles were of the form of clear glass spheres. Cenospheres were recognised at very low densities and intermediate densities were said to be composed of spongy particles. Other researchers have identified these as network structures whereby particles may contain multiple spherical voids with an envelope structure that is either spherical or spheroidal [269]. They also correlated these particle types with a larger size than pure cenospheres. Figure 3.19 along with the literature discussed suggests that particles of density between 1.5-2.0 g/cm^3 are of a spongy, or network structure and it is this that gives rise to their intermediate density. A

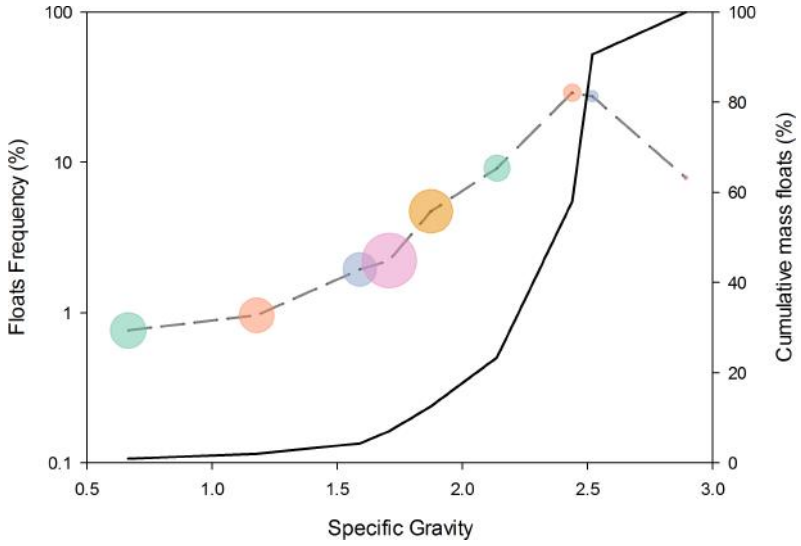

Figure 3.19: Particle density distribution of CFA-3. Bubbles represent d_{50} of density fraction. The first bubble represents a d_{50} of 41.7 µm

more recent study isolated two different types of cenospheres with densities of 0.857 and 1.282 g/cm^3 [270]. Qualitative analysis of SEM images suggested that the cenospheres with the higher density has thicker shells which could be the reason that they are more dense than water.

Table 3.8: Bulk chemical content of density fractionated UK-CFA and an ultra fine fly ash residue IFA-UF.

	SiO_2	Al_2O_3	Fe_2O_3	CaO	MgO	Na_2O	K_2O	Cr_2O_3	TiO_2	MnO	P_2O_5	SrO	BaO	LOI	SiO_2/Al_2O_3
CFA-3	45.8	24.9	6.2	2.1	1.2	0.6	2.1	0.02	0.9	0.1	0.6	0.1	0.2	15.1	1.8
< 1.0	55.6	32.8	2.3	0.6	1.1	0.7	3.8	0.01	0.8	0.0	0.2	0.0	0.1	2.0	1.7
< 1.2	56.3	32.7	2.5	0.5	1.0	0.7	3.5	0.01	0.8	0.0	0.2	0.0	0.1	1.7	1.7
< 1.4	58.1	32.0	2.3	0.5	1.0	0.7	3.4	0.01	0.8	0.0	0.1	0.0	0.1	0.8	1.8
< 1.65	41.9	22.5	2.2	0.5	0.7	0.6	2.1	0.01	0.6	0.0	0.1	0.0	0.1	28.7	1.9
< 2.0	29.5	14.9	1.5	0.3	0.4	0.4	1.3	0.01	0.4	0.0	0.1	0.0	0.1	51.0	2.0
< 2.2	39.1	19.0	2.6	0.6	0.6	0.5	1.7	0.01	0.6	0.0	0.2	0.1	0.1	34.9	2.1
< 2.4	45.7	23.8	5.3	1.0	0.9	0.7	2.0	0.01	0.9	0.1	0.2	0.1	0.2	19.3	1.9
< 2.6	55.0	29.2	4.1	0.9	0.9	0.8	2.7	0.01	1.0	0.1	0.2	0.1	0.2	5.0	1.9
> 2.6	42.4	27.5	20.9	1.9	1.9	0.6	2.0	0.02	1.1	0.3	0.5	0.1	0.2	0.4	1.5
IFA-UF	52.1	31.2	5.7	2.2	1.2	0.7	2.5	0.02	1.0	0.1	0.8	0.1	0.2	2.0	1.7
< 2.0	55.0	33.9	2.5	0.4	0.9	0.8	3.1	0.01	0.7	0.0	0.1	0.0	0.1	2.4	1.6
> 2.0	52.9	31.6	6.1	1.3	1.1	0.8	2.6	0.02	1.1	0.1	0.5	0.1	0.2	1.6	1.7

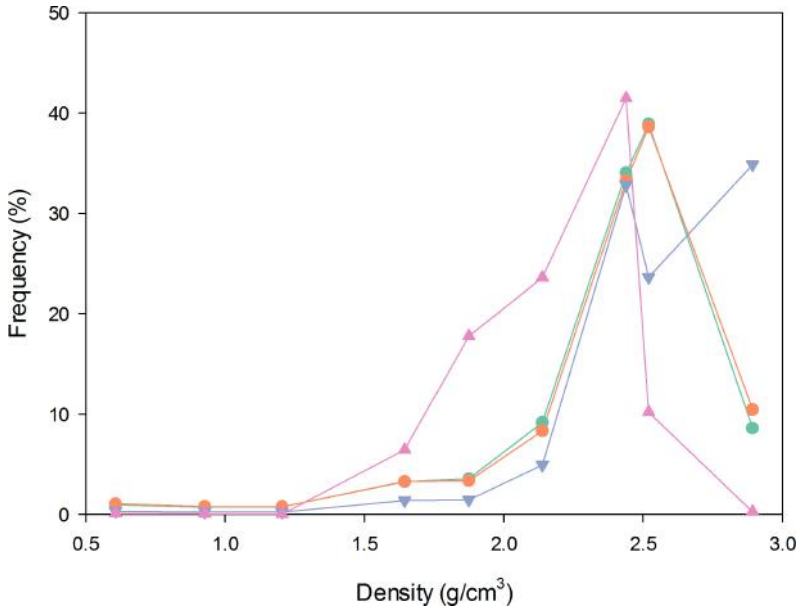

Figure 3.20: Bulk chemical speciation across density fractions for major constituent chemicals of CFA-3: SiO_2 (●), Al_2O_3 (●), Fe_2O_3 (▼), and carbon (▲)

Bulk chemical analysis of the density fractions is summarised in Table 3.8. A very general analysis reveals that fluxing oxides (CaO, Na_2O, MgO, TiO_2) marginally increase in concentration as the denisty fraction increases. However, this analysis is complicated by the fact that some of these occur in CFA in water soluble form and with each successive sink-float operation more of the water soluble compounds leaching into solution is expected. What is clear is that the K_2O concentration shows some correlation with density fraction reducing from 3.8-2.0 wt% from lightest fraction to the heaviest. This observation is important when considering the role that K_2O plays in melt viscosity which will be considered later in the chapter.

The four major forming constituents of the samples are SiO_2 , Al_2O_3 , Fe_2O_3 , and char (represented by LOI). By combining the chemical analysis with the density distribution the speciation of the components can be plotted as a frequency curve (Figure 3.20). The SiO_2 and Al_2O_3 distributions are what might be expected from the bulk density distribution as they strongly peak around 2.5 g/cm^3. The Fe_2O_3 distribution shows much lower concentrations that gradually rise until peaking in the heaviest fraction. Again this is to be expected given the atomic weight of iron is heavier than both silicon and

Table 3.9: Mineral content of density fractionated UK-CFA and an ultra fine fly ash residue IFA-UF

Sample	Glass	Mullite	Quartz	Magnetite	Hematite
CFA-3	89.6	7.5	2.4	0.6	
< 1.0	88.6	11.0	0.4		
< 1.2	89.9	9.8	0.3		
< 1.4	87.1	12.2	0.7		
< 1.65	86.1	13.2	0.7		
< 2.0	83.9	15.1	1.0		
< 2.2	87.3	10.9	1.8		
< 2.4	88.7	8.2	2.6	0.5	
< 2.6	90.6	5.9	3.5		
> 2.6	92.3	2.0	0.7	4.6	0.4
IFA-UF	88.2	10.2	1.6		
< 2.0	79.7	19.6	0.7		
> 2.0	88.1	10.1	1.8		

aluminium. A slight dip in Fe_2O_3 content at 2.5 g/cm^3 signals a very highly pure Si-Al phase and this is reinforced with mineral data presented below. The char distribution is slightly shifted towards lower densities. Prior petrographic and density separation studies [271] of isolated unburned char distinguished three types of char: (1) inertinites, a highly oxidised maceral, that represent unaltered remnants of original coal; (2) isotropic particles that have undergone complete melting and have reacted extensively, unable to achieve any degree of ordering; and (3) anisotropic particles which are those particles that have reacted and reformed with a degree of structural alignment. The densities of the respective char types peaked at *ca.* 1.50-1.65 g/cm^3 for (1), *ca.* 1.72-1.78 g/cm^3 for (2), and *ca.* 1.88-1.95 g/cm^3 for (3). Given the foregoing it is a little surprising that the char content peaks in the current study at 2.4 g/cm^3, however there are some key differences in the two experimental methods that might give lie to the difference. Maroto-Valer, Taulbee, and Hower [272] utilised a centrifugation method that was likely to minimise the carry over of less dense particle into the denser fraction. More importantly the density fractions were tighter which meant that there was a greater degree of resolution in the distribution. The other possibility is that the char in CFA-3 is more highly anisotropic than those studied previously which has resulted in very dense char particles. This appears to be a possibility given the XRD pattern for the fractions as discussed in section 3.1.3.

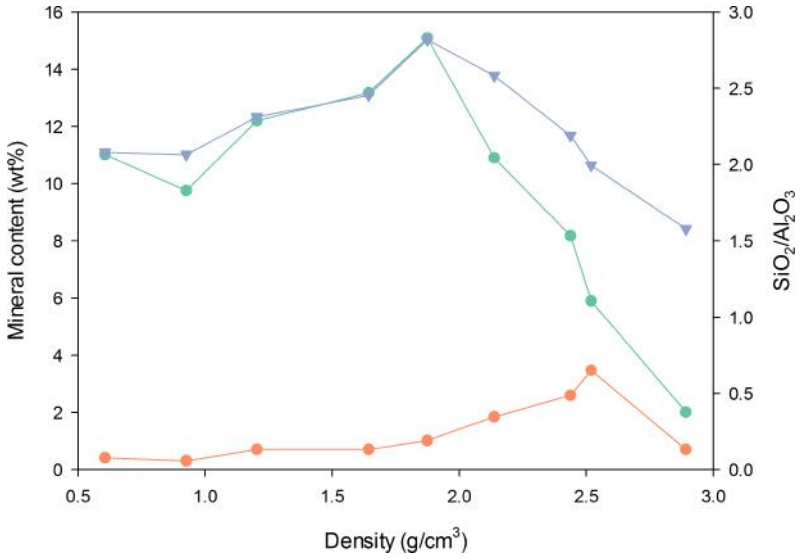

Figure 3.21: Quartz (●) and mullite (●) content across density fractions of CFA-3. SiO_2/Al_2O_3 ratios (▼) are plotted against the right hand axis

The mineral content of the fractionated samples of CFA-3 and IFA-UF was estimated using an internal reference XRD method; the results are presented in Table 3.9. The overall mineral content including glass was determined by subtracting the LOI value from 100. The mineral contents were normalised by the overall mineral content. The glass fraction was determined as a ratio of the overall mineral content minus the crystalline minerals to the overall mineral content. The glass composition of each sample was determined by subtracting the stoichiometric quantities of the minerals from the bulk chemical composition and normalising by the sum of the components; they are shown in Table 3.10.

The normalised mullite concentrations (Figure 3.21) show a rise from *ca.* 10-15 wt% between 0.6-2.0 g/cm^3 and then decline sharply as the density increases past 2.0 g/cm^3. Given that the density of mullite is normally around 3.1 g/cm^3 this strongly suggests that the mullite is incorporated into the aluminosilicate glass melt and is not present as discrete particles. Watt and Thorne's [264] study did not do a comprehensive mineralogical analysis of the fractionated CFAs. A general observation was possible that density fractions below 2.2 g/cm^3 were comprised of significant quantities of integral mullite and quartz and as the density decreases the ratio of mullite to quartz was found to increase.

Figure 3.21 confirms this finding. However, the quartz is not very abundant at densities below 2.4-2.6 g/cm^3 which strongly suggests that the quartz (SG 2.6) occurs as discrete grains as was indicated earlier in the chapter. The mullite concentration change with density fraction appears to mirror the SiO_2/Al_2O_3 ratio in the glass phase of each fraction in contrast to what was reported by Font *et al.* [238]. The authors speculated that mullite formation is favoured if there is excess alumina present. It is shown here that the opposite occurs; the mullite concentration is higher when glasses have a higher ratio of SiO_2 to Al_2O_3 .

Although the text lacks clarity a previous study by the same research group [17] actually supports the current finding. The CFAs with the two highest mullite contents in that study were associated with higher SiO_2/Al_2O_3 ratios. They also plotted the SiO_2/Al_2O_3 against the overall glass content in the mineral portion of the CFAs studied. A similar plot is presented in Figure 3.22 which shows a clear correlation between glass content and the ratio of SiO_2 to Al_2O_3 . The association of mullite content and SiO_2/Al_2O_3 ratio certainly looks compelling, but it must be noted that there is no evidence to support that this ratio causes the mullite to form in greater quantities. Indeed from a stoichiometric point of view this should not be the case. In light of this it is more likely that the greater crystallisation of mullite, which could have been caused by differing combustion histories of the density fractions, depletes the Si-Al glass melt of Al_2O_3 and thus the SiO_2/Al_2O_3 ratio increases accordingly. Table 3.8 gives the SiO_2/Al_2O_3 ratios of the bulk CFA which is a better indication of the composition of the melt prior to crystallisation. The pattern of these ratios with density fraction is similar to that of the glass, but the absolute differences are much lower.

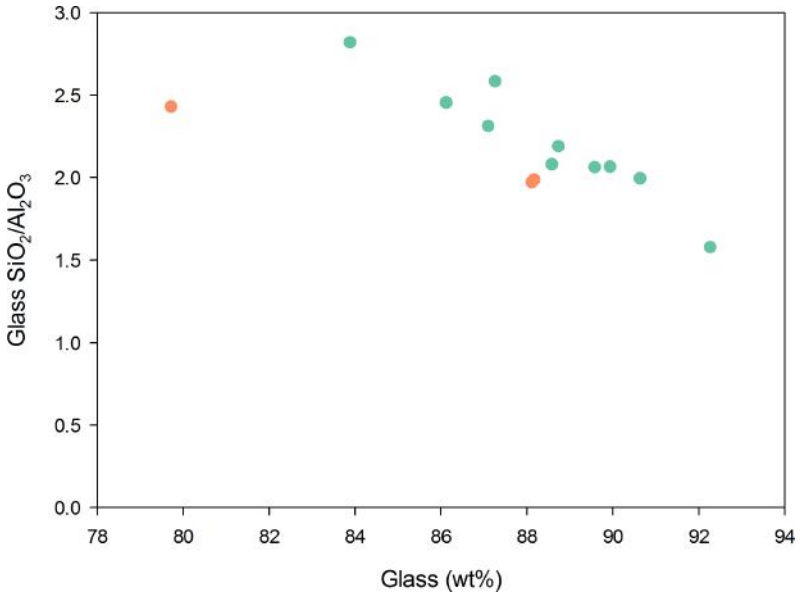

Figure 3.22: CFA-3 (•) and IFA-UF (•) glass SiO_2/Al_2O_3 ratios against glass content.

Table 3.10: Glass composition of density fractionated UK-CFA and an ultra fine fly ash residue IFA-UF

Sample	SiO_2	Al_2O_3	Fe_2O_3	CaO	MgO	Na_2O	K_2O	Cr_2O_3	TiO_2	MnO	P_2O_5	SrO	BaO	SiO_2/Al_2O_3
CFA-3	55.2	26.8	7.5	2.8	1.6	0.8	2.8	0.0	1.1	0.1	0.8	0.1	0.2	2.06
< 1.0	60.1	28.9	2.6	0.7	1.3	0.8	4.4	0.0	0.9	0.0	0.2	0.0	0.1	2.08
< 1.2	60.3	29.2	2.8	0.5	1.1	0.8	4.0	0.0	0.9	0.0	0.2	0.0	0.1	2.07
< 1.4	62.5	27.0	2.7	0.6	1.1	0.8	3.9	0.0	1.0	0.0	0.1	0.0	0.1	2.31
< 1.65	63.1	25.7	3.6	0.8	1.1	0.9	3.4	0.0	1.0	0.0	0.2	0.0	0.1	2.46
< 2.0	65.6	23.2	3.6	0.8	1.0	1.0	3.3	0.0	1.0	0.0	0.2	0.1	0.1	2.82
< 2.2	63.2	24.5	4.5	1.0	1.0	1.0	3.0	0.0	1.1	0.1	0.3	0.1	0.2	2.58
< 2.4	58.2	26.6	6.9	1.3	1.2	0.9	2.8	0.0	1.2	0.1	0.3	0.1	0.2	2.19
< 2.6	58.3	29.2	4.7	1.0	1.1	0.9	3.1	0.0	1.1	0.1	0.3	0.1	0.2	2.00
> 2.6	44.8	28.4	17.2	2.1	2.1	0.6	2.1	0.0	1.2	0.3	0.5	0.2	0.2	1.58
IFA-UF	55.2	27.8	6.6	2.6	1.4	0.8	2.9	0.0	1.2	0.1	0.9	0.1	0.3	1.99
< 2.0	62.9	25.9	3.3	0.5	1.1	1.0	4.0	0.0	0.9	0.0	0.2	0.0	0.1	2.43
> 2.0	55.7	28.2	7.0	1.5	1.3	0.9	3.0	0.0	1.3	0.1	0.6	0.1	0.3	1.97

Figure 3.23 illustrates how the major forming components of the glass phase change with density fraction. In the preceding paragraph the SiO_2/Al_2O_3 ratio and its association with mullite formation was discussed. It is evident that the absolute Al_2O_3 content in the glass phase is relatively stable across the density range. On the other hand, the silica content decreases towards the heavier fractions and is replaced by greater quantities of iron which explains the high densities despite low quantities of crystalline iron oxide species. So it appears given the make-up of the glass composition that the reduction of the SiO_2/Al_2O_3 ratio at higher density fractions is the result of a depletion in SiO_2 content relative to an increase in Fe_2O_3 rather than because a lack of mullite was formed. The particle sizes (Figure 3.19) across the density fractions are another possibility for the relative lack of mullite in denser fractions. The denser fractions are smaller and therefore will achieve faster cooling rates in the combustion process. The larger particle sizes and intermediate densities tend to coincide with the highest mullite contents which adds weight to this explanation.

The K_2O content appears to correlate negatively with density (Figure 3.23). This could have an important mechanistic effect on the formation of hollow or spongy particles that reside in the low density fractions. In high Si glasses, Al_2O_3 markedly reduces the melt viscosity [273]. Ordinarily alkalis or alkaline earth oxides act as fluxing agents and reduce the viscosity further. There is an exception to this rule which is K_2O. Instead of breaking silicate chains to smaller units which reduces the viscosity like other alkali cations, potassium changes the concentration ratio of Al_2O_3, which extend the silicate networks, to Al^{3+} which modify the network. Raask [265] considers that this effect is not very pronounced for the typical amounts of potassium 0.5-3 wt% found in CFA. However he notes that it could be significant for certain CFAs that have high sodium and low SiO_2/Al_2O_3 ratios. Given that at the lowest densities the potassium levels are outside the bounds given by Raask it is worth considering the effect this might have.

In order to examine the possibility that viscosity of the glass melt contributed towards the glass density, the viscosity of the glass phase for each density fraction composition

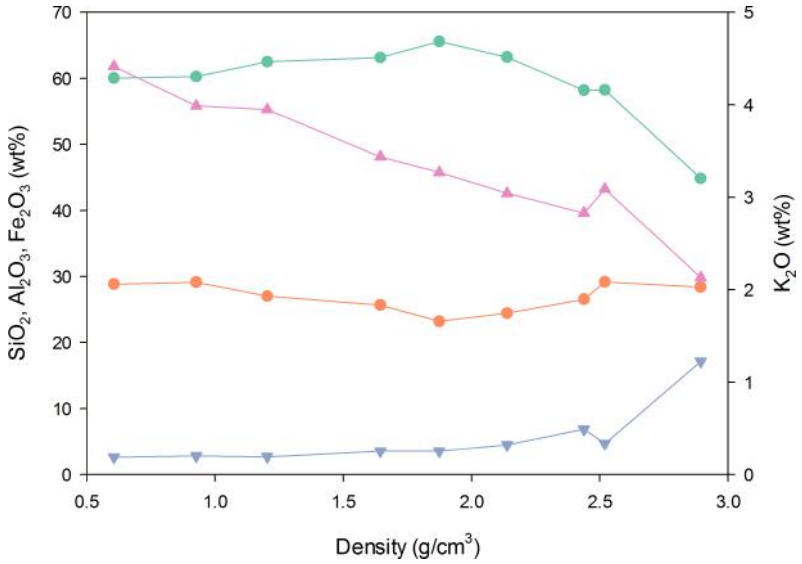

Figure 3.23: Glass composition across density fractions for CFA-3: SiO_2 (●), Al_2O_3 (●), Fe_2O_3 (▼), and K_2O (▲)

requires estimation. Browning *et al.* [274], proposed an empirical method for predicting the viscosity of coal ash slags that is based on data for coal ash slags and synthetic mixtures that are comparable to the compositions under consideration. The method relies on the observation that for any given viscosity, the gradient of the curve of viscosity as a function of temperature is the same for all ash compositions provided they are all in the Newtonian regime. Thus, a translation across the temperature axis ensures that all the curves will overlay. Least square regression to the viscosity temperature curves for 117 ash compositions yielded equation 3.5:

$$\log\left(\frac{\mu}{T-T_s}\right) = \frac{14788}{T-T_s} - 10.931 \tag{3.5}$$

Where T is the temperature in K and T_s is the temperature shift. T_s is related to the ash compositions by a constant A by the following.

$$T_s = 303.63\ln(A) - 574.31 \tag{3.6}$$

In equation 3.6, A is the molar ratio which is given another expression again found by least squares regression to the data of 117 compositions. The quantities of each fraction

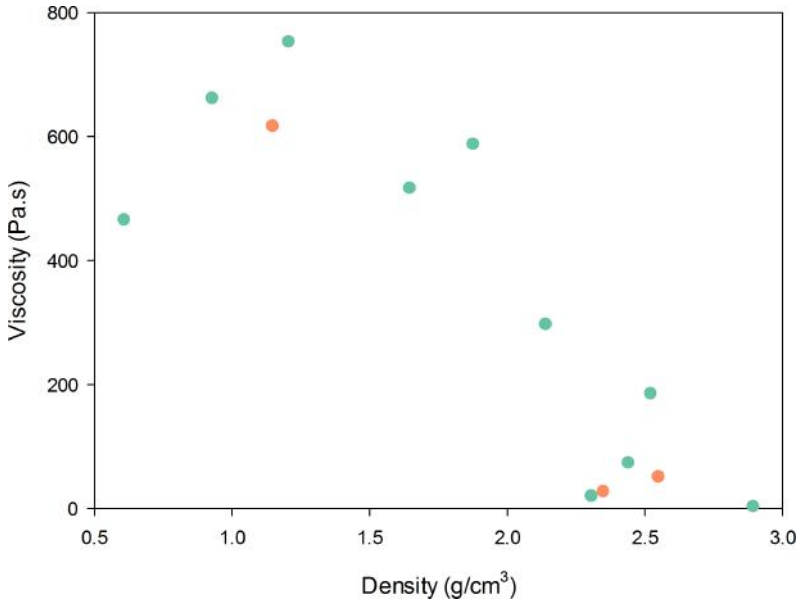

Figure 3.24: Estimated melt viscosity at 1700°C for IFA-UF (•) and CFA-3(•)

are in terms of the mole fraction whereby the given constituents are normalised.

$$A = \frac{3.19Si^{4+} + 0.855Al^{3+} + 1.6K^{+}}{0.93Ca^{2+} + 1.50Fe^{n+} + 1.21Mg^{2+} + 0.69Na^{+} + 1.35Mn^{n+} + 1.47Ti^{4+} + 1.91S^{2-}} \tag{3.7}$$

Equation 3.7 highlights which elements are considered fluxes (the denominators) and those that will increase the viscosity (the numerators). Unlike other viscosity models the current model considers potassium to act as a network extender and increase the viscosity. Using the glass compositions for each density fraction the viscosity is estimated at 1700°C and the results are shown in Figure 3.24. The results suggest that viscosity might play an important role in the formation of ash particles that have significant internal voids. An increase in viscosity from *ca.* 0.6-1.2 g/cm^3 is followed by a decline in viscosity by two orders of magnitude at the opposite end of the density spectrum. The general trend is reinforced by the fact that the results of the IFA-UF samples appear to follow it.

In order to understand if the viscosity might play a role in the formation of particles with internal voids the equation developed by Raask may be used [273]. The growth rate of the radius of a hollow sphere formed by viscous relaxation may be given by:

$$\frac{\mathrm{d}r}{\mathrm{d}t} = \frac{r^2 \Delta p}{4\mu s} \tag{3.8}$$

where r is the sphere radius, Δp is the pressure difference between the sphere interior and exterior, μ is the melt viscosity, and t is the sphere wall thickness. The value of Δp is given by the following.

$$\Delta p = p - p_a - 2\gamma \left(\frac{1}{r} + \frac{1}{r_o} \right) \tag{3.9}$$

In equation 3.9 γ is the surface tension and r_o is the external sphere radius. If the cenosphere is formed by a finite amount of gas throughout the expansion then we may write

$$\Delta p = k r_o^3 \tag{3.10}$$

Combining equations 3.8, 3.9, & 3.10 gives a relationship for the rate of growth of a cenosphere.

$$\frac{\mathrm{d}r}{\mathrm{d}t} = \frac{1}{4\mu(r - r_o)} \frac{k r^2}{r_o^3} - p_a r^2 - 2\gamma \frac{r}{r_o}(r + r_o) \tag{3.11}$$

It is clear from the preceding that the rate of growth of a cenosphere particle is inversely proportional to viscosity. This might be a plausible explanation for the formation of cenospheres that have a greater density than water. If they are more viscous than cenospheres with a SG of less than one, then the rate of growth will be slower, and thus they cool and solidify with thicker walls than the lighter less viscous cenospheres. However this explanation is reliant on a Newtonian description of viscosity. If mullite crystallises in the melt then the effective viscosity is likely to increase. However, whether the differences in mullite concentration are enough to cause significant viscosity differences over and above those caused by the melt composition is uncertain. Tentative evidence in agreement with the foregoing is apparent in Figure 3.25, this is a small particle present

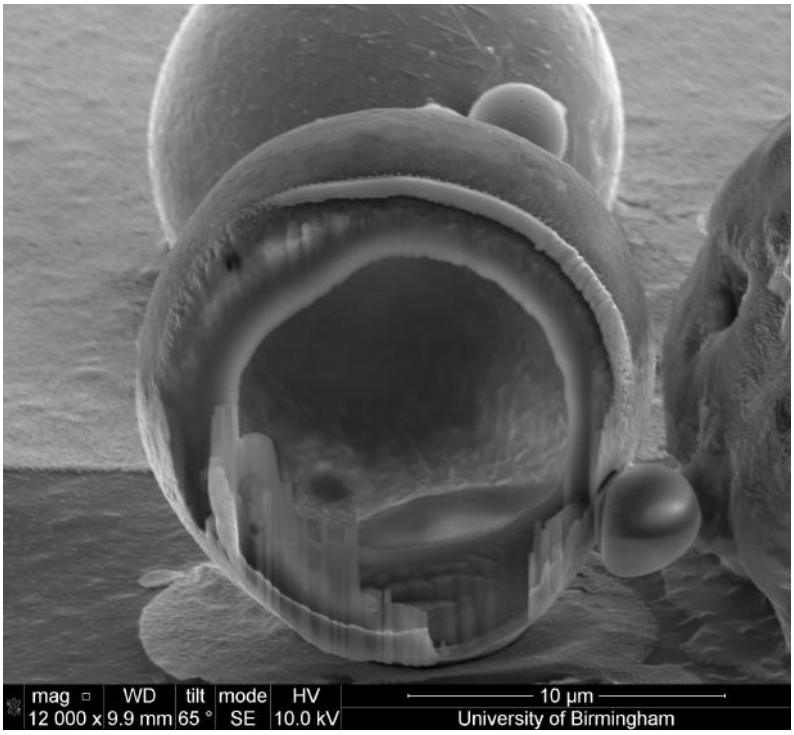

Figure 3.25: FIB cut hollow sphere originating from IFA-UF <2.0 SG

in a density fraction that has a bulk density if 1.0. The particle was cross sectioned using a focused ion beam. The walls are large relative to the particle diameter, certainly more so than was observed in the images of broken cenospheres previously in this chapter.

Table 3.11: Trace elements excluding lanthanides of density fractionated CFA-3 and IFA-UF (ppm)

Sample	Ba	Cr	Cs	Ga	Hf	Nb	Rb	Sn	Sr	Ta	Th	U	V	Zr
CFA-3	1415	110	7.8	38.7	9.9	31.7	90.2	6	1025	2.4	22.3	7.75	177	395
CFA-3 < 1.0	772	70	13.15	21.9	6.1	19	177	4	294	1.8	21.1	4.24	132	257
CFA-3 < 1.2	784	60	11.7	24.9	7.1	18.8	152	6	308	1.9	21.3	4.77	114	260
CFA-3 < 1.4	732	70	11.05	17.7	6.9	19.4	139	4	290	1.9	20.6	4.28	113	256
CFA-3 < 1.65	654	60	7.23	17.3	5.8	16.6	85.2	4	298	1.7	15.45	4.45	87	217
CFA-3 < 2.0	504	50	4.88	13.3	4.4	13.5	59.6	3	231	2.4	11.45	4.83	66	173
CFA-3 < 2.2	855	80	6.12	29.7	7.1	22.5	73.9	8	439	1.9	15.4	5.59	99	281
CFA-3 < 2.4	1250	100	7.71	35.9	10.7	32.5	86.6	4	832	2.6	22.3	7.09	129	394
CFA-3 < 2.6	1240	90	9.43	34.6	10.4	32.6	110	4	778	2.7	24.2	5.9	129	390
CFA-3 > 2.6	1840	160	7.5	60.6	15	43.9	84	9	1300	3.3	27.7	10.25	215	606
IFA-UF	1900	120	10.4	62.6	12.7	38.4	114.5	9	1275	3	30.8	9.87	217	481
IFA-UF < 2.0	871	80	10.8	28.7	6.4	18.6	136	2	331	1.8	20.3	4.71	126	248
IFA-UF > 2.0	1985	130	10.65	65.4	12.4	40.4	118	8	1260	3.2	31.7	9.64	196	506

A striking feature of the density fractionated CFAs is that the excluding Rb, all the trace elements tend to show limited to moderate enrichment in the heavier density fractions relative to the raw CFA (Table 3.11). In terms of particular elements of environmental concern lead and arsenic were not tested for; however the level of chromium in the heaviest density fraction reaches a level of 160 ppm which could present problems if it was able to be mobilised in a particular application. Uranium and thorium are also slightly enriched in the heavier fractions which might also present problems for any exploitation of metal extraction. An element of commercial interest Ga, which as has been discussed is a strategically important material, is concentrated in the heavier fractions of both CFA-3 and IFA-UF by up to a factor of 1.5. Although this might not be an exploitable level in this particular CFA it does suggest that in ashes with Ga levels higher in the raw ash that in the heavier fractions there might be levels approaching the level that might be exploited. The enrichment of certain trace elements has been shown for the smallest size fractions of CFAs [275]. It has already been shown that the heaviest density fractions generally have the smallest particle sizes. The mechanism postulated for enrichment among small particles, was that the elements are volatilised in the combustion chamber and then condense on the surface of the CFAs. The smallest particles have the highest specific surface area and so are enriched preferentially on the smallest particles.

Table 3.12: Lanthanide plus yttrium content of density fractionated CFA-3 and IFA-UF (ppm)

Element	CFA-3	< 1.0	< 1.2	< 1.4	< 1.65	< 2.0	< 2.2	< 2.4	< 2.6	> 2.6	IFA-UF	< 2.0	> 2.0
La	74.7	71.3	68.5	64.9	47.5	35	50.2	66.7	73.2	87.9	99.1	69.1	102
Ce	147.5	144.5	139.5	134.5	97.7	70.5	103.5	138	152	182.5	196	140.5	205
Pr	17.25	16.5	15.4	14.85	11.15	7.76	11.35	15.65	17.1	20.7	22.3	15.45	23.3
Nd	73.1	67	62.4	60.6	45.7	33.4	47.3	66.1	72.5	88.6	96	63.6	96.5
Sm	12.95	10.85	10.6	10.2	7.75	5.19	7.49	11.8	12.85	16.95	17.3	10.1	17.1
Eu	2.59	2.08	2.01	1.89	1.59	1.12	1.63	2.61	2.63	3.41	3.35	2.13	3.35
Gd	13.7	8.89	9.2	8.72	7.15	5.47	7.73	12.2	12.15	18	17.5	8.81	16.7
Tb	2.02	1.38	1.43	1.33	1.14	0.89	1.26	1.93	2.03	2.82	2.77	1.32	2.69
Dy	11.6	7.7	8.12	7.6	6.59	5.14	6.74	11.2	11.45	14.95	15.65	7.49	15.25
Y	65.5	42.8	42.5	42.4	35.8	27.4	43.1	58.9	61.5	83.6	84	43.3	85.4
Ho	2.28	1.53	1.56	1.56	1.22	0.98	1.44	2.16	2.17	2.91	2.97	1.49	2.93
Er	6.34	4.6	5.05	4.66	3.7	2.81	3.94	6.4	6.45	8.56	8.5	4.76	8.23
Tm	0.84	0.66	0.63	0.67	0.53	0.38	0.52	0.84	0.9	1.16	1.13	0.61	1.11
Yb	5.61	4.65	4.52	4.48	3.78	2.53	3.96	5.76	6.16	6.91	7.97	4.2	7.52
Lu	0.82	0.65	0.65	0.66	0.53	0.35	0.54	0.86	0.83	1.14	1.07	0.6	1.11
$\sum$REY	437	385	372	359	272	199	291	401	434	540	576	373	588
LREY (%)	74.5	80.5	79.7	79.4	77.2	76.3	75.6	74.4	75.5	73.4	74.8	80.0	75.5
MREY (%)	21.8	16.3	17.0	17.3	19.2	20.1	20.8	21.6	20.7	22.7	21.4	16.9	21.0
HREY (%)	3.6	3.1	3.3	3.4	3.6	3.5	3.6	4.0	3.8	3.8	3.8	3.1	3.6
Critical	161	126	122	118	95	71	104	147	157	202	210	123	211
Uncritical	119	108	104	99	74	53	77	106	115	144	156	103	159
Excessive	157	152	147	142	104	75	110	148	162	195	209	147	218
Outlook	1.03	0.83	0.83	0.84	0.91	0.95	0.95	1.00	0.97	1.04	1.01	0.83	0.97
Critical %	36.9	32.6	32.7	33.0	34.8	35.6	35.8	36.7	36.1	37.4	36.5	32.8	35.9
TREYO	526	463	448	432	327	240	350	483	523	651	693	450	709
Inor.	84.9	98.0	98.3	99.2	71.3	49.0	65.1	80.7	95.0	99.6	98.0	97.6	98.4
$\sum$REO/Inor.	620	473	455	436	459	489	538	598	550	654	707	461	720

A fuller discussion of the REY content of CFAs and products derived from CFAs was given earlier in the chapter. In order to compare the effect of density fractionating with size fractionating and physical processing, each of the density fractions was also subject to REY determination. The results were analysed as before (Table 3.12. Given the lanthanides position in the periodic table it might be expected that REY elements would concentrate in the heaviest fractions of CFA. However, this enrichment effect is marginal, although it is present if the REY elements are assumed to be present in the mineral (including glass) matter only (see last row of Table 3.12). There are two important features of Table 3.12: (1) the percentage of critical elements progressively increases as a function of particle density which suggests that targeting heavier fractions might not neglect too much potential resource and (2) the heavy fraction of the ultra fine CFA contains over 700 ppm of REY elements on an oxide basis. Given the favourable REY distribution and the small particle size of these elements, then this could probably be relatively easily separated even if, as appears likely the REY content is present throughout the whole of the glass phase. This is the first time such an analysis has been conducted to the best of the author's knowledge.

3.3.4 Conclusions

The specification of a cenosphere derived from CFA has for a long time been informed by the way that they are captured. This is useful for applications where they are required to float on water but restricts their potential yield for applications that do not require this functionality. This section has confirmed previous literature on the subject that there exists a number of particles that have a specific gravity of less than 2 that are either spongy or hollow, but thick-walled, in nature. Particles that have specific gravities of more than 2 decrease in particle size as their density increases. It is suggested that this might be an effect of the viscosity of the glass melt that is lower with reduced K_2O content. Any trapped gas in lower glass viscosities expands the molten bubble too quickly and the molten bubble ruptures before it can solidify. The viscosity was predicted based

on the glass melt composition and this prediction showed a viscosity peak at 1.2-1.5 g/cm^3 which gives an indication of why they might contain thicker walls and hence have a higher density. An unexpected finding of this section is that char peaks in the density fraction around 2.4 g/cm^3. This suggests that there might have been an issue with carry-over in the experimental procedure, or that the char particles are highly anisotropic. The latter suggestion is very relevant to Chapter 6. This section has confirmed the suggestion previously in the chapter that mullite is incorporated in the particle envelope and that quartz occurs as a discrete mineral. Mullite concentration appeared to correlate with SiO_2/Al_2O_3 ratio but it is thought that this is an artefact of the fact that smaller particles, which tend to be heavier, have different rates of cooling which affects the extent of crystallisation. Both REY elements and certain other trace elements have been shown to speciate with density as well as particle size which is a finding novel to this thesis.

CHAPTER 4

AN EMPIRICAL MODEL FOR THE PREDICTION OF COAL FLY ASH SUSPENSION VISCOSITY WITH CONCENTRATION AND SHEAR RATE

4.1 Introduction

The majority of potential unit operations to separate CFA must be run on a wet basis *e.g.* froth flotation for carbon removal, or gravity classification for cenosphere extraction. Thus the CFA must be mixed with water to form a mineral slurry. In order to achieve the highest throughput per unit area, the solids loading must be maximised. In order to adequately design operating equipment to perform in a CFA processing scheme a knowledge of how the slurry viscosity changes with concentration and shear must be obtained. For example, cenospheres can be separated in a process based on similar principles to a mixer settler. It consists of a cylindrical tank, an overflow weir, and an off centre impeller. The objective of the process is to achieve sufficient agitation to maintain an off-bottom suspension and sufficient quiescence in the upper region to ensure a pure cenosphere product. Critical separator variables such as the Zwietering correlation [276] for minimum impeller speed to maintain an off-bottom suspension are dependent on the viscosity of the CFA. Methods for determining the power curves for the impeller system rely on a knowledge of how the viscosity (μ) changes with shear rate ($\dot{\gamma}$).

The hydrodynamics of the separator are complicated because at high solids loadings

($>$ 40wt%), CFA slurry is known to exhibit non-Newtonian behaviour [277]. Although the shear thinning behaviour of coal fly ash has been described previously [278, 279], the viscosity of poly-disperse slurry systems are known to be dependent on particle volume fraction (ϕ), pH, and particle size distribution. It is for this reason that an a priori prediction of the viscosity of a CFA suspension as it changes with shear rate and concentration is difficult. Senapati *et al.* [278] and Bournonville and Nzihou [279] propose viscosity models that incorporate ϕ and $\dot{\gamma}$ terms that were validated for power station and municipal waste station ash respectively. However, these models can not be applied to the ash samples used in this paper over a wide range of suspension concentration.

The forces that exist in a flowing suspension can be grouped into three categories: 1) the hydrodynamic forces that arise from the relative motion of particles to the suspending fluid; 2) the Brownian force is ever-present and comes from the thermal randomising forces which cause particles to undergo rotational and translational movement; and 3) colloidal forces which can be classified as attractive or repulsive [280].

Einstein proposed equation 4.1 for the description of μ-ϕ which is developed from a theoretical basis.

$$\mu_r = 1 + 2.5\phi \tag{4.1}$$

Where μ_r is the viscosity of the slurry relative to the viscosity of the suspending medium. However, equation 4.1 does not consider particle size, position, or the effect of particles on one another and for this reason it is only valid for very dilute suspensions. Batchelor [281] expanded this equation to include higher order terms which account for the effect of other particles. From a theoretical perspective both these equations are independent of shear rate and can only describe dilute suspensions ($\phi \leq 0.1$) [282].

For more concentrated suspensions the semi-empirical equation of Krieger and Dougherty is often applied [283]:

$$\mu_r = (1 - \frac{\phi}{\phi_m})^{-[\mu]\phi_m} \tag{4.2}$$

where $[\mu]$ is the intrinsic viscosity and is equal to 2.5 for rigid spheres. ϕ_m is the maximum packing fraction of particles. The product of $[\mu]\phi_m$ is often observed to be equal to 2 and thus the exponent in equation 4.2 can be replaced by this simplification [284]. Some studies have suggested that deviation from the condition of spherical particles leads to an increase in $[\mu]$ but that this is accompanied by a decrease in ϕ_m [280].

While there are many semi-empirical equations in the literature that can describe μ-ϕ behaviour at higher solids loadings, and there are several equations that can adequately describe μ-$\dot{\gamma}$ behaviour such as the power law, there are few relationships that describe both. Senapati *et al.* [278] modified the model of Bournonville and Nzihou [279], a μ-ϕ equation that incorporates a shear rate term, adding a coefficient, S, to describe the particle size distribution of the particles. The exponent, N, is a suspension dependent adjustable parameter.

$$\mu_r = S[1 + \frac{[\mu]}{\dot{\gamma}^n}(\frac{\phi}{\phi_m - \phi})]^N \tag{4.3}$$

Equation 4.3 predicts the viscosity of CFA slurries studied reasonably well; however, it uses a constant value for the shear thinning index n. For this reason it can not be applied successfully for the range of concentrations considered in the present study due to the considerable variation in n with concentration.

The current study examines two suspension types: a raw unrefined CFA and a processed CFA that has undergone sequential processing to remove, lightweight, carbonaceous, magnetic, and oversize fractions hereafter referred to as improved fly ash residue (IFA) (process described in [7]). The two ashes were investigated with respect to their rheology at a series of concentrations ranging from 10-70 wt%. The particle size, shape, and distribution is discussed in relation to viscosity. The data is used to propose a new general modelling procedure for the purpose of CFA processing equipment design and

scale up that can describe viscosity behaviour with both ϕ and $\dot{\gamma}$.

4.2 Experimental

4.2.1 Raw Materials

CFA and IFA were obtained from RockTron Ltd (UK), a company that specialises in CFA processing technology, in dry powder form. Slurries were prepared using distilled water by weighing quantities of dry powder into glass bottles to make a range of known weight concentrations.

4.2.2 Methods

Sample Characterisation

Samples were characterised according to methods outlined in Section 3.1.2

Rheological Method

CFA and IFA suspensions were made by weighing quantities of ash (dried at 80°C for 24 hours) and distilled water into glass bottles at concentration of 10-70 wt% at intervals of 5 wt%. The suspensions were then immersed in an ultrasonic bath for a period of 10 minutes prior to testing in order to de-agglomerate the particles.

The rheology of CFA and IFA samples was studied using a TA Instruments AR-G2 controlled stress/strain rate rheometer. The system geometry used was that of aluminium DIN concentric cylinders. The dimensions are shown in Figure 4.1 The temperature was controlled to 20°C with a circulating chiller/heater. Prior to use rotational mapping of the spindle was performed to ensure smooth rotation.

The procedure used was a series of steady state flow procedures with controlled shear rate. The tests incorporated 15 flow steps at shear rates from 2-200 s^{-1}. Prior to com-

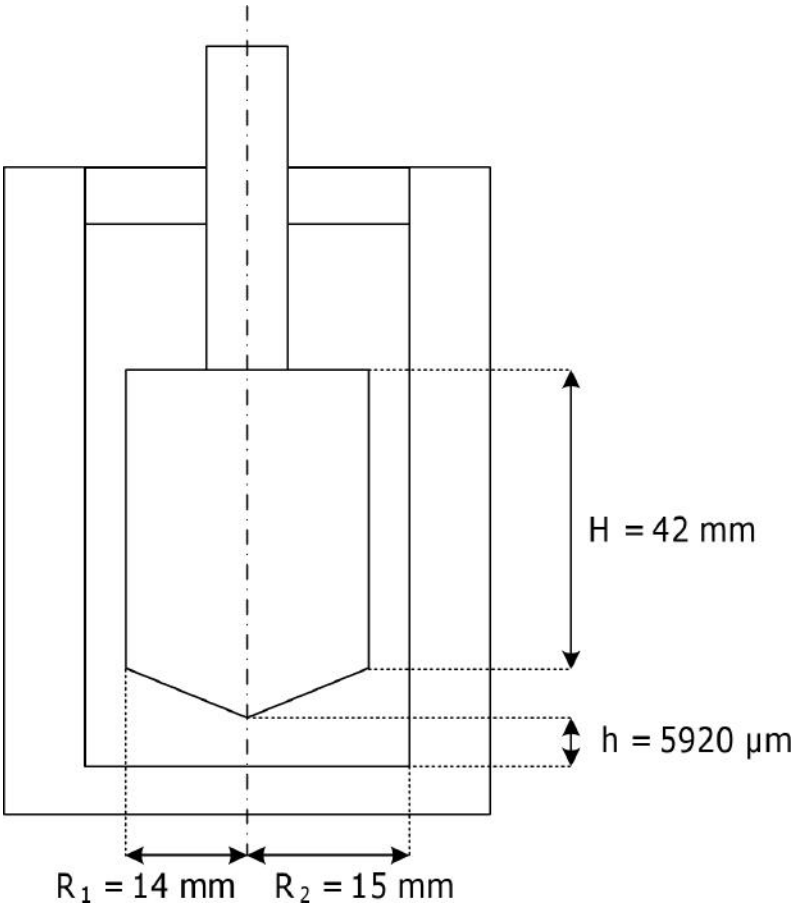

Figure 4.1: Schematic illustrating the concentric cylinder geometry used with the TA instruments AR-G2 rheometer used in this study

mencing each flow step, a conditioning step was performed at a shear rate of 2500 s^{-1} for 15 seconds followed by an equilibration of 15 seconds. The purpose of these conditioning steps was to prevent sedimentation of the particles as low concentrations and shear rates. Although not performed in this study a forward and backward sweep of the shear rates would enable a better judgment of whether sedimentation was occurring in the experimental timescales involved. This would be indicated in an observable experimental hysteresis.

The repeatability of the procedure is shown in Figure 4.2: 3 flow curve measurements were taken at concentrations of 30, 40, and 50 wt% over shear rates of 2-40 s^{-1}. It is clear that the repeatability of the procedure is extremely consistent. As a result, and to improve clarity of presentation, error bars are omitted from the remainder of this paper.

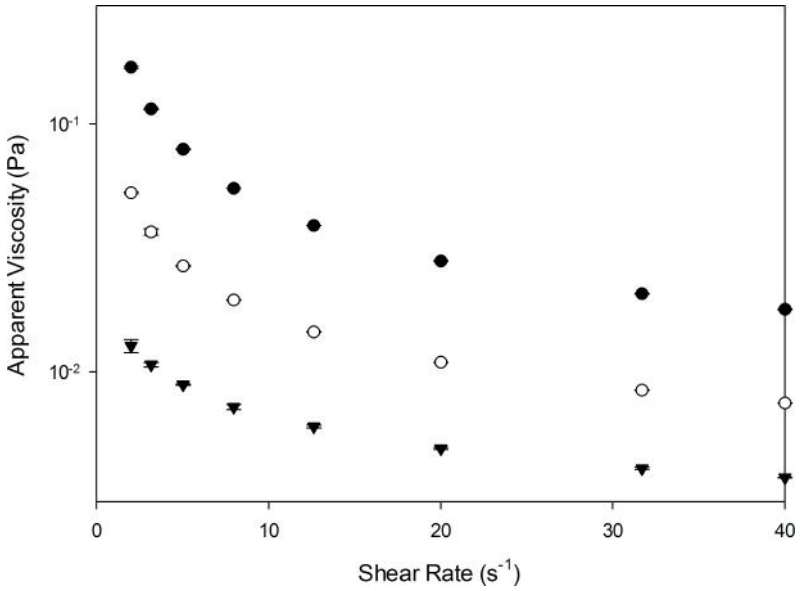

Figure 4.2: Apparent viscosity as a function of shear rate for IFA 30 wt% (▼), 40 wt% (○), and 50 wt% (●). Error bars represent the standard deviation of 3 measurements.

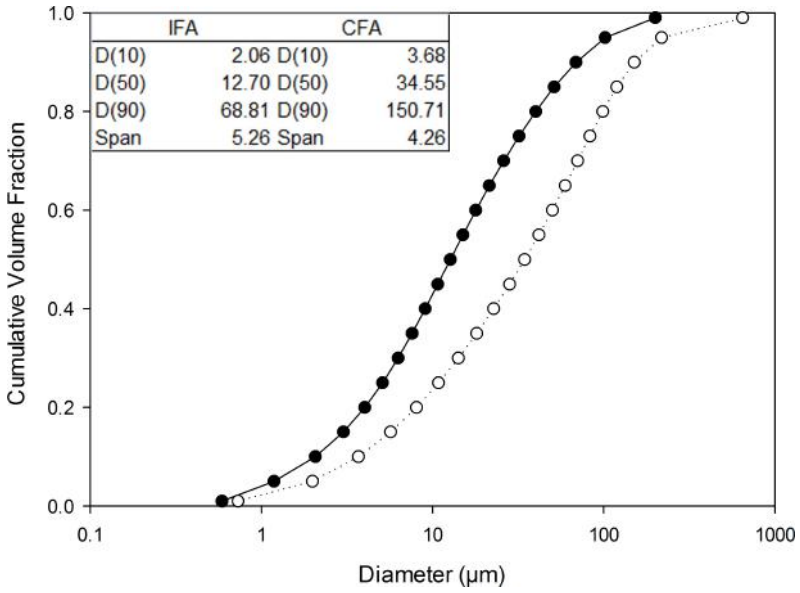

Figure 4.3: Particle size distribution of CFA (○) and IFA (●)

4.3 Results and Discussion

4.3.1 Sample Characterisation

The results from the PSD analysis are presented in Figure 4.3. The IFA is in general much smaller relative to CFA; however, the situation is reversed when observing the two sample's spans which means that the IFA has a broader distribution than CFA. The bulk chemistry and density of the CFA and IFA are provided in Section 3 as CFA-2 and IFA-F respectively. It is notable that IFA has lower LOI values and a lower Fe_2O_3 content than CFA as result of the processing scheme is has been subjected to. Figure 7.1 highlights the difference between the general size and shape of the two samples. While the IFA is predominately spherical, the CFA contains a larger proportion of irregularly shaped particles as shown in the SEM image. There is no significant difference between the densities of the two samples which is perhaps surprising given the larger carbon content in the CFA. The carbon content in CFA has been shown to be more porous and as such the density should be lower [7]. In this case the reduction in carbon in the IFA is probably offset by the reduction in the heavier magnetic species.

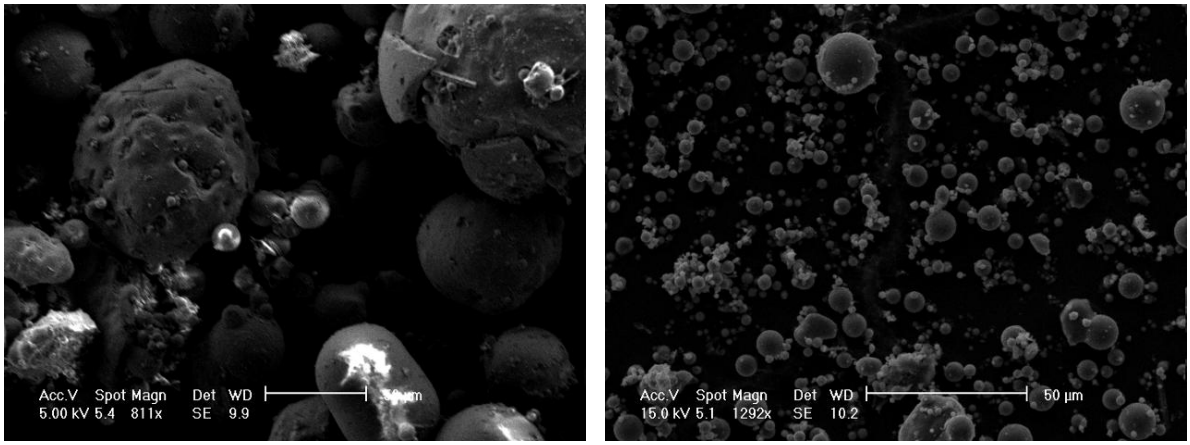

(a) CFA (scale bar 50 μm)) **(b)** IFA

Figure 4.4: SEM images of both ash types

4.3.2 Rheology of CFA Slurry

It can be observed in Figure 4.5 that an increase in slurry concentration is concordant with an increase in the relative viscosity of the suspension. This is to be expected given that the hydrodynamic disturbance of the flow field that is induced by the presence of solid particles in liquid media leads to both an increase in the energy dissipation and an increase in the suspension viscosity [280, 284].

At high concentration, suspensions tend to exhibit a 3-stage dependence with shear rate: 1) Newtonian behaviour at low shear rates with a constant limiting viscosity for zero shear, 2) shear thinning in intermediate shear rate regimes, and 3) constant viscosity at high shear rates with a limiting viscosity for zero shear [284]. Shear thinning is observed to some degree for all the slurry concentrations. However, at low concentration ($<$ 20 wt%) this shear thinning is only apparent over the shear rate change of 2-20 s^{-1} and the decrease in viscosity is marginal. At intermediate concentrations (30-50 wt%) the shear stress-shear rate plots seem to indicate the emergence of a yield stress, with low shear rate stress having a relatively flat profile. This is unusual as yield stresses have previously been reported in suspension concentrations with volume fractions greater than 0.4 [285] (for these slurries 30-50 wt% corresponds to a volume fraction of 0.18-0.33). Although there appears to be the presence of a yield stress, curve fitting to empirical models containing

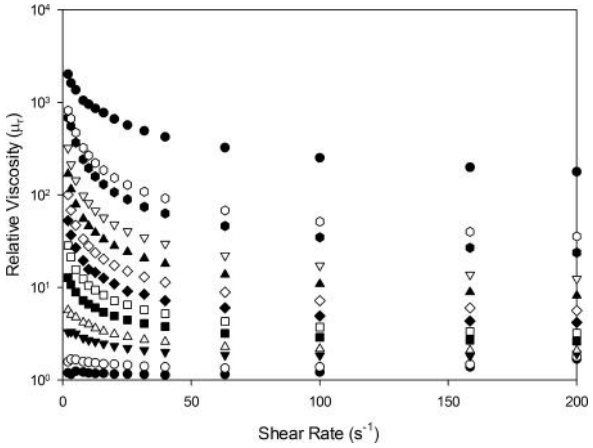

(a) Relative viscosity as a function of shear rate for IFA

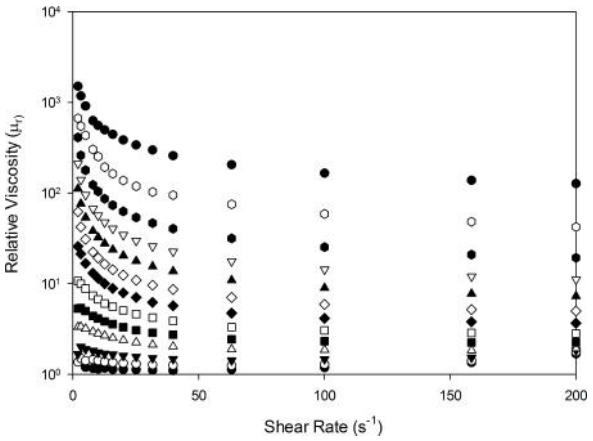

(b) Relative viscosity as a function of shear rate for CFA

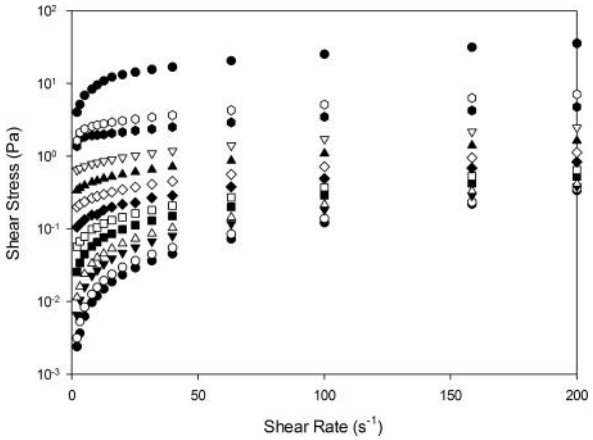

(c) Shear stress-shear rate plot for IFA

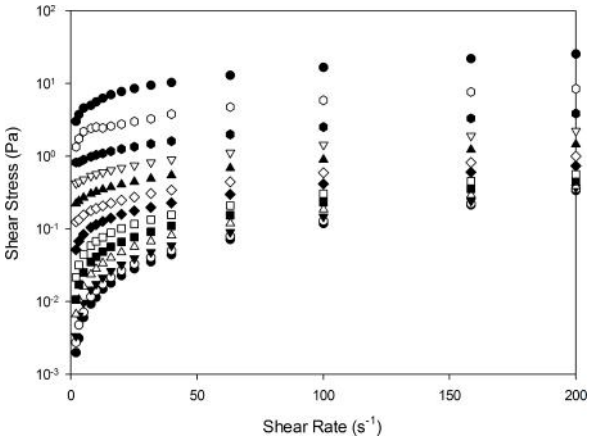

(d) Shear stress-shear rate plot for CFA

Figure 4.5: Rheology of IFA and CFA suspensions. Concentrations 10-70 wt% (ϕ = 0.05-0.5) from bottom to top of each plot.

yield stress terms does not guarantee the accuracy of this value; they must be regarded as model fitting parameters [286]. At high concentration the stress-rate curves return to the sort of shape that low-intermediate concentration slurries have with respect to the steep gradient at low shear rates and potentially a lack of yield stress. The lack of data in the low shear rate region prevents firm conclusions to be drawn. Interestingly this behaviour is observed in both CFA and IFA albeit at slightly different concentrations. This change in behaviour makes a simple universal model very hard to apply.

It is generally accepted that non-Newtonian behaviour is a result of the effect of shear on suspension micro-structure [285]. The random close packing of freshly suspended solids become more ordered as the shear is increased. A random structure in a concentric cylinder viscometer was found to transform into a 2-dimensional hexagonal structure under shear by observing the cylinder with a camera. The temporal decrease in viscosity was found to coincide with this formation [287]. Not only does a more ordered structure suggest an increase in the maximum packing fraction [284], it also thought that the 2-dimensional sheets are able to slide over each other which explains the decrease in viscosity.

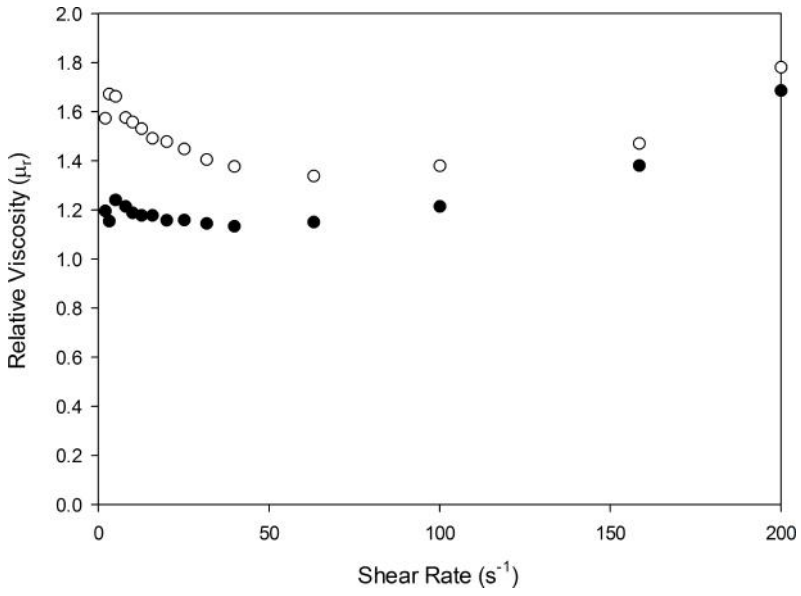

Figure 4.6: Shear thickening behaviour of low concentration IFA slurry: 10 wt% (•) and 15 wt% (○)

Figure 4.6 appears to show the onset of shear thickening behaviour for IFA solids volume fractions of 0.05 and 0.08; a similar pattern was also observed for CFA. After a

small degree of shear thinning behaviour, at a critical shear rate (circa 50-60 s^{-1}), the relative viscosity of the suspensions starts to increase and at 200 s^{-1} it is more viscous than at 2 s^{-1}. This behaviour is extremely unusual. Shear thickening for particulate systems has long been documented (see for example: [288]). However, it is usually reported to occur in highly concentrated suspensions ($\phi > 0.4 - 0.5$) [284]. In addition to this it is often reported that the critical shear rate at which the onset of shear thickening occurs decreases with increasing volume fraction which is the opposite of what has been observed in this case. The explanation for shear thickening tendency in general is that as the shear increases above a certain value the ordered 2-dimensional structures start to break up leading to a decrease in packing fraction and the reduction of the sliding layer effect. Barnes [288] points out that typical shear thickening is expected for de-flocculated systems where there is no attraction between particles. This is certainly the case for the lower concentration but it suggests that there might be some degree of flocculation or aggregation for more highly concentrated CFA and IFA suspensions. There is some uncertainty in the literature regarding flocculated suspensions as to whether an increase in the value of ϕ is accompanied by an increase [289] in the critical shear rate required for shear thickening or a decrease [280]. It is also possible that the finding is a result of sedimentation as described previously; regardless, the finding warrants further investigation.

The relative viscosity of IFA is generally higher than that of CFA at the same volume concentration. Figure 4.7 shows this to be the case for three different weight concentrations (30, 50, and 70 wt%) and in reality all of the data followed this pattern. It might be expected that the suspension with the broader size distribution, IFA, would have a lower viscosity for the following reasons: the smaller particles could act as a lubricant to the larger particles and the smaller particles might be able to occupy the void space created by the larger particles' packing arrangement thus increasing the maximum packing fraction. However, the relative particle size of the two suspensions is the likely explanation for the opposite phenomena occurring. In addition to hydrodynamic forces, as the particle size

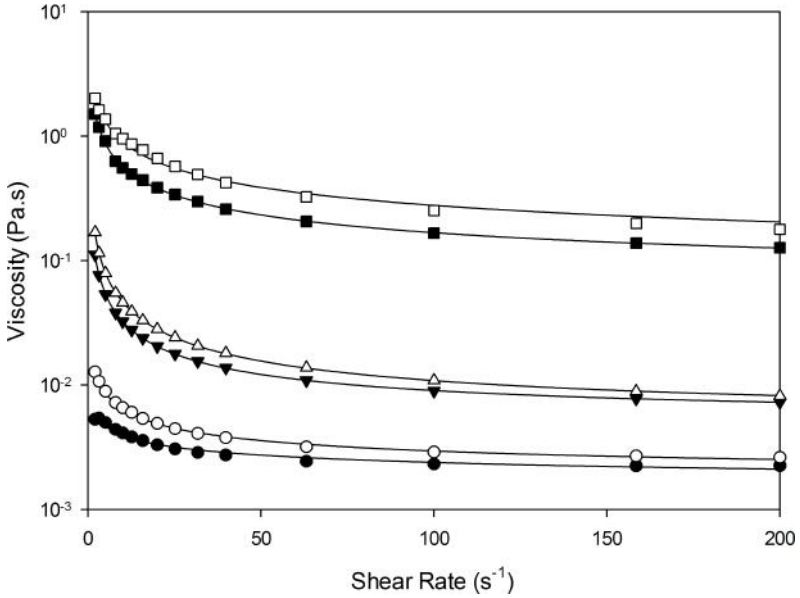

Figure 4.7: Relative viscosity as a function of shear rate: IFA 30 wt% (○), 50 wt % (△), 70 wt% (□); CFA 30 wt% (●), 50 wt% (▼), 70 wt% (■)

decreases, colloidal forces start to contribute to viscosity effects [280]. In a stable colloidal metal oxide dispersion there must be a net repulsive force present. For colloidal particles, this is known as the electrical double layer repulsive force and it is made up of two components: the surface charge and the diffuse ion layer on the particle. For smaller particles the mean separation between adjacent particles is shorter and thus a larger extension of the double layer interaction results. The ionic content of the two suspensions could have been measured at this point. Increased ionic content relative to each other would indicate a zeta potential closer to zero and hence a greater likelihood of coagulation as the effect of surface charges reduced. The consolidated structures would trap water within and so would show an effective increase in volume fraction leading to a larger density.

4.3.3 Modelling

Viscosity change with shear rate

Models such as those of Cross [290] are able to model the 3 stages of high concentration suspension viscosity by fitting them to an infinite shear viscosity and a zero shear viscosity,

μ_∞ and μ_0 respectively. However, for the rheological behaviour shown in Figure 4.5, the apparent yield stresses present lead to inconsistent predictions of μ_0 for some of the suspensions. Other researchers [278] fit the rheological data for power station CFA to the power law model of the following form that describes the shear thinning component, or stage 2) as described in section 4.3.2:

$$\tau = k\dot{\gamma}^n \tag{4.4}$$

where τ is the shear stress, $\dot{\gamma}$ is the shear rate, k is the consistency factor, and n is the power law index. Although equation 4.4 can adequately describe the shear thinning region it deviates from the current experimental data at low shear rates and it does not provide a prediction of μ_∞. Sisko [291] derived a simple relationship that considers the non-Newtonian fluid in two parts: a Newtonian region at high shear and the shear thinning region at lower shear rates. Accordingly the model developed by Sisko has been found to be robust in fitting to rheological data for a variety of non-Newtonian fluids including mineral suspensions [286, 292].

$$\mu = \mu_\infty + m\dot{\gamma}^{n-1} \tag{4.5}$$

The CFA and IFA slurry data was fitted to equation 4.5 using the data analysis software supplied by TA Instruments (UK). The model parameters are listed in Table 4.1. The model parameters for values of $\phi < 0.14$ were not determined as the shape of the viscosity-shear rate curves did not conform to the typical shear thinning followed by Newtonian plateau required by equation 4.5. As expected the consistency index, m, and the power index, n are not constant over the range of concentrations studied. Figure 4.7 shows the comparison between the model and the experimental data for 3 slurry concentrations. It is clear that the model fits the data well; Figure 4.7 is representative of all the suspensions investigated. The relative viscosity at infinite shear has been plotted as a function of ash volume fraction in Figure 4.8. The results suggest that at high

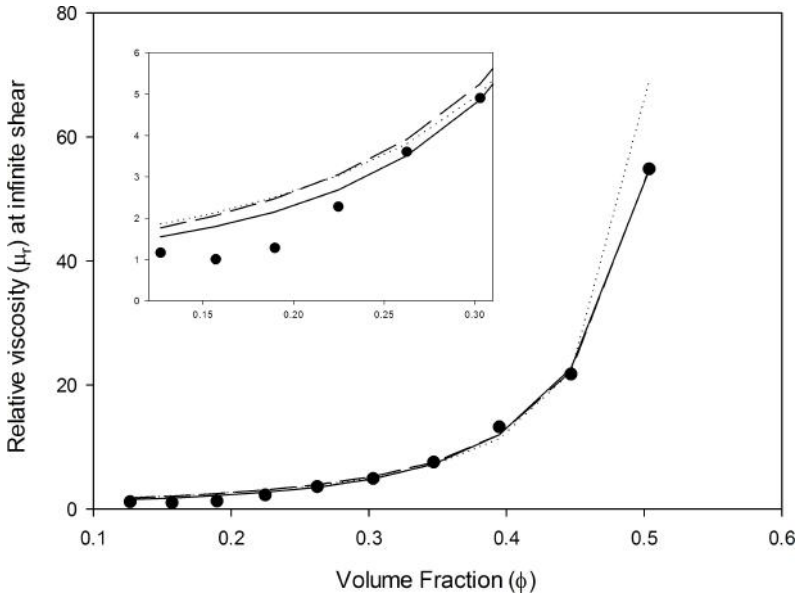

Figure 4.8: Infinite viscosity as a function of volume fraction: Sisko μ_∞ (•), equation 4.9 (solid line), equation 4.2 (long dashed line), equation 4.10 (dotted line)

concentration the beginnings of the expected asymptotic curve can be observed [282].

Viscosity as a function of concentration

It is intuitive that the relative viscosity of a suspension increases with suspension concentration (ϕ) and approaches infinity as ϕ approaches some maximum value (ϕ_m) [285]. ϕ_m is one of the most important parameters in describing the rheological behaviour of a slurry suspension [293]. Although physically ϕ_m represents the maximum packing fraction possible for a particular suspension and geometric arrangement, it is usually used as an adjustable parameter in a variety of viscosity models, such as that of equation 4.6 of the following form [285]:

$$\mu_r = f(\frac{\phi}{\phi_m}) \tag{4.6}$$

When it is used in this way ϕ_m is a direct scalar measure of a given suspension's micro-structure and as such it is dependent on other suspension parameters. The a priori prediction of the maximum packing fraction for a real suspension is not trivial. From a theoretical basis, different geometric arrangements yield different values for ϕ_m. For

well mixed suspensions of spherical particles, a tendency to form random close packed (RCP) arrangements is observed; 0.63 is often given as the value for maximum packing under these conditions [285,294]. However, particle size distribution, particle shape, and a tendency to agglomerate may all affect the maximum packing fraction so for the purposes of further modelling the experimental approach of Liu [293] and best fitting to equation 4.2 and a more recent empirical model was performed.

Liu derived a relationship for the primary purpose of obtaining the ϕ_m value directly using a graphical method. The author found that a number of suspensions with high enough concentration followed the relationship,

$$1 - \mu_r^{-1/n} = a\phi + b \tag{4.7}$$

where n is equal to 2 if the shear rate is sufficiently high. This implies that when the relative viscosity approaches infinity and $\mu_r^{-1/n} = 0$, equation 4.7 can be rearranged with ϕ replaced with ϕ_m.

$$\phi_m = \frac{1-b}{a} \tag{4.8}$$

A plot of $\mu_r^{-1/n}$ as a function of ϕ yields the two constants a and b as the slope and the intercept respectively. Figure 4.9 shows this approach applied to the μ_∞ values for the two series of ash suspensions; the gradient for each suspension is only taken over the straight line portion of the plot high concentration.

Alternatively, the value of ϕ_m is obtained via best fitting equation 4.2 and the following equation 4.9 proposed by Horri *et al.* [295] to the infinite viscosities obtained from applying equation 4.5 that are summarised in Table 4.1. The model parameters were fit to the root mean square error (RMSE) of the data using the solver tool in Microsoft Excel 2007.

$$\mu_r = 1 + 2.5\phi + K\phi\left(\frac{\phi}{\phi_m - \phi}\right) \tag{4.9}$$

Table 4.1: Sisko model parameters

Material	ϕ	μ_∞	m	n
CFA	0.05			
	0.08			
	0.11			
	0.14	1.16 x 10^{-3}	3.04 x 10^{-3}	0.70
	0.18	1.01 x 10^{-3}	6.16 x 10^{-3}	0.67
	0.21	1.28 x 10^{-3}	1.43 x 10^{-2}	0.56
	0.25	2.28 x 10^{-3}	3.98 x 10^{-2}	0.35
	0.29	3.60 x 10^{-3}	0.10	0.18
	0.33	4.91 x 10^{-3}	0.29	0.15
	0.38	7.58 x 10^{-3}	0.36	0.13
	0.43	1.32 x 10^{-2}	0.71	0.11
	0.48	2.18 x 10^{-2}	1.26	0.23
	0.54	5.49 x 10^{-2}	2.36	0.34
IFA	0.05			
	0.08			
	0.11			
	0.14	1.44 x 10^{-3}	6.29 x $^{-3}$	0.62
	0.18	1.60 x 10^{-3}	1.72 x $^{-2}$	0.45
	0.21	2.18 x 10^{-3}	4.35 x $^{-2}$	0.28
	0.25	2.88 x 10^{-3}	8.67 x $^{-2}$	0.20
	0.29	3.70 x 10^{-3}	0.17	0.15
	0.33	5.04 x 10^{-3}	0.19	0.16
	0.38	7.14 x 10^{-3}	0.57	0.12
	0.43	1.10 x 10^{-2}	1.40	0.11
	0.48	1.21 x 10^{-2}	1.56	0.20
	0.54	6.43 x 10^{-2}	3.21	0.46

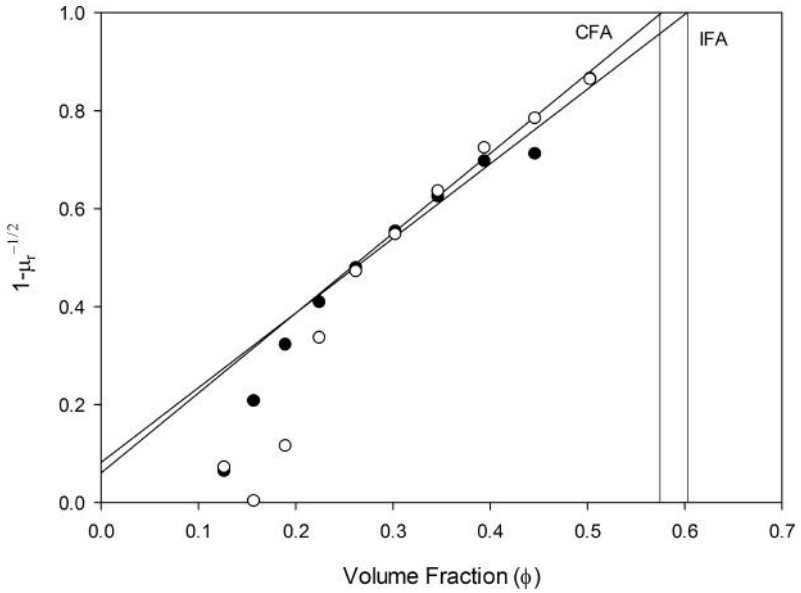

Figure 4.9: (1-$\mu_r^{-1/2}$) vs ϕ for CFA (○) and IFA (●)

Table 4.2 details the ϕ_m values for both CFA and IFA obtained from the three methods described. It is unsurprising that three different values were produced for each sample. Because ϕ_m is used as a fitting parameter some differences between the results from the best fit models are expected as an artifact of the best fit process. The nature of the plotting method as per Figure 4.9 would seem to suggest a better accuracy for ϕ_m prediction; however, this method is very sensitive to experimental error with slight deviations from a straight line fit resulting in significant difference in the value predicted. In this case there are not enough points on the straight section of the plot to justify absolute confidence in the values obtained. There appears to be an erroneous result for IFA at a volume fraction of ϕ=0.45 which has influenced the results. Despite this, it is this method which gives the closest two values between the two suspension types. Conventional thinking regarding particle shape and ϕ_m suggests that ϕ_m decreases as the aspect ratio (length/diameter) of the particles increases [284]. On a very qualitative basis, the observation from the SEM images in Figure 7.1 that the CFA particles appear more irregular could explain the reduction in ϕ_m from 0.60 to 0.58 for IFA and CFA respectively. The same argument may be applied to explain why both suspensions appear to have a ϕ_m value of less than the RCP value of 0.63 that is commonly and theoretically applied for mono-disperse spheres.

Table 4.2: Parameters for the estimation of maximum packing at infinite viscosity

Model	Parameter	CFA	IFA
Equation 4.9	K	13.65	3.04
	ϕ_m	0.68	0.59
	RMSE	0.7991	2.153
	R^2	0.997	0.986
	APE	14.69	42.89
as per Liu [293]	a	1.629	1.523
	ϕ_m	0.58	0.60
	RMSE	4.587	4.427
	R^2	0.987	0.967
	APE	21.71	16.88
Equation 4.2	$[\mu]$	4.05	2.92
	ϕ_m	0.64	0.55
	RMSE	0.7437	1.626
	R^2	0.998	0.991
	APE	18.67	24.26

Liu's model for determination of ϕ_m can be rewritten to describe the relative viscosity as a function of the particle concentration.

$$\mu_r = [a(\phi_m - \phi)]^{-n} \tag{4.10}$$

The term $(\phi_m - \phi)$ represents the effective space in which the particles are free to move in the fluid. It is noticeable both equation 4.10 and equation 4.9 contain this mobility parameter. The infinite relative viscosity ($\mu_{r\infty}$) predicted by the three models for IFA and CFA are compared in Figure 4.8. They are very similar in respect to their correlation with the values obtain via modelling of experimental data. Graphically it is hard to choose between them and so an analysis of the goodness of fit parameters in Table 4.2 is required. In terms of RMSE and the correlation coefficient (R^2), equation 4.2 performs the best. However, in terms of average percentage error (APE), the situation is less clear with equation 4.10 having the lowest combined APE value for the two suspensions. Although all the models tested provide a reasonable approximation of the behaviour of the $\mu_{r\infty}$ as concentration increases, based on the goodness of fit parameters and familiarity of use, it

was decided to use equation 4.2 for further modelling work.

Viscosity as a function of shear rate

None of the models tested are sufficient on their own to describe the viscosity change with both concentration and shear rate. The model of Sisko adequately predicts the behaviour of each individual concentration of CFA and IFA slurry with change in shear rate $> 2\text{s}^{-1}$. However, the parameters of m and n are not independent of the slurry concentration. Thus by substituting equation 4.2 into equation 4.5 the following general viscosity model can be written.

$$\mu = \mu_s(1 - \frac{\phi}{\phi_m})^{-[\mu]\phi_m} + m(\phi)\dot{\gamma}^{n(\phi)-1} \tag{4.11}$$

The parameters $[\mu]$ and ϕ_m are obtained as described in the preceding section and μ_s is the viscosity of the suspending medium. Following a method similar to Turian *et al.* [292] the concentration dependency of m and n is obtained by correlating with ϕ. Upon analysis of the plots of m and n against ϕ, the following correlations were found suitable for the two suspensions considered:

$$m(\phi) = b\phi^c \tag{4.12}$$

$$n(\phi) = d\phi^2 - e\phi + f \tag{4.13}$$

where b, c, d, e, and f are all suspension dependent constants that must be obtained through curve fitting and are presented in Table 4.3. The two correlations are fairly arbitrary mathematical fits to the data with no underlying physical meaning. It would be more desirable to correlate these parameters on a basis that enhanced our understanding of the systems but at present these correlations are deemed sufficient.

The comparison between the new model and the IFA and CFA experimental results are

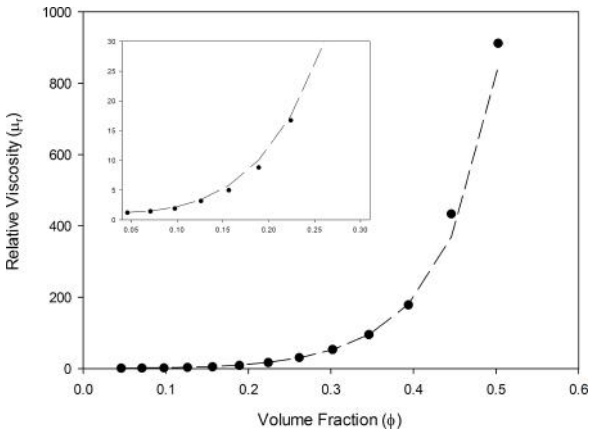

(a) CFA: $5s^{-1}$, RMSE = 29.72, R^2 = 0.998, APE = 7.91

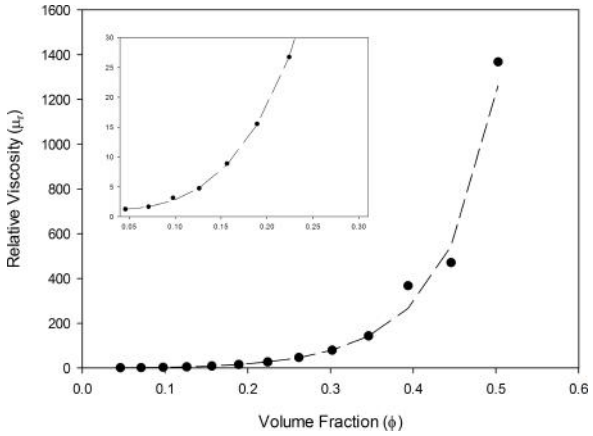

(b) IFA: $5s^{-1}$, RMSE = 51.79, R^2 = 0.989, APE = 5.78

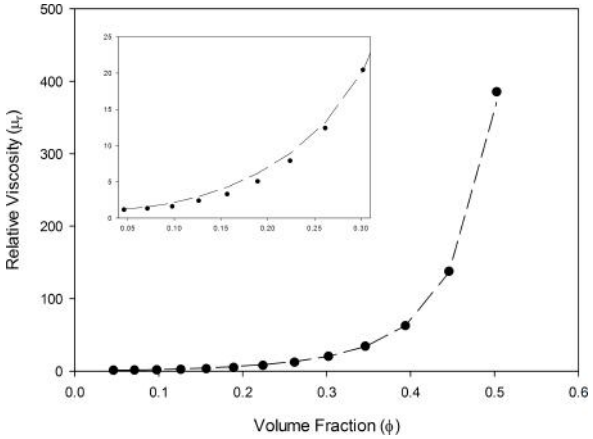

(c) CFA: $20s^{-1}$, RMSE = 4.58, R^2 = 0.999, APE = 12.41

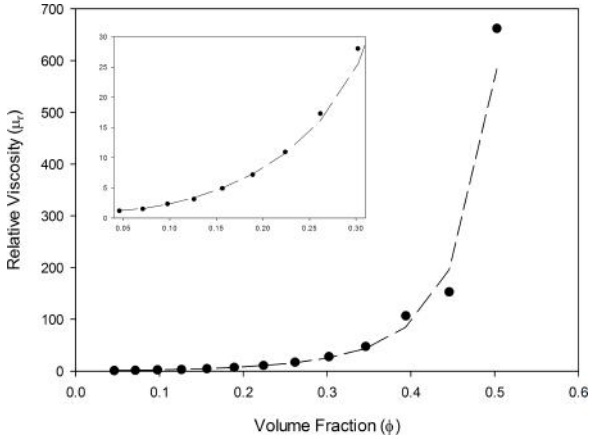

(d) IFA: $20s^{-1}$, RMSE = 29.06, R^2 = 0.989, APE = 8.71

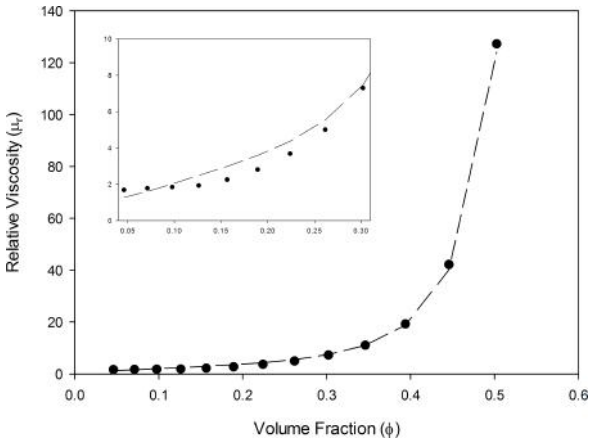

(e) CFA: $200s^{-1}$, RMSE = 1.30, R^2 = 0.998, APE = 13.49

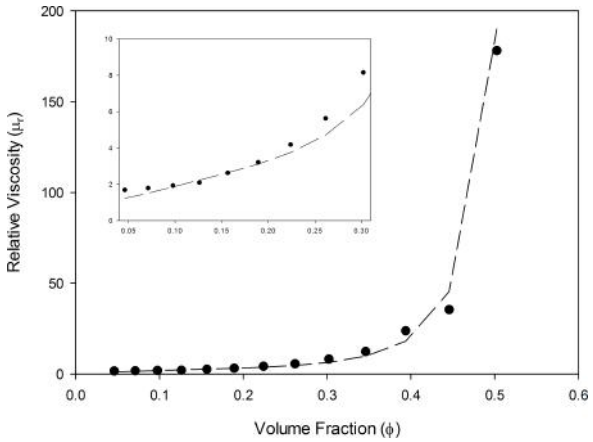

(f) IFA: $200s^{-1}$, RMSE = 5.32, R^2 = 0.996, APE = 14.13

Figure 4.10: Comparison of relative viscosity from experiment (•) and model (dashed line) as a function of slurry concentration at 5, 20, and 200 s^{-1}

Table 4.3: New model parameters

Model Parameter	IFA	CFA
b	68.41	70.023
c	4.4766	4.9734
d	11.278	11.431
e	7.5663	8.3421
f	1.359	1.6456

shown in Figure 4.10. The modelling results for both CFA and IFA fit extremely closely with experimental data over the range of suspension concentrations and shear rates studied. There is some deviation at both ends of the concentration spectrum, particularly with respect to $\phi = 0.45$ for IFA which, given that it occurs for all shear rates, would suggest it is an experimental error. Even small weighing errors at the higher suspension concentrations are magnified by the shape of the $\phi - \mu$ curve at this point, so this explanation seems reasonable. At the lower end of the concentration spectrum the deviation of model to experimental data can be explained by the back extrapolation to $\phi < 0.13$. As the infinite viscosities are obtained at these concentrations by applying the best fit of equation 4.2 to the lower concentrations even though the Sisko infinite viscosities for these values were not included in the analysis. This is an inherent weakness of the model. However, in general the model performs extremely well with $R^2 > 0.989$, and the APE < 14.13. This provides the confidence needed to use the model in the design and scale up of CFA processing equipment. The goodness of fit can also be visualised in Figure 4.11 which highlights the fact that all predicted data point lie well within plus or minus 50% of the experimental data. The expression could be substituted for viscosity in the Reynolds number in order to draw up a power curve for a mixer settler system using the Metzner and Otto definition of shear rate described in Section 5.4. In this way the model can be used to set design criteria for CFA processing plants. However this shear rate is only valid at the impeller as in the case of shear thinning suspensions, there sometimes exists a region of good mixing around the impeller known as *caverns* and regions further away from the impeller that are stagnant.

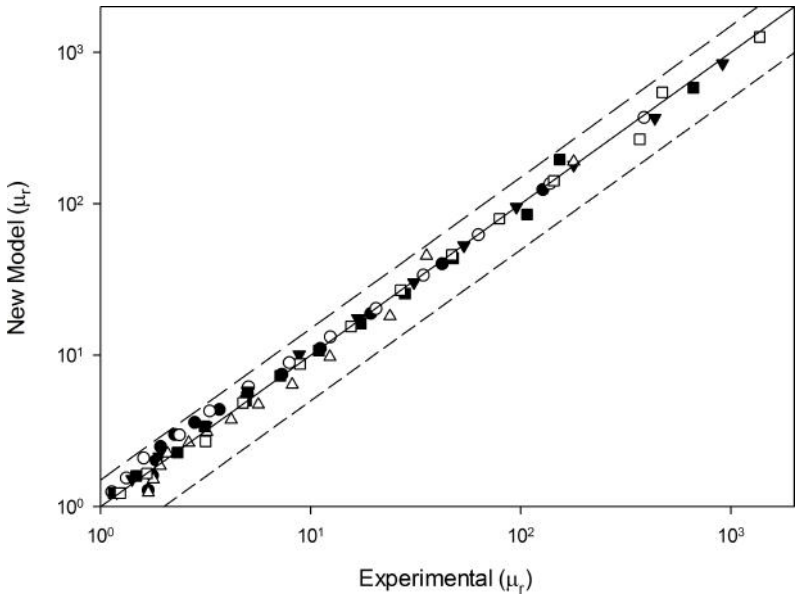

Figure 4.11: (Proposed model against experimental results: IFA at 200s^{-1} (△); IFA at 20s^{-1} (■); IFA at 5s^{-1} (□); CFA at 200s^{-1} (●); CFA at 20s^{-1} (○); CFA at 5^{-1} (▼). Solid line is y = x and dashed lines are plus or minus 50%

4.4 Conclusions

The rheological behaviour of a CFA sample and a processed IFA sample has been presented. The rheological data is highly dependent on the solids concentration. At volume fraction values of 0.05-0.08 the suspensions show little shear thinning and the onset of shear thickening was observed at a shear rate of 60 s^{-1}. At volume fraction values of 0.11-0.25 the suspension become shear thinning showing a typical power law type behaviour. At 0.29-0.43 the suspensions are highly shear thinning but also appear to display an apparent yield stress; the most concentrated solutions 0.48-0.54 also displayed this behaviour but to a lesser extent. The particle size of the suspension had a more pronounced effect on the viscosity than did the broadness of the PSD. This is thought to be due to a larger relative contribution of colloidal forces at low shear rates. A generalised modelling procedure has been proposed that consists of the following steps:

1. perform flow tests on a range of suspension concentrations,

2. model data with Sisko equation to obtain estimate of infinite shear viscosities,

3. fit infinite shear viscosity-concentration data to Kreiger Dougherty equation,

4. correlate Sisko coefficients m and n with concentration,

5. substitute expressions for infinite shear viscosity, m, and n back into Sisko equation to determine relative viscosity.

The proposed modelling procedure performed satisfactorily for both fly ash types and over all concentrations studied. This model is now suitable for further use in CFA processing equipment design.

CHAPTER 5

CENOSPHERE CONCENTRATE RECOVERY USING A STIRRED TANK

5.1 Introduction

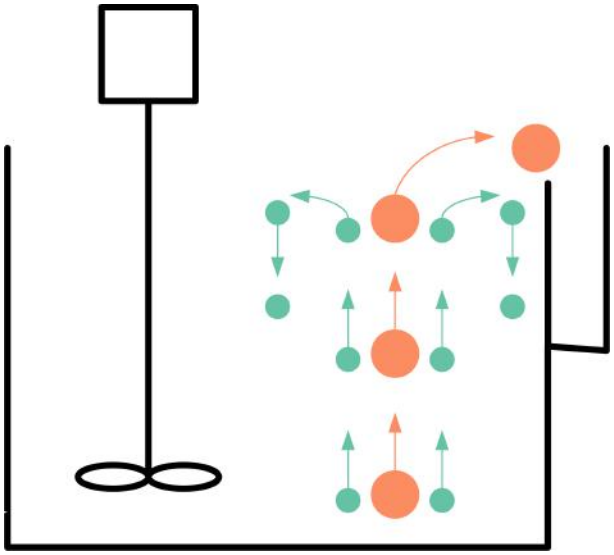

Figure 5.1: Simplified representation of Gale Common separator

There is a remarkable interest in the hollow micro-spheres that can be recovered from coal fly ash. The RockTron pilot plant at Gale Common operates a separation process based on the lightweight density of the cenospheres. Using water as a separating medium the cenopsheres have positive buoyancy and the remaining components of CFA have negative buoyancy. The equipment is essentially a mixing tank with an overflow weir

(Figure 5.1). A CFA slurry is mixed to a degree necessary to maintain off-bottom via an impeller. The cenospheres rise through the suspension and overflow into a collection tank. The impeller was originally designed to be located in the centre of the tank. After operating the tank in this manner the impeller was moved to an off-centre location in order to reduce the central vortex that was pulling cenospheres down from the water surface. There has been a significant problem in achieving optimum recovery of cenospheres from the existing design. One of the original objectives of this chapter was to scale-down the existing design into laboratory processes so that they can be better understood in order to give suggestions on how the design may be improved.

5.2 Scale-down

In this case the pilot scale design had already been built. Unusually then, there was a need to scale down to laboratory scale instead of the more usual scale up to pilot scale. Some scale up methods emphasize the geometric equivalence between the two systems under investigation. This requires maintaining a constant impeller geometry, as well as the impeller dimensional ratios (Impeller diameter/tank diameter (D/T), impeller blade/impeller diameter (W/D), impeller clearance/tank diameter (C/T), the slurry height/tank diameter ratio (H/T)), and the baffles employed [296]. The dimensions and general features of the design of the pilot plant are shown in Figure 5.2. The pilot plant was designed to operate on a continuous basis with slurry input at the bottom of the tank and taken off at a point opposite. The cenospheres were designed to overflow at a rate controlled by the differential between the inlet and outlet into an wash tank. The important dimensions are provided in Table 5.1. Laboratory #1 was specified to have a diameter of 0.5 m. Maintaining H/T and D/T, a new tank design was built in perspex. This tank was originally envisaged to be able to operate on a continuous basis with a feed tank and a collection tank. In order to establish if it was the H/T ratio that was not allowing good recovery of cenospheres a second laboratory scale tank was built with a diameter of 0.25m. This

second tank had no overflow weir and had an H/T ratio of 1.6 relative to the pilot plant which had an H/T ratio of 0.68. Drawings of all the tanks are provided in Appendix 1.

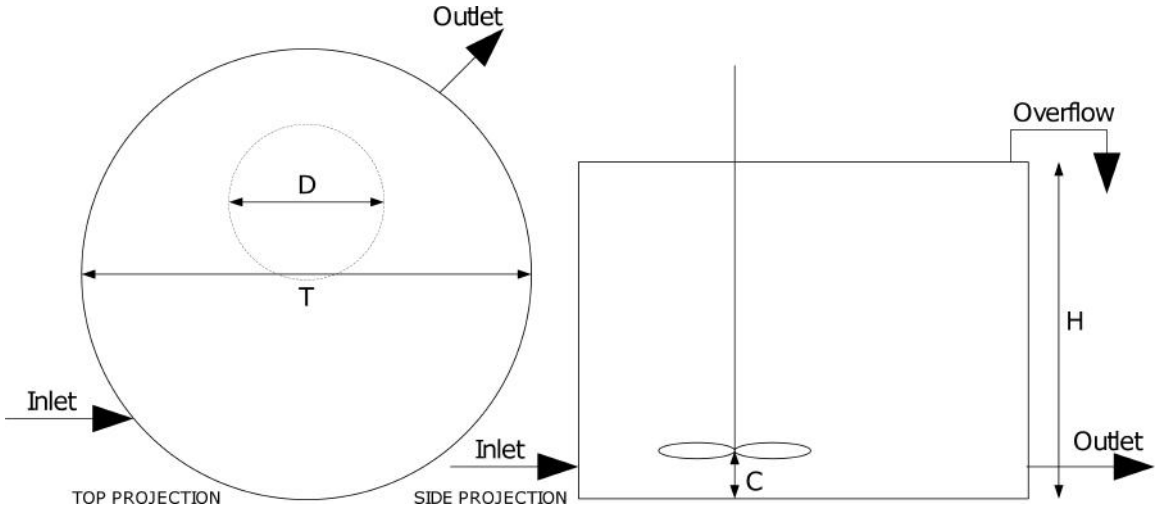

Figure 5.2: Schematic representing the key dimensions of the cenosphere separator design

Table 5.1: Dimensions of the tanks of three different scales used in this chapter

	Q (m^3/h)	V (m^3)	t_r (h)	H (m)	T (m)	D (m)	D/T	H/T
GC Pilot Plant	9	11.78	1.31	1.9	2.81	0.97	0.35	0.68
Laboratory # 1	na	0.07	na	0.338	0.5	0.173	0.35	0.68
Laboratory # 2	na	0.02	na	0.4	0.25	0.087	0.35	1.60

5.3 Continuous operation of Laboratory #1

Operation of Laboratory #1 on a continuous basis was intended to be possible through the use of a feed tank and two tanks for the overflow and tank outlet. The process was extremely problematic: it was difficult to keep the feed suspended; the CFA inventory required for high solids loading (> 30 wt%) was very large; the flow rate was difficult to measure as the slurry blocked the rotameter; the inlet tube distribution holes became blocked; the impeller speeds were not sufficient to maintain solids suspension. Whilst the other problems were solvable it was the last problem of maintaining solids suspension that proved the biggest obstacle. In order to achieve a steady state situation the process had

to be run for a considerable time. However it was found that over time, the outlet solids concentration was much lower than that in the tank. It was visually possible to observe significant accumulations of CFA, particularly in the region of the tank opposite to the offset impeller. It is likely that the problem resulted from the scaling down of the process. The impeller speed necessary for suspension in the pilot plant is lower as a result of the larger diameter of the impeller.

5.4 Semi-continuous operation of Laboratory #1

A different approach was used to assess the cenosphere separation performance of Laboratory #1. It was decided to run on a semi-continuous basis whereby pure water was pumped into the tank through the inlet, the outlet was blocked, and the overflow was collected. Briefly, the experimental procedure consisted of the following. A known mass of CFA was added to the tank and water was added to the level of the overflow. The initial cenospheres were removed by repeated stirring and settling operations. The cenosphere fraction was increased artificially by adding a known mass of 200 g cenospheres to the tank to yield cenosphere fractions of (1.0-3.2 wt%). The tank was mixed for a period of 10 minutes at 300 rpm and samples of the initial CFA slurry were taken to determine the solids concentration (via oven drying at 100°C) and cenosphere fraction (via sink float in a 250 ml separating funnel). The overhead mixer was then set to the designated speed, the timer was started, and a peristaltic pump was used to pump water at a rate of 250 ml/min. The overflow was collected in three vessels each corresponding to 10 minutes of the experimental run; they were filtered and dried in an oven at 100°C for 24 hours to calculate solids content. The dried cenosphere concentrate was mixed to ensure homogeneity and a sample was analysed for density. The concentrates for each time period were then mixed together and a sample was analysed for particle size distribution.

The process variables to be studied were mixing speed and solids concentration. Originally, a 2-factor face centred central composite experimental design was chosen to analyse

the process. This involved runs at the experimental conditions listed in Table 5.2.

Table 5.2: Run conditions for semi-continuous cenosphere separator

Run No.	Solids Loading (wt%)	Impeller Speed (rpm)
1	9.8	50
2	9.4	76
3	9.8	100
4	20.4	50
5	20.3	76
6	20.2	100
7	20.4	76
8	20.6	76
9	30.5	50
10	30.7	76
11	30.4	100

No statistically significant and meaningful models could be applied to the results obtained and so analysis in this way was not possible. However comparisons could still be drawn between individual run conditions.

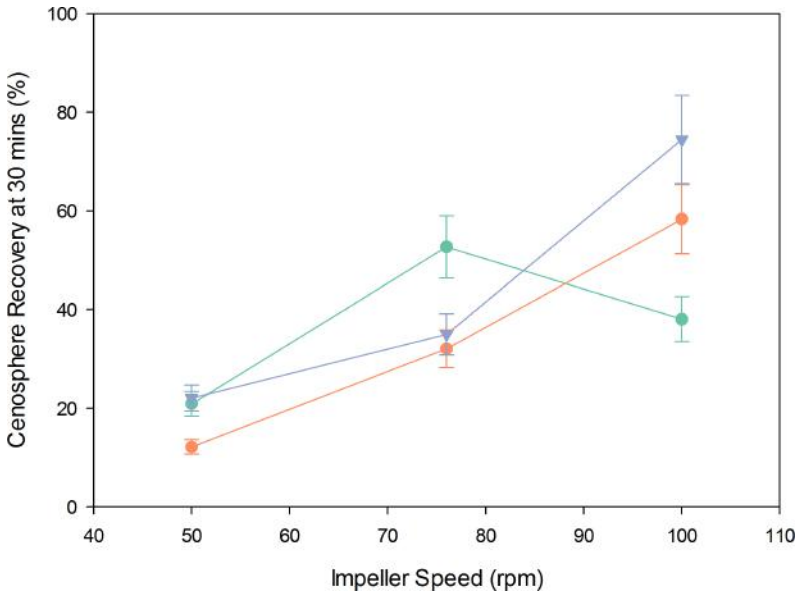

Figure 5.3: Recovery of cenospheres from semi-continuous laboratory #1 at different impeller speeds. Solids loadings were *ca.* 10 wt%(●), *ca.* 20 wt% (●), and *ca.* 30 wt% (▼)

With the limited data available there appears to be a difference between the effect of speed on a CFA concentration of 10 wt% to those of 20 and 30 wt% (Figure 5.3). The

effect of impeller speed on the higher concentrations is roughly linear with increased speed increasing the recovery. This is perhaps contrary to expectation, in that a faster speed should have the effect of pulling down more cenospheres. Indeed, at the concentration of 10 wt% there is a drop off in recovery between an impeller speed of 76-100 rpm. This implies that there is a critical impeller speed beyond which cenosphere pull down starts to retard recovery. The absence of this effect at the higher concentrations implies that this critical speed increases with concentration. The higher the solids loading, the slower the flow streams, and thus the ability to pull down cenospheres is lessened. Below this critical impeller speed the cenosphere recovery is positively correlated with impeller speed presumably because the faster the flow streams the greater the degree of separation between the particles and thus the faster the cenospheres are carried to the surface[1].

There does not appear to be any straightforward relationship between the solids loading and the recovery. At an impeller speed of 50 and 100 rpm a solids of loading of 30 wt% yields the best recovery while at the intermediate impeller speed of 76 rpm a 10 wt% solids loading gives the best recovery. This could be the effect of kinetics in that all the recoveries were calculated after 30 minutes of processing time. As the solids loading increases, so does the effect of other particles on the rise velocity of cenospheres, in effect increased solids content should reduce the rate at which the cenospheres rise due particle-particle interactions counteracting the effect of buoyancy difference. If the major mechanism transporting the cenospheres to the surface is the circulation due to the impeller then this might not have much difference. It also does not explain why, at all impeller speeds tested, a solids loading of 30 wt% is better than 20 wt%. There are two potential reasons for this. The first is that it is actually the reduction in settling velocity due to particle hindrance that increases the yield of the cenospheres because the cenospheres have a lower chance to become trapped by a layer of particles above them. The second is that the higher solids loading results in an increases suspension density which means that there is a larger effective density difference between the cenospheres

[1]observationally all speeds were below the minimum suspension speed

and the suspension which increased the rise velocity. The likelihood is that there is a combinatorial effect of all the mechanisms present which has obscured clear interpretation of them.

It has been shown in Chapter 4 that CFA slurries start to exhibit non-Newtonian, specifically shear thinning behaviour. In order to assess whether the cenosphere recovery results have been impacted by this an estimate of the Reynolds number has been made, treating the suspension as a pseudo fluid with an apparent density and a viscosity that is estimated using the empirical model also developed in Chapter 4. In order to estimate the viscosity the shear rate is required. The shear rate in the impeller region was given by the Metzner-Otto relationship [296]. In this case the value of K was taken to be 11.5 for the A310 impeller and N is the impeller rotational velocity.

$$\dot{\gamma} = \mathrm{KN} \tag{5.1}$$

When the recovery is plotted against the Reynolds number for the pseudo fluid in Figure 5.4, the 3 solids loadings are clearly demarcated and span a fairly wide range of Reynolds numbers from 5000-40000. At the lower end of the range this is close to the transition regime which would mean that there would be fewer turbulent eddies that could pull down the cenospheres. However, for the highest concentration the recovery is correlated with Reynolds number. This suggests that the fluid circulation around the tanks is responsible for an increase of the recovery kinetics; this is also determined by the solids loading. Past a certain Reynolds number the recovery kinetics do not play as important a role, and the turbulence of the surface starts to draw down cenospheres. The fact that there are clear differences in solids loadings when plotted against Reynolds number suggests more generally that the flow pattern is not the only mechanism for the differences that are observed. This is perhaps unsurprising given that the Reynolds number calculated represents that at the impeller and that near the surface of the tank the flow is likely to be far less turbulent.

Good separation of the cenospheres from CFA is reliant on a high purity product re-

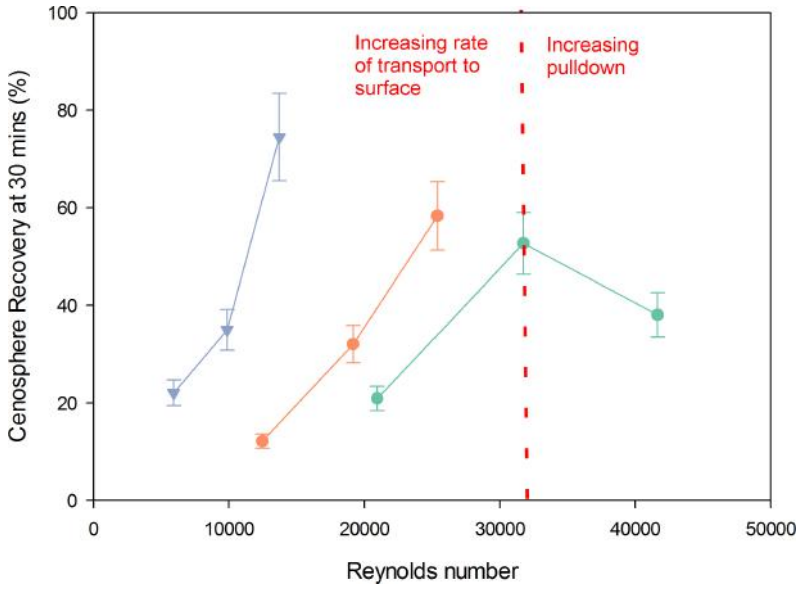

Figure 5.4: Recovery of cenospheres from semi-continuous laboratory #1 at estimated Reynolds numbers. Solids loadings were *ca.* 10 wt%(●), *ca.* 20 wt% (●), and *ca.* 30 wt% (▼)

porting to the overflow. The results for the experiments in terms of grade are different that those in terms of recovery (Figure 5.5). All three solids loadings that were investigated showed relative differences between impeller speeds. Speculatively this might be the result of the solids loading shifting the grade curves along the speed axis, but there are not sufficient data to confirm this observation. At a solids loading of 10 wt% the grade progressively decreases in a seemingly linear fashion. This suggests that as the speed increases more of the negatively buoyant CFA particles are lifted into the overflow with a corresponding decrease in the cenosphere grade. For the intermediate concentration of 20 wt% the grade is flat between 50-76 rpm, but then drops dramatically between 76-100 rpm with a steeper gradient than that observed for 10 wt%. For 30 wt% the grade is relatively flat between all 3 impeller speeds. Using the foregoing, and observations made during processing, it is postulated that at a certain solid loading there exists a formation of an interface between suspended solids and a clear low concentration region. The formation of this interface is dependent on both impeller speed and solids concentration [297]. For certain combinations it exists and the grade is extremely high as cenospheres are able to rise through a very small layer of clean water to the overflow. When either the solids

loading is too low, or the impeller speed is too high it does not exist and the cenosphere grade is very poor because the overflow fills with suspended heavy CFA particles.

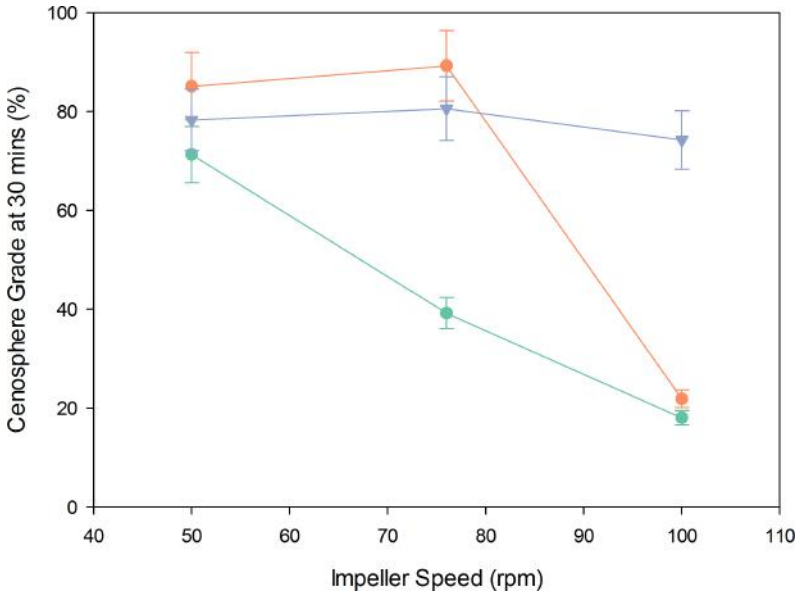

Figure 5.5: Grade of cenospheres from semi-continuous laboratory #1 at different impeller speeds. Solids loadings were *ca.* 10 wt%(●), *ca.* 20 wt% (●), and *ca.* 30 wt% (▼)

It has been shown in chapter 3 that low density particles tend to be larger than high density particles. A relationship between the average particle size and the cenosphere grade is apparent in Figure 5.6. A relatively good correlation is observed that shows a positive linear relationship between the cenosphere grade and the particle size. This suggests that when cenosphere grade is poor at higher impeller speeds, the displaced heavy CFA content is predominantly small in nature. The displacement of particles of heavy particles is only possible when they do not have a sufficiently high settling velocity to overcome the upwards flow imparted by the impeller: *i.e.* when the particles are very small. This manifests in d_{50} particle sizes for low grades of between 10-30 μm. Given that the particle sizes at a high purity are *ca.* 100 μm this suggests that the heavy component of low grade particles is considerably smaller even than the average size. This actually suggests a possible mechanism for control of a separator tank, as measuring particle size online is relatively easy. The separator tank impeller speed could be controlled by an overflow particle size set point to automatically reach the best impeller speed for

separation.

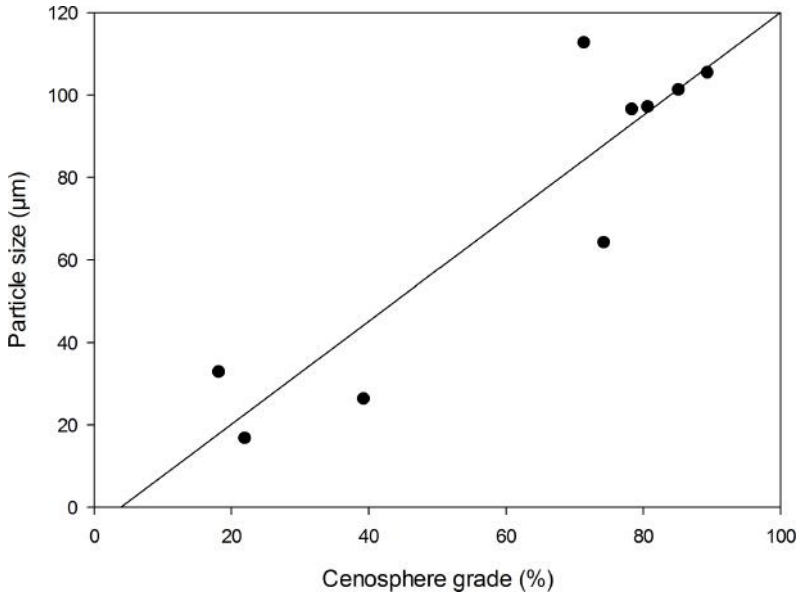

Figure 5.6: The grade of the cenospheres correlates fairly well with the d_{50} particle size

5.5 Minimum suspension velocity of CFA in Laboratory #1

Solid liquid mixing in industrial processes has a variety of objectives. In many of these operations the key objective is to make all of the surface area of the solids available for mass transfer. The power consumption of an impeller increases with the cube of the speed of that impeller and therefore it is desirable to only just satisfy the objective of maintaining all solids in suspension [298]. Zweitering defined a condition he named the just suspended speed N_{js}: the speed of the impeller where no particles remain stationary on the bottom of the tank for more than 1 or 2 seconds [276]. Zweitering also provided a purely empirical correlation for N_{js} that uses the solid and liquid densities ρ_s and ρ_l, the liquid viscosity μ, the particle diameter d_p, the impeller diameter D, the solids loading X, and a constant S that accounts for the tank geometry.

$$N_{js} = S\left(\frac{g(\rho_s - \rho_l)}{\rho_l}\right)^{0.45} \frac{X^{0.13} d_p^{0.2} \mu^{0.1}}{D^{0.85}} \tag{5.2}$$

The same objective can be applied to the current situation. By keeping all the CFA particles in suspension, the regions of very concentrated CFA that result from settled layers and impede cenospheres rising to the surface are eliminated. Although the objective is similar, the criterion according to Zweitering is conservative in terms of design for this case. It is not necessary to ensure all particles are off-bottom for no longer than 1-2 seconds. Cenospheres' progress to the surface are not likely to be hindered if particles rest on the bottom of the tank for longer periods. Indeed as long as there is no obvious bed formation then cenospheres are unlikely to be unduly hindered. This makes the experimental observation of N_{js} easier as this point can be observed from the side of the tank as the impeller speed is reduced. Following a similar approach to that used by Wu, Nguyen and Graham [299], the minimum suspension speed is defined as the point when the settled particle bed height is just not yet visible when reducing impeller speed from that above.

The minimum suspension speeds were determined by mixing a known solids loading at 500 rpm for 15 minutes to ensure homogeneity. The impeller was moved from an off centre position to a central location. The impeller speed was then reduced in intervals of 10 rpm to find a crude measure of N_{js} as described above. For each speed interval a period of 2 minutes was deemed sufficient to examine whether sedimentation was occurring. The experiment was then repeated using an interval of 4 rpm. A series of impeller clearances and concentrations were examined.

The minimum suspensions for the large laboratory tank are much larger than the operating speeds for semi-continuous operation (Figure 5.7). This means that the results for the semi-continuous operation have to be balanced against the fact that cenospheres were rising against a settling bulk of CFA. This is not representative of ideal continuous operation. The Zweitering correlation is usually limited to low solids loadings and unimodal slurries. However, in the current case the Zweitering predictions were drawn for each value of impeller clearance by calculating the value of S in Equation 5.2 for each solids loading and then using the average value. The predictions are relatively good and

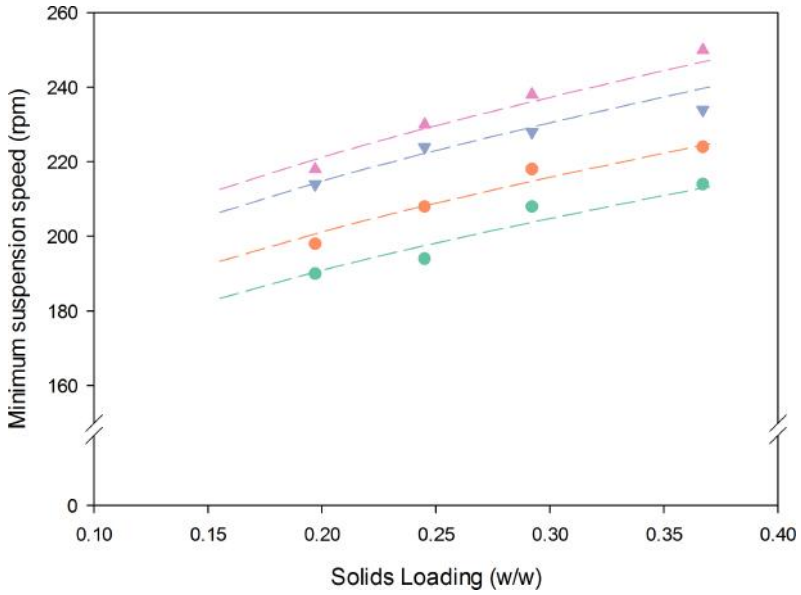

Figure 5.7: Experimental determination of minimum suspension speeds at different impeller clearances: C/T = 0.1 (●), 0.2 (●), 0.3 (▼), and 0.4 (▲). Dashed lines represent the Zweitering correlations.

certainly good enough for the current situation. The solids properties that were used, were the average values for the CFA, in this case a density of 2260 kg/m^3 and a diameter of 35 μm. There are two things that are noteworthy from both Figure 5.7 and Equation 5.2. The first is that speed needed to maintain CFA in suspension for this particular tank geometry rises as the solids loading is increased. The second is that as the impeller is raised from the bottom of the tank the impeller speed required to suspend CFA particles also increases. This kind of dependence of impeller clearance on N_{js} is not directly accounted for in the Zweitering correlations, but manifests itself in differing values of S. This behaviour has been documented previously although the dependence of S on C/T is complex and dependent on impeller type, particle type, and how close the impeller is to the bottom of the tank [298, 300]. In the current case it is shown in Figure 5.8 that the relationship between S and clearance is correlated very well with a linear dependence. This was also reported previously for A310 impellers, but in that case a wider range of particle type were analysed. This suggests that although it is possible to use the current findings for the CFA investigated, it is not necessarily the case that the same relationship will be shown for other CFA types.

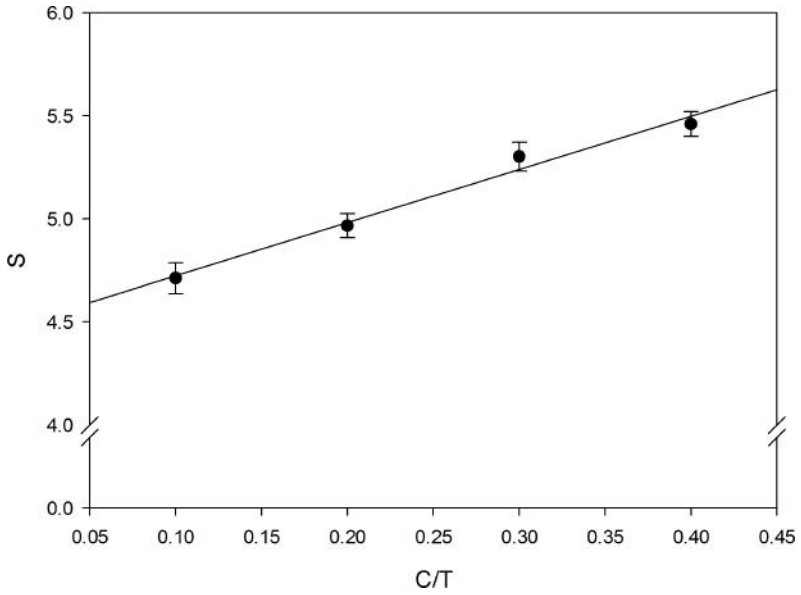

Figure 5.8: The dependence of the Zweitering constant S on the impeller clearance. Error bars represent standard deviation of values obtained for each solids loading. The line is a linear regression and has a correlation coefficient of over 0.99

5.6 Effect of scale and CFA type on minimum suspension speed

In order to assess the effect of scale, and to reduce the CFA inventory required to perform experiments, the second laboratory scale separator tank was built. The second tank had an increased height relative to width for reasons that will be discussed later. Owing to material constraints a different CFA type was used. The bulk properties used in the Zweitering correlations were changed to 2300 kg/m^3 and 25 μm to reflect this. However, the minimum suspension speed experiments were performed in exactly the same manner as for the large scale experiments *i.e.* the tank was only partially filled. Using the same values of S as those determined for the laboratory #1 setup, the Zweitering correlations are shown alongside the experimentally determined values as shown in Figure 5.9. The predictions are relatively good at impeller clearances of 0.3 and 0.4. At impeller clearance of 0.1 and 0.2 the predictions are less good and the prediction from the larger scale over-predicts the minimum suspension velocity than that is observed experimentally. This is not unexpected given that the Zweitering correlation is known not to perform that well at

higher solids loadings with polydisperse particles. The A310 impeller is also not designed to be operated in the lower clearance regimes and this might be a contributing factor [298]. What is interesting is that this effect is more pronounced at lower impeller clearances which suggests that the distance the slurry has to flow from the impeller region to the tank bottom is a determining factor in how the minimum suspension velocity behaves at different scales. Overall the result suggests that with appropriately conservative design factors used, the Zweitering correlations for impeller type and geometry may be used to estimate the speed necessary for suspension at larger scales if the bulk properties of the CFA in question are used.

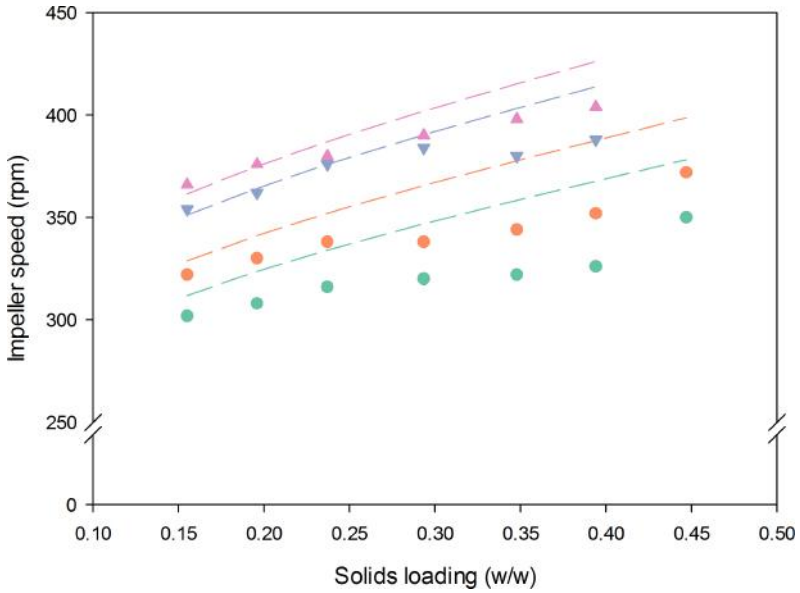

Figure 5.9: Experimental determination of minimum suspension speeds at different impeller clearances: C/T = 0.1 (●), 0.2 (●), 0.3 (▼), and 0.4 (▲). Dashed lines represent the Zweitering correlations.

5.7 Cloud Height of CFA slurry

To achieve a good grade of cenosphere it necessary to ensure that none of the heavy particles are entrained into the cenosphere overflow. One way of achieving this is to operate the tank with an interface between the CFA slurry and a zone of relatively low

concentration[1]. If the separator can be operated with this clear zone present, then a almost pure cenosphere product can be obtained.

5.7.1 Method to determine cloud height

The cloud height was determined at a solids loading of 38 wt%, a fill level of 0.3 m, a series of C/T values from 0.083-0.2 and a series of values of impeller speed above that which CFA particle begin to sediment. The CFA at each condition was mixed at 500 rpm for 30 minutes before turning down the impeller speed to a set value. The tank was left to reach a steady state before a Olympus PEN EP1 camera with a fixed 20 mm pancake lens was used to record video of the tank for a period of 5 minutes. The video frame rate was re-sampled from 30 per second to one per second using freeware called VirtualDub and saved as a series of images. The series of images were then loaded as an image stack into the image analysis software ImageJ. Figure 5.10 illustrates the steps that were then taken. In a batch manner part of the image was selected and then cropped to that selection. It was then converted into an 8 bit image which meant that each pixel is given a value of 0-255 that depends on the intensity *i.e.* how light/dark it is. A custom script was written that treated the picture as an array of values between 0-255. The interface was determined by averaging the values in each pixel row. An algorithm then searched the row averages for the maximum difference between adjacent sets of 3 pixels and this was then defined as the interface height. The interfaces were calculated 300 times for each second in a period of 5 minutes and the standard deviation of the interfaces gives a measure of the stability over that time period. The macro code is provided in Appendix 2.

In order to compare between different impeller clearances the cloud heights were plotted against the impeller speeds normalised by the speed required for suspension. The values of N_{js} were estimated by the Zweitering correlations. However the values for S were estimated using a linear regression line to the experimental values obtained for Lab-

[1]this zone always has some residual ash particles but for practical purposed is considered pure liquid

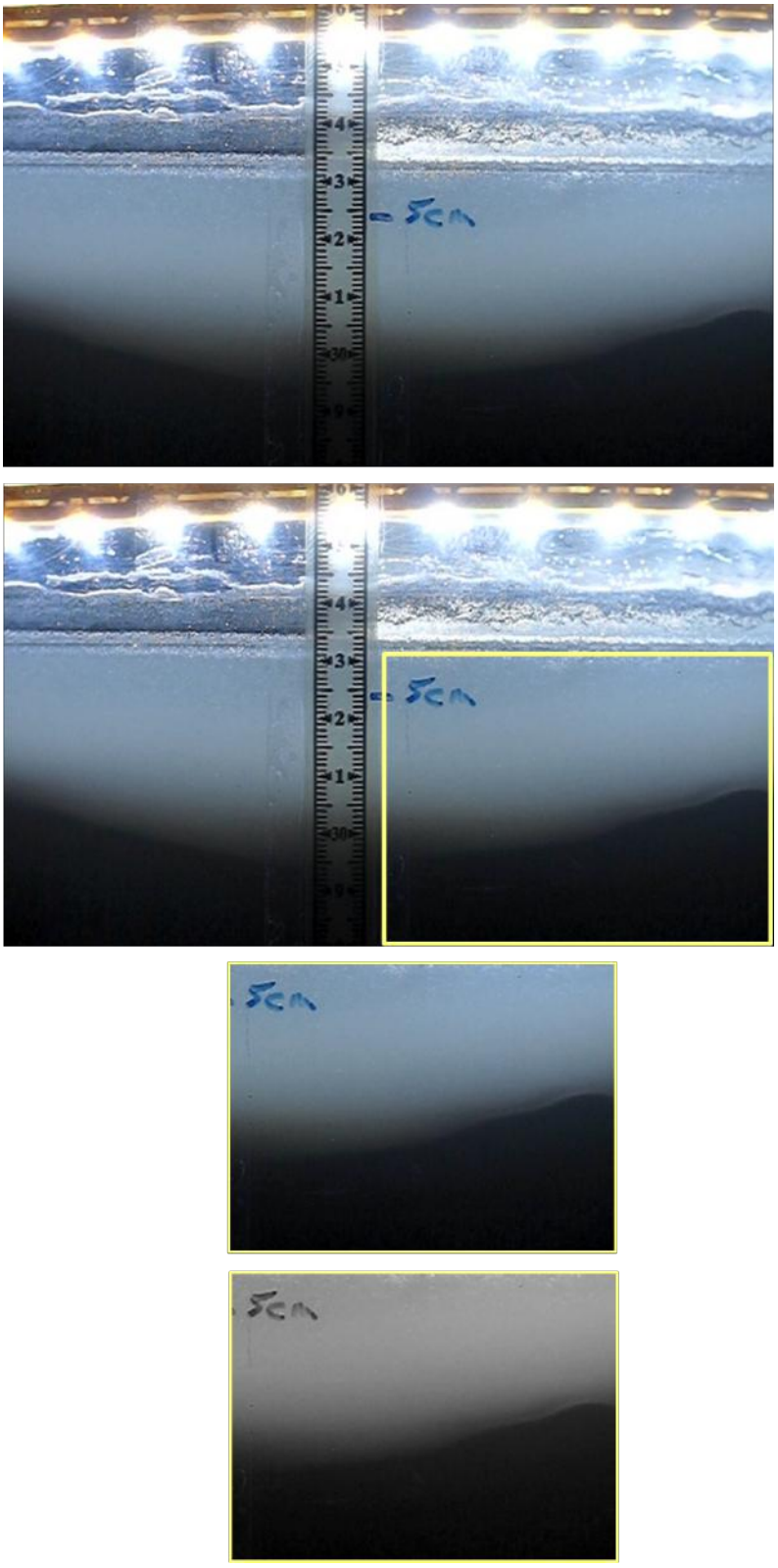

Figure 5.10: Sequence of image manipulation from cloud height videos

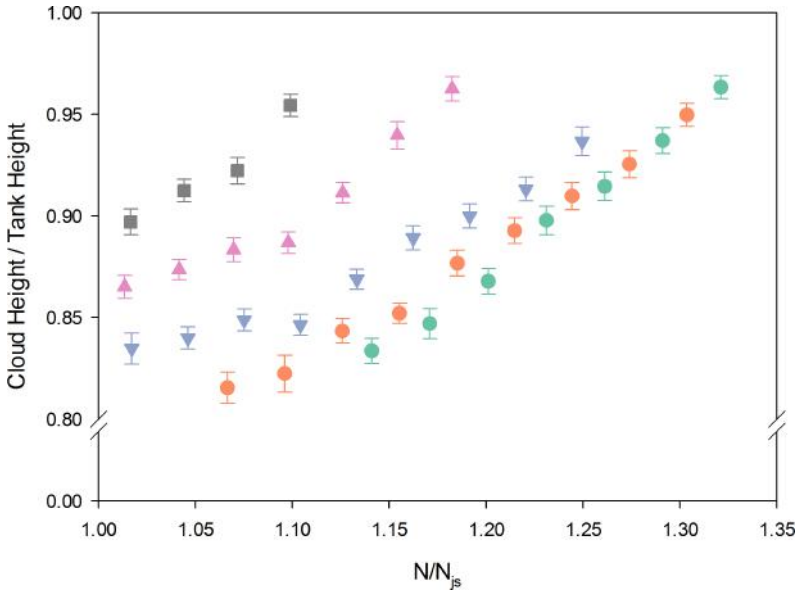

Figure 5.11: Cloud height dependence on impeller speed and clearance from the tank bottom: C/T = 0.083 (●), 0.1 (●), 0.125 (▼), 0.167 (▲), and 0.2 (■)

oratory Tank #2 rather than those from Figure 5.7. Figure 5.11 highlights how the cloud height changes with impeller speed and clearance. There is a clear relationship between impeller speed and cloud hight with an increase in speed able to propel the particles in the suspension to a higher interface. This seems directly related to the speed at which the impeller rotates which transmits this energy to the particles. The particles' velocity then decays with distance from the impeller until the particle velocity is equal to the terminal velocity of the particle, or in this case the hindered settling velocity. It follows then that the higher the starting velocity of the particle, the further the particles on average can travel and hence the higher the interface. The effect of the impeller clearance is not as straightforward. Bittorf and Kresta [297] outlined a relationship between cloud height and the dimensionless impeller speed.

$$CH = \frac{N}{N_{js}}\left[0.84 - 1.05\frac{C}{T} + 0.7\frac{(D/T)^2}{1-(D/T)^2}\right] \tag{5.3}$$

They verified this for a series of conditions with both their own experimental results and those of other researchers. However, the results presented only appeared to encompass a C/T value of 0.25. It is clear from Equation 5.3 that the cloud height is expected to

decline with increasing impeller clearance. The explanation is provided in the justification for the mechanistic equation. The cloud height is determined by the velocity of the jets that travel up the baffles. The results that are presented in Figure 5.11 contradict this relationship. It must be noted that they are strictly outside the stated bounds of validity in the respect of the height of the cloud. However, it does not seem likely that this could reverse the relationship. The experimental result presented here show a clear trend in the opposite direction; the cloud height increases with increasing impeller clearance. It is very interesting to note that the same effect has been noted previously by Hicks *et al.* [301], who also commented on the counter intuitivity of the observation although they provided no explanation. It might be argued that the impeller clearance are extremely low and this has caused deviations in the flow patterns described in Bittorf and Kresta's work [297]. However, Hicks *et al.* [301], carried out experiments with C/T of 0.4 and this effect was still observed. The disparity is worthy of further investigation, but it would be beneficial to use a material that is less polydisperse in nature.

A more general feature of Figure 5.11 is that, with an increase in the ratio of the tank height to diameter, it is possible to operate the impeller at a speed above that needed for suspension but below that required to produce a cloud height above that of the tank overflow. This is informative when designing a cenosphere separator.

5.8 Drawdown of cenospheres

A discussion of the separation performance of a mixer settler system for the separation of cenospheres is not complete without considering the effect of the impeller/tank geometry on the drawdown of solids that are floating on the surface of the tank. Excessive drawdown will impair separation performance by increasing the residence time of cenospheres in the tank and increasing the probability that they will be entrained by the underflow.

For quiescent systems a single particle at the interface between a denser liquid and air stays at the surface if the combined buoyancy and surface tension forces are larger than

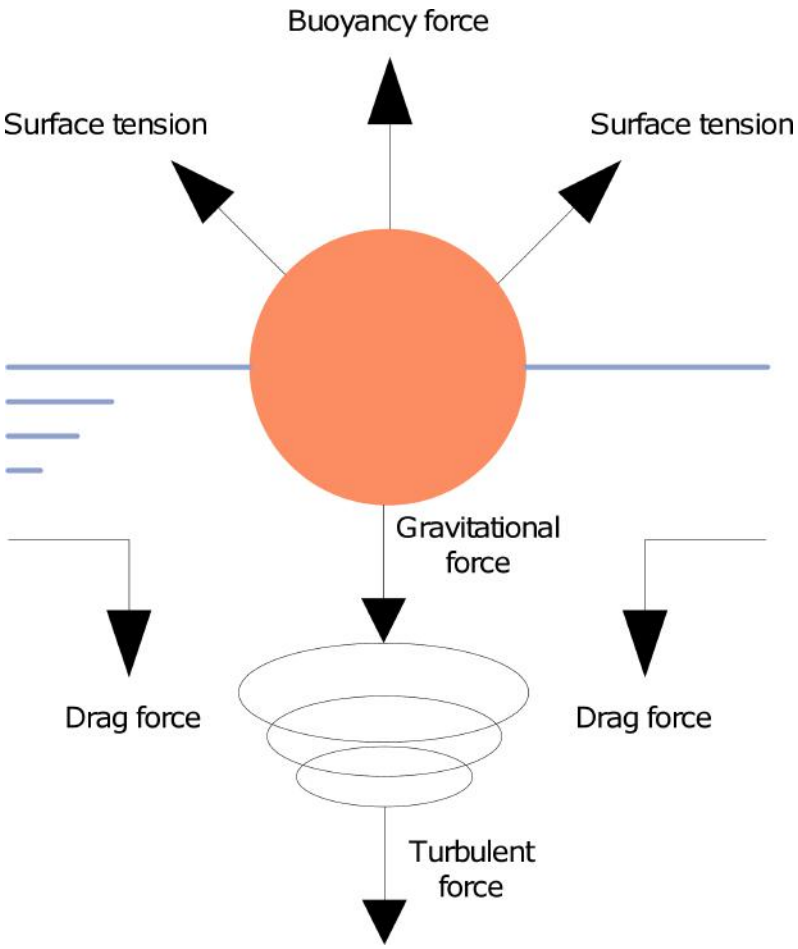

Figure 5.12: Forces operating on a buoyant particle when at the interface of a heavier liquid. After Khazam and Kresta [302]

the gravitational force [302]. Once the tank is agitated with an impeller, the fluid beneath the surface is in motion and two additional forces are present: the mean drag force due to fluid flow and the dynamic forces that result from turbulent velocity fluctuations and meso-scale eddies.

In an analogy to the concept of the minimum speed for full solids suspension, a just drawdown speed N_{jd} is defined as the speed required to drawdown all of the solid particles from the surface with particles only staying at the surface for periods of 1-2 seconds. This criterion is not directly applicable to the case of cenosphere separation. It represents a situation that is not desirable for cenosphere separation where a more suitable limit would be the case of the first cenospheres beginning to be drawn down from the surface. However, the traditional N_{jd} has been studied previously albeit not extensively. The first and still one of the only attempts at correlating the speed required for drawdown of solids and tank parameters was provided in 1977 in terms of the Froude number at just drawdown speed [303].

$$\mathrm{Fr}_{jd} = \frac{N^2 d}{g} = 3.6\mathrm{x}10^{-2} \left(\frac{d}{D}\right)^{-3.65} \left(\frac{\Delta\rho}{\rho_l}\right)^{0.42} \tag{5.4}$$

The correlation was tested with corks between 2-10 mm in size and of two different densities. Equation 5.4 reflects the finding that the density difference between solid and liquid is important, but the size of the particle does not appear to have any effect. Whether these findings hold at the lower size range that the cenospheres occupy is not clear, but it does at least provide a starting point from which to explore at what speed the cenospheres start to become entrained in the tank flow. The predicted values for complete drawdown of cenospheres are presented in Figure 5.13 as a function of the density of solids for the three different tank scales. The effect of increasing scale seems to flatten out the effect of the cenosphere density. This has implications for larger scale devices as it suggests that from a pull down point of view, cenosphere separation should not be affected by the proportion of denser spheres. It also suggests a region that should this type of tank should be operating in. For the heaviest spheres, nominally given here as 975 kg/m^3 the

N_{jd} values for the pilot scale, laboratory #1, and laboratory #2 are 170, 400, and 525 rpm respectively. These compare to N_{js} values[1] of 50, 204, and 390 rpm for the pilot scale, laboratory #1, and laboratory #2 respectively.

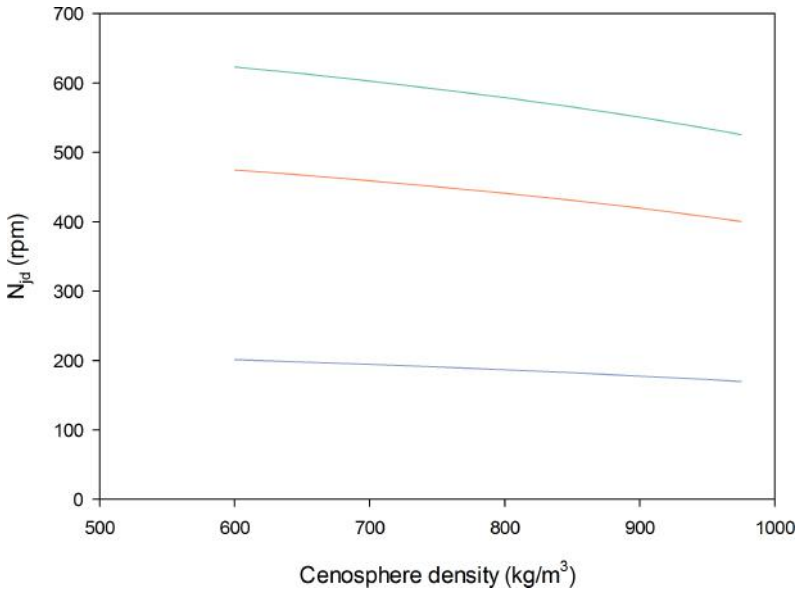

Figure 5.13: The predicted values of N_{jd} for impeller/tank configurations of GC pilot —, Laboratory #1 —, Laboratory #2 — at a solids loading of 38 wt%

The particle size of the cenospheres was too fine to enable accurate visual observation of the solids drawdown speed. An attempt was made to observe the speed at which the first cenospheres were pulled down, but any quantitative comparison between conditions proved to be impossible. Instead a qualitative description of what happened as the speed of the impeller increases is given in Table 5.3. Laboratory #2 tank was filled with distilled water only to a level of 24 cm. A batch of cenospheres were size fractionated and the size fraction between 106-125 μm was retained and subjected to a sink float in water and then a sink float in absolute ethanol. This resulted in a tight size distribution and particles with a density in the region 789-1000 kg/m^3. 5 grams of cenospheres were added to the tank and this was sufficient to ensure a multilayer covering. The tank was agitated at 500 rpm for 2 minutes and then the particles were allowed to settle. The agitator speed was then increased at a speed of 10 rpm per minute and the cenosphere layer was observed

[1]based on fitting the S values to the smallest tank for C/T = 0.3

from above and beneath the surface. Other impeller configurations and different sizes of cenospheres were also examined, but no discernible differences in pattern from Table 5.3 were observed that could distinguish quantitatively between them. What the results do show is that up to the speed of 200 rpm, the cenospheres are pulled down from the surface largely by turbulent eddies and a certain amount in a vortex close to the impeller. However, the baffling of the tank aids in the prevention of this vortex from occurring. It is hard to compare these results with the N_{js} values because in this case the solids loading was practically zero. Therefore the flow regimes of the tank operating only with water are more turbulent compared to those with 38 wt% solids. Extrapolation of the Zweitering correlation predicts that at low solids loadings the N_{js} value at the same tank configuration is *ca.* 189 rpm. This allows the very tentative case to be made that when operating the tank at minimum suspension velocity a similar pattern of cenosphere drawdown might be observed. Even at this level, a portion of the cenospheres are continually pulled from the surface which will both increase residence time in the tank and increase the probability of entrainment in the underflow.

5.9 Comment on existing design

The preceding has shown that it is very hard to reconcile two competing objectives in the mixer settler tank. Namely that, in order to achieve a satisfactory off bottom suspension, it is required that the suspension be agitated at speeds that start to entrain cenospheres in the tank bulk flow. This is problematic as in continuous operation, if cenospheres are entrained in the bulk flow then they are likely to exit the tank with the underflow. Although it has been shown that by increasing the tank height to tank diameter ratio will allow the formation of an interface and hence a clean cenosphere product will be formed, the entrainment of the cenospheres will reduce the total recovery. As such, because the cenospheres are a high value low volume constituent of the CFA, the existing design with

Table 5.3: Qualitative observations of cenosphere behaviour with impeller speed increase H/T

Impeller speed (rpm)	Observations
10	Consistent unbroken cenosphere layer
20	Layer thinning near impeller
30	Concentric circle of thinner layer near impeller
40	Particles largely static apart from near impeller
50	
60	
70	Faster movement of particle in impeller region
80	
90	
100	
110	
120	Breaks in surface appear
130	Frequency of surface breaks increases
140	Lateral particle movement
150	Some individual particles pulled down next to impeller
160	Surface eddies pull down multiple particles
170	Surface eddies increase in regularity
180	
190	Some particles consistently submerged near impeller
200	

modified aspect ratio can not be recommended.

5.10 Design based on Thickener Principles

5.10.1 Settling of concentrated CFA slurries

Moving away from the existing design concept prompted the proposal of a different separator design. Although conservative it should not encounter operational issues that have plagued the existing design. The proposed design would essentially be a thickener. However, the aim of this tank is not to increase the CFA suspension density by a large amount, but to allow the cenospheres to rise through the suspension unimpeded by the suspension. In order to provide the settling data for such a device a series of settling tests were undertaken in a 1 L graduated cylinder. Known concentrations of suspensions of CFA-3 were prepared and mixed thoroughly in the cylinder before being allowed to settle. The interface between suspension and clarified water was tracked over time. The experiments

were performed in triplicate and the averages were taken. The settling velocity was calculated over the initial straight line section of the settling curve and plotted in Figure 5.14. The settling velocity exhibits an exponential decay which is typical of zone settling systems. The two parameter model originally proposed by Veslind has often been used to describe the settling behaviour of concentrated systems [304] [1] .

$$U_s = a\mathrm{e}^{-b\phi} \tag{5.5}$$

The two parameters are essentially model fitting parameters, but if there is physical significance to the model then the parameter a should be equal to the settling velocity at very low concentration. However, because of the heterogeneity of the suspension even this has little physical significance as it is unclear which particle diameter and density is representative of the whole. It is clear, however, that over the range of suspension concentrations studies herein the Vesilind model accurately describes the settling behaviour and so for this purpose it is deemed satisfactory.

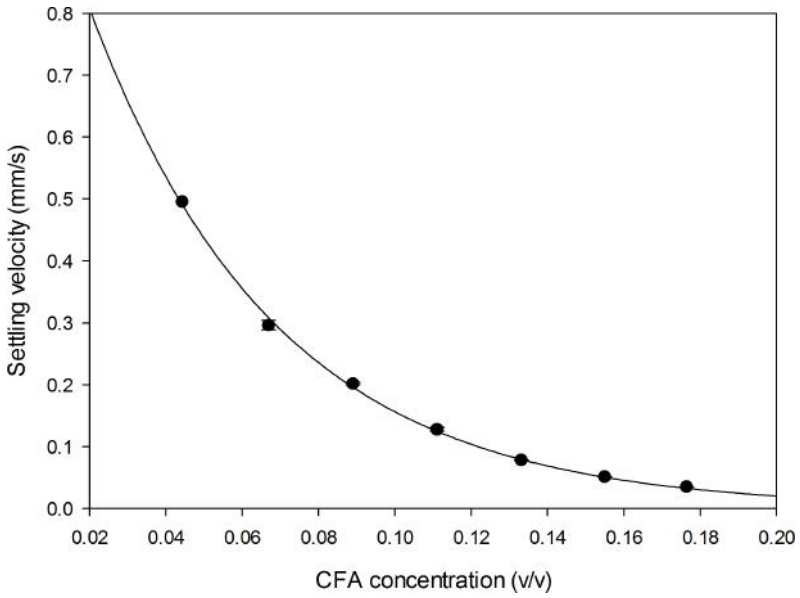

Figure 5.14: Settling velocity of different initial concentrations of CFA. Trials were conducted with the natural concentration of cenospheres present immediately floated to the surface. The solid line is a regression to Equation 5.5: $U_s = 1.217\mathrm{e}^{-20.51\phi}$

[1] The data would also have been fitted well to the Richardson and Zaki equation from which a settling velocity typical of the suspension could have been calculated

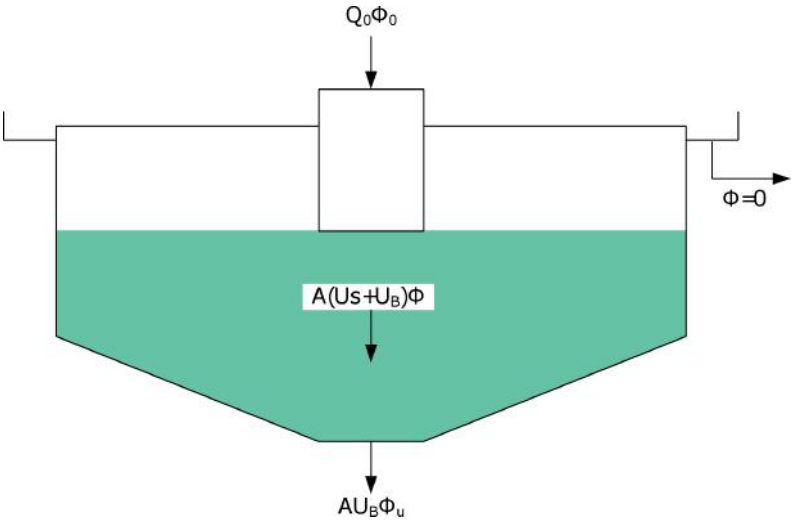

Figure 5.15: Schematic of a macroscopic balance on a continuous thickener

In order to design the thickener the century old principles first espoused by Coe and Clevenger are followed [305, 306]. It is assumed that a hindered settling zone will form in the thickener with the feed concentration and the minimum handling capacity. *A priori* the concentration of this zone is not known so the design method relies on a macroscopic balance at different suspension concentrations. At this point it is assumed that the buoyant particles play no part in the balance therefore the thickener must be able to handle the entirety of the feed solids through the underflow. Thus 3 different equations for the solids flux through the thickener in the feed, somewhere in the hindered settling zone, and in the underflow can be written. The density can be cancelled from each equation and thus the flux, N is expressed in the units of m/s. A is the cross sectional surface area of the tank, U_s is the hindered settling velocity, U_B is the bulk underflow velocity and ϕ is the volume fraction of the solids in the feed and underflow (subscripts 0 and u respectively).

$$N = Q_0\phi_0 \tag{5.6}$$

$$N = A(U_S + U_B)\phi \tag{5.7}$$

$$N = AU_B\phi_u \tag{5.8}$$

By substituting Equation 5.6 into Equations 5.8 and Equation 5.7, rearranging Equation 5.8 in terms of the bulk underflow velocity U_B and substituting into Equation 5.7 the Coe and Clevenger equation is obtained. The settling velocity function as determined in Figure 5.14 is substituted into the Coe and Clevenger equation to allow the minimum area determination as a function of the concentration.

$$A = \frac{Q_0\phi_0}{1.217e^{-20.51\phi}}\left(\frac{1}{\phi} - \frac{1}{\phi_u}\right) \tag{5.9}$$

The design basis for the thickener is for 5 t/hour at 18 vol.% meaning that the feed flow is 12 m^3/h. The feed is thickened to 20 vol%. Substituting these values at intervals between the feed concentration and the underflow concentration allows the area to be evaluated that is required to transmit the solids flux at these concentrations; it is shown in Figure 5.16. From this plot the maximum value of the area is taken to provide the thickener area required. A relatively small thickener plan area is required to cope with 12 m^3/h of feed on the basis specified. This corresponds to a thickener diameter of 3.7 m assuming that a circular cross section is required.

The question remains as to what happens to the low density particles. Theoretically the thickener should make a density split at the suspension density that arises from the concentration of the constant concentration zone that exists in the thickener [306]. For the conditions specified this corresponds to a density split between 1234-1260 kg/m^3. This might sound like an undesirable option, but actually this would double the cenosphere yield and provide an average cenosphere density of around 1000 kg/m^3. This would allow an easier sink float separation on water if floating particle are desired or they could be sold as a low density filler for metal alloys, plastics, or cement to reduce weight. The drawback to this design is that it takes a relatively large plan area, but more importantly there is a requirement to separate the cenospheres from a low volume fraction (*ca.* 8 vol.%) flow

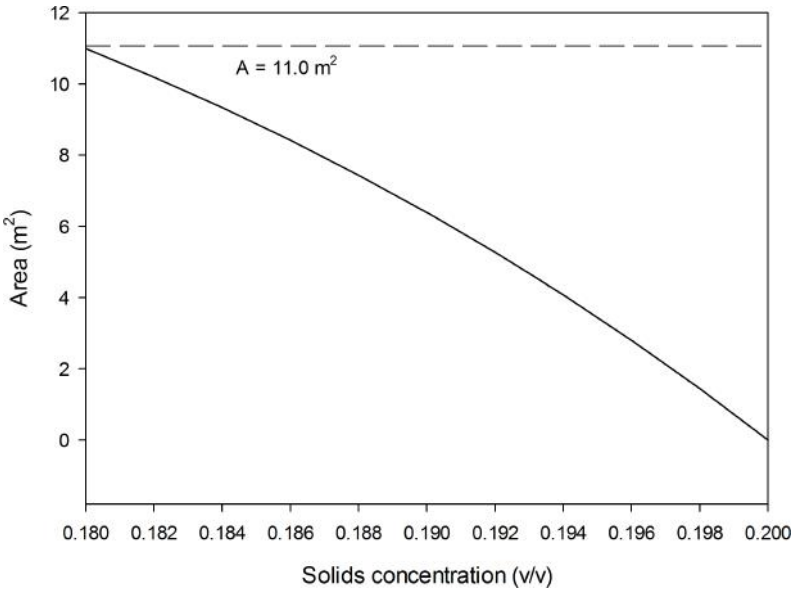

Figure 5.16: Minimum thickener area as a function of concentration

of 1.2 m^3/h of water. This step might be carried out in two stages: the first to separate the particles that sink and the second to separate the particles that float.

5.11 Conclusions

It has been established throughout this chapter that to use the existing separator design concept to separate cenospheres from bulk CFA is difficult. The difficulty resides in the reconciliation of two competing mechanisms: maintaining off bottom suspension so as to free any trapped cenospheres and operating the impeller below the speed at which cenospheres start to become entrained within the bulk tank flow. Although experimental evidence suggests that a compromise between these two conditions may be established, it seems likely that at a speed required for off bottom suspension, there will always be some portion of cenospheres entrained in tank flow which will reduce the overall recovery.

An alternative design has been suggested which borrows principles from the design of thickeners. In this design the flow is fed to the top of the tank and allowed to settle. By maintaining an underflow concentration only slightly higher that the feed, there will be no sediment build up on the bottom of the tank and thus all the cenospheres will be recovered.

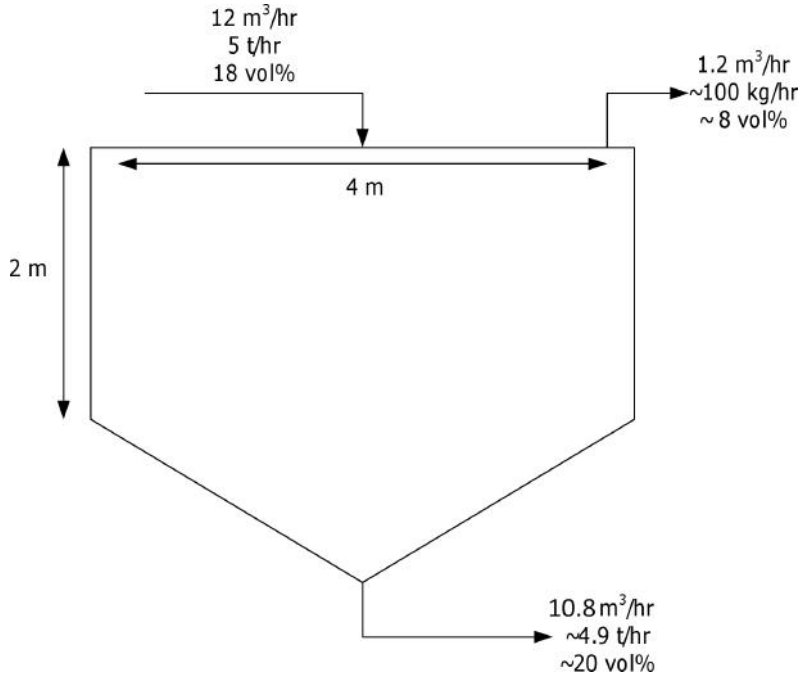

Figure 5.17: Proposed thickener separator design

The drawback to this concept is that high equipment plan areas are required to effect separation as well as secondary devices to recover the cenospheres from a water stream. However, given the nature of the feed, which has overlapping density and size profiles, any other system, a fluidised bed for instance, will be unable to guarantee complete separation. A suggested modification to the design is to provide inclined plates within the separator which would increase the surface area and so reduce the equipment plan area. It is suggested that a pilot scale version of the design as outlined here is built to test the operating concepts.

CHAPTER 6

VEGETABLE OIL AGGLOMERATION OF THE CARBON IN COAL FLY ASH: A PROCESS FOR THE CIRCULAR ECONOMY?

6.1 Introduction

CFA has pozzolanic properties which make it a good candidate to blend with cement to reduce the reliance of the cement mix on calcined limestone. In order to be used in cement blends most countries proscribe standards which limit the content of unburned carbon. For instance in the European Union, the highest grade CFA for cement blends is limited to a maximum of 5% Loss on Ignition as measured by a furnace test. Therefore, for CFAs that contain more carbon content than this, the only option is to perform some processing option on it to bring it in line with building standards. There are a variety of options available to perform this beneficiation such as electrostatic separation, fluidised bed burn out, froth flotation and oil agglomeration. Further information has been provided in Chapter 2.

Oil agglomeration is a technique that relies on differences in the tendency for materials to be hydrophilic or oleophilic. Generally it consists of vigorously agitating a three phase system consisting of an organic liquid, water, and particulate material. The heterogeneous material to be separated will usually contain two materials: one that is wetted by the organic liquid and one that is not. Under agitation, the oleophilic particles collide and

form agglomerates via the bridging of the oil phase. These agglomerates have a larger size than the hydrophilic particles. Consequently they can be easily separated using sieves or froth flotation. The advantage of bigger particles in froth flotation stems from the increase in the probability of collision with air bubbles.

Agglomerates form in regimes that differ according to the availability of wetting material. The first requirement is for a complete wetting of the agglomerate particles. This will differ according to the irregularity of the surface and the extent of porosity. Porous materials are able to draw wetting agent internally and thus reduce its availability to form bonds. The wetting of particles is also dependent on particle size. Smaller particle sizes have a greater surface area per unit mass and so more oil is required to completely wet the particles. Once wetting is achieved, increases in oil concentration will result in the forming of pendular aggregates. These are network structures in which particles may form bonds from one to three other particles. Further increases mean that more bonds are formed and particles start to achieve a three-dimensional consolidated structure. As oil increases past this point, the agglomerates can be regarded as droplets of suspended particles. Eventually the volume fraction of the solid particles in these droplets becomes so low that they essentially revert to the properties of the pure oils. At this point macroscopic phase separation might be observed. It is usually the case that separation performance is best in the three-dimensional aggregate regime [307].

Oil agglomeration has been successfully used in the removal of inorganic material from coal fines prior to combustion. The barrier to commercial implementation of this type of technology is the excessive application rates of the oil. Recently efforts have been made to reduce the consumption of oil in these processes by forming a high internal phase water in oil emulsion prior to agglomeration with promising results [308]. There is also an environmental aspect to consider in that commonly used oils are kerosene or diesel that originate from fossil fuel sources. However, vegetable oil has been considered as an oil for the separation of inorganic material from coal with the intention of utilising vegetable oil from non-edible vegetation or preferably vegetable oil from waste sources [309, 310].

There is an intrinsic limit to the separation efficiency when attempting to clean coal fines unless energy consuming size reduction techniques are used to liberate inorganic particle from within carbon matrix. When considering the *inverse* case of separating carbon from a majority inorganic phase in coal fly ash there are inherent factors that make the process better suited. During the combustion process much of the ash has been liberated from the carbon matrix so there is a higher ceiling for separation efficiency. In addition, the carbon is the minority constituent and so application rates per tonne of material processed will lower than for coal cleaning. Agglomeration has been used to separate carbon from coal fly ash before [175] but to the author's knowledge this is the first time that it has been attempted with vegetable oil in emulsified form. The current study utilises a response surface experimental design to assess the impact of the dominating factors governing separation and then the effect that emulsion formulation can have. The system is an ideal representation of the circular economy: a waste material is used two process a waste material, generating two useful product streams and zero waste.

6.2 Experimental

Table 6.1: Bulk chemical composition and density of CFA

Bulk Chemical (oxide basis)	wt%
SiO_2	45.8
Al_2O_3	24.93
Fe_2O_3	6.19
CaO	2.14
MgO	1.24
Na_2O	0.64
K_2O	2.15
Cr_2O_3	0.02
TiO_2	0.85
MnO	0.08
P_2O_5	0.6
SrO	0.1
BaO	0.17
LOI	15.4
Density (g/cm^3)	2.30

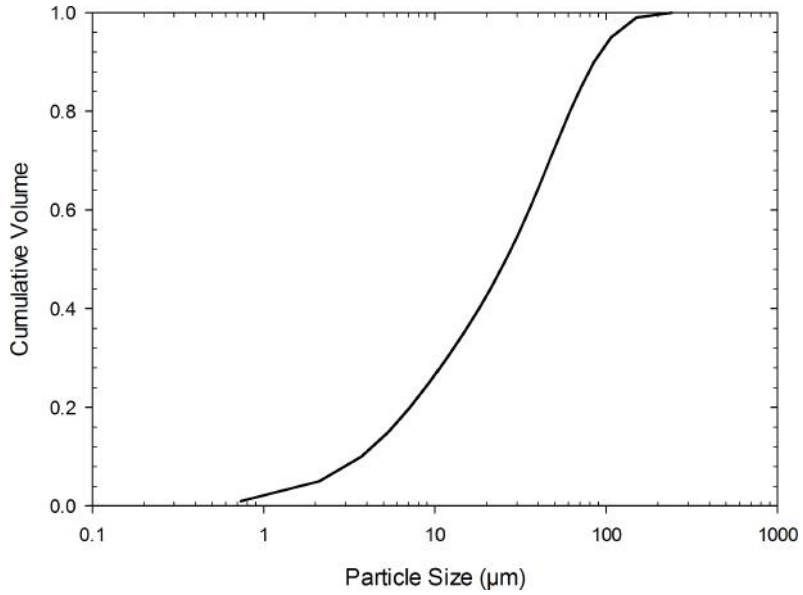

Figure 6.1: Particle size distribution of CFA used in this study.

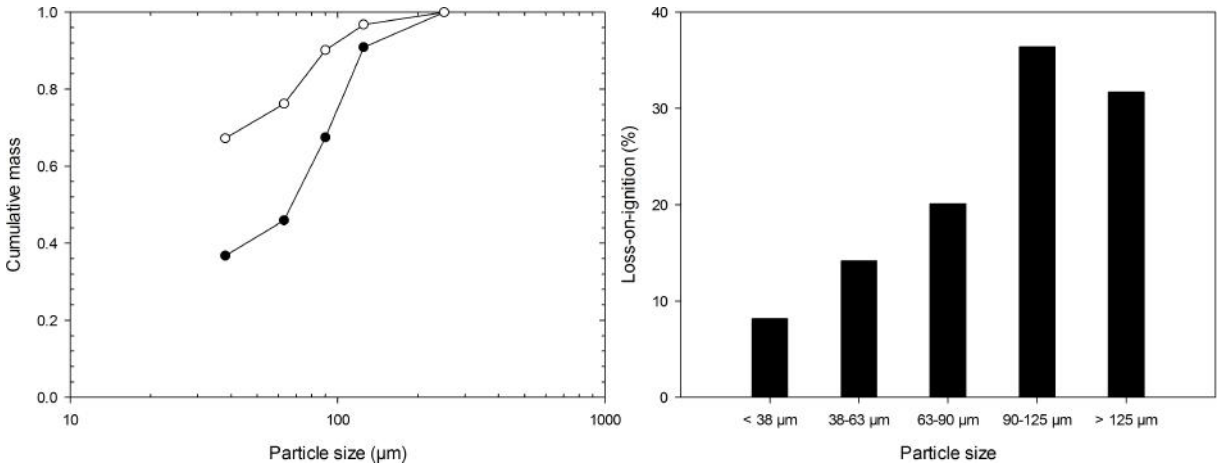

Figure 6.2: (Left) Cumulative size distribution of inorganic (○) and organic (●). (Right) LOI of size classified CFA

6.2.1 Materials

Coal fly ash was obtained via the fly ash processing technology company RockTron Mineral Services Ltd from a power station in the United Kingdom. The CFA is CFA-3 and the characterisation methods used are the same as those detailed in Section 3.1.2. The bulk chemical content and density of the CFA is provided in Table 6.1, the particle size is given in Figure 6.1, and the size distribution of the organic and inorganic component of the CFA as well as the LOI of size classified CFA is provided in Figure 6.2. Vegetable oil was bought from a United Kingdom supermarket and is labelled 100% rapeseed oil. The

surfactants PGPR and polysorbate 80 were obtained from an on-line cosmetics ingredients supplier. Acetone was purchased from Fisher Scientific UK.

6.2.2 Methods

Agglomeration experiments were conducted in a 1 L round bottom flask agitated with a Heidolph mixer. 50 g of CFA was introduced to the vessel and conditioned with 450 ml of distilled water and conditioned for a time of 5 minutes. A designated amount of oil was then introduced.and then slurry was agitated for a period of time at a specified agitation speed. After agitation the agglomerates were conducted with a variety of methods: sieving at 125 micron, sink/float in a separation funnel followed by sieving, or froth flotation. Froth flotation was carried out in a 2 L cell with a Denver mixer at 1000 rpm. No extra reagents were employed in the froth flotation recovery.

Both the ash concentrate and the carbon concentrate were collected and dried overnight at 80°C . The carbon concentrate was washed with acetone and polysorbate 80 for a period of 30 minutes on a magnetic stirrer. It was then filtered and dried overnight at 80°C . For the calculation of carbon and ash recoveries 2 g samples were placed in crucibles and subject to a furnace at 850°C for 1 hour. The mass loss was recorded and used to determine the loss on ignition (LOI).

Coarse water in vegetable oil emulsions were prepared on a magnetic stirrer. Briefly an amount of Polyglycerol polyricinoleate (PGPR) was dissolved in vegetable oil. A known mass of water was then added dropwise to the mixture under vigorous stirring. The emulsion was then stirred for a further 10 minuted to homogenise. All emulsions were used on the same day as they were prepared and showed stability against phase separation for well over 1 day. Optical micrographs were taken on a calibrated microscope for qualitative assessment of dispersed phase droplet size. Emulsion agglomeration performance was carried out at 12.5 wt% emulsion, at an impeller speed of 1100 rpm, and a 15 minute mixing time. For each condition 3 repeats were undertaken and an average taken.

Unpublished preliminary work determined that the most important factors governing

the agglomeration process were the agitation speed, the agglomeration time, and the wetting oil concentration (defined as wt% of CFA). This is also supported by an review of work on the subject area [311]. Initially in order to minimise the runs that were required a two level three factorial design was implemented with two replicates and 5 centre points. The level choices were partly influenced by the restrictions imposed by the equipment *i.e.* the mixer had difficulty sustaining speeds greater than 1500 rpm for any significant degree of time, or with any consistency. The agglomeration times were set for expediency with a time of 25 minutes adjudged to be sufficient as a higher level based on previous experimental work. The oil concentrations used were chosen based on the work of Heidelbaugh *et al.* [307] who conducted an investigation into agglomeration of ternary phase systems. The low level was chosen to roughly coincide with a point at which three-dimensional aggregates should form and the higher level of oil concentration was chosen such that oil was in excess.

An analysis of curvature for the factorial design indicated that it was present in statistically significant measure. Some of the factor levels could not be extended outside the experimental space so a face centred central composite design was developed by adding the necessary experimental points. The full experimental matrix is given in Table 6.2. The experimental results were analysed in terms of three responses: the carbon grade, defined as the mass fraction of carbon in the concentrate (X_{CC}); the ash grade, defined as the mass fraction of carbon in the tailings (X_{CT}); and the separation efficiency (SE). The envisaged process has two potential products, the inorganic component and the organic component. Therefore the SE was defined as measure of complete separation and was calculated in terms of the partition of each product to the respective concentrate - *i.e.* the ash recovery (AR) and carbon recovery (CR).

$$\text{CR } (\%) = \frac{100 X_{CC} M_C}{X_{CF} M_F} \tag{6.1}$$

$$\text{AR } (\%) = \frac{(100 - X_{CT})M_T}{(100 - X_{CF})M_F} \tag{6.2}$$

$$\text{SE } (\%) = \text{CR} + \text{AR} - 100 \tag{6.3}$$

Table 6.2: Experimental matrix

Standard Order	Run Order	Speed (RPM)	Time (min)	Oil (wt%)
1	7	700	5	2.5
2	21	1500	5	2.5
3	2	700	25	2.5
4	5	1500	25	2.5
5	19	700	5	25
6	15	1500	5	25
7	10	700	25	25
8	6	1500	25	25
9	1	700	5	2.5
10	12	1500	5	2.5
11	17	700	25	2.5
12	13	1500	25	2.5
13	20	700	5	25
14	14	1500	5	25
15	8	700	25	25
16	11	1500	25	25
17	16	1100	15	13.75
18	9	1100	15	13.75
19	4	1100	15	13.75
20	3	1100	15	13.75
21	18	1100	15	13.75
22	22	700	15	13.75
23	23	1500	15	13.75
24	24	1100	5	13.75
25	25	1100	25	13.75
26	26	1100	15	2.5
27	27	1100	15	25
28	28	1100	15	13.75

The model output followed the form of Equation 6.4. Initially all terms were included in each model. The commercial software Minitab 17 was used for analysis. In order to simplify the models and reduce the likelihood of over fitting, terms were excluded if they failed to meet statistical significance at a level of $p \leq 0.05$.

$$Y = \beta_0 + \beta_1 V + \beta_2 t + \beta_3 X_o + \beta_4 V^2 + \beta_5 t^2 + \beta_6 X_o^2 + \beta_7 V t + \beta_8 V X_o + \beta_9 t X_o \qquad (6.4)$$

6.3 Results

6.3.1 Ash grade

Results were analysed in Minitab to produce models over the entire experimental space. Although adequate standard error and adjusted R^2 values could be obtained without transforming the response variable (ash grade), the lack-of-fit test showed a statistically significant effect that could not be ignored. A Box-Cox transformation was applied with a λ value of 0 which corresponds to taking the natural log. This had the effect of creating a more easily definable random pattern in the residual plots against fitted values. The reason that the original data fails the lack-of-fit test is most likely due to the low values of ash grade that were obtained for a large majority of the data in combination with nearly an order of magnitude difference for just a few data points. It is clear from Table 6.3 that the model of the transformed data explains the variation in the transform very well. Adjusted and predicted R^2 are well over 0.9. It is also apparent that what contributes the most towards the variation in data, are the linear terms contributing 62.7%, two-way interactions 14.6%, and square terms 4.3%. Of the linear terms it is apparent that the impeller speed had the strongest effect on the ash grade.

What is shown in the ANOVA table is reflected graphically in Figure 6.3. The impeller speed has a strong influence over the ash grade; it declines sharply as the impeller speed increases past 1250 rpm and then levels off which is why the squared term in Table 6.3 is required to fit the data. The sharply negative effect from 700 to *ca.* 1250 rpm can be explained in terms of the degree of mixing in the agglomeration vessel. As the mixing becomes more rigorous, the oil phase is dispersed through the CFA slurry more

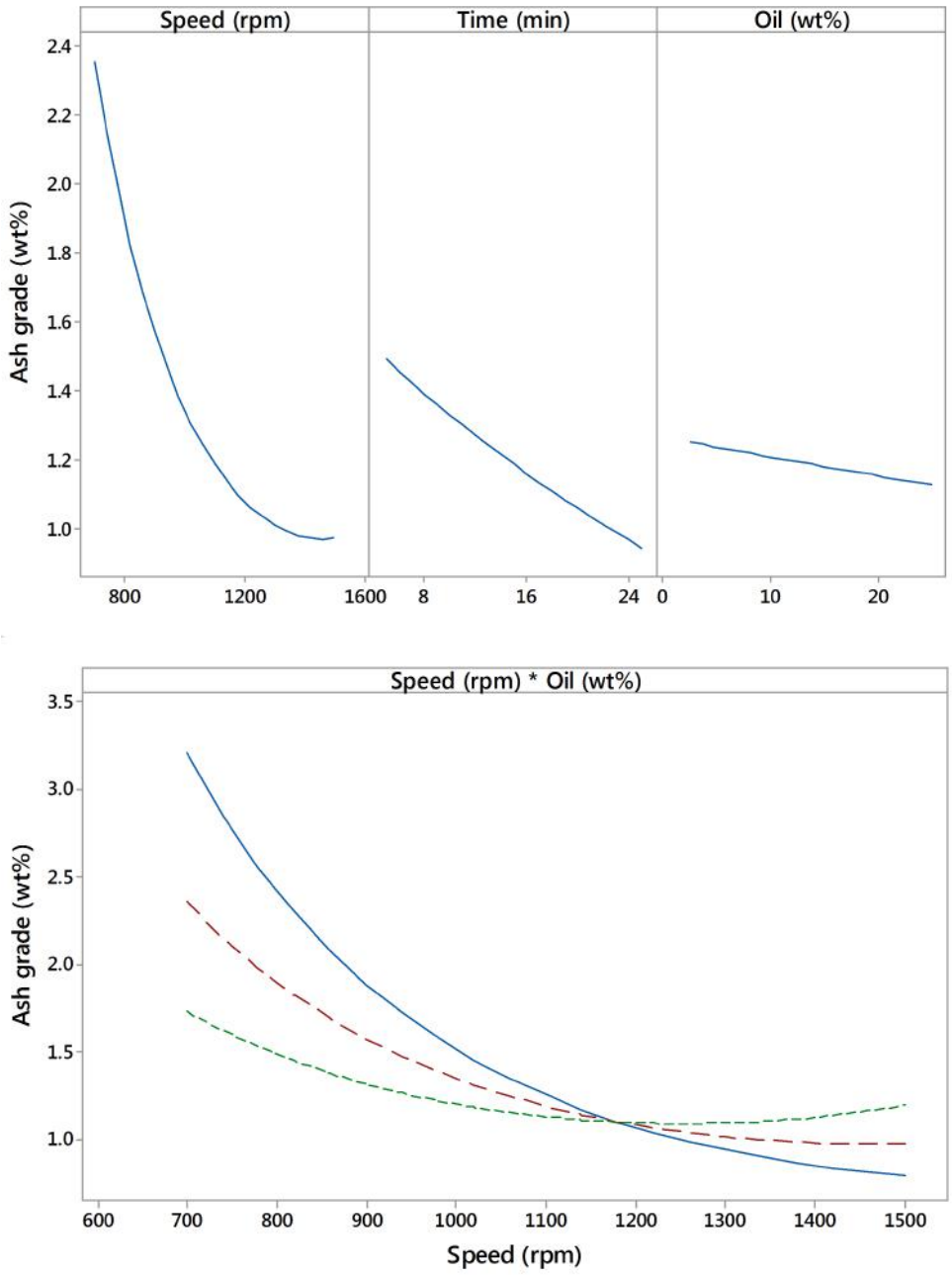

Figure 6.3: (top) Fitted means for the main effects in ash grade response model (bottom) fitted means for the speed-oil interaction in the ash grade response model: solid line is 2.5 wt% oil, long dashed line is 13.75 wt% oil and short dash is 25 wt% oil

Table 6.3: Analysis of variance for reponse surface ash grade model: note reponse variable transformed by natual log.

Source	Deg. Freedom	Sum squares	Contribution	P-Value
Model	6	6.85	95.8%	0.000
Blocks	1	1.01	14.2%	0.000
Linear	3	4.48	62.7%	0.000
Speed	1	3.51	49.0%	0.000
Time	1	0.93	13.0%	0.000
Oil	1	0.05	0.7%	0.079
Square	1	0.31	4.3%	0.000
Speed*Speed	1	0.31	4.3%	0.000
Interactions	1	1.05	14.6%	0.000
Speed*Oil	1	1.05	14.6%	0.000
Error	21	0.30	4.3%	
Lack-of-Fit	9	0.16	2.3%	0.246
Pure Error	12	0.14	2.0%	
Total	27	7.16	100.0%	
Model Summary				
Standard Error	R^2	R^2 adj.	R^2 pred.	
0.120	95.8%	94.5%	92.7%	

homogeneously which increases the probability of contact between coal particles and oil droplets; this results in a greater degree of agglomeration which directly translates into lowered ash grade [309]. The non-linearity in the speed data is more difficult to interpret and there are two possibilities. The first is that the process is taking ash with a grade of 15.4% and reducing it to around 1% at the highest impeller speeds. This might represent the intrinsic lower limit to the carbon content in the ash because the carbon particles are agglomerated, or included in an inorganic matrix, and this prevents the oleophilic surface of the carbon from exposure to the oil droplets. The second possibility is that as the impeller speed imparts a shear rate above a certain point, the strength of the bridge holding the carbon particles together is overcome and some of the agglomerates start to break up. This line of argument is in agreement with the theoretical model for agglomerate size postulated in Ref. [312]. In this model the author balances the strength of the bond which is a function of the bond diameter and the surface tension of the oil with the centrifugal force imparted by the flow of the slurry in the agitated tank.

The effect of agitation time on the ash grade is more straightforwardly linear; increasing the agitation time yields a cleaner ash product. This would appear to follow similar

reasoning to the effect of the impeller speed. The probability of oil-carbon contact is directly related to the duration of the experiment, and so the longer the CFA slurry and oil is agitated, the greater number and size of agglomerates are formed. For the time frames studied, there does not seem to be any evidence of a limit of ash grade at 1% as postulated for the agitation speed which leads to the likelihood that it is the increased shear from the impeller that starts to impact on the ash grade.

The oil appears to have much less of an effect on the ash grade over the experimental conditions studied. Although there is a reduction in ash grade the slope of this line is much flatter than for the other two terms. This is in line with previous studies of [309,310,312]. These broadly find that at very low oil concentrations there is insufficient oil to wet the carbon particles and at high oil concentrations the carbon particles become dispersed in an oil phase much like the mechanisms observed recently [307]. When the carbon particle content and density are taken into account the lowest oil concentration used in the current study is equal to $0.35\phi_p$ where ϕ_p is the volume fraction of the carbon particles. Using a geometric argument Heidelbaugh *et al.* [307], suggest that the beginning of consolidated aggregate formation is at $0.22\phi_p$ although this argument neglects the requirement for particles to be fully wetted. In between these two concentrations the combustible recovery of carbon remains practically constant. Although the oil concentration effect is small it is not constant and there is probably some form of kinetic effect here. The hydrodynamics of the process are limiting and so an increase in oil concentration improves the rate of collision between the carbon particles and the oil droplets.

The experimental design also allows the observation of an interesting interaction effect shown in the bottom plot in Figure 6.3. This shows the effect of the impeller speed with different concentrations of oil. For the lowest level of oil used (2.5 wt%), the ash grade reduces with some form of power law. It appears that increases of speed still reduce the ash grade, but with lessening extent. However at the mid and high levels (13.75 and 25 wt%), the shape of this curve changes. Whilst caution must be exercised not to draw firm conclusions based on model fitting, it does appear that as the oil concentration increases,

the curves shift position along the speed axis. The excess oil appears to be inhibitory. This can be explained in reference to the particle concentration inside oil droplets. As the oil concentration increases the carbon concentration inside the oil decreases and the viscosity of these droplets reduces according to suspension rheological theory and observation (see Chapter 4 for example). This reduction in viscosity might cause the yield strength of the droplets to reduce and therefore their break up becomes more likely as the shear rate increases. The resulting agglomerates being smaller are less likely to be collected in the froth flotation stage.

Table 6.4: Analysis of variance for reponse surface carbon grade model.

Source	**Deg. Freedom**	**Sum squares**	**Contribution**	**P-Value**
Model	4	1096.7	67.4%	0.000
Linear	3	871.6	53.5%	0.000
Speed	1	431.8	26.5%	0.000
Time	1	264.7	16.3%	0.003
Oil	1	175.1	10.8%	0.011
Interactions	1	225.0	13.8%	0.005
Time*Oil	1	225	13.8%	0.005
Error	23	531.8	32.7%	
Lack-of-Fit	10	143.2	8.8%	0.876
Pure Error	13	388.6	23.9%	
Total	27	1628.4	100.0%	
Model Summary				
Standard Error	R^2	R^2 adj.	R^2 pred.	
4.808	67.4%	61.7%	49.9%	

6.3.2 Carbon grade

The carbon grade was analysed similarly to the ash grade. The response values required no transformation as is evident from the statistically insignificant lack-of-fit value shown in Table 6.4. Unlike the ash grade term there was no curvature in the model with the three linear terms plus an interaction term between time and oil content sufficient to describe around 67% of the variance in the data. However, the model fit is clearly not as good as for ash grade and it is thought that this is as a result of the highly variable way in which inorganic ash might be entrained into the carbon concentrate, either in the agglomeration

stage or in the froth flotation separation. Although the model has predicted R^2 values of around 50%, it is statistically significant and so remains useful for the purposes of analysis.

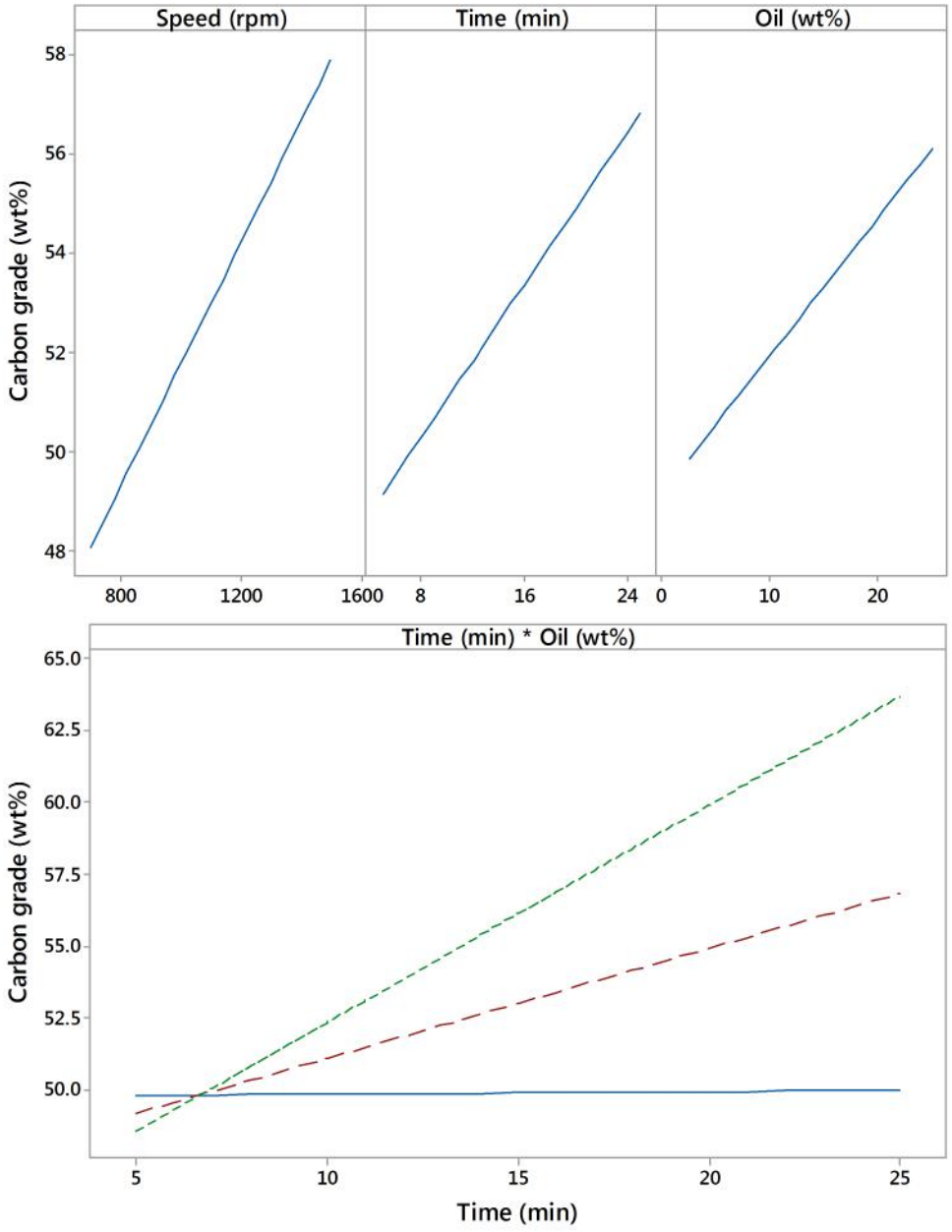

Figure 6.4: (top) Fitted means for the main effects in carbon grade response model (bottom) fitted means for the time-oil interaction in the carbon grade response model: solid line is 2.5 wt% oil, long dashed line is 13.75 wt% oil and short dash is 25 wt% oil

The main effects plots for the carbon grade show that all three factors influence the carbon grade with a positive linear relationship in the order speed > time > oil. These trends are unusual relative to previous studies in which it was found that increased agitation rates

past a certain optimum value were associated with ash rejection decreases: where the ash rejection is equivalent to the carbon grade in the current terminology [309, 313]. The reasoning for such behaviour is that an increase in impeller speed increases the proportion of large agglomerates which in turn entrains more inorganic constituents. Both of these studies were carried out using screening as the carbon recovery step. It is possible that using froth flotation as the recovery step leads to a cleaning effect on the agglomerates such that the emergence of a critical impeller speed for carbon grade does not occur until higher speeds or not at all.

In terms of oil concentration it has previously been shown that, in the vegetable oil agglomeration of high rank coals, increments in oil concentration were observed to reduce the ash rejection [310] and in that study froth flotation was also used as the recovery step. The authors explained this result as the effect of competitive wetting. At low oil concentrations, the oil wets only the most hydrophobic particles and these contained the highest carbon content. As the oil concentration increases other particles with more included mineral matter also become wetted by the oil and thus are agglomerated (or merely collected in the froth flotation step).

Agitation time has been found to adversely effect the ash rejection in coal cleaning studies [313]. It was attributed to the increased chance of entrainment of mineral matter into agglomerates. A similar observation has also been attributed to the increased size of agglomerates as the process time increases [309]; however, a mechanistic explanation for why this increase in size affects ash rejection is lacking.

The results shown in Figure 6.4 appear to contradict the consensus in the coal cleaning literature. It is proposed that the reason for this is a function of the formation mechanism of the CFA particles which is discussed in Section 2.1.2. It is possible to distinguish two type of char particles: those that are slightly changed and those that are fully or semi-coked. The slightly changed particles are more representative of the primary coal and thus are likely to contain inherent mineral matter. They are typically larger than 100 μm in size and it is for this reason that the larger size fractions of the feed ash are so rich

in carbon as evidenced by Figure 6.2; the size fraction of the parent CFA > 90 μm is over 30% carbon and this comprises around 50% of the overall carbon in the CFA. The coked or semi-coked particles undergo melting and condense as spheres or spheroids and are much smaller. The larger, more irregular char particles are also more porous. If the larger particles preferentially adsorb more of the wetting oil, then it is likely that being larger they would be easily floated in the carbon recovery step. Therefore the observed increases in carbon grade with agitation speed, time and oil content are the result of a greater tendency to encourage agglomeration of the smaller semi-coked/coked particles which have a greater carbon purity. As they agglomerate this increases their likelihood to report to the flotation concentrate [34].

The preceding explanation is given greater weight when considering the time-oil interaction effect shown in Figure 6.4. This shows that the agitation time is only relevant at the mid-point and high oil concentration level. This suggests that at the low concentration level the coarser grained slightly changed particles adsorb all of the available oil and the agitation time has no effect on increasing the agglomeration extent of the smaller semi-coked/coked particles. When excess oil is added these particles do agglomerate and correspondingly increase the carbon grade but only after they have been agitated for sufficient time to increase in size.

6.3.3 Separation efficiency

In coal cleaning operations the process usually has only one product, the clean coal. It is normal to define a separation efficiency using the combustible recovery to the coal product and the ash rejection to the waste stream. This can also be used to describe the separation performance of the current *two* product process. In this case the ash recovery to the froth flotation tailings is exactly equivalent to the ash rejection. By maximising both ash recovery and carbon recovery the process moves towards perfect separation. As the separation efficiency is governed by the values obtained from the carbon and ash LOI analysis, the terms that were found to be significant in the surface response

models were used in order to model the separation efficiency; the results are provided in Table 6.5 The overall fit is adequate with adjusted and predicted R^2 values of 83.4% and 74.0% respectively. All terms are significant apart from the Time*Oil term which is not statistically significant. A decision was made not reduce this term because it was shown to affect the carbon grade. It appears that this effect becomes dwarfed by the others when combining the model.

Table 6.5: Analysis of variance for reponse surface separation efficiency.

Source	**Deg. Freedom**	**Sum squares**	**Contribution**	**P-Value**
Model	6	1435.6	87.1%	0.000
Linear	3	1130.4	68.6%	0.000
Speed	1	719.2	43.6%	0.000
Time	1	256.7	15.6%	0.000
Oil	1	154.5	9.4%	0.001
Square	1	185.2	11.2%	0.000
Speed*Speed	1	185.2	11.2%	0.000
Interactions	2	120.1	7.3%	0.009
Speed*Oil	1	100.6	6.1%	0.005
Time*Oil	1	19.5	1.2%	0.18
Error	21	212.6	12.9%	
Lack-of-Fit	8	118.7	7.2%	0.119
Pure Error	13	93.8	5.7%	
Total	27	1628.4	100.0%	
Model Summary				
Standard Error	R^2	R^2 adj.	R^2 pred.	
3.182	87.1%	83.4%	74.0%	

In terms of separation efficiency, Figure 6.5 clearly shows that optimal process conditions are at the highest levels for oil concentration and agitation time, but that the curvature in the ash grade against speed curve is dominant in the separation efficiency models resulting in a plateau before the highest speeds are reached. In fact when optimising the carbon grade and the separation efficiency in Minitab a separation efficiency of 86.9% and a carbon grade of 68.0% were predicted at 1450 rpm, 25 minutes and 25 wt% oil. These results compare extremely favourably to a previous study on the a column hybrid agglomeration-froth flotation procedure which obtained similar carbon grades of 55-70% but carbon recovery was much lower at just over 60% [175]. The results are superior to a previous conventional froth flotation study [314] and are similar to the results

achieved in a concurrent froth flotation column [171].

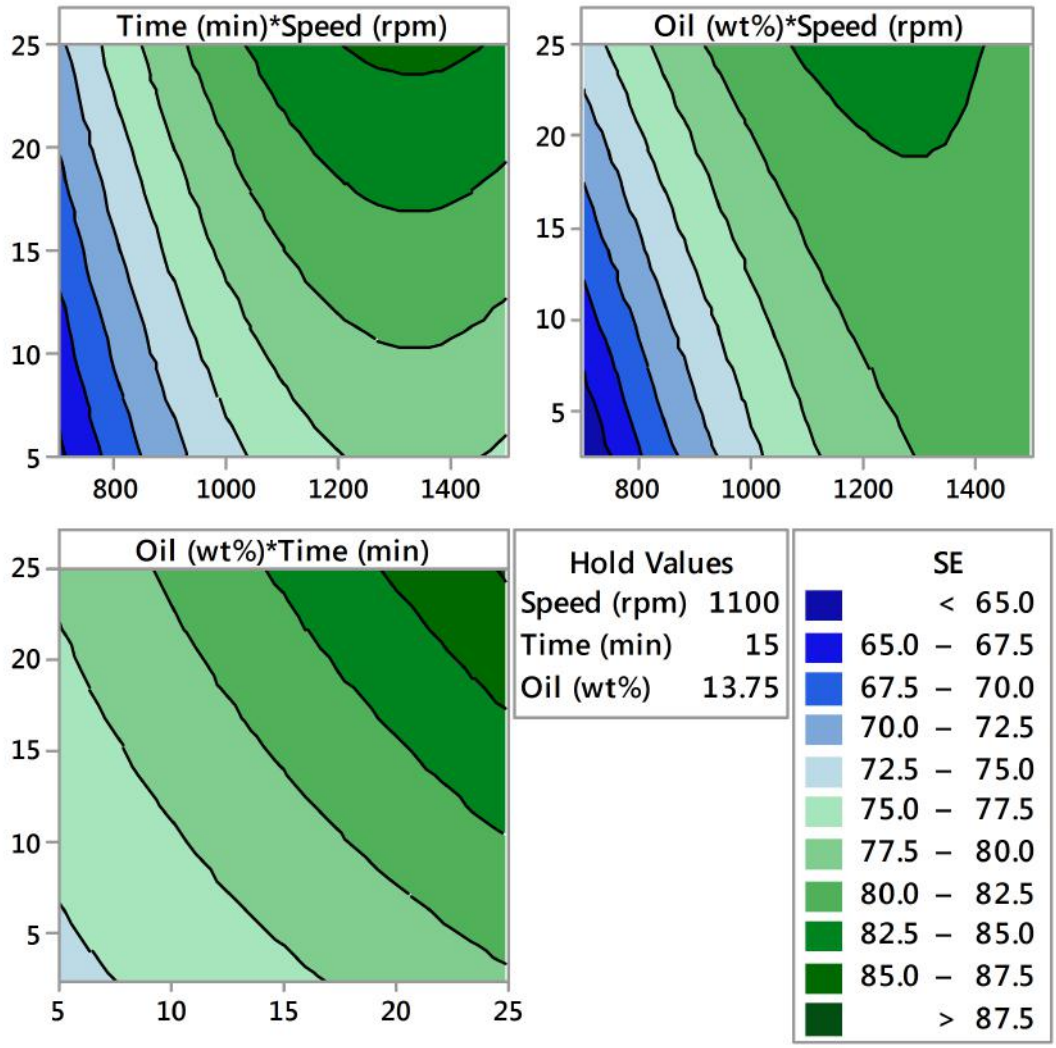

Figure 6.5: Contour plots for the separation efficiency as a function of agitation speed, agitation time, and oil concentration

6.3.4 Emulsified wetting agents

The use of an emulsified wetting agent can potentially reduce the amount of oil required. Most reports have concentrated on oil in water (O/W) emulsions where the objective of pre-emulsifying the oil is to reduce the energy requirement to achieve a particular droplet size: to improve dispersion of the oil [174, 311]. The use of water in oil (W/O) emulsions has the same objective, but this reduction is intended to be brought about via a volume reduction mechanism whereby water droplets within the oil droplets act as inert space

fillers while the droplet surface properties remain the same [308].

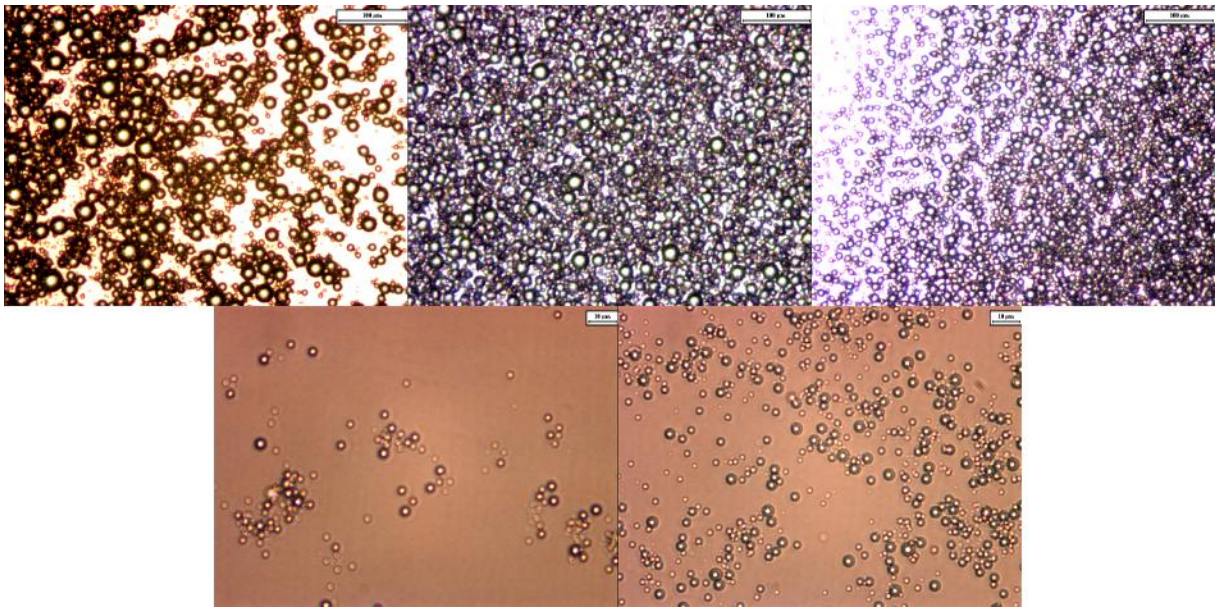

Figure 6.6: Optical microscope images of 50:50 W/O emulsion of different surfactant concentrations (% oil): (top left) 0.625; (top middle) 1.25; (top right) 2.5; (bottom left) 5; and (bottom right) 10. Scale bars represent 100 μm in the top images and 10 μm

In order to prepare W/O emulsions a surface active molecule must be added in sufficient quantities to stabilise the dispersed water droplets against coalescence. It is known that the addition of PGPR reduces the interfacial tension of water in oil [315]. By increasing the surfactant concentration the internal droplet size decreases, as shown in Figure 6.6; although ultimately this droplet size will be limited by the method of preparation [316]. Figure 6.7 shows that at a surfactant concentration of 0.3 wt%, the carbon grade is lower than that between 0.6-5 wt% indicating that more ash forming components have been entrained in, or with, oil droplets. This could be because the surfactant concentration was insufficient to stabilise the emulsion fully so that when it was introduced into the agglomeration vessel, rather than break down into a water in oil in water (W/O/W) double emulsion, it reverts to a O/W emulsion. The reduction in surface tension as a result of the surfactant in the oil phase means that there is a corresponding reduction in the bond strength between particles [312] and that the agglomerate strength is reduced. Weaker bonds between particles allow slurry water containing ash particles to be entrained in unconsolidated aggregates [311]. The value at which full stability is likely to be achieved

should coincide with the critical micelle concentration which for PGPR is <1wt% [315]. This is supported weakly by the experimental data which would be improved by doing further experimental runs between 0.1-1wt% surfactant.

There is also a reduction in carbon grade at the highest surfactant concentration. This lends credence to the theory that it is the effect of the surfactant that leads to a reduction in carbon grade. At the lowest concentration the emulsion instability causes an oil with lower surface tension than pure oil to form agglomerates with weaker bonds. There is an intermediate region in which the emulsion is stabilised more effectively by the PGPR molecules. As the surfactant concentration is above the concentration at which the surfactant molecules form micelles, any increase at this stage does not result in any improvement of reduction in carbon grade. The second effect directly influences the carbon grade. At the highest PGPR concentration the carbon grade is the lowest for any of those tested. In order to understand why this effect may be happening it is necessary to consider a double emulsion system. Effectively, in the agglomeration process a W/O emulsion is broken down in water to become an W/O/W double emulsion. It is noted that in such systems the lipophillic surfactant does not exclusively adsorb on the interface between inner water droplets and oil phase [317]. It may also cover the interface between the oils drops and the outer aqueous phase. It seems plausible that above a certain concentration of surfactant, the surfactant starts to adsorb on the outer droplet interface and causes instability and the break up of emulsion droplets which will eventually lead to a release of the internal water phase. The reduced surface tension oil is now a single phase and so has a corresponding reduction in both bond strength and volume which creates a greater degree of ash entrainment. The foregoing leads to the conclusion that emulsion formulation can not be neglected in considering agglomeration performance. It also leads to the suggestion that a better emulsion formulation with an order of magnitude reduction in droplet sizes should lead to an improvement in agglomeration performance. It is noteworthy that in the intermediate region the separation efficiency observed was very close to that expected by the response surface model for pure oil, however, given that

only half the oil was used, this represents an improvement in performance by a factor of two [308].

Ideally the effect of the emulsion concentration mirrors that of pure oil. Figure 6.8 shows that broadly speaking this is the case. The separation efficiency as a function of emulsion concentration follows the trends predicted by the response surface model for pure oil when both the confidence intervals and error bars are taken into account. This again illustrates that it is possible to achieve a factor of two reduction in oil use for the same separation performance. What is most notable from Figure 6.8 is that the ash grade shows a marked drop from *ca.* 1% down to *ca.* 0.4% with an increase in emulsion concentration from 2 to 4% of the CFA feed. This can be attributed in a transition from pendular bonds between droplets, triplets and quadruplets to more fully formed agglomerates [318]. When taking the dispersed phase of the emulsion onto account, even allowing for dispersed droplet deformation the emulsion concentration at which this transition occurs agrees relatively well with that predicted in Heidelbaugh et al [307]. The more fully formed agglomerates are larger in size and therefore have a greater probability of colliding with bubbles in the flotation stage [319]. This leads directly to an increase in quality of the ash grade.

The dispersed phase concentration has an effect on the emulsion viscosity that it similar to that observed for concentrated suspensions (Chapter 4, [320]). This is evident in Figure 6.9. As the internal water concentration increases, the viscosity of the emulsion increases according to a Krieger Dougherty type relationship. This results in bigger emulsion droplets for the more concentrated emulsions. It is this behaviour that is the cause of the reduction in ash grade from *ca.* 1% to *ca.* 0.4% between dispersed phase concentrations of 20-40 wt% even though the absolute concentration of oil in the agglomeration process reduces. At the lower dispersed phase concentrations the less viscous emulsion is easier to break down and so the droplet size is able to approach the internal droplet size of the emulsions. It is interesting to note that relative to the instability caused by low surfactant concentration (see Figure 6.7), the ash grade is more adversely affected when

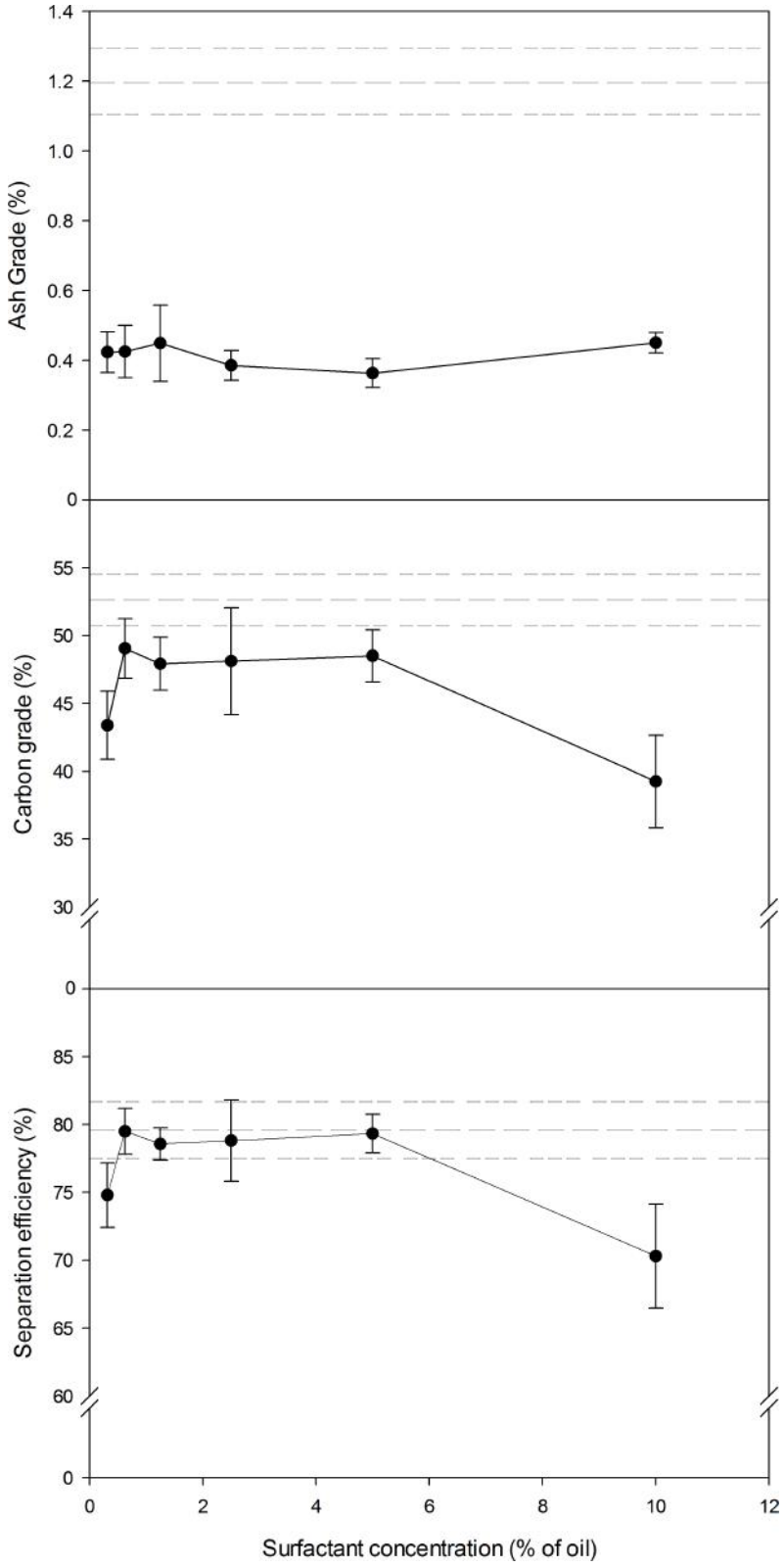

Figure 6.7: Ash grade, carbon grade, and separation efficiency as a function of surfactant concentration. Dashed lines represent the model prediction for non-emulsified oil and the prediction intervals of the model.

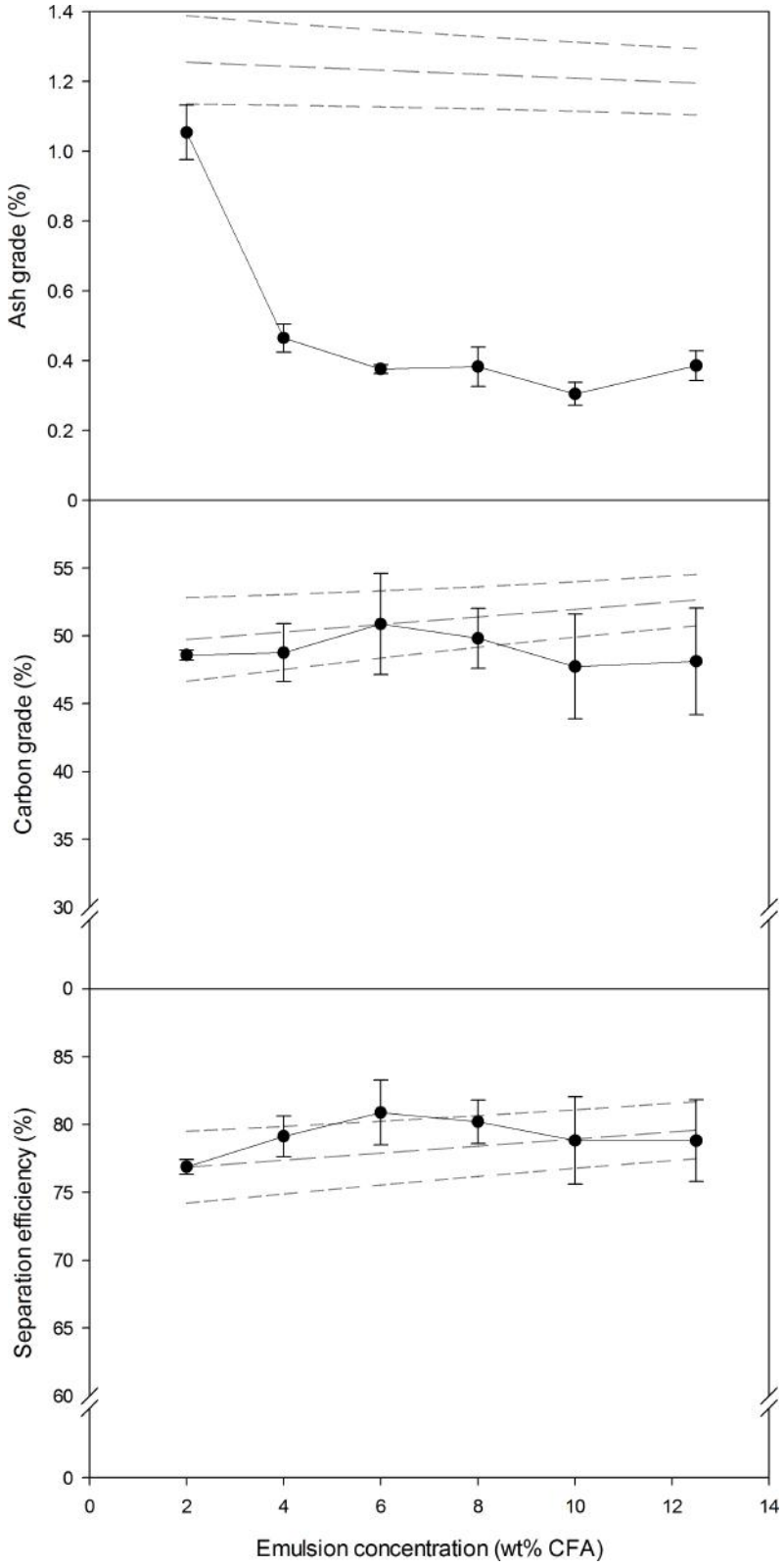

Figure 6.8: Ash grade, carbon grade, and separation efficiency as a function of binder concentration. Dashed lines represent the model prediction for non-emulsified oil and the prediction intervals of the model.

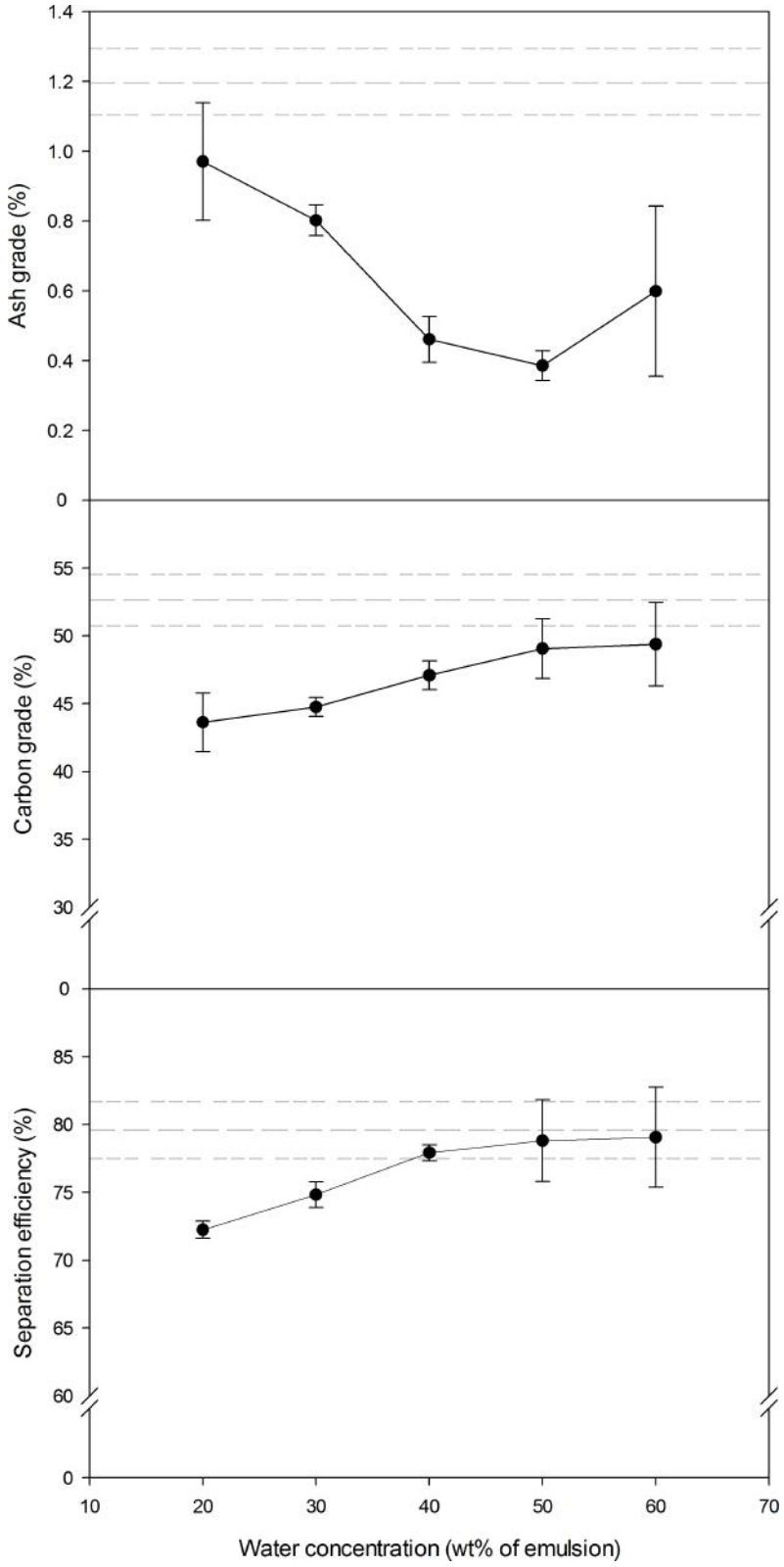

Figure 6.9: Ash grade, carbon grade, and separation efficiency as a function of dispersed phase concentration. Dashed lines represent the model prediction for non-emulsified oil and the prediction intervals of the model.

the emulsions contain less dispersed phase. This leads to the observation that the separation performance of the binder containing 60 wt% water is the same as that for the 50 wt% and that the reduction in oil content required can be increased with further increases in dispersed water content. Better emulsion formulation to even higher dispersed phase concentrations is therefore necessary. The only constraint that should be mentioned is that previous studies with extremely high internal phase emulsions use emulsifier concentrations of 50% [308]. This might be excessive from an economic viewpoint if the emulsifier cost is much higher than the oil cost. Regardless the results of even such a crudely made emulsion suggest that more sophisticated methods of emulsion manufacture will yield even greater improvements in oil reduction.

6.3.5 Economic considerations

The cost of oil has long been recognised as the barrier to implementation in the cleaning of coal fines. The same economic constraints apply to the process of separating carbon particles from inorganic ash particles. One of the drivers of using vegetable oil is that it is conceivable that waste sources may be used without too much detriment to the processing performance. The UK produces large volumes of waste vegetable oil. Such a potential resource has not gone unnoticed and it now being used to produce biodiesel in some large scale operations. As a result of this it commands a fairly high price. In the UK waste vegetable oil of inferior quality sells for £0.25 per litre while good quality oil sells for up to £0.60 per litre [321]. Given that there is a ceiling on the price that biodiesel can command, extra demand for vegetable oil should not affect the price. Using the separation performances obtained in this study these prices would lead to raw materials costs of £2.70-6.50 per tonne CFA. Although it is not possible to provide an accurate processing cost at this level of investigation, given that the process produces a product ash of less than 1% carbon, and that cement prices are *ca.* £70 per tonne, the use of treated CFA as a cement extender might be possible and certainly worthy of further investigation. It should also be noted that all the processes in this study are not optimised. The agglomeration set-

up was not a dedicated mixing process, the froth flotation variables were not optimised, and the emulsion formulation and preparation was crude in the extreme. Overall this indicates that there is a lot of potential in the agglomeration flotation process.

6.3.6 Environmental considerations

Decomposition of limestone into equimolar quantities of CaO and CO_2 is an essential process in the production of cement clinker. Through stoichiometry it can be shown that for every tonne of CaO produced, 0.79 tonnes of CO_2 are generated. In addition, the decomposition requires thermal energy to proceed; the high energy consumption of the kiln adds an emission load depending on the nature of the fuel and its location. A recent LCA reports that for Australian cement production a figure of 0.8 t CO_2-e/tonne is typical, which fits into the global range of 0.7-1.0 t CO_2-e/tonne [121]. The same analysis calculated that by using a mix of 25% CFA a reduction in overall concrete greenhouse gas (GHG) emissions of 13 to 15% is possible in typical concrete mixes.

It has been discussed in section 2.3.8 that replacement levels of up to 100% are possible with certain CFA compositions. Even accepting that not all of the different CFAs produced around the world will yield the required properties at substitutions of 100%, there is still good field evidence to suggest that (<55%) CFA blends can be used now if care is taken over mixing and construction practices [122].

O'Brien et al. [322] undertook a life cycle analysis (LCA) study on the impact of CFA content on embodied CO_2 emissions in concrete. They presented an equation that can be used to estimate the reduction in Portland cement required to meet a specific emissions target. This equation was derived using data from Australia and caution should be exercised when using it for other locations.

$$\mathrm{GHG}_{concrete} = 66\frac{\mathrm{kgCO_2\_e}}{\mathrm{m^3}} + 790.7\frac{\mathrm{kgCO_2\_e}}{\mathrm{tonne}}\ \mathrm{x}\ \mathrm{mass}_{cement}\frac{\mathrm{tonne}}{\mathrm{m^3}} \tag{6.5}$$

The 66 kg CO_2-e/m^3 represents the embodied emissions for the concrete in the absence of any cement addition (the CFA is assumed to have travelled 100 km to site), and the 790.7 kg CO_2-e/tonne are the emissions per tonne of cement (assumed to have travelled 10 km to site).

Applying this formula to a medium strength (30 MPa) high volume fly ash (HVFA) mix given by Mehta [122] allows the CO_2 emissions reduction factor for 55% CFA cement to be calculated:

$$100\%\ \text{OPC} : 66 + (790 * 0.33) = 326.7\ \text{kg}CO_{2\_}\text{e/m}^3$$

$$55\%\ \text{CFA} : 66 + (790 * 0.15) = 184.5\ \text{kg}CO_{2\_}\text{e/m}^3$$

A reduction of 44% is possible from the base level case. The use of HVFA offers a holistic solution to the problems brought about by the triple requirements of sustainable development. In the short term the use of cement and coal fired power stations will drive growth in countries such as China and India. In order to do so in a sustainable manner HVFA concrete could be part of the solution and by processing the CFA to remove the excess carbon more of the CFA becomes suitable for cement blending operations.

6.4 Conclusions

The most important finding of this study is that it is possible to achieve an extremely high degree of separation of the carbon from a particular UK CFA using an environmentally benign waste vegetable source. Three process variables were explored within an experimental design to probe their impact on both the ash and carbon grades. It was found that increases in impeller speed, agglomeration duration and oil concentration all reduced the carbon content of the ash product. The effect of impeller speed was found to diminish past a certain point; this was attributed to a reduction in agglomerate diameter resulting

from an increase in shear stress which reduced the flotation efficiency. An interaction effect was found that suggested that the effect of the impeller speed is lessened at elevated oil concentrations due to the reduction in viscosity of the droplets of carbon particles suspended in oil that are more easily broken up by the increase in shear stress. The carbon grade was increased with increases in all three experimental factors in the order speed > time > oil. Although this goes against previous literature on the subject, it is thought that the manner of CFA formation is the cause of such behaviour. Two different forms of carbon particles with different combustion histories agglomerate at different rates as a result of their different particle sizes. The larger particles are more likely to be associated with higher mineral content and therefore, if they agglomerate first, the carbon grade is not as good as when the smaller more pure particles are agglomerated. Although the experimental equipment used was not a dedicated mixing set-up, separation efficiencies achieved were as good and in some cases better than those reported previously.

The use of emulsified oil binder is capable of achieving greater than a two fold reduction in oil content required. Although the emulsion preparation procedure was crude the effect of the surfactant concentration, emulsion concentration, and dispersed phase content were examined. The formulation of the emulsion is important as optimal surfactant concentrations were found in intermediate quantities. In the current study this was explained as a result of the decrease in surface tension of the oil with added surfactant. This meant that emulsion droplets are more easily dispersed, but crucially it also means that the bond strength is lower. A reduction in surface tension also allows the break up of the emulsion external droplets to a greater degree. If parity is reached between the internal and external droplet sizes, the internal phase is released and the separation performance goes down. The effect of the dispersed phase concentration has been shown to be important in the separation efficiency. It is thought that the viscosity of the more concentrated emulsion is actually beneficial.

The current work provides the first attempt of its kind. It suggests strongly that further work is necessary to improve both emulsion formulation and agglomeration pro-

cessing. It highlights that there a great potential is using this process to form a separation that fits in perfectly with the concept of the circular economy.

CHAPTER 7

THE IMMOBILISATION OF SILVER ACTIVATED TITANIUM DIOXIDE ON COAL FLY ASH CENOSPHERES

7.1 Introduction

The photocatalytic potential of TiO_2 has been known since the late 1970s. Essentially, when the TiO_2 in its anatase form is exposed to ultraviolet (UV) light at wavelengths of around 365 nm, electrons are promoted from the valence to the conduction band. The energised electrons and the holes that are created are both then able to undergo reactions. These reactions can lead to the formation of highly reactive species such as hydroxyl radicals ($\dot{O}H$), superoxide (O_2^-), and hydrogen peroxide (H_2O_2) [323]. It is a popular choice for photocatalysis not only for its high activity under UV light, but also because it is non-toxic and readily available [324].

The most effective form of TiO_2 for photocatalytic application comes in the form of a nano powder with an average particle size of close to 25 nm. However there are two major drawbacks that have prevented the use of this form of TiO_2 in more commercial applications.

1. It has been reported that only 3-5% of total sunlight is made up of the UV light that is required to initiate photo degradation of organic contaminants using TiO_2. Of this, only 1% can penetrate to depths of 0.5 m below the surface of any water

system. There is, therefore, a large problem with UV light utilisation efficiency. On the other hand 45-50% of sunlight is comprised of visible light of which 20% is available at 0.5 m below the surface [324, 325].

2. The post treatment recovery of suspended TiO_2 is problematic due to the long settling times or very fine filters that must be employed in order to remove nano scale powder from an aqueous phase [326].

To overcome the latter problem, immobilisation of TiO_2 on a high surface area substrate such as zeolites [327, 328] or activated carbon [329, 330] has been conducted by various researchers. Overcoming the former requires the immobilisation of TiO_2 on a substrate that has positive buoyancy such that is able to float at the air-water interface. To date many potential methods of achieving buoyancy have been attempted such as TiO_2 immobilised on hollow glass micro beads [331], a TiO_2 porous ceramic made by a camphene-based freeze-casting process and high-temperature calcination [332], using commercial nano sized TiO_2 as a Pickering particle to stabilise oil in water emulsions [323], and TiO_2 immobilisation on polypropylene particles [324].

One particularly resourceful way of tackling this problem is to immobilise TiO_2 on lightweight waste materials. In the early 1990's researchers attached nano titania particles to fly ash cenospheres (FACs) [191]. Although their formation is not fully understood, it is thought that they result from internal gas bubble expansion of the inorganic component of coal. They are generally considered to have a specific gravity of less than one as a result of the way they are collected: using water as a separating medium. They are generally larger than the heavier fraction of CFA and have a size range of between 40-250 μm [333]. They make up anywhere from 0.01-4.8% of the CFA, but this is usually in the region 0.3-1.5% [11].

Table 7.1: Sample properties

Sample code	$\bar{d_p}$ (μm)	$\sigma\bar{d_p}$ (μm)	$d_{pmax} - d_{pmin}$ (μm)	Anatase (wt%)	Mullite (wt%)	Quartz(wt%)	Amorphous (wt%)
2 M HNO_3 Acid Wash							
FAC-TiO_2-139	139	21.7	119.8	3.8	6.6	2.9	86.7
FAC-TiO_2-79	79	6.8	40.4	6.6	9.5	1.9	82.0
0.5 M HNO_3 Acid Wash							
FAC-TiO_2-142	142	17.6	87.1	0.7	6.9	3.2	89.2
FAC-TiO_2-113	113	9.1	40.4	1.7	7.2	2.0	89.1
FAC-TiO_2-78	78	8.3	53.5	1.2	10.7	1.5	86.5
FAC-TiO_2-58	58	6.1	34.6	10.8	10.8	1.1	77.2
SCFAC-TiO_2-58	58	17.1	137.4	2.5	11.9	nd	85.6

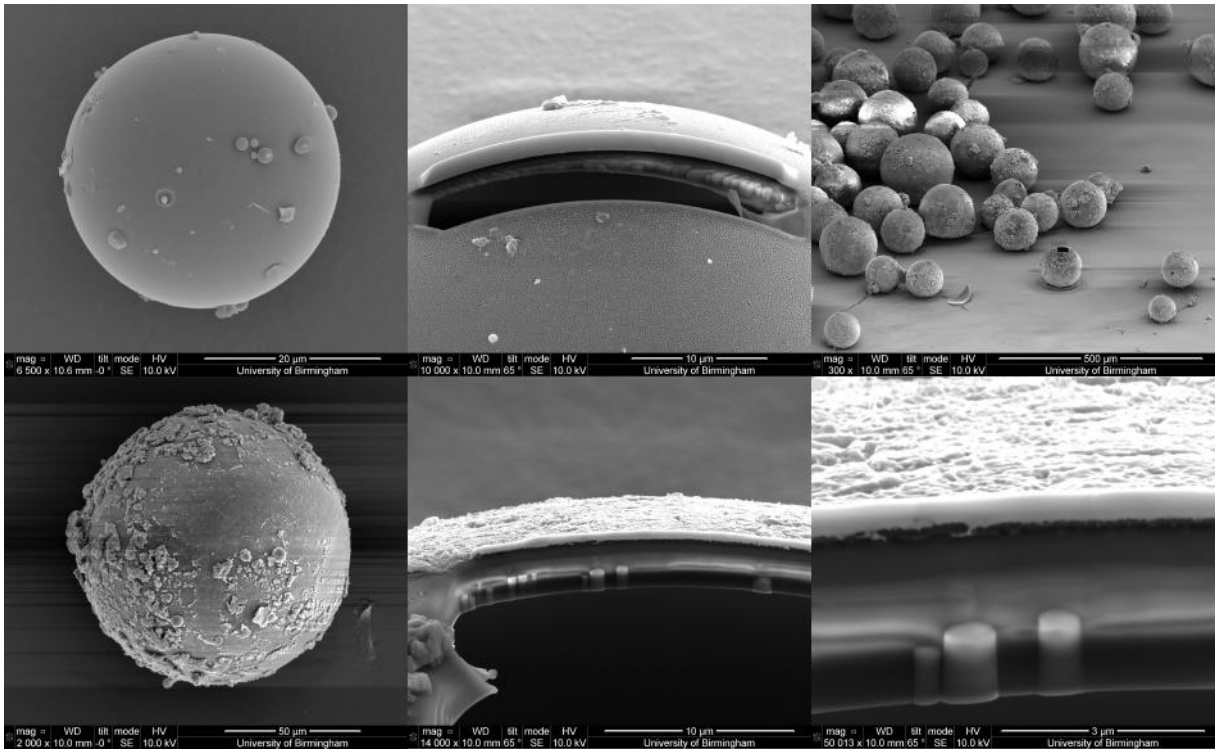

Figure 7.1: SEM-FIB images (from top left clockwise, scale bar values in parentheses): single pristine FAC (20 μm), single pristine FAC with ion beam milled trench (10 μm), multiple FAC-TiO_2-139 (500 μm), single FAC-TiO_2-139 (50 μm), single FAC-TiO_2-139 with ion beam milled trench (10 μm), single FAC-TiO_2-139 with ion beam milled trench high magnification (3 μm)

Coating methods have varied. Nair, Luo, and Heller [191] used a high temperature immobilisation procedure to attach commercial TiO_2 nano particles. Direct immersion slurry coating following the hydrolysis of titanium isopropoxide with water is one of the simplest methods reported [194]. Sol-gel coating is a popular choice of base coating method [193, 195, 334] in which a titanium alkoxide is first subject to acid catalysed hydrolysis which is then followed by condensation reactions to produce Ti-O-Ti polymeric chains [335].

The improvement of photo-catalytic activity of FAC-TiO_2 composites has also been an area of keen interest. In order to utilise the 45-50 % of sunlight that the planet's surface receives in the form of visible light significant efforts have been made to reduce the relatively large bandgap of pure TiO_2 that limits its activation to irradiation with photons of light in the UV domain ($\lambda \leq 387$ nm for anatase) [336]. Nitrogen doping of FAC-TiO_2 resulted in progressive reduction in the band gap (3.2-2.7 eV) of the materials

with increasing nitrogen loading; the doping was carried out by incorporating the addition of urea into the sol gel coating [334]. Fe^{3+} doping has been shown to increase the photo-catatytic activity of FAC-TiO_2 composites: again the effect appears to be as a result of shifting the absorption edge into the visible range [195]. A novel method of inducing an increase in visible light photo-catalytic activity involved treating FAC-TiO_2 with hydrogen peroxide (H_2O_2) to form surface complexes between titanium (IV) and H_2O_2 [193]. Other efforts to improve FAC-TiO_2 performance have centred around the selectivity to a particular pollutant. The concept of molecular imprinting technology has been applied in order to introduce a molecular template to the coating process that then leaves a cavity on the surface which the targeted pollutant can selectively bind to [337–339].

Silver has also been used as a dopant for FAC-TiO_2 composites [266]. Silver nitrate was added in a sol-gel coating process to produce a bulk chemically doped FAC-TiO_2-AgCl composite which exhibited improved photo-catalytic at an optimum silver loading intermediate in the range of loadings tested. The best performance came from a doping ratio of 13.5 wt% (of FAC). In order to reduce the amount of expensive silver nitrate used, the current study synthesised FAC-TiO_2 via a slurry evaporation technique followed by a silver photo deposition procedure. Different FAC particle sizes were used as substrates and the effects investigated. As far as the author is aware this is the first report of the effect of the substrate size on the photo-catalytic activity of FAC-TiO_2 composites.

7.2 Experimental

7.2.1 Materials

FACs and a size classified coal fly ash (SCFA) were provided by RockTron Mineral Services Ltd. All other materials were reagent grade: titanium isopropoxide (TITP), Degussa P25 and methyl orange (MO) were supplied by Sigma Aldrich (UK); nitric acid (HNO_3)silver nitrate ($AgNO_3$), oxalic acid, corundum and ethanol were supplied by Fisher Scientific

(UK); distilled water was used throughout.

7.2.2 Methods

FAC-TiO_2 Synthesis

FAC as supplied was sieved into 5 size fractions using sequentially stacked sieves and a mechanical shaker. FACs were obtained from the SCFA via sink float separation in a separating funnel with water. A slurry procedure was adapted from the hybrid slurry procedure for coating of CFA by Shi et al [340]. To increase the coating uniformity the FAC samples were washed with 250 ml of either 0.5 M or 2 M HNO_3 for a period of 30 minutes under magnetic stirring. The slurry of acid and FAC was then placed in a separating funnel and the remaining floating fraction was collected, washed with distilled water, filtered and then dried in an overnight in an oven at 80°C.

TiTP and ethanol (mol ratio 12.695:1) were added to a beaker and stirred magnetically for 10 minutes. An amount of FACs (to result in a theoretical loading of TiO_2 of 24.5 wt%) were added to the beaker and further stirring took place for one hour. Distilled water was added to induce hydrolysis dropwise at a H_2O/TiTP molar ratio of 2.7:1. The slurry was then immediately poured over a large enamel tray into a thin film and the alcohols allowed to evaporate in a fume cupboard. Once evaporated the tray was placed in an oven at 80°C and the samples were dried overnight. The samples were then calcined in a furnace at various temperature and times to increase the crystallinity of the TiO_2. After calcining the FAC-TiO_2 composites were placed into a separating funnel with distilled water, sonicated for one minute to encourage loosely attached TiO_2 to be released and only the particles that retained the ability to float were collected.

FAC-TiO_2-Ag Synthesis

Deposition of silver particles onto the TiO_2 surface was conducted utilising an adapted photo-deposition method [323, 341]. Known amounts of a 0.001 M $AgNO_3$ solution were

mixed with Oxalic Acid at a molar ratio of 1:25 on a magnetic stirrer for two minutes. Then FAC-TiO_2 particles were added and the magnetic stirrer was placed under a UV-vis irradiation exposure panel consisting of two black UV fluorescent lamps and three white light fluorescent lamps for a period of 2 hours. The particles were then placed in a separating funnel, the floating particles were retained, washed and dried in an oven at 80°C.

Materials Characterisation

The particle size of the FAC-TiO_2 particles was analysed directly using an optical microscope fitted with a digital camera and the image analysis software ImageJ, for each sample at least 200 particles were sized. A CFEI Quanta 3D FEG focused ion beam scanning electron microscope (FIB-SEM) fitted with an energy dispersive spectrometer was used to analyse one FAC-TiO_2 composite. Gallium milling enabled a composite particle to be cut directly into to reveal the hollow particle internally. The optical properties of the FAC, FAC-TiO_2, and FAC-TiO_2 were determined using Lambda 35 spectrometer, equipped with integrated sphere. The total diffuse transmittance of the samples was measured. XPS analysis was carried out using a Kratos AXIS Supra: the area of acquisition was 700 by 300 μm, the x-ray power 300 W, a pass energy of 40 eV was used, the charge neutraliser was on, and calibration was to C1s for C-C/H at 285.0 eV. XRD was conducted using a Bruker/Siemens powder diffractometer D5000. In order to perform Rietveld analysis the sample was mixed with 10 wt% corundum and ground using an agate pestle and mortar for 5 minutes. The sample was then pressed into a sampler holder and the XRD scan was run from a 2θ of 15-60° with a step size of 0.04° and a step duration of six seconds. Rietveld analysis was conducted using MAUD [236]. The accuracy of the method was assessed using cenospheres and 5 wt% Degussa P25. The Rietveld analysis was determined to be accurate to within 4%.

Photo-catalytic testing

An irradiation exposure panel was fitted with two 12 W UV black fluorescent lamps and three white fluorescent lights. The exposure panel was mounted on four legs to allow an enamel tray to fit directly underneath. The enamel tray was centred and placed in the same place for each experiment, it was filled with 250 ml of a desired concentration of methyl orange, and the liquid surface area measured 0.17 by 0.23 metres. Samples were added to the tray and mixed. Prior to the start of the experiment the tray was covered and left for 30 minutes for dye adsorption to equilibrate. After 30 minutes the tray was placed under the exposure panel and the lights turned on. Aliquots were removed every 15 minutes taking care not to remove particles, passed through a syringe filter to remove any residual turbidity and analysed in a spectrophotometer for absorption at a wavelength 460 nm.

To assess the effect of mixing on the degradation of MO, the experimental set-up was adjusted such that a magnetic stirrer was incorporated under the exposure panel and the reaction vessel was a borosilicate evaporating dish into which 100 ml of MO was added. Stirring was always conducted at a nominal speed of 1 out of a scale of 6.

For all the photo-catalytic testing experiments conducted, the cenospheres exhibited a tendency to slide up the sides of the containing vessel. In order to attempt to combat this particles were washed from the sides during each sample aliquot removal, however there were undoubtedly some differences in experimental conditions experienced as a result of the particles attaching to the vessel sides; this was unavoidable with the current setup. In future modifications to the vessel material might be made to make it less attractive to the cenospheres.

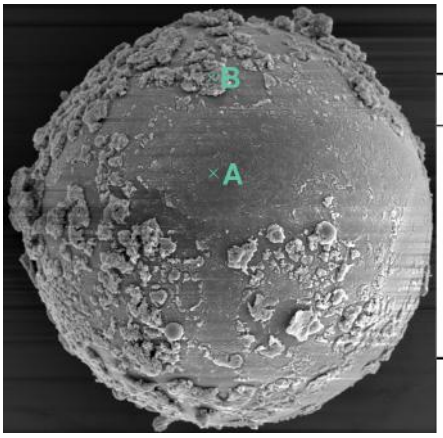

Component	A	B
SiO_2	38.1	2.1
Al_2O_3	41.4	nd
TiO_2	16.2	97.9
MgO	0.5	nd
K_2O	3.1	nd
Na_2O	0.6	nd

Figure 7.2: Shows crop of bottom left image in Fig7.1 and EDS scan spectra from two different points on FAC-TiO_2-139

7.3 Results and Discussion

7.3.1 Photocatalyst characterisation

A total of seven different samples were prepared. Table 7.1 shows the CFA source, the washing acid molarity, and the measured particle size and standard deviation of the samples. XRD analysis was performed on each of the samples and the results were refined using a Rietveld process. The bulk anatase contents are also shown in Table 7.1. It is clear that the coating process contains a significant measure of variability. There are no clear trends over the small sample size analysed, with respect to anatase loading against specimen particle size. Despite this the highest loading of all samples was found for FAC-TiO_2 which were also the joint smallest. It does appear that there is some evidence to suggest that washing the samples in 2M acid prior to coating allowed for greater overall anatase loading: for nominally similar particle sizes loading was 3.8 wt% vs 0.7 wt% and 6.6 wt% vs 1.2 wt%. The data also suggest that the source of the cenospheres might have an effect. The SCFAC-TiO_2-58 and the FAC-TiO_2-58 are both the same size but have loadings of 2.8 and 10.5 wt% respectively. It is possible that they have a different chemical make-up: indeed the XRD results suggest a complete absence of quartz in the SCFAC-TiO_2 sample, although decreasing quartz content also correlates with higher anatase content in the other samples. Without more detailed

chemical characterisation this is impossible to say. Between these two samples the other potential for differences in anatase loading stem from the difference in monodispersity. If the particles are polydisperse, then they could potentially pack together more tightly than a monodisperse system. This would mean that in general, as the slurry system dried the gaps between FACs, filled with the much smaller TiO_2 particles would be smaller, encouraging a more even coating. Because of the rudimentary nature of the coating method, which is desirable from a process point of view, more detailed characterisation work is required on the FACs at each particle size range in order to establish more robust conclusions.

Figure 7.1 shows electron images of specimen samples both prior and after coating. Coating has had a marked effect. Smooth pristine FACs are replaced by rough, textured surfaces with uneven coating thickness. This agrees well previous reports of TiO_2 coating on CFA microspheres from which the coating methodology used herein was developed [340]. It is possible to observe in the current micrographs the same granular agglomerations along with a smoother membrane which cracks upon possible heat shrinking when the particles are calcined [342]. However, the current work used a theoretical loading of TiO_2 of 24.5 wt%. At a loading level of 28.5 wt% Shi *et al.*, observed very little coating had taken place and found higher loading levels were required. The disparity could have occurred for any number of reasons including, but not limited to, using a different titanium alkoxide precursor, using fly ash cenospheres rather than coal fly ash, and the addition of the acid washing step. Evidence for the smooth membrane thin film coating is strongest in the bottom right of the images in Figure 7.1. After a trench has been cut out of the hollow sphere, a close up image reveals the existence of a thin film of discrete particles are suggested to be TiO_2 particles. Image analysis suggests a layer thickness of 200-300 nm. The results of an EDS scan on the area suggested the presence of TiO_2. Also revealed in this scan was the presence of Tungsten so an argument might be made that they consist of the Tungsten layer put down prior to the milling step. The absence of this layer in the corresponding close up of a pristine FAC suggests otherwise. The results of

two further EDS scans on two regions of the pre-milled FAC-TiO_2 particle are given in Figure 7.2. The results show that the EDS scan from the granular agglomerate is almost entirely made up of TiO_2. This means that at this point upon the sphere the layer was thick enough so that only the smallest amount of silica from the FAC can be detected. At point A, the film appears much more even and thinner, and this is confirmed by the resulting chemical composition which is much lower in titanium, as has been reported for CFA/TiO_2 composites [342].

The UV-vis spectra of pristine, TiO_2 coated, and Ag activated FAC samples are shown in Figure 7.3. It is evident that coating the samples with TiO_2 shifts the absorption edge towards the red end of the spectrum. There appears to be a significant increase in absorption at 400 nm for the TiO_2 coated samples which corresponds to a band gap of circa 3.0-3.2 eV [343]. The absorption from 400 nm to the rest of the visible region is increased further for both of the silver activated samples; the highest silver loading corresponding to the highest absorption which is consistent with other reports [344, 345]. The increased absorbance between 400-800 nm can be attributed to surface plasmon absorption. In the inset in Figure 7.3 it is evident that for the highest silver loading there is a small but discernible band around 440 nm which is consistent with some reports [344] but not with others [345]. The most probable reason for the differences in the position of the absorption bands is due to the likely differences in silver particle morphology between studies. Furthermore, because the band at 440 nm does not appear strongly, it is possible that the red shift in the absorption is not solely due to surface plasmon resonance [344]. Instead the greater contributing factor is that the band gap absorption shifts to a slightly higher wavelength.

Based on the UV-Vis measurements, the energy band gap of the samples was determined based on the absorption spectra, using Taucs relation [346, 347]:

$$\alpha h\nu = A(h\nu - E_g)^m \tag{7.1}$$

Where α is the absorption coefficient, hν is photon energy, A is an energy dependent

constant and m is an integer depending on the nature of electronic transitions. For the direct allowed transitions, m has a value of 1/2 while for indirect allowed transitions, n=2 [347]. The absorption coefficient, α, was calculated with the formula:

$$\alpha = \frac{1}{d}\ln\frac{1}{\tau} \tag{7.2}$$

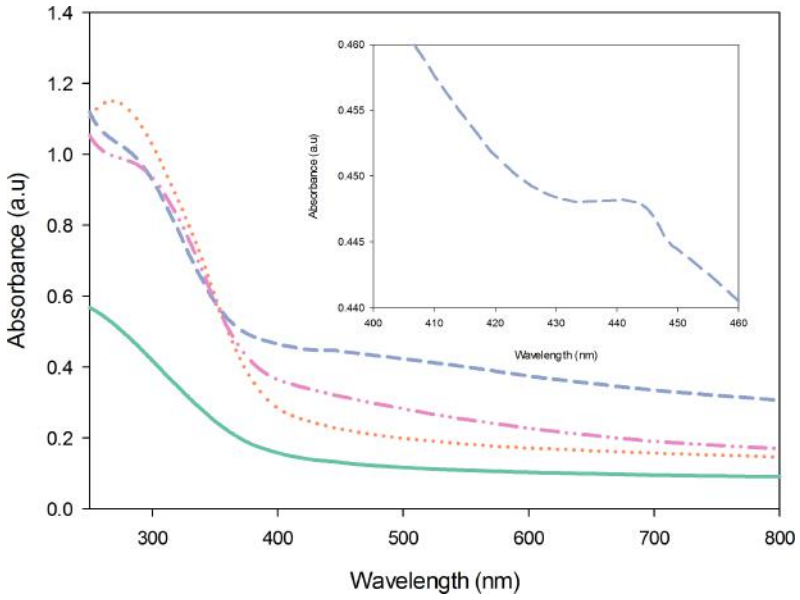

Figure 7.3: UV absorbance of FAC-78 (——), FAC-78-TiO_2 (·····), FAC-78-TiO_2-AG-H (– – –), and FAC-78-TiO_2-AG-L (– · –).

Where d is the thickness of the film (in this case film thickness was taken to be 90 μm) and τ is the transmittance. Figure 7.4 shows how the band gaps were calculated and the results show that the band gap of pristine FAC is 3.5 eV, FAC-TiO_2 is 3.32 eV, FAC-TiO_2-Ag-L is 3.28 eV, and that of the highest loading of silver FAC-TiO_2-Ag-H is reduced to 3.18 eV. The decrease in band gap value of silver deposited photocatalysts relative to their pristine state has been reported before [345] and is thought to be a result of the metallic clusters that introduce localised energy levels in the TiO_2 band gap. Electrons can be excited with lower energy from the valence band to these localised energy levels rather than to the conduction band of the TiO_2 [344]. These results, and those of Figure 7.3, suggest that the metal clusters are poly-disperse in size because the absorption in the visible region that corresponds to excitation from the valence band of the TiO_2 to

the unoccupied level of the silver cluster, is not constant and instead exhibits a gradual decline towards the red wavelengths.

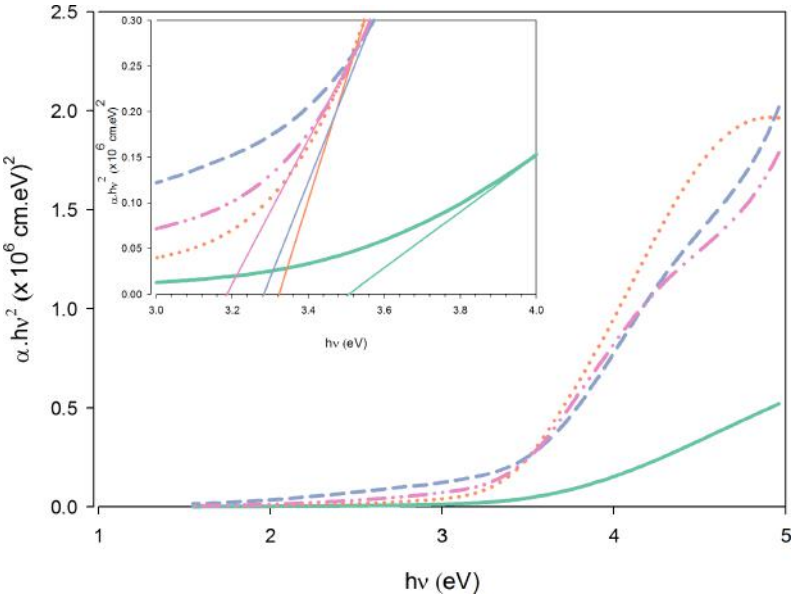

Figure 7.4: Tauc plots of FAC-78 (——), FAC-78-TiO_2 (·····), FAC-78-TiO_2-AG-H (– – –), and FAC-78-TiO_2-AG-L (– · · –).

The XPS survey scans shown in Figure 7.5 reveal the surface chemistry of pristine FAC, TiO_2 coated FAC, and Ag deposited samples at two different loadings. The results are broadly aligned with expectation. Adventitious carbon is consistently present throughout all the samples, exhibiting itself with peaks at 285.0 eV that correspond to C1s. For pristine FAC peaks at between 101-103 eV can be assigned to Si2s in an oxide form and between 73-75 eV can be assigned to Al2s again in oxide form [348]. A narrow region scan (not shown here) of FAC-TiO_2 features a strong peak at 458.8 eV which corresponds to $Ti2p_{3/2}$ and indicates that the Ti atoms are present in the form Ti^{4+} [345]; this confirms the results of the SEM-EDS examination. A detailed scan on the Ti2p region revealed that the $Ti2p_{3/2}$ peaks were all in identical positions and were not shifted towards higher energies as has been reported for other incorporation methods that involve a calcination step [346, 349].

The O1s spectra of Figure 7.6 are difficult to interpret because of the possibility of peaks for different species overlapping. However, assigning peaks can assist in understanding the nature of the coating processes. For the uncoated spheres we may assign

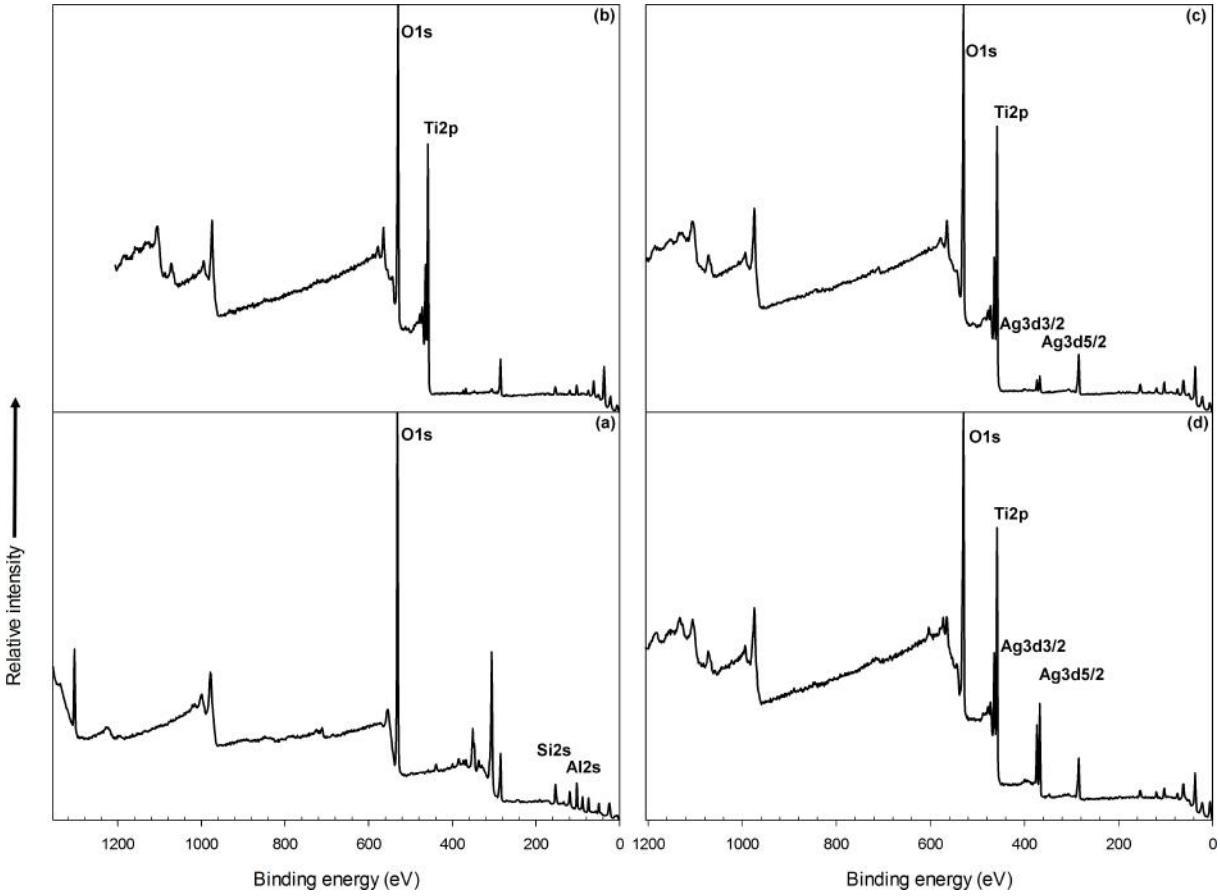

Figure 7.5: XPS survey scans of (a) FAC-78, (b) FAC-78-TiO_2, (c) FAC-78-TiO_2-AG-L, and FAC-78-TiO_2-AG-H.

peaks at 531.2 eV and 532.2 eV to Si-O-Si and Si-O-Al respectively [350] which represents the aluminosilicate glass, mullite, and quartz of the FAC matrix. In addition, two more smaller peaks may be observed at 532.7 eV and 533.7 eV which are probably the result of adventitious carbon in the form of C-O-C/C-OH and C-O=C respectively. In Figure 7.6(b) the appearance of an extra peak at 530.1 eV is observed which corresponds to the lattice oxygen in anatase [351]. In Figure 7.6(c) that shows the O1s spectra of FAC-TiO_2-AG-H, the same peaks are observed as for the particles with no silver deposition, however it is apparent that the peak at 532.2 eV has increased in intensity which puts it in parity with the peak at 531.2 eV. Since there is little chance of affecting the Si-O-Al bonds, this increasing intensity must be the result of another bonding feature. Peaks at 532.2 eV have been described to have been the result of any of the following: adsorbed oxygen, surface oxygen vacancies, hydroxyl groups, and adsorbed water although surface hydroxyl groups were thought to be the most likely. [352]. Despite the uncertainty in interpretation of Figure 7.6 there definitely appears to be a broadening of the shoulder of the O1s peak with deposition of silver on the FAC-TiO_2 composites. There is a some possibility that this effect is caused by an increase in Ti-OH groups since adsorbed water would likely be removed int he ultra high vacuum environment of the XPS equipment.

It is possible to deconvolute the XPS signals of the Ag3d level such that a qualitative assessment of the oxidation state of silver can be conducted. The bonding energy values Ag^0, Ag_2O and AgO are all very similar: for $3d_{5/2}$ they have been reported as 368-368.3, 367.6-367.8, and 367.3-367.4 eV respectively. The narrow range of peaks results in too much uncertainty for any quantitative analysis. However, following the approach of Pulido Melian *et al.*, [345], the spectra were deconvoluted into a peak representing metallic silver at 368.3 eV and one at 367.4 eV which is assigned to oxidised silver on a general basis. Figure 7.7 shows that in terms of relative intensity, there is not much difference between the samples. However, the higher Ag loading shows a greater intensity which is unsurprising as it relates to the level of dispersion of the Ag on the TiO_2 surface. Interestingly, both samples exhibit an extremely high Ag^0/oxidised Ag ratio which is

higher even than that reported previously [345]. The deposition process of silver particles onto the TiO_2 surface proceeds according to the following scheme [341]:

$$TiO_2\{e^-,h^+\} + Ag^+_{adsorbed} \rightarrow TiO_2Ag^0\{h^+\} \tag{7.3}$$

When the UV light excites an electron from the valence band to the conduction band an electron hole (e^- ,h^+) pair is formed. The electron from the excited TiO_2 is able to transfer to the silver ion and in doing so reducing it to metallic silver which explains the results found in Figure 7.7. Therefore according to this analysis, if sufficient time and intensity of UV irradiation is supplied, then using a photo-deposition method to load silver onto TiO_2 should result in metallic silver.

7.3.2 Photocatalytic decoloration of methyl orange (MO)

Although MO has been employed in this study as a model pollutant to illustrate a more general photocatalytic effectiveness, in reality it is highly applicable to the effluent treatment of the textile industry. From this point of view it was desirable to study the dependence of the reaction rate on reactant concentration. When TiO_2 is irradiated with light energy that equals, or exceeds its band gap energy (E_g), conduction band electrons (e^-) and valence band holes (h^+) are formed. A number of reactions are then possible: (1) e^- reduces the dye; (2) e^- reacts with O_2 reducing it to the superoxide radical anion (O_2^-); (3) h^+ oxidises the organic molecule to form R^+; (4) h^+ reacts with H_2O to form OH radicals; or (5) h^+ reacts with hydroxide ions to form OH radicals [353].

OH radicals are a strong oxidising agent and are able to oxidise most azo dyes such as methyl orange to mineral end products [353]. Figure 7.8(a) shows the photo oxidation of methyl orange with initial concentration ranging from 10-20 ppm using FAC-TiO_2-139 at a solids liquid ratio of 4.8 g/L. A photocatalytic reaction occurs on the surface of the catalyst and so it seems intuitive that good adsorption capacity improves the rate of reaction. Adsorption-kinetic models, most commonly the Langmuir Hinshelwood (L-H),

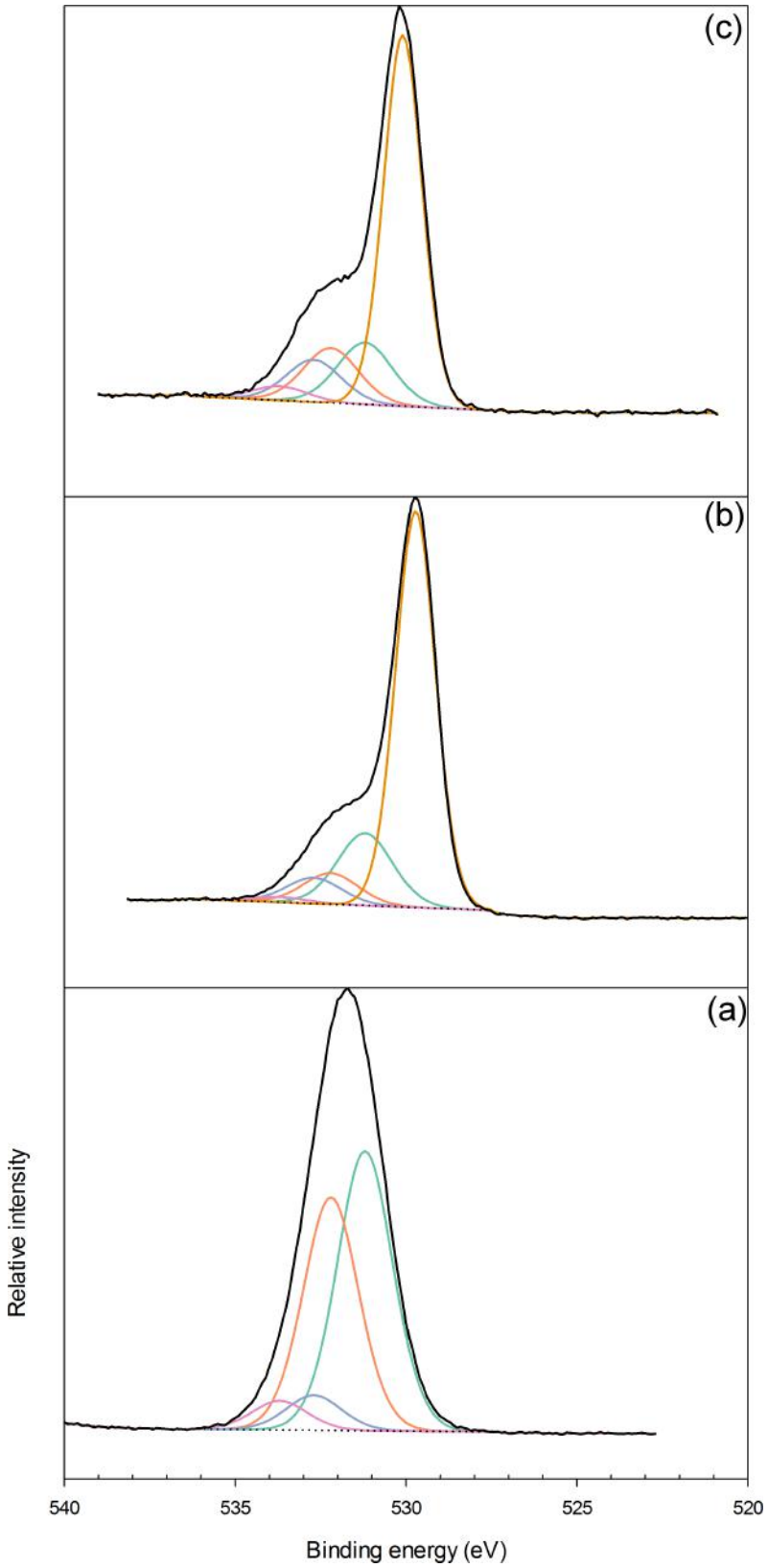

Figure 7.6: XPS O1s spectra (a) FAC-78, (b) FAC-78-TiO_2, and (c) FAC-78-TiO_2-AG-H.

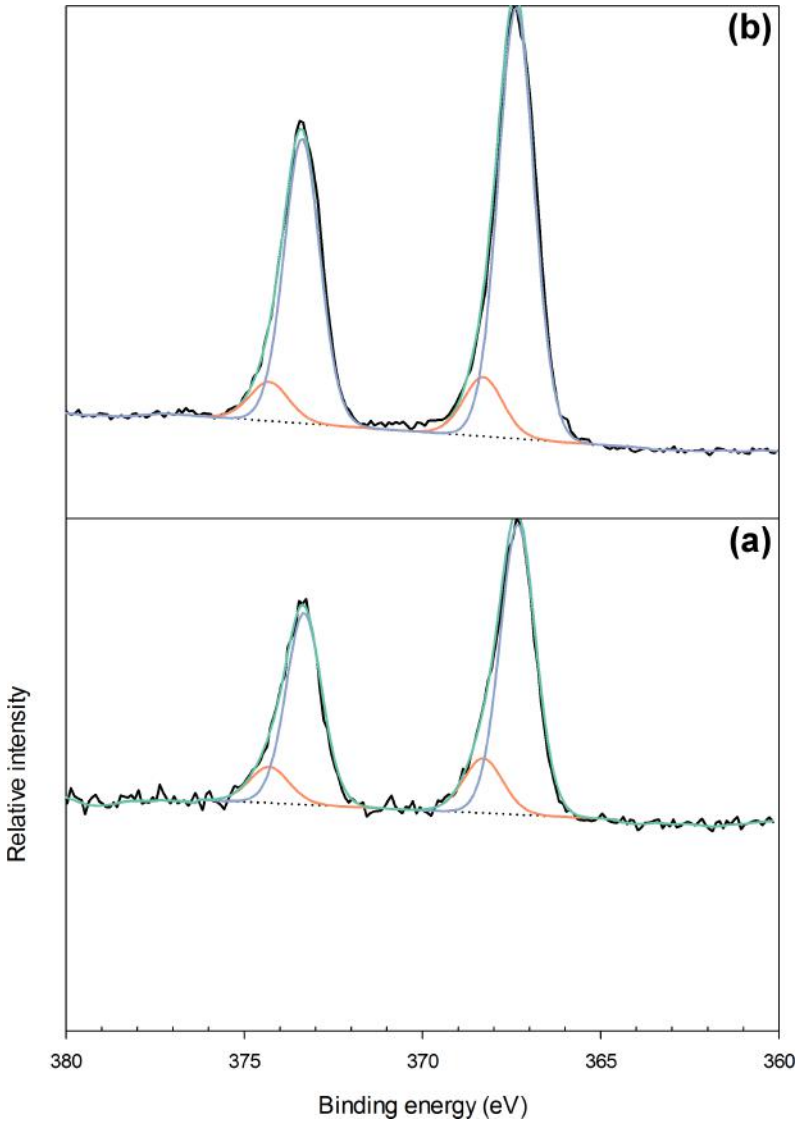

Figure 7.7: XPS Ag3d spectra (a) FAC-78-TiO_2-AG-L, and (b) FAC-78-TiO_2-AG-H.

are applied to model the degradation of organic compounds via photocatalysis [354]. In this study the reaction progress has been modelled with a first order rate expression such that an apparent reaction rate constant k_{obs} can be obtained using via regression. At this stage these reaction rate constants are merely fitting parameters as it is not known whether L-H kinetics can be applied.

$$r = \frac{\mathrm{d}C}{\mathrm{d}t} = k_{\mathrm{obs}}C \tag{7.4}$$

In this case the data was fit to the integrated form of the rate equation without linear transform.

$$C = C_0 \mathrm{e}^{-k_{\mathrm{obs}}t} \tag{7.5}$$

The fits yield very good correlation coefficients and low residual values but caution must be taken when interpreting these results. It has been shown that for systems that are exhibiting an inhibiting effect of the reactant there is the chance that by fitting the curves blindly to (L-H) kinetics and assuming that the resulting rate expression reduces to Equation 7.4 then erroneous conclusions can be drawn [355].

Figure 7.8(b) shows the apparent reaction rate constant increase slightly between 10-12.5 μM and then steadily decrease as the concentration increases past this point. The apparent rate constants were then used to obtain the initial rate of reaction at initial concentration and the results are plotted in Figure 7.8(c). It becomes clear if considering a L-H reaction mechanism whereby the rate of a single component on the surface is proportional to the extent of surface coverage [354], that past 10 μM the sites are saturated with dye molecules. As the reaction proceeds the excess dye molecules actively start to inhibit the reaction as shown by the decreases in apparent reaction rate constant as the concentration is increased. A competing, or perhaps assisting explanation is that at higher dye concentrations UV light might be absorbed by the MO itself reducing the production of OH radicals and therefore leading to reduced reaction rates. Although it would have

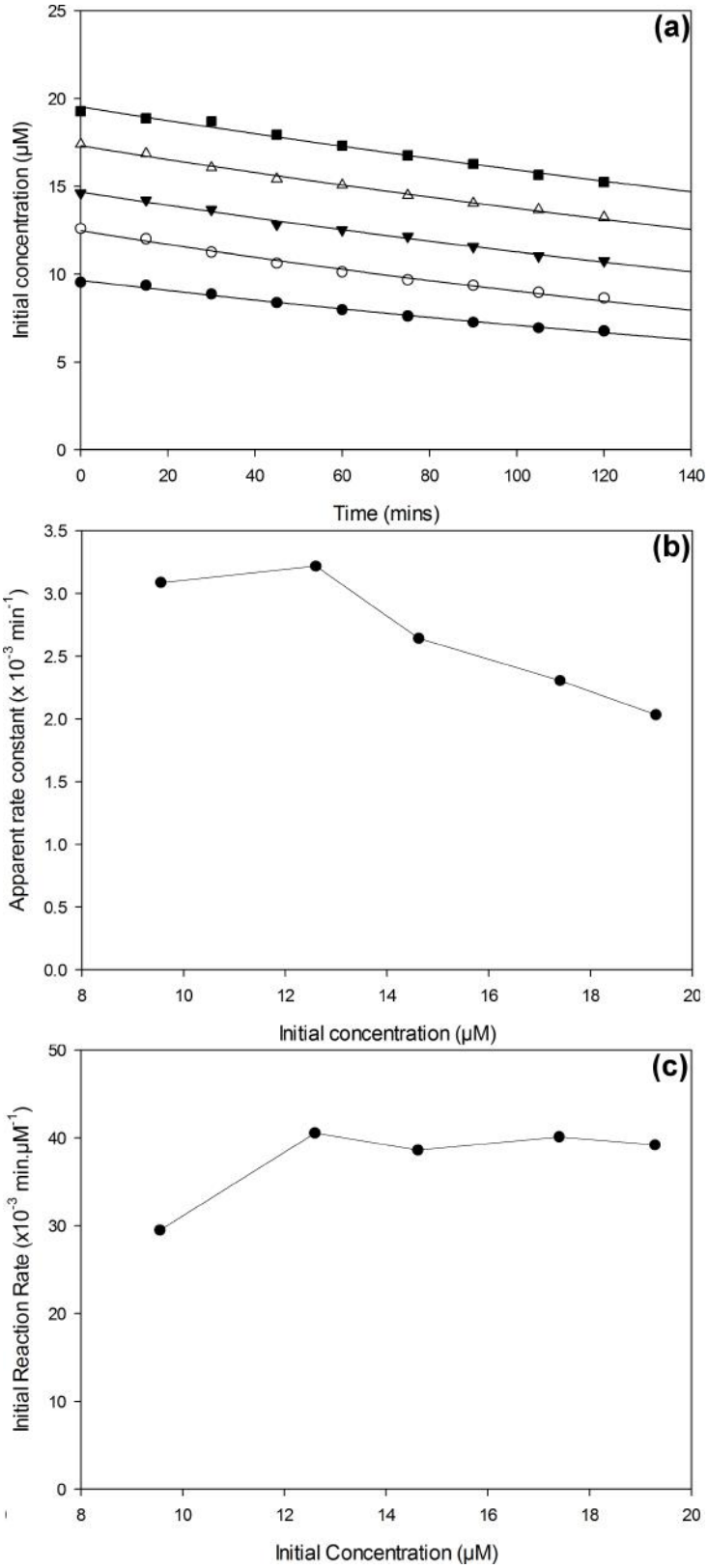

Figure 7.8: Effect of methyl orange concentration: (a) decoloration of FAC-TiO_2 -113 at 4.8 g/L from different initial methyl orange concentrations, (b) apparent rate constant, k_{obs} as a function of initial concentration, and (c) initial reaction rate (r_0) as a function of methyl orange concentration.

been preferable to have more experimental points in the lower concentration range the results of Figure 7.8 are entirely consistent with another study conducted using TiO_2 and MO [356]. Despite the fact that first order kinetics describes the reactions well over the time period studied, there is a strong possibility that as reaction time proceeds and the concentration reaches lower levels then the inhibition effect of higher concentrations will be less apparent and the experimental data will deviate from the exponential fit. For the remainder of this chapter the initial concentration was held constant at the lowest concentration of 10 μM. Initially this appears too high to be confident that L-H pseudo first order kinetics apply; however the experimental curve of Figure 7.9 shows that the decoloration of 10 μM MO with 4 g/L follows a first order dependence on concentration. There is a very slight deviation from the fitted line at large reaction times but this is not conclusive.

There is much debate in the academic literature about the relevance of L-H kinetics to photocatalysis with a variety of different mechanistic concerns [354]. For instance for systems that degrade via OH radical attack, there is a strong possibility that adsorption might not account for the entirety of the reaction as OH radicals have been shown to be able to diffuse into solution. A more thorough consideration of these issues surrounding the kinetics is certainly of great interest, but unfortunately outside the scope of this study. For the remainder of the results analysis, apparent rate reaction constants were used disregarding the afore mentioned. Because the initial concentrations and light intensities used were constant throughout, this should be sufficient to capture kinetic differences between samples.

7.3.3 Catalyst loading and diameter

The catalyst particles that were washed with 0.5 M HNO_3 are presented in Figure 7.10 which shows how the reaction rate constant changes with diameter. The rate constant increases as the diameter of the catalyst particles decreases. This implies a dependence on the catalyst specific surface area (a_s). As the catalyst surface area increases, so does

the quantity of OH radicals forming on that surface. However, if only this were the case, then the reaction rate constant could be normalised by a_s and it would be possible to draw a regression line through the data with $k_{obs} = K^* d_p^{-1}$ as a_s is only proportional to the diameter:

$$a_s = \frac{s}{m} = \frac{6\pi d^2}{\rho \pi d^3} = \frac{6}{\pi d} \tag{7.6}$$

where s is the surface area per particle and m is the mass per particle. What is seen in Figure 7.10 is that $k = K^* d^{-2}$. There is a physically meaningful explanation for this that considers the unusual position of the floating photocatalyst particles. If these particles are considered to form a monolayer, and are randomly packed, then the theoretical area (A_c) that they can cover is given by the following:

$$A_c = \frac{n_p}{n} = \frac{6M\pi d^2}{\rho \pi d^3 4\phi} = \frac{6M}{4\phi\rho d} \tag{7.7}$$

where n_p is the number of particles, n is the number of particles per unit area, M is the mass of particles in the area A_c, and ϕ is the two-dimensional packing fraction. It becomes obvious that to normalise the reaction rate against area requires to divide by both a_s and A_c which both contain a diameter term. Because all the parameters that form are assumed constant between samples the apparent rate constants can be normalised by multiplying by (d^2/M). Table 7.2 shows that the deviation between samples is only 13% which is a fairly good reflection of the foregoing analysis.

$$k_r = \frac{4\phi\rho^2 d^2 k_{obs}}{36M} = B\frac{d^2 k_{obs}}{M} \tag{7.8}$$

Since the experimental planar surface area can be directly measured, it was possible define a particle loading that represented the theoretical maximum that could exist as a mono-layer that would still cover the total area. In order to do so a choice was necessary as to what packing fraction should be used. For perfectly mono-disperse discs, theoreti-

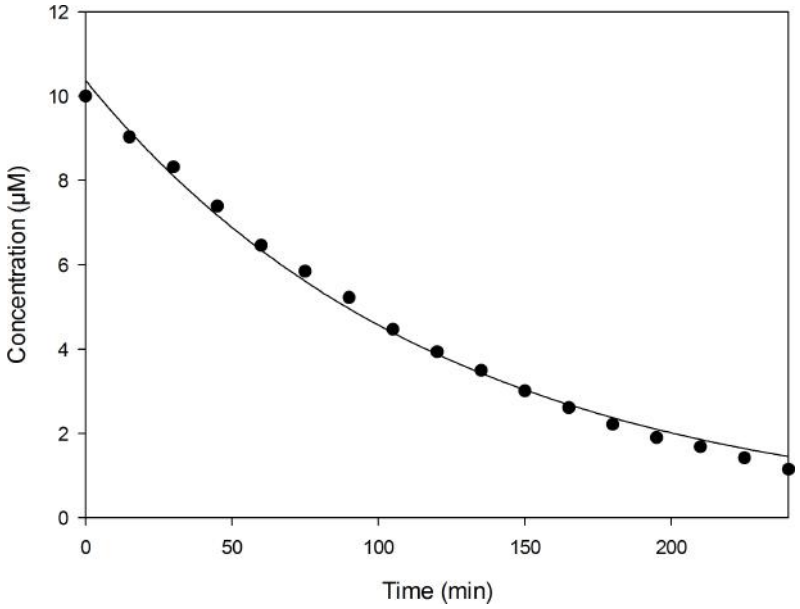

Figure 7.9: Decoloration of 10 μM methyl orange with 4 g/L FAC-TiO2-79. Line is the experimental data fitted to Equation 7.5

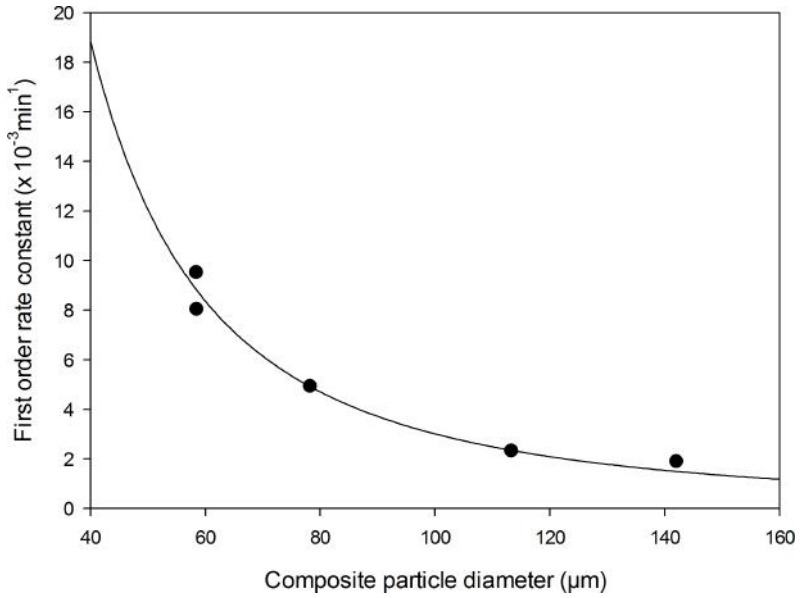

Figure 7.10: Apparent rate constant shows inverse proportionality to the square of the particle diameter. Fitted line represents $k_{obs} = K^{*}d^{-2}$.

Table 7.2: Intrinsic reaction rates normalised by both substrate article surface area and illumination area

Sample	k_r (x 10^{-8} $m^2g^{-1}min^{-1}$)
FAC-TiO_2-142	3.2
FAC-TiO_2-113	2.7
FAC-TiO_2-78	3.0
FAC-TiO_2-58	3.0
SCFAC-TiO_2-58	3.8
Average	3.2
Standard Deviation (%)	13.1

cal and experimental investigations confirm that random jammed packing has a packing fraction of 0.813 [357]. In this case, the total planar irradiation area could be filled with particles that were packed more loosely, and in any case spheres with just a slight degree of polydispersity are more likely to do so. For the purposes of this analysis a packing fraction of 0.64 was used. After rearrangement of Equation 7.7 for the particle mass and substitution of the irradiation area, the theoretical mass required for monolayer packing for each set of particles was determined. Figure 7.11 shows the particle loading normalised against this theoretical quantity. It can be observed when this normalised catalyst loading reaches or is close to unity in all three cases, the reaction rate increase levels off. Below this level the reaction rate increases with increased particle loading. In many previous photocatalytic studies, the reaction rate is seen to increase up to a maximum and then either level off or in some case decrease. The explanation for this if often that as the loading increases the turbidity of the solution increases which attenuates the radiation. In the case of a decrease in reaction rate, it has been said that the TiO_2 might be reflecting the irradiation back out of the reaction chamber. In this case the situation is slightly different in that the catalyst is able to form an opaque layer at the interface of the liquid and air. However the mechanisms are broadly similar, at complete coverage of particles, there is little added benefit to increasing the loading as this will likely result in particles blocking light from each other. Indeed in a similar study of Holdich et al. [323], it was found that reflection caused a drop off in activity at 100% surface coverage. Reasons for the same effect not being observed here are unclear but might be caused by differences in where the

two particle systems reside at the air-water interface. The striking feature of Figure 7.11 is that the point at which this occurs has been predicted so successfully. Another feature of this analysis is that using Equation 7.8 and the average value for k_r from Table 7.2 a fitted line was drawn through the points for one of the samples by altering the value of M.

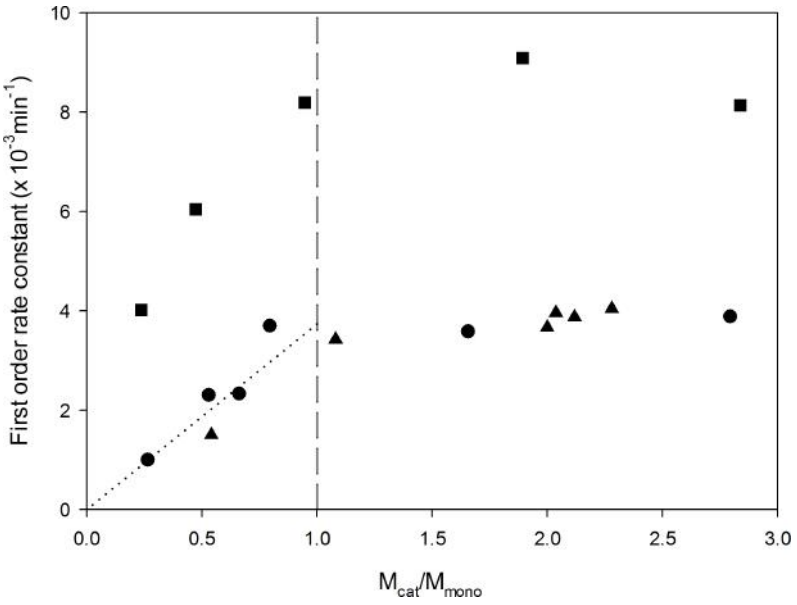

Figure 7.11: Apparent rate constant as a function of catalyst loading normalised by the loading required to form a monolayer of particles at the air liquid interface: FAC-TiO_2 -79 (■), FAC-TiO_2 -113 (●), FAC-TiO_2 -137 (▲).

7.3.4 Catalyst stability

A particular feature of photocatalysed reactions is that the catalyst may be reused many times, therefore providing a cheap method of the treatment of effluent contaminated by organic pollutants. Deactivation of TiO_2 photocatalysts over time has proven to be a barrier to successful commercialisation. This occurs when partially oxidised intermediates block the active catalytic sites on the surface. It is more predominant in gas phase reaction than aqueous, but should still be considered [336]. For immobilised TiO_2 there is also the possibility that TiO_2 will removed from the substrate surface via attrition. Any assessment of a particular immobilised photocatayst solution must include a measure

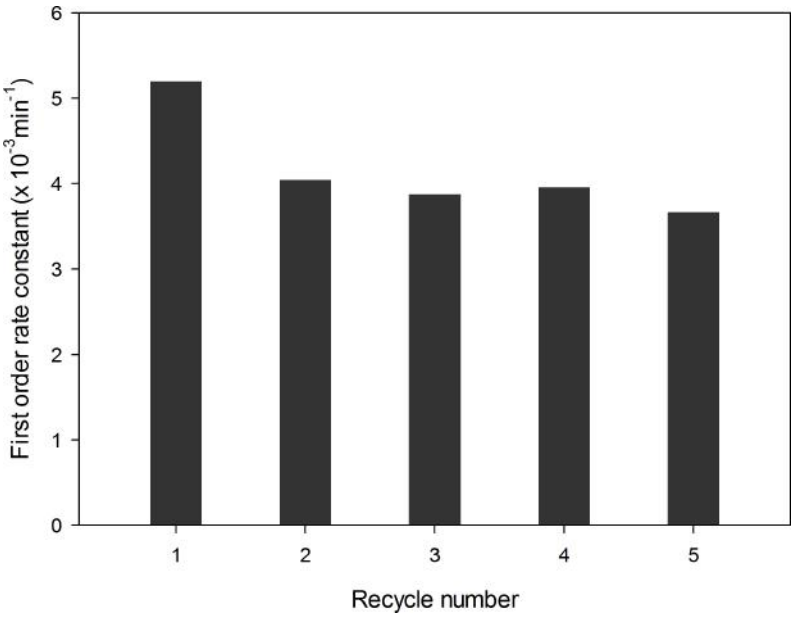

Figure 7.12: Apparent rate constant over a series of sequential experiments

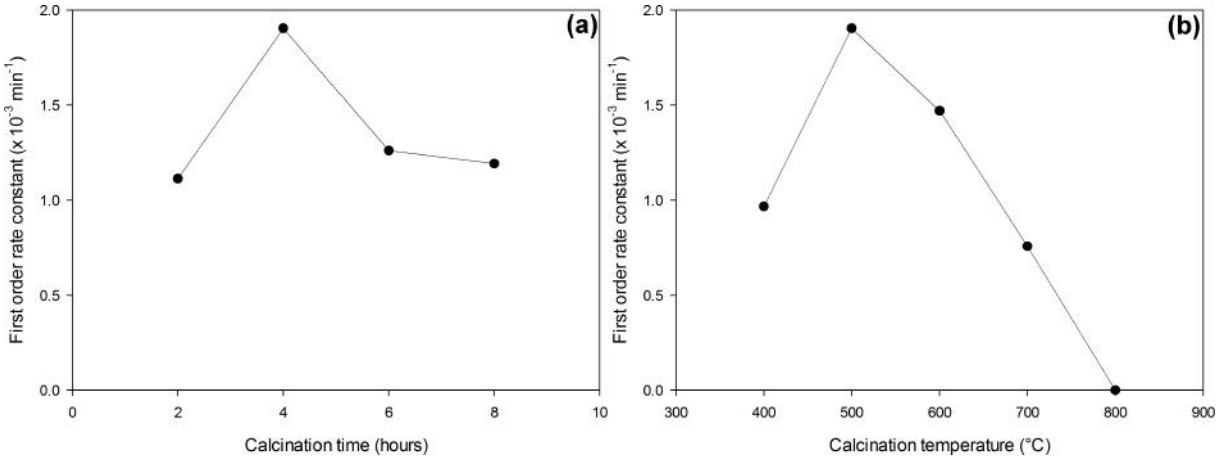

Figure 7.13: Apparent rate constant variation with calcination conditions: (a) different durations at 500°C and (b) different temperatures for a duration of 4 hours

of the performance over a series of sequential cycles. Figure 7.12 illustrates a series of experiments with the same catalyst sample. After each samples the catalyst was recovered via filtration, washed dried and then reused. It is clear that after the first run there is a slight drop off of activity. It appears as if there is some residual loosely attached TiO_2 on the cenosphere surface that breaks away after an experimental run. However after this the activity stabilises very well with very little difference between runs 1-4. Therefore it appears that intrinsic TiO_2 deactivation is not occurring on the experimental time scales investigated.

7.3.5 Catalyst calcination

The effectiveness of TiO_2 manufactured from the hydrolysis of a titanium alkoxide is highly dependent on the operating variables of the calcination process. The effect of the two most important variables, time and temperature, on the photocatalytic activity is shown in Figure 7.13. There is a clear non linear relationship for both with optimal conditions found somewhere between 3-5 hours and 450-550°C . At temperatures exceeding 500°C the effectiveness of the catalyst deteriorates sharply until at 800°C there is no activity at all. There are a variety of factors that might be responsible for this behaviour. Some of the most important are the extent of crystallisation, the crystal size, the specific surface area, and the crystal phase [358]. Both temperature and time have significant effects and indeed similar effects on the preceding factors. For instance, as the crystallisation temperature increases for a given time period, the extent of crystallisation increases which means more of the TiO_2 coating is in the catalytically useful phase of anatase. However, above a certain temperature the phase starts to transform to rutile which is not photocatalytically active. Conversely as the temperature increases, the specific surface area decreases as a result of the TiO_2 crystal size gradually increasing. As the specific surface area decreases there are less active sites to which the MO molecules can adsorb and photooxidise and so the reaction rate decreases accordingly. The results presented in here are consistent with this explanation. The increase of activity between 2-4 hours and 400-500°C is as result

of increased anatase content. From 4-8 hours and 500-700°C the crystal size of anatase increases and so the specific surface area decreases which results in the lowering of activity. At 800°C the complete lack of activity must be ascribed to a total phase transformation of the amorphous TiO_2 into rutile. The results are broadly aligned with previous studies of TiO_2 immobilised on CFA [358], although that report suggested optimal temperatures of 700°C for a calcination time of 2 hours. They highlight the importance of the calcination step on catalytic activity. In addition they suggest that it might be important to consider the interaction effect between time and temperature which can only be determined with a factorial experimental design unfortunately outside the scope of this study.

7.3.6 The effect of silver deposition on reaction rate

It has already been shown that the addition of silver shifts the absorption spectrum towards the red and slightly reduces the band gap energy. However when using the photodeposited Ag-TiO_2 in the degradation of MO there is a noticeable increase in the photocatalytic degradation rates. Figure 7.14 shows how reaction rate relative to that of pristine TiO_2 . It is noticeable that reaction rates increase up to a maximum at a theoretical Ag (at%) content of around 1.8% and then decline slightly. The increase can be attributed to the electronic interaction that takes places between the silver and TiO_2 surfaces. When exposed to irradiation energy sufficient to excite a valence band electron, the silver particle is able to act as an electron trap. The transference of an electron from the conduction band of the TiO_2 to the silver particles is possible because the Fermi level of TiO_2 is higher than that of silver. This can cause the formation of Schottky barrier which improves the charge separation and reduces the amount of electron hole recombination [345]. The speed of the transfer from TiO_2 to silver is faster than the recombination step and the transfer of electron to oxygen. Therefore the silver deposits can act as electron scavengers and ultimately transfer them to oxygen to form $O_2^{\bullet -}$ superoxide and then ultimately highly oxidising hydroperoxyl radicals via the following reaction [341]:

$$e^-_{Ag} + O_{2ads} \longrightarrow {O_{2ads}}^{\bullet -} \tag{7.9}$$

$${O_{2ads}}^{\bullet -} + H^+ \longleftrightarrow HO_2^{\bullet} \tag{7.10}$$

Valence band holes can then form OH radicals via reaction with surface OH groups and/or surface H_2O molecules [344]. This is a plausible explanation for the behaviour shown in Figure 7.14 where the Ag content is positively associated with an increase in photocatalytic activity. It does not explain the drop off of activity past a certain Ag content. Some authors have reported that the catalytic activity merely stabilises as the Ag content is increased past a certain level [345]. The reasoning behind this was that the addition of silver creates a finite number of extra $\{e^-$, $h^+\}$ pairs and that if these are sufficient to degrade the initial concentration of pollutant then further silver addition has no marginal benefit. It seems likely that this depends on whether the system is operating in the region of increasing rate constant with initial pollutant concentration or in the decreasing region (as discussed in section 7.3.2). If in the non-saturated region an increase of oxidising species would increasing the probability of reaction with dye molecules. If in the saturated region, however, then increasing the oxidising species would have a limited effect assuming that oxidising species were unable to diffuse into the bulk. In this case the situation is different again as an active drop off in activity is observed at a loading in the region 1.8-2 atomic%. This agrees with Sobana *et al.* [344], who reported a slight decline in activity at a very similar silver content to that reported here. This is possibly because at excessive silver loadings the Ag particles start to become recombination centres. For the quiescent system in question it is plausible that there was a finite amount of dissolved oxygen available to accept electrons and this had the effect of increasing relatively the rate of electron hole recombination [359]. Although this would explain a plateau it would not explain an inhibitory effect so it is perhaps more likely that a reduction in activity past a certain silver loading is responsible for a reduction inactive sites.

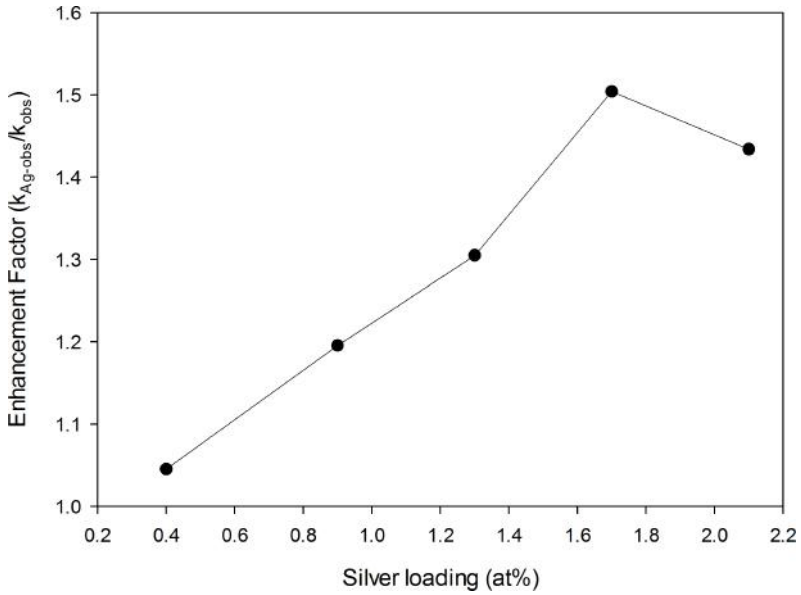

Figure 7.14: Apparent rate constant as a function of theoretical silver loading: FAC-TiO_2 -79 at a catalyst loading of 4 g/L of 10 μM MO using experimental set-up 2

7.3.7 Mixing improves the decoloration efficiency

The second set-up used was designed to assess the effect of mixing on the system. Previously the results were obtained whilst simulating a static water body such as a sea or lake that required pollution remediation. If designing a process to treat effluent from an industrial process then it is natural that some form of mixing/dynamic system is considered. In order to do so, the effect of mixing is shown on the photocatalytic performance of six samples in Figure 7.15. At first glance the reactions shown do not appear to be representative of 1st order kinetics, but this is largely due to the much slower kinetics of the 2nd reaction setup which has a lower catalyst to solution loading ratio, as well as being further away from the light source. The mixing was turned on after 90 minutes and in this stage 1st order kinetics appears to be occurring. The effect is pronounced and the results require careful interpretation. The first conclusion is that the system is displaying evidence of mass transfer limitation as reported for a similar system [191]. The rate of external mass transfer of reactant molecules to the catalyst surface is the rate limiting step and so increasing this rate consequently increases the reaction rate. However, given that it was possible to improve the performance of the catalyst with Ag deposition under

identical static conditions, this suggests that external mass transfer of dye molecules was not rate limiting, or at least the system is in some form of intermediate regime.

In a slurry system a transport limited regime has been identified [359]. Although external mass transfer limitation was discounted, the authors posited three other different factors that might influence either the light transport or the internal mass transfer resistance. Although the system in question is quite different the concepts are transferable: (1) reactant is unable to reach all of the catalyst surface area because of catalyst particle agglomeration, (2) light is unable to reach catalyst surface area because of light attenuation, and (3) light can not penetrate the agglomerates and reach the inner surfaces. In a slurry system the catalyst loading starts to show a light shielding effect at high loadings. It has been shown in this chapter that this light shielding effect starts when a complete illumination surface coverage has been reached as a result of the comparability large FAC particles. This is likely why the transition from a static to a mixed system increases the reaction rate. It allows for particles to form a dynamic layer that increases the amount of light reaching the catalyst surface. This has important implications for application - *i.e.* under wavy conditions. It would interesting to investigate whether this effect increases monotonically with agitation rate or whether there is an optimum.

7.4 Conclusions

Size classified FACs have been used as a carrier for TiO_2 with the intention of creating robust floating photocatalysts for the purpose of pollution control. The content of photoactive anatase was found to differ with no discernible pattern with FAC particle size although there is some evidence that an increase in acid washing strength improves anatase attachment. The particle size has been shown to have more of an effect that it might in suspended TiO_2 systems. The apparent reaction rate constant is inversely proportional to the square of the diameter instead of the diameter. This underlines the importance of choosing FACs that are the smallest that is practical for economic and

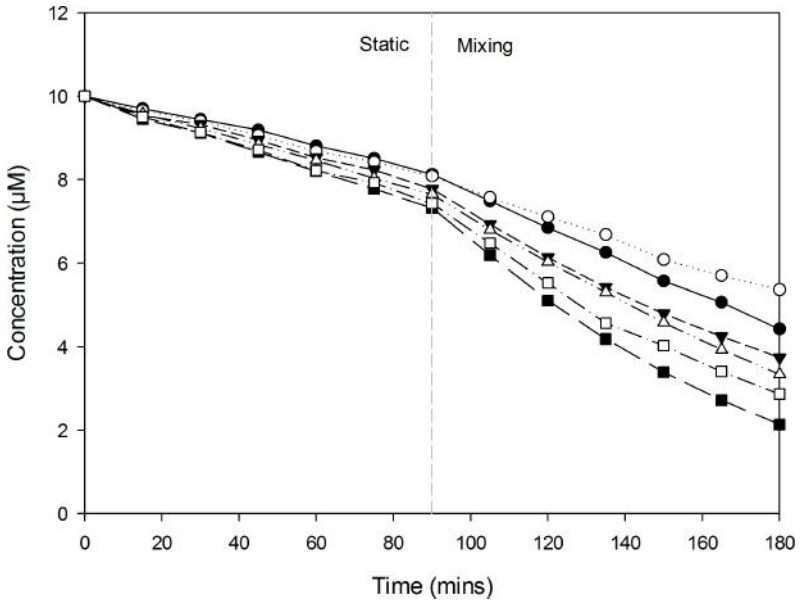

Figure 7.15: Effect of mixing on experimental set-up 2 using 2 g/L of FAC-TiO_2 -79 and 10 μM MO: 0% Ag (○), 0.4% Ag (●), 0.9% Ag (▼), 1.3% Ag (△), 1.7% Ag (□), 2.1% Ag (■)

logistical reasons. A method for predicting the optimal loading of FAC-TiO_2 composites has been suggested. A subset of particles have been used for silver deposition. UV-vis spectroscopy has shown that silver addition increases light absorption in the visible region although photocatalytic activity in this region was not altered. XPS has been used to show that the silver deposits were in the form of metallic silver. Increases in photoactivity of the silver deposited samples relative to pure TiO_2 were attributed to an electron trapping mechanism of the metallic silver. It has been shown that with the optimal formulation a TiO_2 catalyst can be significantly enhanced by a small amount of silver. Although kinetics have been tentatively explored in this study, further more targeted work would be hugely beneficial to evaluting the possibility of using FACs as carrier for TiO_2 in pilot and field scale studies. Clearly the opportunity to use a waste material (FACs) as an agent in pollution control is very compelling from a conceptual viewpoint. It is envisaged that such materials would be perfect for treating effluent streams - possibly from the textile industries - in developing countries with high levels of solar irradiance. The current study provides additional evidence that this is possible.

CHAPTER 8

CONCLUSIONS AND FUTURE WORK

8.1 Conclusions

The overarching objective of this thesis was to further the understanding of the properties, processing, and applications of CFA. These three features are not independent topics and there is a large degree of interconnectivity between them. All of the investigations are focused on an assessment of a way to use, or process, CFA which follows an ideology of industrial ecology or the circular economy. The various investigations presented thus far have made some important contributions to the knowledge of CFA and its processes. They are summarised in the following sections.

8.1.1 Commerical scale CFA derived products show considerable differences

While the concept of multicomponent utilisation of CFA is certainly not new, there have been no previous attempts to characterise the products of a commercial scale CFA processing system. This work has demonstrated that there are considerable differences between these products and that the differences can be quantified such that they can be targeted for particular applications. The value of detailed characterisation studies in order to assess the potential to use processed waste products for added value applications is highlighted.

In terms of chemistry, the cenospheres are enriched in SiO_2 and Al_2O_3 , while magnetic

concentrate is high in Fe_2O_3 , and the carbon concentrate is almost 75 wt% organic. Elements of environmental concern such as As, Cr, and Pb are present in relatively high levels in some of the CFA components but particularly in IFA-F. This situation is mirrored with regards to gallium concentration and IFA-F contains 47 ppm which is the same concentration as in bauxite. Mineral contents also varied considerably: the cenospheres contained a large amount of mullite (17.2 wt%), the magnetic concentrate contained a relatively large amount of magnetite (17.1 wt%), and the IFA-C had a relatively large amount of quartz (8.3%). These mineralogy results indicated that the cenospheres are likely to contain relatively large amounts of fine mullite spheres in their skeletal walls and as such might be a good candidate for applications where they require resistance to chemical or temperature attack. The relatively large amount of quartz in IFA-C in addition to the absence of cristabolite suggests that the quartz occurred as a relict material from the parent coal and as such might be present in distinct grains. This indicates that it might be possible to use a density classification system to separate the quartz from the less dense amorphous aluminosilicate particles and hence provide a raw material for the manufacture of zeolites or mesoporous silica.

Some of these results are unexpected; the magnetic concentrate actually contains a surprisingly small amount of magnetite relative to the quantity of Fe_2O_3 . Because of this, care must be taken not to assume that these particles can act as a direct replacement for magnetite, for instance in coal cleaning or sound proofing applications. The use of SEM imaging was revealing: it showed that, at high magnification particles are not smooth; the presence of fused porous network structures in the IFA-C suggests that there may be low density particles that do not float on water; that cenospheres can contain voids in the wall structure; magnetic spheres contain crystals which protrude from the surface which, combined with the surprisingly low magnetite content might indicate preferential crystallisation at the surface due to faster cooling.

8.1.2 A UK CFA contains elevated levels of REY elements

REY elements have been identified as critical raw materials. This indicates that the demand for them within the European economy is very high. Strategically, the prospect of accessing a source of REY elements from an abundant waste stockpile, is very exciting. A particular stockpile of CFA in the UK has been shown to contain levels of REY that are approaching economic viability. Previous studies have been confirmed that the content of REY increases as particle size decreases. For the first time CFA derived products were examined for REY element content. It was found that the residual ash fractions are enriched in REY relative to the carbon and magnetic concentrates which suggests that a REY element extraction process could be built into the existing flow sheet.

8.1.3 Relatively large numbers of cenospheres exist with a density greater than water

Cenospheres have traditionally been defined as having a density less than water. However this definition is a reflection of how they have been traditionally captured. This work has shown that as many cenospheres exist in the range 1-1.2 g/cm^3 as those with a density of less than 1 g/cm^3 . This could potentially have major implementations on the process economics of CFA separation as the cenospheres are by far the highest value product. This work also represents probably the most detailed chemical and mineralogical characterisation of density fractionated CFA to date. This has enabled some interesting observations on the nature of cenosphere formation to be made. Particles with a density of 1.0 - 2.0 g/cm^3 are either thick walled or spongy in nature and they are the largest in the size range 1.6 - 2.0 g/cm^3. Past a density of 2.0 g/cm^3 the particle size dramatically decreases. K_2O reduces in content from 3.8 - 2.0 wt% from lightest to heaviest fraction. K_2O acts as a network extender and increases viscosity which allows cenospheres to form. Viscosity was predicted to peak at density between 1.2-1.5 cm^3 which suggests that this might be why they have thicker walls and hence larger apparent densities. This knowledge might eventually enable the combustion of coal which has been tailored in order to provide

glass melts of sufficient viscosity for cenospheres to preferentially form.

8.1.4 CFA slurries are non-Newtonian at elevated particle concentration

Understanding the rheology of CFA suspensions is important not just in order to enable efficient processing but also in any area that requires the pumping of a CFA slurry over long distances. That concentrated CFA suspensions are shear thinning has been observed before and it is entirely consistent with a large body of literature on suspensions of inorganic particles. In this work, at particle volume fractions greater than 0.11, CFA slurry starts to become shear thinning. However, there is currently no method to predict how the viscosity of a suspension changes with both shear rate and slurry concentration. A pragmatic approach was taken which is unlikely to satisfy the purists. An empirical modelling procedure was proposed. The modelling procedure was satisfactory in describing behaviour of the two CFA types studied but does not utilise any physical properties of the CFA and so is unable to make *a priori* predictions. The empirical mode does allow an assessment of how the shear thinning behaviour of a concentrated CFA slurry might affect tank mixing or transport pumping. This could have a direct effect on processing operating costs.

8.1.5 Cenosphere recovery is inefficient in a stirred tank type vessel and requires a new design concept

The existing Gale Common cenosphere tank design is difficult to operate because of the reconciliation of two competing mechanisms: maintaining an off bottom suspension to free any trapped cenospheres and operating the impeller at a speed below that at which cenospheres start to become entrained in bulk flow. Experimental evidence suggests compromise conditions might be found but that there will always remain some portion of cenospheres entrained within the tank flow which would reduce separation efficiency. It has been suggested that the current design will not achieved the necessary yields of

cenospheres and therefore a new design is proposed based on the principles of a thickening tank. Theoretically this design should ensure complete separation but this comes at the expense of large tank volume and cross sectional area.

8.1.6 A high degree of separation of carbon from fly ash can be achieved with the application of an environmentally benign waste material

A well established use of CFA is as a cement replacement material. Since CFA is currently considered a waste material it does not have any embodied CO_2 emissions associated with it. It therefore makes the perfect material to represent the concept of the circular economy; it is both resource and energy efficient. Agglomeration of the carbon in CFA to enable it to meet building standards was investigated within an experimental design matrix: agglomeration impeller speed, duration, and oil concentration were all found to be correlated with a reduction in the carbon content of the product ash. The agglomerate carbon grade increased with increases in all three experimental factors in the order speed $>$ time $>$ oil. This is contrary to previous literature in the area. An explanation is provided with reference to the nature of CFA formation in that larger carbon particles were associated with higher mineral content. As these particles were larger they agglomerated before the smaller more pure carbon particles started to agglomerate. A crude water-in-oil emulsification procedure was able to extend the oil binder to achieve a two-fold reduction in oil content required. The surface tension of the emulsified oil is reduced by increasing the surfactant concentration. This was found to have two competing effect: (1) the emulsion droplets are more easily dispersed which aids agglomeration, and (2) this also allows increased droplet break-up which will hinder agglomeration if the internal droplet size equals the external. The use of waste vegetable oil increases the interlinks in the industrial ecosystem; if the process is economically viable it is a powerful illustration of how we can be more resource and energy efficient as an industrially advanced economy.

8.1.7 Silver activated TiO_2 coated floating cenosphere activity is highly dependent on particle size and catalyst formulation

The manufacture of a water treatment catalyst from a waste material is also a powerful illustration of the concept of the circular economy. By utilising the functionality (low density) of a particular component of CFA, a real solution to an industrially relevant problem has been suggested. The characterisation of FAC-TiO_2 composites has revealed some interesting features. For floating photocatalyst systems the substrate diameter has more of an effect than it might in suspended TiO_2 systems. This has been shown from first principles to be due to the apparent reaction rate constant's proportionality to the inverse of the square of the substrate diameter instead of the diameter. This underlines the importance of choosing the smallest possible cenosphere that the end application will allow. Silver activation was found to enhance the activity of the TiO_2 -cenosphere composite relative to pure TiO_2 . This was attributed to an electron trapping mechanism of the metallic silver. Mixing of the system was shown to improve decoloration efficiency. It is suggested that the system was operating in a form of transport limitation. The static nature of the particles at the air water interface had the effect of shielding light from some of the other particles. With a degree of mixing a dynamic layer is formed which increases the particle's exposure to light and thus the reaction rate. This has important implications for industrial use such as the effect of wavy conditions.

8.2 Future Work

The areas studied in this thesis are ripe for further investigation and there are potentially many follow up studies. In the order in which they are related to topics presented in this work, some specific suggestions of investigations that might be conducted are provided below.

- Acid leaching studies of the IFA-F that is derived from UK-CFA-3. This CFA is highly amorphous and the finer fractions of residual ash have increased levels of

REY, Ga, Ge, and Al_2O_3 . It would be an extremely valuable exercise to assess this material as a potential resource for alumina extraction with valuable metals as a by-product.

- Further density classifications on CFA to which SEM-EDS analysis on material that has been set in a resin and polished to reveal particle cross-sections. Such work has been attempted before, and indeed was the original purpose of the SEM-FIB study in this thesis, but it has not been conducted with sufficient detail and resolution in terms of density fractions. The findings of a study like this would help to market a new low density CFA fraction that incorporated higher density than water particles as well as shedding new light on the mechanisms of cenosphere formation.

- A more general rheological model of concentrated suspensions is required that can attempt to predict *a priori* the viscosity of a suspension at a particular concentration and shear rate. Progress towards this aim might be made by doing comprehensive studies of the sort conducted in Chapter 4 with model inorganic particles of tightly classified size and shape and combinations thereof.

- Pilot scale testing of the proposed cenosphere separator design to examine the effect of operating variables such as feed and underflow concentrations, flow rate, and the effect of inclined plates on the separation performance.

- The effect of scale on agglomeration performance should be evaluated by conducting some pilot scale testing of a dedicated agglomeration flotation set-up. The findings of this work on the effect of experimental parameters should be confirmed as well as a techno-economic appraisal of the process' viability.

- The investigation of emulsified oil for agglomeration applications in Chapter 6 should be regarded as preliminary. The experiments should be repeated with a more sophisticated emulsification technique such that the effect of internal droplet size and emulsion stability can be better evaluated. The use of confocal microscopy to reveal

the internal morphology of emulsion particle systems should also be considered.

- The kinetics of floating photo-catalyst systems warrant a dedicated investigation. By using better controlled mixing conditions and light intensity and sources, an better understanding of the intrinsic kinetics of the system may be gained. Within this study it would be possible to also evaluate whether photo-catalytic activity increases monotonically with mixing speed or whether an optimal value exists. Such work would be crucial for designing an industrial system based on the catalysts manufactured during the course of this thesis.

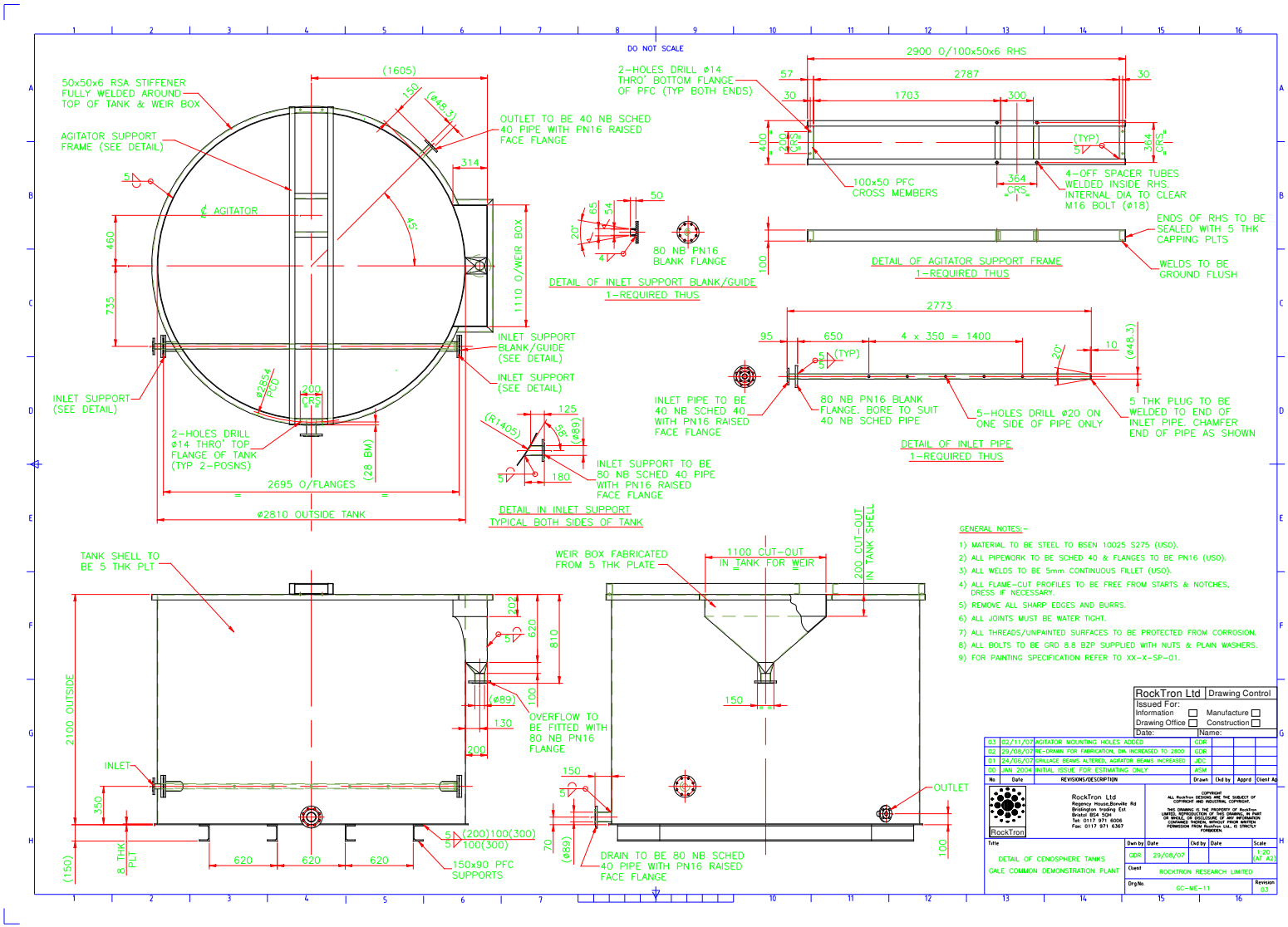
DO NOT SCALE
50x50x6 RSA STIFFENER FULLY WELDED AROUND TOP OF TANK & WEIR BOX
AGITATOR SUPPORT FRAME (SEE DETAIL)
℄ AGITATOR
OUTLET TO BE 40 NB SCHED 40 PIPE WITH PN16 RAISED FACE FLANGE
INLET SUPPORT BLANK/GUIDE (SEE DETAIL)
INLET SUPPORT (SEE DETAIL)
INLET SUPPORT (SEE DETAIL)
2-HOLES DRILL ø14 THRO' TOP FLANGE OF TANK (TYP 2-POSNS)
2695 O/FLANGES
ø2810 OUTSIDE TANK
1110 O/WEIR BOX
2-HOLES DRILL ø14 THRO' BOTTOM FLANGE OF PFC (TYP BOTH ENDS)
2900 O/100x50x6 RHS
100x50 PFC CROSS MEMBERS
4-OFF SPACER TUBES WELDED INSIDE RHS. INTERNAL DIA TO CLEAR M16 BOLT (ø18)
80 NB PN16 BLANK FLANGE
DETAIL OF INLET SUPPORT BLANK/GUIDE 1-REQUIRED THUS
DETAIL OF AGITATOR SUPPORT FRAME 1-REQUIRED THUS
ENDS OF RHS TO BE SEALED WITH 5 THK CAPPING PLTS
WELDS TO BE GROUND FLUSH
INLET PIPE TO BE 40 NB SCHED 40 WITH PN16 RAISED FACE FLANGE
80 NB PN16 BLANK FLANGE, BORE TO SUIT 40 NB SCHED PIPE
5-HOLES DRILL ø20 ON ONE SIDE OF PIPE ONLY
5 THK PLUG TO BE WELDED TO END OF INLET PIPE, CHAMFER END OF PIPE AS SHOWN
DETAIL OF INLET PIPE 1-REQUIRED THUS
INLET SUPPORT TO BE 80 NB SCHED 40 PIPE WITH PN16 RAISED FACE FLANGE
DETAIL IN INLET SUPPORT TYPICAL BOTH SIDES OF TANK
TANK SHELL TO BE 5 THK PLT
2100 OUTSIDE
INLET
OVERFLOW TO BE FITTED WITH 80 NB PN16 FLANGE
8 THK PLT
620
620
620
150x90 PFC SUPPORTS
WEIR BOX FABRICATED FROM 5 THK PLATE
1100 CUT-OUT IN TANK FOR WEIR
200 CUT-OUT IN TANK SHELL
OUTLET
DRAIN TO BE 80 NB SCHED 40 PIPE WITH PN16 RAISED FACE FLANGE
GENERAL NOTES:-
1) MATERIAL TO BE STEEL TO BSEN 10025 S275 (USO).
2) ALL PIPEWORK TO BE SCHED 40 & FLANGES TO BE PN16 (USO).
3) ALL WELDS TO BE 5mm CONTINUOUS FILLET (USO).
4) ALL FLAME-CUT PROFILES TO BE FREE FROM STARTS & NOTCHES, DRESS IF NECESSARY.
5) REMOVE ALL SHARP EDGES AND BURRS.
6) ALL JOINTS MUST BE WATER TIGHT.
7) ALL THREADS/UNPAINTED SURFACES TO BE PROTECTED FROM CORROSION.
8) ALL BOLTS TO BE GRD 8.8 BZP SUPPLIED WITH NUTS & PLAIN WASHERS.
9) FOR PAINTING SPECIFICATION REFER TO XX-X-SP-01.
RockTron Ltd Drawing Control
Issued For:
Information
Drawing Office
Manufacture
Construction
Date:
Name:
03 02/11/07 AGITATOR MOUNTING HOLES ADDED GDR
02 29/08/07 RE-DRAWN FOR FABRICATION, DIA INCREASED TO 2800 GDR
01 24/08/07 GRILLAGE BEAMS ALTERED, AGITATOR BEAMS INCREASED JDC
00 JAN 2004 INITIAL ISSUE FOR ESTIMATING ONLY AGM
RockTron Ltd
Regency House,Barnoke Rd
Bridlington trading Est
Bristol BS4 5QH
Tel: 0117 971 6006
Fax: 0117 971 6367
COPYRIGHT
ALL RockTron DESIGNS ARE THE SUBJECT OF COPYRIGHT AND INDUSTRIAL COPYRIGHT.
THIS DRAWING IS THE PROPERTY OF RockTron LIMITED. REPRODUCTION OF THIS DRAWING, IN PART OR WHOLE, OR DISCLOSURE OF ANY INFORMATION CONTAINED THEREIN IS PROHIBITED WITHOUT THE PERMISSION FROM RockTron Ltd., IS STRICTLY FORBIDDEN.
Title
DETAIL OF CENOSPHERE TANKS
GALE COMMON DEMONSTRATION PLANT
Dwn by GDR Date 29/08/07
Chd by Date
Scale 1:20 (AT A2)
Client ROCKTRON RESEARCH LIMITED
Drg.No. CC-ME-11
Revision 03

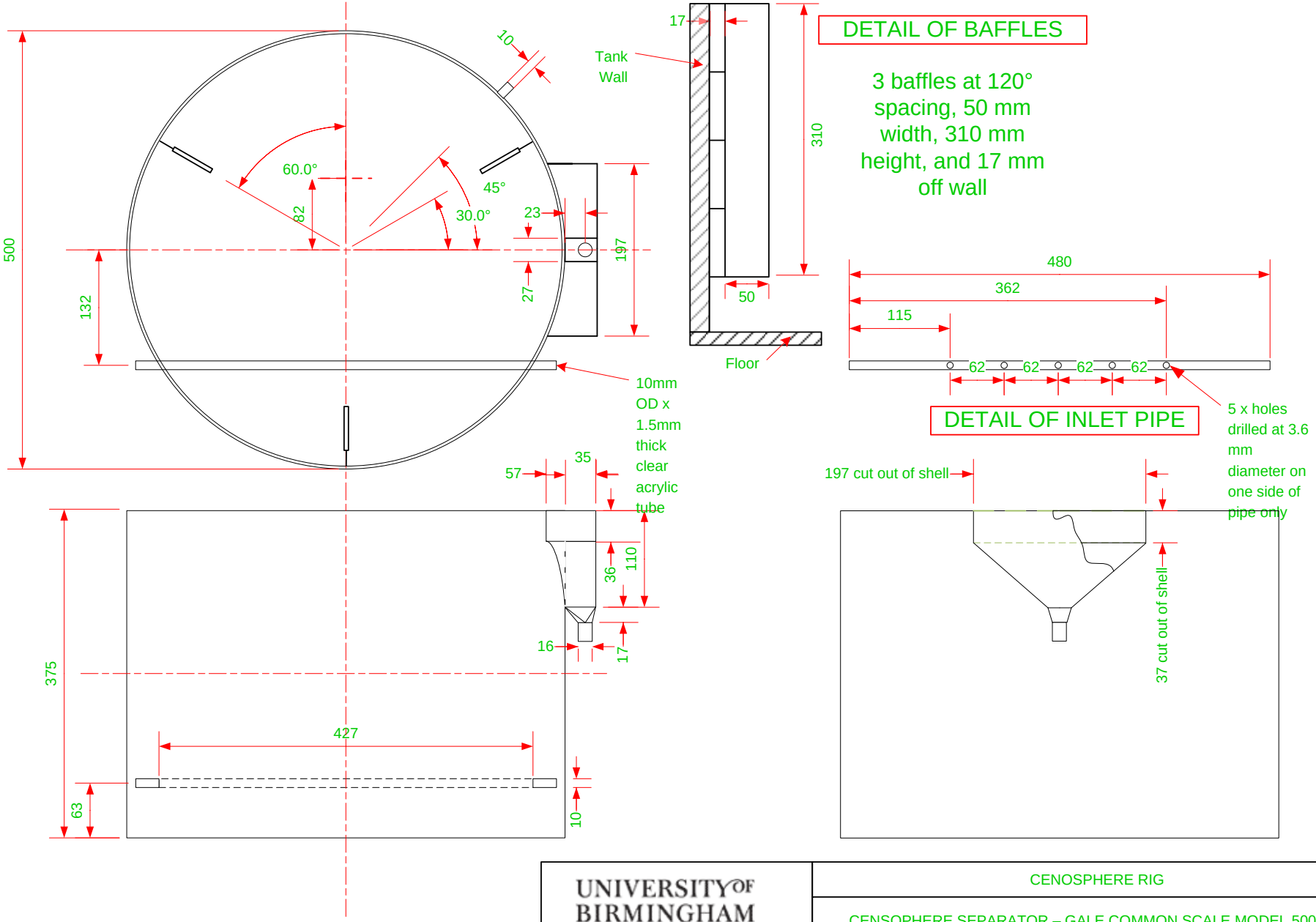

UNIVERSITY OF BIRMINGHAM

CENOSPHERE RIG

CENSOPHERE SEPARATOR – GALE COMMON SCALE MODEL 500 mm

SIZE	FSCM NO	DWG NO	REV
			0
SCALE 1:6		SHEET 1 OF 5	

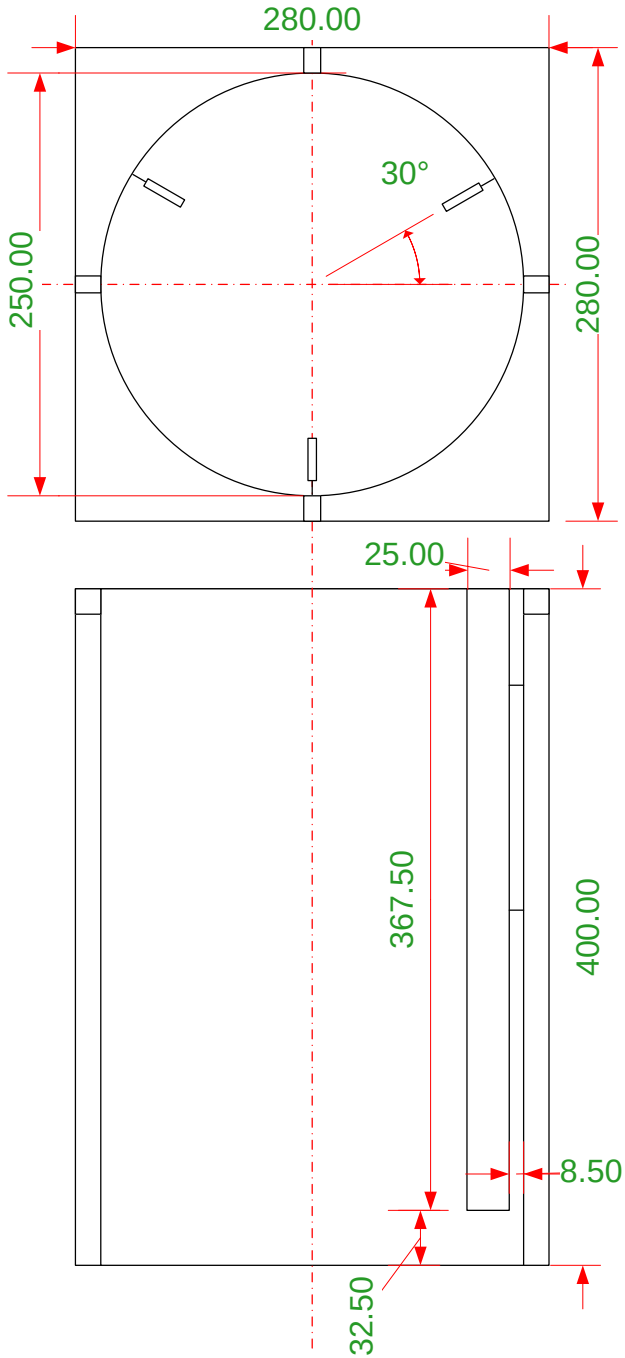

DETAIL OF BAFFLES

3 BAFFLES AT 120° SPACING
WIDTH, 25 MM
HEIGHT, 367.5 MM
WALL CLEARANCE, 8.5 MM
FLOOR CLEARANCE, 32.5 MM

DESIGN DESCRIPTION

CONSISTS OF CIRCULAR ACRYLIC TANK TO BE PLACED INSIDE (AND REMOVABLE FROM) AN ACRYLIC 5 SIDED BOX OPEN TOP WITH 3 VERTICAL SIDES WHITE AND 1 CLEAR. BOX BOTTOM TO BE CLEAR

IMPELLER GUIDE

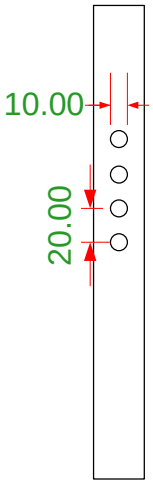

GUIDE TO CLIP OVER CENTRE LINE OF TANK SUCH THAT IMPELLER SHAFT CAN BE FED THROUGH IN CORRECT POSITION

230

PEPT MIXING VESSEL – FLY ASH

SIZE	FSCM NO	DWG NO	REV
		1	1

SCALE	NONE	SHEET	1 OF 1

Appendix 2

```
macro "Find Interface" {
setBatchMode(true);

width = getWidth;
height = getHeight;
depth = nSlices;
getPixelSize(unit, pw, ph, pd);

heightVals = newArray(height);
for (h=0;h<height;h++){
   heightVals[h]= h * ph;
}
numAvs = floor((height+1)/3)-1;
numDiffs = numAvs - 1;
newheightvals = newArray(numDiffs);
for (h=0;h<numDiffs;h++){
   newheightvals[h] = heightVals[(h*3)+3];
   //setResult("Height, "+ unit, h, newheightvals[h]);
}

avVals = newArray(height);
yVals = newArray(depth);
xVals = newArray(depth);

for (n=1;n<=depth;n++){
   nn = n-1;
   sum = 0;
```

```
showProgress(n, depth);
   setSlice(n);
for (j=0;j<height;j++){
   sum = 0;
   for (i=0;i<width;i++){
      sum = sum + getPixel(i,j);
   }
   avVals[j] = sum / width ;
   //setResult(n +"Values", j, avVals[j]);
   avValsb = Array.copy(avVals);
   AvValsb = Array.reverse(avValsb);

}

pixAvs = newArray(numAvs);
for (z=0;z<numAvs;z++){
   pixAvs[z] = (avValsb[(z*3)] + avValsb[(z*3)+1] + avValsb[(z*3)+2]) / 3;
   //setResult(n +" Avs", z, pixAvs[z]);
}

Diffs = newArray(numDiffs);
for (z=0;z<numDiffs;z++){
   Diffs[z] = abs(pixAvs[z]-pixAvs[z+1])/pixAvs[z+1]*100;
   //setResult(n +" Diffs", z, Diffs[z]);
}
rankPosArr = newArray(numDiffs);
rankPosArr = Array.reverse(Diffs);
rankPosArr = Array.rankPositions(rankPosArr);
arrIndex = rankPosArr[numDiffs-1];
yVals[nn] = newheightvals[arrIndex];
```

```
   xVals[nn] = nn;
   lineH = round(newheightvals[arrIndex]*(1/ph));
   drawLine(0,lineH,width,lineH);
   setColor("yellow");
   setLineWidth(3);
   //setResult(n +" Interface Height", 0,newheightvals[arrIndex]);
}
Plot.create("Interface Height as a function of time", "Time series","Interface
    Height");
Plot.setLimits(0, depth-1, 0, 60);
Plot.setColor("blue");
Plot.add("line", xVals, yVals);
setBatchMode(false);
}
```

LIST OF REFERENCES

[1] Robinson, J. *Ecological Economics* **48**(4), 369–384 (2004).

[2] Brundtland, G. H. *Our Common Future /[report by the] World Commission on Environment and Development; [chairman: Gro Harlem Brundtland]*. Oxford University Press, Oxford [etc.], (1987).

[3] Quijorna, N., Miguel, G. S., and Andrés, A. *Industrial & Engineering Chemistry Research* **50**(9), 5806–5814 (2011).

[4] COM (2014) 398 final.

[5] Vassilev, S. V. and Menendez, R. *Fuel* **84**(7-8), 973 – 991 (2005).

[6] Simmonds, P. *Waste products and undeveloped substances; a synopsis of progress made in their economic utilisation during the last quarter of a century at home and abroad*. London, R. Hardwicke, (1873).

[7] Blissett, R. and Rowson, N. *Fuel* **97**, 1 – 23 (2012).

[8] Blissett, R., Smalley, N., and Rowson, N. *Fuel* **119**(0), 236 – 239 (2014).

[9] Vassilev, S. V., Menendez, R., Borrego, A. G., Diaz-Somoano, M., and Rosa Martinez-Tarazona, M. *Fuel* **83**(11-12), 1563–1583 (2004).

[10] Vassilev, S. V., Menendez, R., Alvarez, D., Diaz-Somoano, M., and Martinez-Tarazona, M. *Fuel* **82**(14), 1793 – 1811 (2003).

[11] Vassilev, S. V., Menendez, R., Diaz-Somoano, M., and Martinez-Tarazona, M. *Fuel* **83**(4-5), 585 – 603 (2004).

[12] Ahmaruzzaman, M. *Progress in Energy and Combustion Science* **36**(3), 327–363 (2010).

[13] Lior, N. *Energy* **35**(10), 3976–3994 (2010).

[14] Vassilev, S. V., Menendez, R., Alvarez, D., and Borredo, A. G. In *International Ash Utilization Symposium* (, Lexington, Kentucky, Oct 22-24, 2001, Ash Library - http://www.flyash.info/, 2001).

[15] Blissett, R. and Rowson, N. *Fuel* **111**(0), 555 – 563 (2013).

[16] Manz, O. E. *Fuel* **78**(2), 133 – 136 (1999).

[17] Moreno, N., Querol, X., Andrés, J. M., Stanton, K., Towler, M., Nugteren, H., Janssen-Jurkovicová, M., and Jones, R. *Fuel* **84**(11), 1351–1363 (2005).

[18] Vassilev, S. V. and Vassileva, C. G. *Fuel* **86**(1011), 1490 – 1512 (2007).

[19] Hower, J. C., Robertson, J., Thomas, G. A., Wong, A. S., Schram, W. H., Graham, U. M., Rathbone, R. F., and Robl, T. L. *Fuel* **75**(4), 403 – 411 (1996).

[20] Kim, B. and Prezzi, M. *Waste Management* **28**(3), 649 – 659 (2008).

[21] Diaz, E., Allouche, E., and Eklund, S. *Fuel* **89**(5), 992 – 996 (2010).

[22] Yan, L., Wang, Y., Ma, H., Han, Z., Zhang, Q., and Chen, Y. *Journal of Hazardous Materials* **203-204**, 221 – 228 (2012).

[23] Liu, G., Zhang, H., Gao, L., Zheng, L., and Peng, Z. *Fuel Processing Technology*

85(15), 1635 – 1646 (2004).
[24] Qi, L. and Yuan, Y. *Journal of Hazardous Materials* **192**(1), 222 – 225 (2011).
[25] Mishra, D. P. and Das, S. K. *Materials Characterization* **61**(11), 1252 – 1259 (2010).
[26] Dutta, B. K., Khanra, S., and Mallick, D. *Fuel* **88**(7), 1314 – 1323 (2009). Selected Papers from the 2007 World of Coal Ash Conference.
[27] Jankowski, J., Ward, C. R., French, D., and Groves, S. *Fuel* **85**(2), 243 – 256 (2006). Special Issue: The 21st Annual International Pittsburgh Coal Conference.
[28] Wang, S. *Environmental Science & Technology* **42**(19), 7055–7063 (2008).
[29] Izquierdo, M. and Querol, X. *International Journal of Coal Geology* , – (2011).
[30] Benezet, J.-C., Adamiec, P., and Benhassaine, A. *Particuology* **6**(2), 85–92 (2008).
[31] Kutchko, B. G. and Kim, A. G. *Fuel* **85**(17-18), 2537–2544 (2006).
[32] Tomeczek, J. and Palugniok, H. *Fuel* **81**(10), 1251 – 1258 (2002).
[33] Sarkar, A., Rano, R., Mishra, K., and Sinha, I. *Fuel Processing Technology* **86**(11), 1221 – 1238 (2005).
[34] Vassilev, S. V. and Vassileva, C. G. *Fuel Processing Technology* **47**(3), 261 – 280 (1996).
[35] Rubio, B., Izquierdo, M. T., Mayoral, M. C., Bona, M. T., and Martínez-Tarazona, R. M. *Journal of Environmental Management* **88**(4), 1562–1570 (2008).
[36] Pedersen, K. H., Jensen, A. D., Skjøth-Rasmussen, M. S., and Dam-Johansen, K. *Progress in Energy and Combustion Science* **34**(2), 135–154 (2008).
[37] González, A., Navia, R., and Moreno, N. *Waste Management & Research* **27**(10), 976–987 (2009).
[38] European Coal Combustion Products Association e.V. (2008). Available from `http://www.ecoba.com/evjm,media/ccps/Ecoba_Stat_2008_EU15.pdf` [Accessed online: 25.10.2011].
[39] Kikuchi, R. *Resources, Conservation and Recycling* **27**(4), 333–346 (1999).
[40] Sears, L. *Future trends for PFA in cementitious systems.* 1st Future Cement Conference and Exhibition, London Chamber of Commerce and Industry, (2011).
[41] Cammarota, A., Chirone, R., Solimene, R., and Urciuolo, M. *Experimental Thermal and Fluid Science* **32**(7), 1324–1333 (2008).
[42] Freeman, E., Gao, Y.-M., Hurt, R., and Suuberg, E. *Fuel* **76**(8), 761–765 (1997).
[43] Nalbantoglu, Z. *Construction and Building Materials* **18**(6), 377–381 (2004).
[44] Zha, F., Liu, S., Du, Y., and Cui, K. *Natural Hazards* **47**(3), 509–523 (2008).
[45] Panday, K. K., Prasad, G., and Singh, V. N. *Water Research* **19**(7), 869–873 (1985).
[46] Héquet, V., Ricou, P., Lecuyer, I., and Le Cloirec, P. *Fuel* **80**(6), 851–856 (2001).
[47] Cho, H., Oh, D., and Kim, K. *Journal of Hazardous Materials* **127**(1-3), 187–195 (2005).
[48] Alinnor, I. J. *Fuel* **86**(5-6), 853–857 (2007).
[49] Mohan, S. and Gandhimathi, R. *Journal of Hazardous Materials* **169**(1-3), 351–359 (2009).
[50] Itskos, G., Koukouzas, N., Vasilatos, C., Megremi, I., and Moutsatsou, A. *Journal of Hazardous Materials* **183**(1-3), 787–792 (2010).
[51] Ahmaruzzaman, M. *Advances in Colloid and Interface Science* **166**(1-2), 36–59 (2011).
[52] Aksu, Z. and Yener, J. *Journal of Environmental Science and Health, Part A* **34**(9), 1777–1796 (1999).

[53] Kao, P.-C., Tzeng, J.-H., and Huang, T. *Journal of Hazardous Materials* **76**(2-3), 237–249 (2000).
[54] Aksu, Z. and Yener, J. *Waste Management* **21**(8), 695–702 (2001).
[55] Estevinho, B. N., Martins, I., Ratola, N., Alves, A., and Santos, L. *Journal of Hazardous Materials* **143**(1-2), 535–540 (2007).
[56] Nollet, H., Roels, M., Lutgen, P., Van der Meeren, P., and Verstraete, W. *Chemosphere* **53**(6), 655–665 (2003).
[57] Davini, P. *Resources, Conservation and Recycling* **15**(3-4), 193–201 (1995).
[58] Davini, P. *Fuel* **75**(6), 713–716 (1996).
[59] Lee, K. T., Bhatia, S., Mohamed, A. R., and Chu, K. H. *Chemosphere* **62**(1), 89–96 (2006).
[60] Jala, S. and Goyal, D. *Bioresource Technology* **97**(9), 1136–1147 (2006).
[61] Pandey, V. C. and Singh, N. *Agriculture, Ecosystems & Environment* **136**(1-2), 16–27 (2010).
[62] Ram, L. C. and Masto, R. E. *Journal of Environmental Management* **91**(3), 603–617 (2010).
[63] Manoharan, V., Yunusa, I. A. M., Loganathan, P., Lawrie, R., Skilbeck, C. G., Burchett, M. D., Murray, B. R., and Eamus, D. *Fuel* **89**(11), 3498–3504 (2010).
[64] Nayak, N. and Panda, C. R. *Fuel* **89**(1), 53–58 (2010).
[65] Matjie, R. H., Bunt, J. R., and van Heerden, J. H. P. *Minerals Engineering* **18**(3), 299–310 (2005).
[66] Shabtai, Y. and Mukmenev, I. *Journal of Biotechnology* **51**(3), 209–217 (1996).
[67] Bai, G., Teng, W., Wang, X., Qin, J.-g., Xu, P., and Li, P. *Transactions of Nonferrous Metals Society of China* **20, Supplement 1**(0), s169–s175 (2010).
[68] Park, H. C., Park, Y. J., and Stevens, R. *Materials Science and Engineering: A* **367**(1-2), 166–170 (2004).
[69] Wang, S. and Lu, G. Q. In *Studies in Surface Science and Catalysis,* Fbio Bellot Noronha, M. S. and Eduardo Falabella, S.-A., editors, volume Volume 167, 275–280. Elsevier (2007).
[70] Xuan, X., Yue, C., Li, S., and Yao, Q. *Fuel* **82**(5), 575–579 (2003).
[71] Yu, Y.-t. *Powder Technology* **146**(1-2), 154–159 (2004).
[72] Flores, Y., Flores, R., and Gallegos, A. A. *Journal of Molecular Catalysis A: Chemical* **281**(1-2), 184–191 (2008).
[73] Li, Y. and Zhang, F. *Chemical Engineering Journal* **158**(2), 148–153 (2010).
[74] Khatri, C., Mishra, M. K., and Rani, A. *Fuel Processing Technology* **91**(10), 1288–1295 (2010).
[75] Li, L., Wang, S., Zhu, Z., Yao, X., and Yan, Z. *Fuel Processing Technology* **89**(11), 1106–1112 (2008).
[76] Born, J. G. P., Mulder, P., and Louw, R. *Environmental Science & Technology* **27**(9), 1849–1863 (1993).
[77] Mallick, D., Khanra, S., and Chaudhuri, S. K. *Journal of Chemical Technology & Biotechnology* **70**(3), 231–240 (1997).
[78] Chatterjee, D., Ruj, B., and Mahata, A. *Catalysis Communications* **2**(3-4), 113–117 (2001).
[79] Khatri, C. and Rani, A. *Fuel* **87**(13-14), 2886–2892 (2008).
[80] Jain, D., Khatri, C., and Rani, A. *Fuel* **90**(6), 2083–2088 (2011).

[81] Erol, M., Küçükbayrak, S., and Ersoy-Meriçboyu, A. *Journal of Hazardous Materials* **153**(1-2), 418–425 (2008).
[82] He, Y., Cheng, W., and Cai, H. *Journal of Hazardous Materials* **120**(1-3), 265–269 (2005).
[83] Peng, F., Liang, K., and Hu, A. *Fuel* **84**(4), 341–346 (2005).
[84] Sokolar, R. and Vodova, L. *Ceramics International* **37**(7), 2879–2885 (2011).
[85] Kim, J. M. and Kim, H. S. *Journal of the European Ceramic Society* **24**(9), 2825–2833 (2004).
[86] Vasilopoulos, K. C., Tulyaganov, D. U., Agathopoulos, S., Karakassides, M. A., Ferreira, J. M. F., and Tsipas, D. *Ceramics International* **35**(2), 555–558 (2009).
[87] Jedidi, I., Saïdi, S., Khemakhem, S., Larbot, A., Elloumi-Ammar, N., Fourati, A., Charfi, A., Salah, A. B., and Amar, R. B. *Journal of Hazardous Materials* **172**(1), 152–158 (2009).
[88] Jedidi, I., Khemakhem, S., Saïdi, S., Larbot, A., Elloumi-Ammar, N., Fourati, A., Charfi, A., Salah, A. B., and Amar, R. B. *Powder Technology* **208**(2), 427–432 (2011).
[89] Fang, J., Qin, G., Wei, W., and Zhao, X. *Separation and Purification Technology* **80**(3), 585–591 (2011).
[90] Swanepoel, J. C. and Strydom, C. A. *Applied Geochemistry* **17**(8), 1143–1148 (2002).
[91] Barbosa, V. F. F. and MacKenzie, K. J. D. *Materials Research Bulletin* **38**(2), 319–331 (2003).
[92] Panias, D., Giannopoulou, I. P., and Perraki, T. *Colloids and Surfaces A: Physicochemical and Engineering Aspects* **301**(1-3), 246–254 (2007).
[93] Chen-Tan, N. W., Van Riessen, A., Ly, C. V., and Southam, D. C. *Journal of the American Ceramic Society* **92**(4), 881–887 (2009).
[94] Shi, C., Jiménez, A. F., and Palomo, A. *Cement and Concrete Research* **41**(7), 750 – 763 (2011). Special Issue: 13th International Congress on the Chemistry of Cement.
[95] Duxson, P., Fernández-Jiménez, A., Provis, J., Lukey, G., Palomo, A., and van Deventer, J. *Journal of Materials Science* **42**, 2917–2933 (2007).
[96] Kumar, R., Kumar, S., and Mehrotra, S. *Resources, Conservation and Recycling* **52**(2), 157 – 179 (2007).
[97] Kumar, S., Kumar, R., Alex, T. C., Bandopadhyay, A., and Mehrotra, S. P. *Advances in Applied Ceramics* **106**(3), 120–127 (2007).
[98] Chindaprasirt, P., Chareerat, T., Hatanaka, S., and Cao, T. *Journal of Materials in Civil Engineering* **23**(3), 264–270 (2011).
[99] Hardjito, D., Wallah, S. E., Sumajouw, D. M. J., and Rangan, B. V. *ACI Materials Journal* **101**(6), 467–472 (2004).
[100] van Deventer, J. S., Provis, J. L., and Duxson, P. *Minerals Engineering* , – (2011).
[101] Komljenović, M., Baščarević, Z., and Bradić, V. *Journal of Hazardous Materials* **181**(1-3), 35–42 (2010).
[102] Lee, W. K. W. and van Deventer, J. S. J. *Colloids and Surfaces A: Physicochemical and Engineering Aspects* **211**(1), 49–66 (2002).
[103] Provis, J. L., Yong, C. Z., Duxson, P., and van Deventer, J. S. J. *Colloids and Surfaces A: Physicochemical and Engineering Aspects* **336**(1-3), 57–63 (2009).

[104] Rickard, W. D. A., Williams, R., Temuujin, J., and van Riessen, A. *Materials Science and Engineering: A* **528**(9), 3390–3397 (2011).
[105] Bakharev, T. *Cement and Concrete Research* **36**(6), 1134–1147 (2006).
[106] Rickard, W. D. A., Riessen, A. v., and Walls, P. *International Journal of Applied Ceramic Technology* **7**(1), 81–88 (2010).
[107] Ramdoo, I. *Shopping for raw materials: Should Africa be worried about EU Raw Materials Initiative*. ECDPM Discussion Paper 105, (2011).
[108] Spears, D. A. and Zheng, Y. *International Journal of Coal Geology* **38**(3-4), 161–179 (1999).
[109] Arroyo, F., Font, O., Fernández-Pereira, C., Querol, X., Juan, R., Ruiz, C., and Coca, P. *Journal of Hazardous Materials* **167**(1-3), 582–588 (2009).
[110] Moskalyk, R. R. *Minerals Engineering* **17**(3), 393–402 (2004).
[111] Hernández-Expósito, A., Chimenos, J. M., Fernández, A. I., Font, O., Querol, X., Coca, P., and García Peña, F. *Chemical Engineering Journal* **118**(1-2), 69–75 (2006).
[112] Marco-Lozar, J. P., Cazorla-Amorós, D., and Linares-Solano, A. *Carbon* **45**(13), 2519–2528 (2007).
[113] Torralvo, F. A. and Fernández-Pereira, C. *Minerals Engineering* **24**(1), 35 – 41 (2011).
[114] Arroyo, F. and Fernández-Pereira, C. *Industrial & Engineering Chemistry Research* **47**(9), 3186–3191 (2008).
[115] Arroyo, F., Fernández-Pereira, C., Bermejo Oroz, P., and Olivares del Valle, J. *Industrial equipment for the recovery of germanium from coal fly ash leachates by solvent extraction*. World of Coal Ash Conference, (2011).
[116] Arroyo, F., Fernández-Pereira, C., Olivares, J., and Coca, P. *Industrial & Engineering Chemistry Research* **48**(7), 3573–3579 (2009).
[117] Moskalyk, R. R. *Minerals Engineering* **16**(10), 921–929 (2003).
[118] Fang, Z. and Gesser, H. *Hydrometallurgy* **41**(2-3), 187 – 200 (1996).
[119] Font, O., Querol, X., Juan, R., Casado, R., Ruiz, C. R., López-Soler, A., Coca, P., and García Peña, F. *Journal of Hazardous Materials* **139**(3), 413–423 (2007).
[120] Gutiérrez, B., Pazos, C., and Coca, J. *Waste Management & Research* **15**(4), 371–382 (1997).
[121] Flower, D. and Sanjayan, J. *The International Journal of Life Cycle Assessment* **12**(5), 282–288 (2007).
[122] Mehta, P. K. In *International workshop on sutainable development and concrete technology,* Wank, K., editor (Iowa State University Publication, Beijing, 2004).
[123] Reiner, M. and Rens, K. *Practice Periodical on Structural Design and Construction* **11**(1), 58–64 (2006).
[124] Crouch, L. K. and Phillips, J. In *World of Coal Ash Conference* (, Lexington, Kentucky, 2009).
[125] Durán-Herrera, A., Juárez, C., Valdez, P., and Bentz, D. *Cement and Concrete Composites* **33**(1), 39 – 45 (2011).
[126] Bentz, D. P. and Ferraris, C. F. *Cement and Concrete Composites* **32**(4), 265 – 270 (2010).
[127] Felekoglu, B. *Fuel* **85**(1213), 1944 – 1949 (2006).
[128] McCarthy, M. and Dhir, R. *Fuel* **84**(11), 1423 – 1432 (2005). 2003 International

Ash Utilization Symposium.
[129] Cross, D., Stephens, J., and Vollmer, J. In *World of Coal Ash Conference*, 131 (, Lexington, Kentucky, 2005).
[130] Berry, M., Stephens, J., and Cross, D. *ACI Materials Journal* **108**, 378–384 (2011).
[131] Kresge, C. T., Leonowicz, M. E., Roth, W. J., Vartuli, J. C., and Beck, J. S. *Nature* **359**(6397), 710–712 (1992).
[132] Kumar, P., Mal, N., Oumi, Y., Yamana, K., and Sano, T. *Journal of Materials Chemistry* **11**(12), 3285–3290 (2001).
[133] Misran, H., Singh, R., Begum, S., and Yarmo, M. A. *Journal of Materials Processing Technology* **186**(1-3), 8–13 (2007).
[134] Halina, M., Ramesh, S., Yarmo, M. A., and Kamarudin, R. A. *Materials Chemistry and Physics* **101**(2-3), 344–351 (2007).
[135] Chandrasekar, G. and Ahn, W.-S. *Journal of Non-Crystalline Solids* **354**(33), 4027–4030 (2008).
[136] Hui, K. S. and Chao, C. Y. H. *Journal of Hazardous Materials* **137**(1), 401–409 (2006).
[137] Dhokte, A. O., Khillare, S. L., Lande, M. K., and Arbad, B. R. *Journal of Industrial and Engineering Chemistry* **17**(4), 742–746 (2011).
[138] Querol, X., Moreno, N., Umaña, J. C., Alastuey, A., Hernández, E., López-Soler, A., and Plana, F. *International Journal of Coal Geology* **50**(1-4), 413–423 (2002).
[139] Barrer, R. M. *Zeolites* **1**(3), 130–140 (1981).
[140] Höller, H. and Wirsching, U. *Fortschritte Der Mineralogie* **63**(1), 21–43 (1985).
[141] Berkgaut, V. and Singer, A. *Applied Clay Science* **10**(5), 369–378 (1996).
[142] Querol, X., Alastuey, A., López-Soler, A., Plana, F., Andrés, J. M., Juan, R., Ferrer, P., and Ruiz, C. R. *Environmental Science & Technology* **31**(9), 2527–2533 (1997).
[143] Hollman, G. G., Steenbruggen, G., and Janssen-Jurkovičová, M. *Fuel* **78**(10), 1225–1230 (1999).
[144] Querol, X., Umaña, J. C., Plana, F., Alastuey, A., Lopez-Soler, A., Medinaceli, A., Valero, A., Domingo, M. J., and Garcia-Rojo, E. *Fuel* **80**(6), 857–865 (2001).
[145] Murayama, N., Yamamoto, H., and Shibata, J. *International Journal of Mineral Processing* **64**(1), 1–17 (2002).
[146] Inada, M., Eguchi, Y., Enomoto, N., and Hojo, J. *Fuel* **84**(2-3), 299–304 (2005).
[147] Moriyama, R., Takeda, S., Onozaki, M., Katayama, Y., Shiota, K., Fukuda, T., Sugihara, H., and Tani, Y. *Fuel* **84**(12-13), 1455–1461 (2005).
[148] Walek, T. T., Saito, F., and Zhang, Q. *Fuel* **87**(15-16), 3194–3199 (2008).
[149] Jha, V. K., Nagae, M., Matsuda, M., and Miyake, M. *Journal of Environmental Management* **90**(8), 2507–2514 (2009).
[150] Shigemoto, N., Hayashi, H., and Miyaura, K. *Journal of Materials Science* **28**(17), 4781–4786 (1993).
[151] Molina, A. and Poole, C. *Minerals Engineering* **17**(2), 167–173 (2004).
[152] Mishra, T. and Tiwari, S. K. *Journal of Hazardous Materials* **137**(1), 299–303 (2006).
[153] Ríos R, C. A., Williams, C. D., and Roberts, C. L. *Fuel* **88**(8), 1403–1416 (2009).
[154] Yao, Z. T., Xia, M. S., Ye, Y., and Zhang, L. *Journal of Hazardous Materials* **170**(2-3), 639–644 (2009).
[155] Kazemian, H., Naghdali, Z., Ghaffari Kashani, T., and Farhadi, F. *Advanced Powder*

Technology **21**(3), 279–283 (2010).
[156] Moreno, N., Querol, X., Plana, F., Andrés, J. M., Janssen, M., and Nugteren, H. *Journal of Chemical Technology and Biotechnology* **77**(3), 274–279 (2002).
[157] Tanaka, H., Fujii, A., Fujimoto, S., and Tanaka, Y. *Advanced Powder Technology* **19**(1), 83–94 (2008).
[158] Font, O., Moreno, N., Díez, S., Querol, X., López-Soler, A., Coca, P., and García Peña, F. *Journal of Hazardous Materials* **166**(1), 94–102 (2009).
[159] Kim, J. K. and Lee, H. D. *Journal of Industrial and Engineering Chemistry* **15**(5), 736–742 (2009).
[160] Tanaka, H. and Fujii, A. *Advanced Powder Technology* **20**(5), 473–479 (2009).
[161] Otal, E., Vilches, L. F., Moreno, N., Querol, X., Vale, J., and Fernández-Pereira, C. *Fuel* **84**(11), 1440 – 1446 (2005).
[162] Park, M., Choi, C. L., Lim, W. T., Kim, M. C., Choi, J., and Heo, N. H. *Microporous and Mesoporous Materials* **37**(1-2), 81–89 (2000).
[163] Park, M., Choi, C. L., Lim, W. T., Kim, M. C., Choi, J., and Heo, N. H. *Microporous and Mesoporous Materials* **37**(1-2), 91–98 (2000).
[164] Ban, H., Li, T. X., Hower, J. C., Schaefer, J. L., and Stencel, J. M. *Fuel* **76**(8), 801–805 (1997).
[165] Gray, M. L., Champagne, K. J., Soong, Y., Killmeyer, R. P., Maroto-Valer, M. M., Andrésen, J. M., Ciocco, M. V., and Zandhuis, P. H. *Fuel Processing Technology* **76**(1), 11–21 (2002).
[166] Soong, Y., Schoffstall, M. R., Gray, M. L., Knoer, J. P., Champagne, K. J., Jones, R. J., and Fauth, D. J. *Separation and Purification Technology* **26**(2-3), 177–184 (2002).
[167] Cangialosi, F., Notarnicola, M., Liberti, L., and Stencel, J. *Journal of Hazardous Materials* **164**(2-3), 683–688 (2009).
[168] Keppler, J. G. In *International Ash Utilization Symposium* (, Lexington, Kentucky, 2001).
[169] Aplan, F. In *Advances in flotation technology,* Parekh, B. K. and Miller, J. D., editors. Society for Mining, Metallurgy, and Exploration, Littleton, CO (1999).
[170] Uçurum, M. *Powder Technology* **191**(3), 240–246 (2009).
[171] Emre Altun, N., Xiao, C., and Hwang, J.-Y. *Fuel Processing Technology* **90**(12), 1464–1470 (2009).
[172] Baltrus, J. P., Wells, A. W., Fauth, D. J., Diehl, J. R., and White, C. M. *Energy & Fuels* **15**(2), 455–462 (2001).
[173] Niewiadomski, M., Hupka, J., Bokotko, R., and Miller, J. D. *Fuel* **78**(2), 161–168 (1999).
[174] Mehrotra, V. P., Sastry, K. V. S., and Morey, B. W. *International Journal of Mineral Processing* **11**(3), 175–201 (1983).
[175] Gray, M. L., Champagne, K. J., Soong, Y., and Finseth, D. H. *Fuel* **80**(6), 867–871 (2001).
[176] Fisher, G. L., Chang, D. P. Y., and Brummer, M. *Science* **192**(4239), 553–555 (1976).
[177] Hirajima, T., Petrus, H. T. B. M., Oosako, Y., Nonaka, M., Sasaki, K., and Ando, T. *International Journal of Mineral Processing* **95**(1-4), 18–24 (2010).
[178] Jegadeesan, G., Al-Abed, S. R., and Pinto, P. *Fuel* **87**(10-11), 1887–1893 (2008).

[179] Gurupira, T., Jones, C. L., Howard, A., Lockert, C., Wandell, T., and Stencel, J. M. In *International Ash Utilization Symposium* (, Lexington, Kentucky, 2001).
[180] Ghosal, S. and Self, S. A. *Fuel* **74**(4), 522–529 (1995).
[181] Petrus, H. T. B. M., Hirajima, T., Oosako, Y., Nonaka, M., Sasaki, K., and Ando, T. *International Journal of Mineral Processing* **98**(1-2), 15–23 (2011).
[182] Zyryanov, V. V., Petrov, S. A., and Matvienko, A. A. *Fuel* **90**(2), 486–492 (2011).
[183] Yavuz, C. T., Prakash, A., Mayo, J. T., and Colvin, V. L. *Chemical Engineering Science* **64**(10), 2510–2521 (2009).
[184] Gomes, S., François, M., Abdelmoula, M., Refait, P., Pellissier, C., and Evrard, O. *Cement and Concrete Research* **29**(11), 1705–1711 (1999).
[185] Sokol, E. V., Kalugin, V. M., Nigmatulina, E. N., Volkova, N. I., Frenkel, A. E., and Maksimova, N. V. *Fuel* **81**(7), 867–876 (2002).
[186] Zyryanov, V. and Zyryanov, D. *Journal of Environmental Protection* **1**(3), 293–301 (2010).
[187] Groppo, J. and Honaker, R. In *World of Coal Ash Conference* (, Lexington, Kentucky, 2009).
[188] Bertling, J., Blömer, J., and Kümmel, R. *Chemical Engineering & Technology* **27**(8), 829–837 (2004).
[189] IEA. Technical report, OECD, (2011).
[190] USGS. *Mineral commodity summaries 2011: U.S. Geological Survey.* (2011).
[191] Nair, M., Luo, Z., and Heller, A. *Industrial & Engineering Chemistry Research* **32**(10), 2318–2323 (1993).
[192] Huo, P., Yan, Y., Li, S., Li, H., and Huang, W. *Applied Surface Science* **255**(15), 6914–6917 (2009).
[193] Huo, P., Yan, Y., Li, S., Li, H., Huang, W., Chen, S., and Zhang, X. *Desalination* **263**(1-3), 258–263 (2010).
[194] Surolia, P. K., Tayade, R. J., and Jasra, R. V. *Industrial & Engineering Chemistry Research* **49**(19), 8908–8919 (2010).
[195] Wang, B., Li, Q., Wang, W., Li, Y., and Zhai, J. *Applied Surface Science* **257**(8), 3473–3479 (2011).
[196] Xu, X., Li, Q., Cui, H., Pang, J., Sun, L., An, H., and Zhai, J. *Desalination* **272**(1-3), 233–239 (2011).
[197] Tao, H., Yao, J., Zhang, L., and Xu, N. *Materials Letters* **63**(2), 203–205 (2009).
[198] Aixiang, Z., Weihao, X., and Jian, X. *Surface and Coatings Technology* **197**(2-3), 142–147 (2005).
[199] Wang, W., Li, Q., Li, Y., Xu, H., and Zhai, J. *Journal of Physics D: Applied Physics* **42**(21), 215306 (2009).
[200] Hu, Y., Zhang, H., Li, F., Cheng, X., and Chen, T. *Polymer Testing* **29**(5), 609–612 (2010).
[201] Pang, J., Li, Q., Wang, W., Xu, X., and Zhai, J. *Surface and Coatings Technology* **205**(17-18), 4237–4242 (2011).
[202] Cai, C., Yu, X., Shen, Z., and Xing, Y. *Journal of Physics D: Applied Physics* **40**(19), 6026 (2007).
[203] Yu, X., Shen, Z., and Xu, Z. *Nuclear Instruments and Methods in Physics Research Section B: Beam Interactions with Materials and Atoms* **265**(2), 637–640 (2007).
[204] Yu, X., Xu, Z., and Shen, Z. *Journal of Physics D: Applied Physics* **40**(9), 2894

(2007).
[205] Liu, W., Shen, X., and Li, D. *Powder Technology* **186**(3), 273–277 (2008).
[206] Meng, X., Li, D., Shen, X., and Liu, W. *Applied Surface Science* **256**(12), 3753–3756 (2010).
[207] Blanco, F., García, P., Mateos, P., and Ayala, J. *Cement and Concrete Research* **30**(11), 1715–1722 (2000).
[208] Barbare, N., Shukla, A., and Bose, A. *Cement and Concrete Research* **33**(10), 1681–1686 (2003).
[209] Johnson, A. A., Mukherje.K, Schlosse.S, and Raask, E. *Ocean Engineering* **2**(1), 45–46 (1970).
[210] Chand, N., Sharma, P., and Fahim, M. *Materials Science and Engineering: A* **527**(21-22), 5873–5878 (2010).
[211] Deepthi, M. V., Sharma, M., Sailaja, R. R. N., Anantha, P., Sampathkumaran, P., and Seetharamu, S. *Materials & Design* **31**(4), 2051–2060 (2010).
[212] Jha, N., Badkul, A., Mondal, D., Das, S., and Singh, M. *Tribology International* **44**(3), 220 – 231 (2011).
[213] Luong, D., Gupta, N., and Rohatgi, P. *JOM Journal of the Minerals, Metals and Materials Society* **63**(2), 48–52 (2011).
[214] Rohatgi, P., Gupta, N., Schultz, B., and Luong, D. *JOM Journal of the Minerals, Metals and Materials Society* **63**(2), 36–42 (2011).
[215] Ozcivici, E. and Singh, R. P. *Journal of the American Ceramic Society* **88**(12), 3338–3345 (2005).
[216] Chávez-Valdez, A., Arizmendi-Morquecho, A., Vargas, G., Almanza, J. M., and Alvarez-Quintana, J. *Acta Materialia* **59**(6), 2556–2562 (2011).
[217] Anshits, A., Anshits, N., Deribas, A., Karakhanov, S., Kasatkina, N., Plastinin, A., Reshetnyak, A., and Sil'vestrov, V. *Combustion, Explosion, and Shock Waves* **41**(5), 591–598 (2005).
[218] Yang, F. and Hlavacek, V. *Powder Technology* **104**(2), 190–195 (1999).
[219] Rubio, B. n., Izquierdo, M. T., Mayoral, M. C., Bona, M. T., and Andres, J. M. *Journal of Hazardous Materials* **143**(1-2), 561–566 (2007).
[220] Izquierdo, M. T. and Rubio, B. *Journal of Hazardous Materials* **155**(1-2), 199–205 (2008).
[221] Rubio, B. and Izquierdo, M. T. *Waste Management* **30**(7), 1341–1347 (2010).
[222] Maroto-Valer, M. M., Zhang, Y., Granite, E. J., Tang, Z., and Pennline, H. W. *Fuel* **84**(1), 105–108 (2005).
[223] Lu, Z., Maroto-Valer, M. M., and Schobert, H. H. *Fuel* **89**(11), 3436–3441 (2010).
[224] Wu, F., Wu, P., Tseng, R., and Juang, R. *Journal of Environmental Management* **91**(5), 1097–1102 (2010).
[225] Li, J. J., Cui, J., Zhao, N. Q., Shi, C. S., and Du, X. W. *Carbon* **44**(7), 1346–1348 (2006).
[226] Davini, P. *Carbon* **40**(11), 1973–1979 (2002).
[227] Cabielles, M., Montes-Morán, M. A., and Garcia, A. B. *Energy & Fuels* **22**(2), 1239–1243 (2008).
[228] Cabielles, M., Rouzaud, J.-N., and Garcia, A. B. *Energy & Fuels* **23**(2), 942–950 (2008).
[229] Cameán, I. and Garcia, A. B. *Journal of Power Sources* **196**(10), 4816–4820 (2011).

[230] Qiu, G., Zeng, W., Shi, Z., Fang, M., and Luo, Z. In *Digital Manufacturing and Automation (ICDMA), 2010 International Conference on*, volume 2, 738 –741, dec. (2010).

[231] Wang, C., Li, J., Wang, L., and Sun, X. *Journal of Hazardous Materials* **155**(1-2), 58 – 64 (2008).

[232] Potgieter-Vermaak, S., Potgieter, J., Kruger, R., Spolnik, Z., and van Grieken, R. *Fuel* **84**(18), 2295 – 2300 (2005).

[233] Yang, Y.-F., Gai, G.-S., Cai, Z.-F., and Chen, Q.-R. *Journal of Hazardous Materials* **133**(13), 276 – 282 (2006).

[234] Weidenfeller, B., Höfer, M., and Schilling, F. *Composites Part A: Applied Science and Manufacturing* **33**(8), 1041–1053 (2002).

[235] Anshits, A. G., Kondratenko, E. V., Fomenko, E. V., Kovalev, A. M., Anshits, N. N., Bajukov, O. A., Sokol, E. V., and Salanov, A. N. *Catalysis Today* **64**(1-2), 59–67 (2001).

[236] Lutterotti, L. *Nuclear Instruments and Methods in Physics Research Section B: Beam Interactions with Materials and Atoms* **268**(3-4), 334 – 340 (2010). X-ray Techniques for Advanced Materials, Nanostructures and Thin Films: from Laboratory Sources to Synchrotron Radiation Proceedings of the {EMRS} 2009 Spring Meeting - Symposium R.

[237] Downs, R. and Hall-Wallace, M. *American Mineralogist* **88**, 247–250 (2003).

[238] Font, O., Moreno, N., Querol, X., Izquierdo, M., Alvarez, E., Diez, S., Elvira, J., Antenucci, D., Nugteren, H., Plana, F., Lopez, A., Coca, P., and Pena, F. *Fuel* **89**(10), 2971 – 2976 (2010).

[239] Hurt, R. H., Davis, K. A., Yang, N. Y., Headley, T. J., and Mitchell, G. D. *Fuel* **74**(9), 1297 – 1306 (1995).

[240] Sommerville, R., Blissett, R., Rowson, N., and Blackburn, S. *International Journal of Mineral Processing* **124**(0), 20 – 25 (2013).

[241] Raw Materials Supply Group of the European Commission. (2010). Available from `http://ec.europa.eu/enterprise/policies/rawmaterials/documents/index_en.htm` [accessed online: 29-08-2013].

[242] Seredin, V. V., Dai, S., Sun, Y., and Chekryzhov, I. Y. *Applied Geochemistry* **31**, 1 – 11 (2013).

[243] Ketris, M. and Yudovich, Y. *International Journal of Coal Geology* **78**(2), 135 – 148 (2009).

[244] Seredin, V. *Doklady of the Academy of Sciences of the USSR (Translations)* **320**, 1446–1450 (1991).

[245] Seredin, V. *International Journal of Coal Geology* **30**(1-2), 101 – 129 (1996).

[246] Seredin, V. *Geology of Ore Deposits* **40**, 357–371 (1998).

[247] Seredin, V., Arbuzov, S., and Alekseev, V. *Doklady Earth Sciences* **409**(2), 967–972 (2006).

[248] Dai, S., Li, D., Chou, C.-L., Zhao, L., Zhang, Y., Ren, D., Ma, Y., and Sun, Y. *International Journal of Coal Geology* **74**(3-4), 185 – 202 (2008).

[249] Dai, S., Zhao, L., Peng, S., Chou, C.-L., Wang, X., Zhang, Y., Li, D., and Sun, Y. *International Journal of Coal Geology* **81**(4), 320 – 332 (2010).

[250] Dai, S., Jiang, Y., Ward, C. R., Gu, L., Seredin, V. V., Liu, H., Zhou, D., Wang, X., Sun, Y., Zou, J., and Ren, D. *International Journal of Coal Geology* **98**, 10 –

40 (2012).
[251] Dai, S., Zou, J., Jiang, Y., Ward, C. R., Wang, X., Li, T., Xue, W., Liu, S., Tian, H., Sun, X., and Zhou, D. *International Journal of Coal Geology* **94**, 250 – 270 (2012).
[252] Dai, S., Zhang, W., Seredin, V. V., Ward, C. R., Hower, J. C., Song, W., Wang, X., Li, X., Zhao, L., Kang, H., Zheng, L., Wang, P., and Zhou, D. *International Journal of Coal Geology* **109-110**, 77 – 100 (2013).
[253] Dai, S., Zhang, W., Ward, C. R., Seredin, V. V., Hower, J. C., Li, X., Song, W., Wang, X., Kang, H., Zheng, L., Wang, P., and Zhou, D. *International Journal of Coal Geology* **105**, 60 – 84 (2013).
[254] Dai, S., Zhou, Y., Ren, D., Wang, X., Li, D., and Zhao, L. *Science in China Series D: Earth Sciences* **50**(5), 678–688 (2007).
[255] Dai, S., Li, T., Seredin, V. V., Ward, C. R., Hower, J. C., Zhou, Y., Zhang, M., Song, X., and Song, W. *International Journal of Coal Geology.* (2013). In Press, Accepted Manuscript.
[256] Hower, J. C., Ruppert, L. F., and Eble, C. F. *International Journal of Coal Geology* **39**(1-3), 141 – 153 (1999).
[257] Mardon, S. M. and Hower, J. C. *International Journal of Coal Geology* **59**(3-4), 153 – 169 (2004).
[258] Seredin, V. V. and Dai, S. *International Journal of Coal Geology* **94**, 67 – 93 (2012).
[259] Hower, J. C., Dai, S., Seredin, V. V., Zhao, L., Kostova, I. J., Silva, L. F. O., Mardon, S. M., and Gurdal, G. *Coal Combustion and Gasification Products* **5**, 39–47 (2013).
[260] Taylor, S. R. and McLennan, S. M. *Reviews of Geophysics* **33**(2), 241–265 (1995).
[261] Hower, J. C., Groppo, J. G., Joshi, P., Dai, S., Moecher, D. P., and Johnston, M. N. *Coal Combustion and Gasification Products.* (2013). In print, Accepted Manuscript.
[262] U.S Geological Survey. (2013). Available from `http://minerals.usgs.gov/minerals/pubs/mcs/2013/mcs2013.pdf` [Accessed online: 21/11/2013].
[263] Sinnatt, F. S. *Journal of the Society of Chemical Industry* **T**, 151–160 (1928).
[264] Watt, J. D. and Thorne, D. J. *Journal of Applied Chemistry* **15**(12), 585–594 (1965).
[265] Raask, E. *Journal of the Institue of Fuel* **43**, 339 (1968).
[266] Huo, P., Yan, Y., Li, S., Li, H., and Huang, W. *Desalination* **256**(1-3), 196–200 (2010).
[267] Wang, B., Li, C., Pang, J., Qing, X., Zhai, J., and Li, Q. *Applied Surface Science* **258**(24), 9989 – 9996 (2012).
[268] Rohatgi, P., Daoud, A., Schultz, B., and Puri, T. *Composites Part A: Applied Science and Manufacturing* **40**(67), 883 – 896 (2009).
[269] Ngu, L.-n., Wu, H., and Zhang, D.-k. *Energy & Fuels* **21**(6), 3437–3445 (2007).
[270] Kolay, P. K. and Bhusal, S. *Fuel* **117, Part A**, 118 – 124 (2014).
[271] Maroto-Valer, M. M., Taulbee, D. N., and Hower, J. C. *Energy & Fuels* **13**(4), 947–953 (1999).
[272] Maroto-Valer, M., Taulbee, D., and Hower, J. *Fuel* **80**(6), 795 – 800 (2001).
[273] Raask, E. *Mineral Impurities in Coal Combusion.* Hemisphere Publishing, (1985).
[274] Browning, G. J., Bryant, G. W., Hurst, H. J., Lucas, J. A., and Wall, T. F. *Energy & Fuels* **17**(3), 731–737 (2003).

[275] Davison, R. L., Natusch, D. F. S., Wallace, J. R., and Evans, C. A. *Environmental Science & Technology* **8**(13), 1107–1113 (1974).
[276] Zwietering, T. *Chemical Engineering Science* **8**(3-4), 244 – 253 (1958).
[277] Naik, H., Mishra, M., Karanam, U. R., and Deb, D. *Journal of Hazardous Materials* **169**(1-3), 1134 – 1140 (2009).
[278] Senapati, P., Mishra, B., and Parida, A. *Powder Technology* **197**(1-2), 1 – 8 (2010).
[279] Bournonville, B. and Nzihou, A. *Powder Technology* **128**(2-3), 148 – 158 (2002). 3rd French Colloquium on Powder Science & Technology.
[280] Zhou, Z., Scales, P. J., and Boger, D. V. *Chemical Engineering Science* **56**(9), 2901 – 2920 (2001). NEPTIS 8.
[281] Batchelor, G. K. *Journal of Fluid Mechanics* **83**, 97–117 (1977).
[282] Barnes, H. A., Hutton, J. F., and Walters, K. *An Introduction to Rheology (Rheology Series)*. Elsevier Science, (1989).
[283] Krieger, I. M. and Dougherty, T. J. *Transactions of the Society of Rheology* **3**(1), 137–152 (1959).
[284] Genovese, D. B. *Advances in Colloid and Interface Science* **171-172**, 1 – 16 (2012).
[285] Stickel, J. J. and Powell, R. L. *Annual Review of Fluid Mechanics* **37**(1), 129–149 (2005).
[286] Bailey, W. J. and Weir, I. S. *Journal of Petroleum Science and Engineering* **21**(1-2), 1 – 13 (1998).
[287] Voltz, C., Nitschke, M., Heymann, L., and Rehberg, I. *Phys. Rev. E* **65**, 051402 May (2002).
[288] Barnes, H. A. *Journal of Rheology* **33**(2), 329–366 (1989).
[289] Tseng, W. J. and Wu, C. H. *Ceramics International* **29**(7), 821 – 828 (2003).
[290] Cross, M. M. *Journal of Colloid and Interface Science* **33**(1), 30 – 35 (1970).
[291] Sisko, A. W. *Industrial & Engineering Chemistry* **50**(12), 1789–1792 (1958).
[292] Turian, R., Ma, T., Hsu, F., and Sung, D. *Powder Technology* **93**(3), 219 – 233 (1997).
[293] Liu, D.-M. *Journal of Materials Science* **35**, 5503–5507 (2000).
[294] Qi, F. and Tanner, R. *Rheologica Acta* **51**, 289–302 (2012).
[295] Horri, B. A., Ranganathan, P., Selomulya, C., and Wang, H. *Chemical Engineering Science* **66**(12), 2798 – 2806 (2011).
[296] Hemrajani, R. R. and Tatterson, G. B. *Mechanically Stirred Vessels*, chapter 6, 345–390. John Wiley & Sons, Inc. (2004).
[297] Bittorf, K. and Kresta, S. *Chemical Engineering Research and Design* **81**(5), 568 – 577 (2003). Process Design.
[298] Ayranci, I. and Kresta, S. M. *Chemical Engineering Research and Design* **89**(10), 1961 – 1971 (2011).
[299] Wu, J., Nguyen, B., and Graham, L. *The Canadian Journal of Chemical Engineering* **88**(2), 287–294 (2010).
[300] Armenante, P. M. and Nagamine, E. U. *Chemical Engineering Science* **53**(9), 1757 – 1775 (1998).
[301] Hicks, M. T., Myers, K. J., and Bakker, A. *Chemical Engineering Communications* **160**(1), 137–155 (1997).
[302] Khazam, O. and Kresta, S. M. *The Canadian Journal of Chemical Engineering* **86**(4), 622–634 (2008).

[303] Joosten, G. E. H., Schilder, J. G. M., and Broere, A. M. *Trans IChemE* **55**, 220–222 (1977).
[304] Li, B. and Stenstrom, M. K. *Water Research* **50**(0), 160 – 170 (2014).
[305] Coe, H. and Clevenger, G. *Trans AIME* **55**, 356–385 (1916).
[306] Concha, F. and Barrientos, A. *KONA Powder and Particle Journal* **11**, 79–104 (1993).
[307] Heidlebaugh, S. J., Domenech, T., Iasella, S. V., and Velankar, S. S. *Langmuir* **30**(1), 63–74 (2014).
[308] van Netten, K., Moreno-Atanasio, R., and Galvin, K. P. *Industrial& Engineering Chemistry Research* **53**(40), 15747–15754 (2014).
[309] Chary, G. and Dastidar, M. *Fuel* **106**(0), 285 – 292 (2013).
[310] Alonso, M. I., Valdes, A. F., Martinez-Tarazona, R. M., and Garcia, A. B. *Fuel* **78**(7), 753 – 759 (1999).
[311] Capes, C. and Darcovich, K. *Powder Technology* **40**(1-3), 43 – 52 (1984).
[312] Petela, R. *Fuel* **70**(4), 509 – 517 (1991).
[313] Sahinoglu, E. and Uslu, T. *Energy Conversion and Management* **49**(12), 3684 – 3690 (2008).
[314] Oz, D., Koca, S., and Koca, H. *Waste Management & Research* **27**(3), 267–273 (2009).
[315] Marze, S. *Langmuir* **25**(20), 12066–12072 (2009). PMID: 19764774.
[316] Beri, A., Norton, J. E., and Norton, I. T. *International Journal of Cosmetic Science* **35**(6), 613–621 (2013).
[317] Schuch, A., Helfenritter, C., Funck, M., and Schuchmann, H. *Colloids and Surfaces A: Physicochemical and Engineering Aspects* **475**(0), 2 – 8 (2015). Selected papers from the 15th Food Colloids ConferenceDate: 14 16 April 2014Karlsruhe, Germany.
[318] Darcovich, K., Capes, C. E., and Talbot, F. D. F. *Energy & Fuels* **3**(1), 64–70 (1989).
[319] Fan, M., Tao, D., Honaker, R., and Luo, Z. *Mining Science and Technology (China)* **20**(2), 159 – 177 (2010).
[320] Schuch, A., Deiters, P., Henne, J., Kahler, K., and Schuchmann, H. P. *Journal of Colloid and Interface Science* **402**, 157 – 164 (2013).
[321] Smith, H., Winfield, J., and Thompson, L. September (2013). Available from `https://www.london.gov.uk/sites/default/files/The%20market%20for%20biodiesel%20production%20from%20UCOs%20and%20FOGs%20in%20London%20-%20September%202013.pdf` [Accessed 04-11-2014].
[322] O'Brien, K., Ménaché, J., and O'Moore, L. *The International Journal of Life Cycle Assessment* **14**(7), 621–629 (2009).
[323] Holdich, R. G., Ipek, I. Y., Lazrigh, M., and Shama, G. *Industrial & Engineering Chemistry Research* **51**(38), 12509–12516 (2012).
[324] Han, H. and Bai, R. *Industrial & Engineering Chemistry Research* **48**(6), 2891–2898 (2009).
[325] Singh, S., Mahalingam, H., and Singh, P. K. *Applied Catalysis A: General* **462-463**, 178–95 (2013).
[326] Krysa, J., Waldner, G., Mestankova, H., Jirkovsky, J., and Grabner, G. *Applied Catalysis B: Environmental* **64**(3-4), 290 – 301 (2006).
[327] Hashimoto, K., Wasada, K., Osaki, M., Shono, E., Adachi, K., Toukai, N., Kom-

inami, H., and Kera, Y. *Applied Catalysis B: Environmental* **30**(3-4), 429 – 436 (2001).

[328] Tayade, R. J., Kulkarni, R. G., and Jasra, R. V. *Industrial & Engineering Chemistry Research* **46**(2), 369–376 (2007).

[329] Subramani, A., Byrappa, K., Ananda, S., Lokanatha Rai, K., Ranganathaiah, C., and Yoshimura, M. *Bulletin of Materials Science* **30**(1), 37–41 (2007).

[330] Torimoto, T., Okawa, Y., Takeda, N., and Yoneyama, H. *Journal of Photochemistry and Photobiology A: Chemistry* **103**(1-2), 153 – 157 (1997).

[331] Jackson, N. B., Wang, C. M., Luo, Z., Schwitzgebel, J., Ekerdt, J. G., Brock, J. R., and Heller, A. *Journal of The Electrochemical Society* **138**(12), 3660–3664 (1991).

[332] Xing, Z., Li, J., Wang, Q., Zhou, W., Tian, G., Pan, K., Tian, C., Zou, J., and Fu, H. *European Journal of Inorganic Chemistry* **2013**(13), 2411–2417 (2013).

[333] Kruger, R. A. *Fuel* **76**(8), 777 – 779 (1997).

[334] Li, C., Wang, B., Cui, H., Zhai, J., and Li, Q. *Journal of Materials Science & Technology* **29**(9), 835 – 840 (2013).

[335] Chen, X. and Mao, S. S. *Chemical Reviews* **107**(7), 2891–2959 (2007). PMID: 17590053.

[336] Pelaez, M., Nolan, N. T., Pillai, S. C., Seery, M. K., Falaras, P., Kontos, A. G., Dunlop, P. S., Hamilton, J. W., Byrne, J., O'Shea, K., Entezari, M. H., and Dionysiou, D. D. *Applied Catalysis B: Environmental* **125**(0), 331 – 349 (2012).

[337] Lu, Z., Luo, Y., He, M., Huo, P., Chen, T., Shi, W., Yan, Y., Pan, J., Ma, Z., and Yang, S. *RSC Adv.* **3**, 18373–18382 (2013).

[338] Lu, Z., Huo, P., Luo, Y., Liu, X., Wu, D., Gao, X., Li, C., and Yan, Y. *Journal of Molecular Catalysis A: Chemical* **378**(0), 91 – 98 (2013).

[339] Huo, P., Lu, Z., Wang, H., Pan, J., Li, H., Wu, X., Huang, W., and Yan, Y. *Chemical Engineering Journal* **172**(2-3), 615 – 622 (2011).

[340] wen Shi, J., hua Chen, S., mei Wang, S., Wu, P., and hua Xu, G. *Journal of Molecular Catalysis A: Chemical* **303**(1-2), 141 – 147 (2009).

[341] Szabo-Bardos, E., Czili, H., and Horvath, A. *Journal of Photochemistry and Photobiology A: Chemistry* **154**(2-3), 195 – 201 (2003).

[342] wen Shi, J., hua Chen, S., long Ye, Z., mei Wang, S., and Wu, P. *Applied Surface Science* **257**(3), 1068 – 1074 (2010).

[343] Devi, L. G. and Reddy, K. M. *Applied Surface Science* **256**(10), 3116 – 3121 (2010).

[344] Sobana, N., Muruganadham, M., and Swaminathan, M. *Journal of Molecular Catalysis A: Chemical* **258**(1-2), 124 – 132 (2006).

[345] Melian, E. P., Diaz, O. G., Rodriguez, J. D., Colon, G., Navio, J., Macias, M., and Pena, J. P. *Applied Catalysis B: Environmental* **127**(0), 112 – 120 (2012).

[346] Mai, L., Wang, D., Zhang, S., Xie, Y., Huang, C., and Zhang, Z. *Applied Surface Science* **257**(3), 974 – 978 (2010).

[347] Tauc, J., Grigorovici, R., and Vancu, A. *Physica Status Solidi (b)* **15**(2), 627–637 (1966).

[348] Mollah, M. A., Hess, T. R., and Cocke, D. L. *Cement and Concrete Research* **24**(1), 109 – 118 (1994).

[349] Xin, B., Jing, L., Ren, Z., Wang, B., and Fu, H. *The Journal of Physical Chemistry B* **109**(7), 2805–2809 (2005).

[350] Deshpande, R. R. and Eckert, H. *J. Mater. Chem.* **19**, 3419–3426 (2009).

[351] Li, J. and Zeng, H. C. *Chemistry of Materials* **18**(18), 4270–4277 (2006).
[352] Zhao, B. and Chen, Y.-W. *Journal of Physics and Chemistry of Solids* **72**(11), 1312 – 1318 (2011).
[353] Konstantinou, I. K. and Albanis, T. A. *Applied Catalysis B: Environmental* **49**(1), 1 – 14 (2004).
[354] Friedmann, D., Mendive, C., and Bahnemann, D. *Applied Catalysis B: Environmental* **99**(3-4), 398 – 406 (2010).
[355] Asenjo, N. G., Santamaria, R., Blanco, C., Granda, M., Alvarez, P., and Menendez, R. *Carbon* **55**, 62 – 69 (2013).
[356] Al-Qaradawi, S. and Salman, S. R. *Journal of Photochemistry and Photobiology A: Chemistry* **148**(1-3), 161 – 168 (2002).
[357] Williams, D. *Phys. Rev. E* **57**, 7344–7345 Jun (1998).
[358] wen Shi, J., hua Chen, S., mei Wang, S., long Ye, Z., Wu, P., and Xu, B. *Journal of Molecular Catalysis A: Chemical* **330**(1-2), 41 – 48 (2010).
[359] Mehrotra, K., Yablonsky, G. S., and Ray, A. K. *Industrial & Engineering Chemistry Research* **42**(11), 2273–2281 (2003).